A Biophysical Rationalization of Type II and Reverse Type I Inhibitor Interactions in CYP450 with Implications for Enzyme Function

Kip Patrick Conner

A dissertation submitted in partial fulfillment of the requirements for the degree of

Doctor of Philosophy

University of Washington

2013

Reading Committee:

William M. Atkins, Chair

Kent L. Kunze

Nina Isoherranen

Program Authorized to Offer Degree:

Pharmacy—Medicinal Chemistry

University of Washington

Abstract

A Biophysical Rationalization of Type II and Reverse Type I Inhibitor Interactions in CYP450 with Implications for Enzyme Function

Kip Patrick Conner

Chair of the Supervisory Committee:

Professor William M. Atkins

Department of Medicinal Chemistry

This work is a characterization of small molecule azole-based inhibitor interactions in cytochrome P450 (CYP) using a complement of biophysical methodologies to provide molecular level details of the underappreciated structural complexity of low-spin (Type II and associated reverse Type I) CYP-ligand complexes. Specifically, the results herein demonstrate the tenuous structural interpretations of 'type II' ligand-induced heme spin state changes, associated UΔvis absorbance spectral signatures, and derived expectations of metabolic fate. The aim of this thesis is to challenge the historical binary classification paradigm of 'high-spin substrate' and 'low-spin inhibitor.' Chapter 1 presents an overview of the range of low-spin CYP-ligand interactions that occur within this diverse enzyme family, with an emphasis on the importance of H_2O to ligand binding and oxidative catalysis. Additionally, select literature examples are provided that demonstrate that the current understanding of type II binding and inhibition mechanism is incomplete. Chapter 2 presents evidence for several non-canonical 'type II' ligand species of diverse CYPs that were identified using a range of biophysical approaches, including electron paramagnetic resonance (EPR). During the course of characterization of the molecular details for these interactions, efforts were made to understand the catalytic properties of this category of

low-spin CYP-ligand complexes. Chapter 3 presents our findings that molecular addition of 1H-1,2,3-triazole fragment—a popular drug-like azole moiety that we have determined to favor non-canonical low-spin binding structure—to a well-documented CYP3A4 substrate 17α-ethynylestradiol, dramatically alters the binding mechanism while 'steering' the regioselectivity of oxidative turnover. Lastly, chapter 4 presents an analog azole library study that was conducted using two diverse CYPs: the promiscuous mammalian liver isoform CYP3A4, often considered a source of problematic drug-drug interactions; and the paradigmatic drug-target CYP, CYP19 (aromatase). The data suggest a large degree of variability in the importance of azole-heme interactions in the context of overall ligand binding energetics, even for high-affinity binders. Furthermore, we demonstrate by EPR and magnetic circular dichroism (MCD) that significant structural heterogeneity can be identified in the low-spin enzyme fraction in complex with tight-binding drug-like imidazoles. This heterogeneity is examined as a possible source of metabolic susceptibility and as a more accurate reporter of low-spin equilibrium conversion. The functional ramifications of heterogeneous type II interactions within this compound library will be presented in the context of a steady-state turnover analysis and metabolite characterization in CYP3A4.

TABLE OF CONTENTS

Page

LIST OF FIGURES

Figure Number Page

LIST OF TABLES

ACKNOWLEDGMENTS

I would like to thank Bill Atkins for his continuous support and friendship over the course of this thesis work—from his guidance I owe my maturation as a both a scientist and a professional. Additionally, I would like to thank Mike Dabrowski, Caleb Woods, and Matt Honaker for making my time in the Atkins lab an intellectually stimulating and enjoyable endeavor, and I especially thank them for their friendship. Finally, I thank the entire Medicinal Chemistry department for making these last six years at the UW a chapter in my life that I will always cherish.

DEDICATION

To Amber, my wife and stalwart companion—I love you.

Chapter 1

Introduction to Type II and Reverse Type I Cytochrome P450 Ligand Binding and Turnover

Note: portions of this chapter have been taken from published manuscript:

Conner, K. P., Woods, C. M., and Atkins, W. M. (2011) Interactions of cytochrome P450s with their ligands, *Archives of Biochemistry and Biophysics 507*, 56-65.

1.1 Cytochrome P450

1.1.1 Structure and Function

Cytochrome P450s (CYPs) constitute a superfamily of enzymes that have been identified in all domains of life (*1*). CYPs are formally classified as monooxygenases due to their most common role as the catalyst of atomic oxygen incorporation into saturated organic substrates, although they are sometimes referred to as 'mixed-function' oxidases due to formal oxidase activity as well (Rxn. 1). For initiation of catalysis, CYPs require 2-electron reduction from redox partner proteins which vary depending on the organism and/or the location of the isoform within the cell (*2*). Within the cell, most CYPs are located in the endoplasmic reticulum or inner mitochondrial membrane, the exception being the microbial CYPs, which are soluble (*3*). There are now several published crystal structures of a wide range of CYPs from different organisms, but most of our knowledge of CYP structure comes from earlier work conducted with the camphor 5-exo hydroxylase CYP101A1 (P450cam) from *P. putida*. P450cam is ~ 45 kDa in size (414 residues) and comprised mostly of alpha-helical secondary structure (*4, 5*). Like other CYP isoforms, P450cam contains a secluded hydrophobic interior that harbors an iron protoporphyrin IX (heme) prosthetic group, which serves as the catalytic redox center of the

enzyme. CYP heme is ligated to the protein via a cysteine residue (C357 in P450cam), which provides the axial thiolate iron ligand that is important in regulating both iron spin equilibria and oxidation state essential to the catalytic function of the enzyme (*1, 4, 6*). In the low-spin (S = ½) ferric resting state, the heme is coordinated by a water molecule at the distal axial position, which provides the six ligand necessary to maintain the relatively unreactive hexacoordinate heme geometry that predominates for most purified CYPs (*7-10*).

(Rxn. 1) $NADPH + O_2 + RH \rightarrow NADP^+ + H_2O + ROH$

1.1.2 Physiological Role

The monooxygenase activity harnessed by CYPs serves many functions to many different organisms, including de novo biosynthesis and oxidation of key metabolic intermediates essential to homeostasis. For example, in humans, enzymes CYP11B2 and CYP51 catalyze key biotransfomations during corticosteroid and cholesterol production, respectively. The importance of CYPs to human health is unquestionable. CYPs play a crucial role in mammalian detoxification; the membrane-bound hepatic CYPs serve to oxidize lipophilic xenobiotics, such as pharmaceutical drugs, to more water-soluble forms that can then be easily excreted (*4*). In addition, CYPs comprise a wide range of therapeutic targets both of human origin and contained within deadly pathogens. For example, the attenuation of estrogen production in women through inhibition of CYP19 (aromatase) is an important breast cancer treatment (*11*); and in pathogenic fungi and yeast, inhibition of CYP51A1 is a strategy to combat infection by depriving the microbe of the essential cell wall component ergosterol (*12*). Recently, the discovery of at least twenty CYPs encoded in the genome of *Mycobacterium tuberculosis* (*Mtb*) (*13, 14*), some

demonstrated to be essential for viability (*15*), implicate CYPs as urgently needed novel drug targets to combat Tb infection.

1.1.3 Spin state, redox potential, and catalytic mechanism

CYP function is inextricably linked with the electronic properties of the heme cofactor. When attempting to rationalize CYP-mediated catalysis, it is necessary to take into consideration the complex relationship between the iron spin state equilibrium (Figure 1.1), its effects on the redox potential of the heme to favor/disfavor reduction by redox partner proteins, and ultimately how ligand binding influences all of these processes. Much of our knowledge of the complex catalytic machinery of CYPs comes from early work with P450cam. In this bacterial isoform, Sligar demonstrated that ligand binding-induced spin state shifts are well-coupled to changes in redox potential (*16*). Based on these early findings, it was tempting to speculate that *all* CYP enzymes orchestrate these processes as an efficient gating mechanism to avoid the unnecessary and potentially deleterious effects of redox cycling in the organism. However, over the years it has become apparent that P450cam represents the exception more than the rule, at least in vitro, and a definitive relationship between ligand binding, spin state equilibria, and electrochemical midpoint potential has yet to be demonstrated (*7*). This apparent incongruence is perhaps most evident for the detoxification CYPs (*7*).

1.1.4 Historical CYP-ligand biophysical classification paradigm

Fortuitously, the complex electronic machinery of the CYP heme provides an accessible 'spectroscopic handle' that allows for the application of several informative biophysical techniques to characterize the molecular and electronic structural details of ligand binding, which can be useful when rationalizing metabolism (or lack thereof). The most convenient technique to monitor heme spin state equilibrium is UV/vis absorbance, and it has historically served as a reporter of ligand binding as well. Depending on the isoform, the diversity of CYP ligands both endogenous and xenobiotic, is enormous, and so any simple classification of substrates and inhibitors would seem impossible. Yet despite this impracticality, a simple absorbance-based spectral classification paradigm (*17-19*) was contrived early on that grouped ligands on the basis of up to three generic absorbance spectral signatures: type I, type II, and reverse type I. A type I spectral response is characterized by an apparent blueshift of the heme Soret band that results from an increase in fractional high-spin (heme iron, S = 5/2) enzyme form that exhibits spectral features in the region between ~380 - 390 nm (*18*). These spectral changes are observed most clearly in absorbance difference spectra (Figure 1.2). Structurally, a type I spectrum is often indicative of a change in heme coordination geometry to a pentacoordinate state, and it is generally accepted that ligand binding can affect the elimination of the H_2O axial heme ligand (*20*). In P450cam, type I binding of camphor substrate is thermodynamically coupled with the heme iron spin and redox equilibria, as was elegantly demonstrated by Sligar and Gunsales (*16, 21*). Traditionally, type I ligands are anticipated to be good substrates based on these early observations. In contrast, a type II spectral response is characterized by a redshift of the heme Soret band concomitant with a decrease in fractional high-spin enzyme content (*22*). Type II ligand complexes are anticipated to consist of a hexacoordinate heme geometry with coordinate bond donor function provided by the ligand to *replace* axial H_2O (*22, 23*). Functionally, type II

CYP-ligand complexes are anticipated to be catalytically inactive because hexacoordinate low-spin heme is difficult to reduce (*24*). Lastly, the rather anomalous reverse type I or 'modified type II' spectral classification is reserved for cases where ligand binding induces an increased fraction of the *native* low-spin enzyme species, observed by absorbance as an increase in intensity of the Soret band with little or no corresponding redshift. Some reverse type I ligand complexes have been shown to negatively affect the rate of heme reduction in P450cam, possibly indicating a depressed redox potential relative to the ligand-free state (*19*). However, no consensus has been reached for reverse type I ligand structure.

The following two sections provide an extensive literature review with emphasis on the more recent CYP research to provide key examples that illustrate additional levels of structural complexity related to low-spin ligand binding and its often irreconcilable effects upon enzyme catalysis. Additionally, the importance of H_2O to binding and catalysis in CYPs will be highlighted, a topic we feel is necessary to review prior to presentation of our novel structural results in chapters two and three.

1.2 Literature Review: Kinetic and structural complexity related to type II CYP ligand binding

A general classification of a ligand as high-spin or low-spin, substrate or inhibitor, can be a difficult task because kinetic and structural data confound such superficial distinctions. For example, Guengerich and co-workers have observed complex binding kinetics of the CYP3A4 substrates (type I) bromocriptine and α-naphthoflavone using stopped-flow absorbance and fluorescence methods that monitor binding during the pre-steady state (*25*). Isothermal titration calorimetry (ITC) and equilibrium absorbance suggested a 1:1 binding stoichiometry that

prompted the authors to propose a multi-step binding mechanism involving an initial fast interaction at a peripheral, or 'heme-silent' binding site. A follow up study by the same group focused on low-spin inhibitor binding (ketoconazole, itraconazole, clotrimazole, indinavir, and morphiceptin) to CYP3A4 and determined that these ligands bind by a three-step sequential binding mechanism that appears to be even *more* complex than that of high-spin substrates, although it is unlikely that a clear mechanistic distinction between high-spin and low-spin ligands exists (*26*). The fluorescent species morphiceptin was utilized to confirm that inhibitors can also form a similar heme-silent 'encounter complex' represented by the initial fast phase not detected by absorbance. Interestingly, significant differences between the individual kinetic parameters were recovered for inhibitors of similar binding affinity. One alternative explanation to the complex kinetics observed is the existence of a heterogeneous mixture of enzyme populations in dynamic equilibrium, each population harboring a different affinity for ligand (*27*). A novel sequential mixing approach was used to address this issue in which testosterone pre-mixing followed by injection of low-spin inhibitor indinavir did not reveal a slow conformational rearrangement, suggesting a single enzyme species or rapidly interconverting species. Others have proposed similar heme-silent binding sites based on structural and spectroscopic data acquired at equilibrium (*28, 29*) and molecular dynamics (MD) calculations have been used to rationalize the functional relevance of these sites (*30*). Alternative explanations of heme-silent binding to the *active site* of CYPs have been suggested as well, which are supported by crystallographic evidence of CYP-H_2O-ligand ternary complexes, as well as by discrepancies between K_s values measured by UV/vis absorbance titration and K_i via functional assay (*31-34*). This highlights the potential inadequacy of heme spin state perturbation as a marker to distinguish between substrates and inhibitors.

All of these observations suggest that low-spin CYP ligands should not be equated with CYP inhibition. Several lines of evidence suggest low-spin species can bind CYPs in complex ways and at many different points in the catalytic cycle; in fact, there are numerous examples of inhibitors that also behave as substrates. In an investigation into the apparent heterotropic cooperativity observed between 1-alkoxy-4-nitrobenzenes (ANBs) and 1,4-phenylene diisocyanide (PDI), Isin et al. reported complex association kinetics for the low-spin isocyanide inhibitor binding to rabbit CYP1A2 in both the ferric and ferrous enzyme states as measured by stopped-flow absorbance (*35, 36*). PDI binding to both redox states was multiphasic, each interaction marked by a zero-order slow phase which was suggested to represent a ligand-induced CYP conformational change on the basis of circular dichroism (CD) results. Intriguingly, PDI was found to increase the affinity of ANBs for CYP1A2 but resulted in inhibition of turnover. Notably, the unique absorbance properties of ferrous-CYP-bound PDI (λ_{max}= 455 nm) as well as its reversible binding nature may render this molecule a potential probe for characterizing mechanisms of CYP inhibition by type II species that have additional access points within the CYP catalytic cycle. Structural characterization by X-ray crystallography and FT-IR of alkyl isocyanide binding to P450cam and P450nor (of *Fusarium oxysporum*) provides insight into the origin of these peculiar low-spin spectral signatures (*37*). It must be emphasized that the unique spectral properties of PDI allowed the authors to monitor *direct reduction* of a hexacoordinate ferriheme—a task that is difficult to achieve with type II species. Furthermore, observations of direct reduction of ligand-coordinated heme may be useful for explaining type II ligand turnover, a phenomenon described by Jones and co-workers who screened a series of pyridinyl quinoline-4-carboxamide analogs against CYP3A4 and observed marked turnover of tight-binding type II ligands (*38*). Results such as this suggest that high

affinity heme Fe-N interactions do not always equate with metabolic stability or inhibition (Figure 1.3).

This is suggested also by results from surface plasmon resonance (SPR) study of azole antifungal drugs binding CYP3A4. These experiments provided further insight into the complexity of type II ligand interactions with their CYP binding partners. Pearson et al. observed characteristically slow and multiphasic rates of dissociation for the CYP3A4 inhibitors itraconazole (ITZ) and ketoconazole and attributed this behavior to partially rate-limiting Fe-N bond scission (*39*). An imidazole pre-loading scheme was employed that nearly eliminated the slow component of ligand dissociation, prompting the authors to propose a parallel trajectory binding model in which both productive and inhibitory binding modes are possible. This was consistent with ITZ oxidation at a site ~ 25 Å away from the triazole moiety that coordinates heme iron. The attractiveness of SPR to monitor CYP-ligand interactions lies in its ability to provide both kinetic and thermodynamic insight without reliance on spin state perturbation.

It has been suggested that additional details of low-spin binding to CYPs can be gleaned by comparing conventional UV/vis binding spectra to reference molecules containing the same heme coordinate ligand moiety. In particular, it has been suggested that sub-optimal Fe-N dative bonding can be deduced on the basis of decreased magnitude of the Soret band redshift or less than maximal fractional decrease in intensity for high-spin absorbance (~ 388 nm) relative to the parent spectrum at protein saturation (*40*). Insight into the relationship between spin state equilibrium elicited by a ligand and its rate of oxidation have been a historical challenge in the CYP field and would be invaluable for rationalizing complex behavior exhibited by low-spin species. Compounds that display spectrally discernable complex heme-binding interactions, such as the pyrimidineimidazole iNOS inhibitor PH-302 investigated by Hutzler et al., may be useful

as low-spin CYP probes of molecular reorientation at the level of the heme once bound (*41*). PH-302 contains both an imidazole moiety as well as a methylenedioxyphenyl function, and as a result was found to display both competitive and mechanism-based inhibition properties during midazolam and testosterone turnover by CYP3A4. Two separate heme ligation states were observable by absorbance during turnover conditions which can be accounted for by the formation of a pseudo-irreversible carbene complex in addition to the anticipated imidazole type II interaction. Spectral binding analysis suggested incomplete coordination of the imidazole moiety to the ferric heme state, as judged by only 72% conversion of maximal absorbance difference relative to the steric-free reference compound imidazole (*40*). Interestingly, under turnover conditions MI complex formation was biphasic in which a fast inhibitory phase was found to plateau after only 3min. Both imidazole and carbene ligation modes were detected simultaneously, supporting either a heterogeneous enzyme population model, or slowly equilibrating complexes.

The possibility for a range of unique type II binding modes is now appreciated in the drug design arena. Ortiz de Montellano and co-workers have designed CYP-selective imidazole inhibitors in silico (*42*). Using both wild-type and L244A mutant structures of P450cam, a modified version of the program DOCK was employed to design a library of imidazole-based inhibitors and the top-scoring compounds were selected for synthesis. This was the first report of computer-assisted CYP drug design where the Fe-N coordinate bond was explicitly parameterized to accommodate a range of bond lengths and bond angles to account for the possibility that multiple low-spin ligand binding modes exist for this scaffold. Remarkably, multiple compounds selected for synthesis displayed a high degree of selectivity (some up to 100-fold) on the basis of IC_{50}, where a series of 1,5-disubstituted imidazole species preferred the

augmented active site volume of the L244A mutant. Furthermore, a large discrepancy between IC_{50} results and K_s values was reported; the affinity measured by equilibrium absorbance did not display a similar CYP selectivity. Results such as this highlight the potential perils of screening type II inhibitor candidates solely by absorbance measures. Lastly, both P450cam and its L244A mutant displayed near identical affinity and coupling efficiency with camphor as substrate but when titrated with imidazole via UV/vis, the mutant displayed a 43-fold lower affinity for the type II reference ligand, suggesting that intrinsic heme affinity was altered by the mutation, possibly due to alterations in active site hydrodynamics or field effects as suggested by others (*43*). Additional studies by Peng et al. have demonstrated the importance of 'optimal' Fe-N coordinate bond formation for maximizing low-spin ligand affinity. This group assessed the steric requirements for a series of pyridinyl quinoline-4-carboxamide analogs and found that optimal positioning of the nitrogen atom in the pyridine moiety can increase ligand affinity up to 1200-fold in binding to CYP3A4 (*38, 44*). However, as was mentioned earlier in this review, the same group found no apparent correlation between type II compound affinity and metabolic stability. In addition to sterics, additional physicochemical properties of a given type II species are expected to influence interactions at the level of the heme (*31, 45-48*). Electronic effects have been observed to influence type II compound affinity for a series of para-substituted arylamines binding to rabbit CYP2B4; surprisingly, a negative correlation was observed between compound basicity and type II binding affinity on the basis of Hammett substituent constants (σ_p), suggesting a complex interplay between ligand protonation state and overall molecular dipole as determinants of low-spin binding (*49*).

Recent work by the Munro group to characterize reduction kinetics of *Mycobacterium tuberculosis* CYPs 121 and 51B1 has illuminated additional complexity that may exist for type II

species interacting with heme under turnover conditions (*50*). Rapid reduction of CYP by laser photoexcitation of NADPH across a range of CO concentrations revealed key differences between the two isoforms. CYP121-CO complex formation was biphasic and reduction rates exhibited a hyperbolic dependence on CO concentration, consistent with the presence of a CO binding site in ferric CYP121. In contrast, reduction kinetics for CYP51B1 were monophasic and second order with respect to CO concentration suggesting that CO did not bind ferric CYP51B1. Most interestingly, CO binding to CYP121 induced an equilibrium between P450 and P420 species that was pH dependent, suggestive of thiolate protonation and subsequent dissociation from the heme upon binding of this low-spin diatomic ligand to form a stable pentacoordinate complex. P420 was detected upon reduction of CYP51B1 as well but was *not* dependent on CO binding, and this conversion was found to be essentially irreversible within a pH range compatible with the stability of the enzyme. These unusual findings suggest type II ligand interactions with these potential drug target CYPs may be expected to be highly complex.

Additional work by the Ortiz de Montellano group aimed at characterizing novel *Mtb* CYPs and their interaction with type II ligands was reported for CYP130 binding to a series of arylamines as well as the antifungals econazole and clotrimazole (*51, 52*). Interaction of this CYP with econazole induced a ‘closed’ dimer structure during co-crystallization studies. In addition, the conserved Gly-Gly I-helix sequence element, also observed in related *Mtb* isoforms CYP141 and CYP142, appears to favor an angular coordination mode. Multiple species screened displayed affinity for the ferrous-heme state. Interestingly, mutation of this sequence element (G243A) reverted the spectral binding properties of multiple species to type I; however, for clotrimazole and econazole type I reversion was met with a surprisingly minor loss in binding affinity, possibly reflecting the strain already present in their unique coordinate-bonding pose.

This sequence element was shown to affect the hydration state of the heme, as the G243A mutation induced the loss of three crystallographic water molecules in the x-ray structure in between the I-helix and Fe. The authors point out that the Fe-O bond distance (H_2O-coordinated resting state) grows slightly shorter in the mutant, which agrees with the slight redshift in the resting state Soret maxima.

One final structural example that highlights the complexity of low-spin ligand binding to CYPs comes from a recent article by Lampe et al. describing conformational sub-states of CYP119 of archeabacterium *Sulfolobus acidocaldarius* as resolved by 2D $^{13}C/^{1}H$ HSQC NMR (*53*). The site-specific labeling scheme of Shultz et al. (*54*) was utilized to insert ^{13}C-methoxyphenylalanine residues into the F/G helix 'hinge' region of the protein at three unique phenylalanine residues. Upon titration of each single mutant with either imidazole or 4-phenylimidazole inhibitor, a new chemical shift was observed at intermediate concentrations, which then faded into a new unique signal at protein saturation. Interestingly, the resonance associated with the ligand-free protein conformation did not disappear even when the enzyme was saturated with inhibitor species. Conversely, when the CYP119 single mutants were titrated with high affinity type I substrate lauric acid, only one unique resonance appeared, attributed to a substrate bound enzyme conformation. The authors suggest these spectra indicate the presence of different accessible conformational substates of the inhibitor-bound CYP119, and that these are unique from the predominant conformation in substrate bound CYP119.

Ligand interactions with CYPs often lend themselves to ambiguity, rendering any generalization or classification of the particular complex formed tenuous. The aim of this portion of the review was to present kinetic and structural observations of 'low-spin' CYP-ligand binding that highlight the inherent difficulty in extrapolating functional expectations for a given

CYP-ligand complex based on classic criteria such as heme spin state perturbation, or more recent approaches such as crystallographic analysis. It should be apparent to the reader that there exists a continuum of potential 'type II' interactions between species bearing an available electron pair for coordination to heme iron of CYPs. Low-spin species do not behave exclusively as inhibitors of CYPs, and complete characterization of a given low-spin CYP ligand would have to account for the possibility of ensembles of heme ligation geometries, coordinate bonding energies, the possibility of ligand affinity for multiple redox states and catalytic cycle entry points, as well as a preference for binding locations other than heme in the often plastic interior of the CYP active site. Thus, our current understanding of low-spin CYP-ligand interactions is incomplete. It is now clear, however, that ligands that increase the apparent fraction of low-spin ferric heme are not simply competitive inhibitors.

1.3 Literature Review: The role of H_2O in ligand binding to CYPs

The hydration state of a protein is a key determinant for ligand binding. When attempting to rationalize ligand affinity, bulk hydrophobic effects are often invoked to explain the thermodynamic driving force behind the formation of a given ligand-receptor complex. However, it is now well-appreciated on the basis of structural, spectroscopic, and computational evidence that H_2O plays an integral role in CYP-ligand interactions by affecting CYP substrate/inhibitor specificity *or* promiscuity, as well as the CYP catalytic cycle. In fact, H_2O must be considered as a specific ligand in order to understand fully the catalytic cycle and binding behavior of substrates and inhibitors, and our inclusion of this topic reflects the recent appreciation of this. This portion of the review will address the intricate role that active site

water plays in the interaction between CYPs and their ligands. In addition, recent computational approaches that aim to characterize CYP active site hydrodynamics so as to improve the predictive power of docking and molecular dynamics simulations will be discussed.

As is the case when attempting to categorize interactions between CYPs and their ligands, no general rules exist to describe the dynamics of H_2O at the active site for the entire CYP protein family. Active site hydration appears to be a variable property among CYP isoforms of both prokaryotes and eukaryotes, and water participates in ligand binding and catalysis to differing extents across the enzyme family (*55-57*). The interplay between heme electronic spin state and H_2O residence as the 6^{th} coordinate-axial ligand is perhaps the most well-studied phenomenon, with much of our understanding derived from work with P450cam (*8, 9, 16, 58*). However, a definitive relationship between heme aqua ligation state, free and ligand-bound spin state equilibrium, and electrochemical midpoint potential remains tentative despite the intuitive advantages for catalysis, as demonstrated for P450cam (*7*).

The oversimplification of many CYP-ligand binding models in which substrates/inhibitors completely displace the water molecule from the 6^{th} axial iron coordination position to generate a high-spin ferric heme, or replace the axial water to generate an alternate low-spin heme, is emphasized in literature reports of incomplete conversion of the resting spin state upon ligand saturation (*7, 59*). In 2001, Haines et al. proposed a possible mechanism based on high-resolution x-ray crystal data to explain the apparent equilibrium that exists between high and low-spin states for bacterial P450 BM3 (CYP102A1) when saturated with a novel high-affinity fatty acid substrate N-palmitoylglycine (*60*). The crystal structure of the recombinantly expressed heme-binding domain of P450 BM3 (BMP) bound to N-palmitoylglycine revealed an intricate interplay of interactions between two crystallographic water molecules (wat500 &

wat501) and specific residues of the I-helix, which the authors hypothesize to be an example of a ligand-induced 'molecular switch.' Comparison to the apo-BMP structure shows that ligand binding triggers F-G helical lid closure and relieves a slight kink in the I-helix by displacement of wat501; this I-helical shift displaces wat500 from the 6th coordinate heme position (termed "L" site) to a position parallel and displaced to the side of the heme (termed "H" site) where it is involved in H-bonding with Ala264 and a conserved Thr268. The close proximity of wat500 to the heme oxygen binding site could explain the low-spin BMP detected at saturating ligand concentrations: equilibrium partitioning between H and L sites is proposed because there is only enough room to accommodate a single water molecule in the combined regions. Wat500 is also ideally positioned to facilitate proton delivery during the O_2 heterolytic bond-scission step of catalysis. The fact that substrate binding alone cannot account for direct displacement of the axial water ligand because of its inadequate proximity to the heme suggests that these structural features are indeed a molecular switch involving structural waters, at least for this heme-binding domain. Interestingly, the conservation of I-helix residue Thr268 across the CYP family suggests ordered water in ligand-induced structural/functional dynamics to be a general case in many CYPs (*61-63*).

As an interesting contrast, P450eryF (CYP107A1) exemplifies the importance of water-directing machinery for ligand binding and catalysis in a unique fashion. P450eryF lacks the Thr268 that is essential for water positioning and oxygen binding for efficient turnover in P450 BM3, but harbors two similarly ordered water molecules in complex with its natural substrate 6-deoxyerythronolide B (*61, 62, 64, 65*). Nature has apparently accommodated a deficiency in P450eryF water-directing machinery through a high degree of substrate selectivity, in which the preferred substrate contains a hydroxyl group that directs water to the required locations. Thus,

one possible evolutionary mechanism for achieving promiscuous behavior displayed by certain mammalian CYPs may have been to incorporate water-directing active site architecture to facilitate proton transfer (and co-substrate positioning) rather than rely on a ligand bearing the necessary functional group.

In addition to H_2O-heme interactions, hydration of substrates and inhibitors is a critical determinant of their binding affinity and orientation. Crystal structures demonstrate unique interactions between ordered water molecules and CYP ligands that may help rationalize their conformational binding modes, affinity, and catalytic fate. Seminal crystallographic studies by Poulos et al. with P450cam bound to phenylimidazole inhibitors reveal vastly different binding modes for ligands of similar structure (*23*). The 2-phenylimidazole complex contains two crystallographic waters, one forming key H-bonds (95% occupancy, B-factor of 0.25 nm^2) with imidazole nitrogen. The other water remains ligated to the 6^{th} coordinate position of the heme, and the phenyl moiety of 2-PI apparently is not positioned to induce a high-spin conversion. Subsequent MD simulations performed by Harris et al. have confirmed the importance of the former water for ligand orientation (*66*). Comparison of the 4-PI and 1-PI inhibitor complexes is interesting because both have similar type II binding modes, with an imidazole nitrogen coordinating directly to heme iron, but their experimentally measured binding affinities differ by 400-fold (40 μM vs. 100 nM for 4-PI and 1-PI respectively). This discrepancy is postulated to be the result of an additional dehydration energy penalty with 4-PI binding due to the lack of H-bond donors close to the heme that can interact with the free sp^2 nitrogen atom on the imidazole ring, not present in the 1-PI structure. Additional P450cam ternary complexes have been published for other substrates—all contain axially ligated water (*32, 67*).

Recently, a 'ternary' complex between water and the azole antifungal drug fluconazole (FLU) bound to CYP121 of *Mycobacterium tuberculosis* was resolved by x-ray crystallography, revealing a novel type II inhibitor binding mode to be dominant within the crystallographic asymmetric unit (*33*). Binding of FLU to CYP121 as measured by UV/vis absorbance led to a slightly lower than average absolute Soret band redshift for an azole ligand centered at ~ 422 nm, which others have postulated to signify 'incomplete' heme coordination (*40*). Both magnetic circular dichroism (MCD) and electron paramagnetic resonance (EPR) measurements corroborated this ligation state to be the dominant binding mode; interestingly, only the water bridged low-spin binding mode was detected by EPR until the addition of 50% glycerol. Density functional theoretical calculations performed by Balding et al. examined the energetics of complex formation between model azole species and a heme center, and showed that there was only a slight difference in energy between the water-bound resting heme state and that of the methyltriazolate-bound complex, supporting the existence of these two equilibrated binding modes (*68*). The unusual ligation mode of FLU in CYP121 was the impetus for incorporation of an additional H-bond interaction between an ethanol molecule and the 6th coordinate water ligand into calculations of inhibitor complexation, an adaptation that mimics the interaction between Ser237 and the distal heme ligand in the CYP121 active site. These results suggest that additional H-bonding interactions with CYP active site residues can determine the relative proportion of these the two low-spin binding modes (Figure 1.4).

Given the complexity of the behavior of water with regards to CYP-ligand interactions, it may come as a surprise that CYPs are actually an attractive receptor system for computational modeling of active site hydrodynamics due to their internalized active sites that are normally isolated from the bulk solvent. This aspect of CYPs allows for clear distinctions to be drawn

between active site water and solvent water and many groups have devised methods aimed at minimizing the subjectivity in this distinction (*55, 69*). An increasing number of groups are now employing water in MD and docking simulations in an attempt at quantifying its precise role in mediating CYP-ligand interactions. Helms et al. have employed a unique MD approach to calculate the energetics of hydrating cavities that form at protein-ligand interfaces in P450cam (*70*). The authors had previously utilized GRID-based methods to calculate interaction energies between a probe water molecule and grid points along the ligand-protein interface of a camphor-bound P450cam structure (*71*). A site for specific water molecule addition was hypothesized to explain the regioselectivity of camphor oxidation, termed site D, which would place water near a hydrophobic Phe cluster but would be stabilized by the H-bond accepting carbonyl of camphor (*71-74*). The group employed MD simulations using the methods of multiconfigurational thermodynamic integration (MCTI). The results of this study confirmed the validity of the crystallographic findings in that hydration of site D with camphor bound was 15.8 ± 5.0 kJ/mol unfavorable. An equivalent calculation with the 2-phenylimidazole-bound P450cam complex also agreed with the structural data, predicting the interaction between a water molecule and 2-PI to be favorable by 11.6 +/- 6.6 kJ/mol. Importantly, this comparison demonstrates the ability of the technique to differentiate between a hydrated and dehydrated active site. Similar MCTI approaches have estimated 5 to 6 water molecules to be the optimal hydration state of ligand-free P450cam, also in agreement with structural data and hydrostatic pressure studies (*75, 76*). More recent simulations include those conducted by Santos et al. in which 'thermodynamic' waters were identified in the mammalian CYP2D6 in complex with (R)-3,4-methylenedioxy-N-ethylamphetamine (MDEA), also by GRID methods (*77*). Top-scoring water clusters were chosen on the basis of average residence times at specific grid points within the 2D6 active site.

Interestingly, the inclusion of water at the identified clustering (or thermodynamic clustering) sites when docking MDEA and MDEA-like ligands improved the predictive power of the docking simulations. Furthermore, it is worth mentioning that inclusion of these same water molecules in docking calculations with substrates of disparate structure relative to MDEA were not successful, highlighting the possibility that water networks within the CYP active site may adapt as necessary to optimize a given CYP-ligand binding interaction. Rydberg et al. have also utilized MD simulations to study water dynamics within the active sites of CYPs 2A6, 2C8, 2C9, and 3A4 in order to assess any discrepancy between actual hydration state of the protein in solution and that observed in the available crystal structures (*55*). MD was able to identify numerous access/egress channels available for water exchange, with no two CYPs displaying the same usage of these conduits. The extent of hydration amongst the isoforms is highly variable, and the density of resident water was estimated to be ~20% less than that of bulk solvent. In addition, many of the channels identified were only observable over the course of the simulation, highlighting the dynamic interaction that exists between CYPs and their external solvent environs. Interestingly, there are no waters close to the heme during these simulations, which was parameterized in the high-spin ferric state. Similar ligand access/egress channels (Figure 1.5) have been defined by Wade et al. for these four CYPs using alternate computational approaches (vide infra) (*69, 78*).

These examples highlight the potential importance of specific roles for H_2O in mediating ligand-protein contacts, ligand-heme interactions, and ligand-dependent protein conformational changes. The progress demonstrated in computational treatment of water in the past few years will likely result in increased understanding of these roles in additional CYP-ligand complexes.

1.4 Summary

The literature examples included in this introductory chapter were intended to emphasize that CYP-ligand interactions are inherently complex, so any attempt to categorize substrates and inhibitors based solely on generic optical absorbance criteria appears futile. However, as will be demonstrated throughout this dissertation, the spectroscopic properties of CYPs do render the molecular details of their ligand-bound structures accessible as long as one shrugs aside structural expectations based on inveterate dogma. The remainder of this dissertation will highlight our efforts to identify and characterize, via spectroscopic methods, novel low-spin CYP-ligand complexes in hopes of drawing forth an appreciation for the inherently complex CYP-ligand, CYP-H_2O, and CYP-H_2O-ligand interactions that occur at the level of the heme cofactor. It is our belief that only when the full *range* of CYP-ligand interactions that occur is fully appreciated, can we begin to rationalize unexpected functional outcomes such as facile metabolism of apparent type II ligands.

Figures

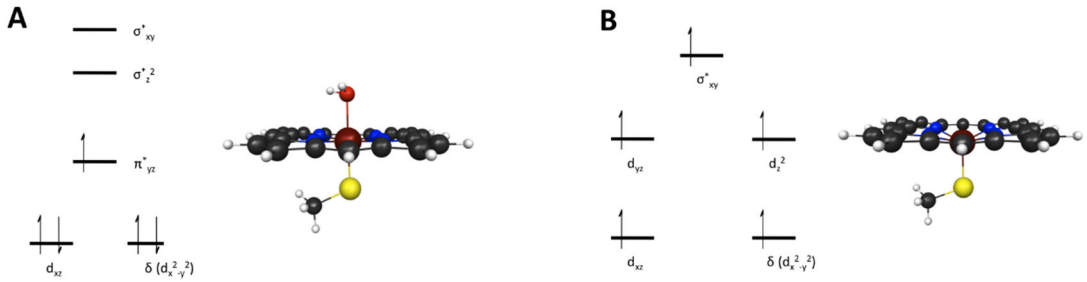

Figure 1.1. (A) The low-spin (S = 1/2) hexacoordinate resting state of a model porphyrin is represented with relative orbital energies, labels, and occupancy adapted from Shaik et al. (*10*). (B) The high-spin (S = 5/2) pentacoordinate state of a model porphyrin with orbital occupancy is also shown. The authors would like to draw attention to the differences in heme geometries, with the iron in the plane of the porphyrin macrocycle for the low-spin species and slightly below the plane for the high-spin species. In both high and low-spin cases, the relative energies of the d-type orbitals are not degenerate, and do not adopt the 'two over three' splitting pattern common for ferric iron in an octahedral geometry because of the heterogeneous nature of the coordinating ligands.

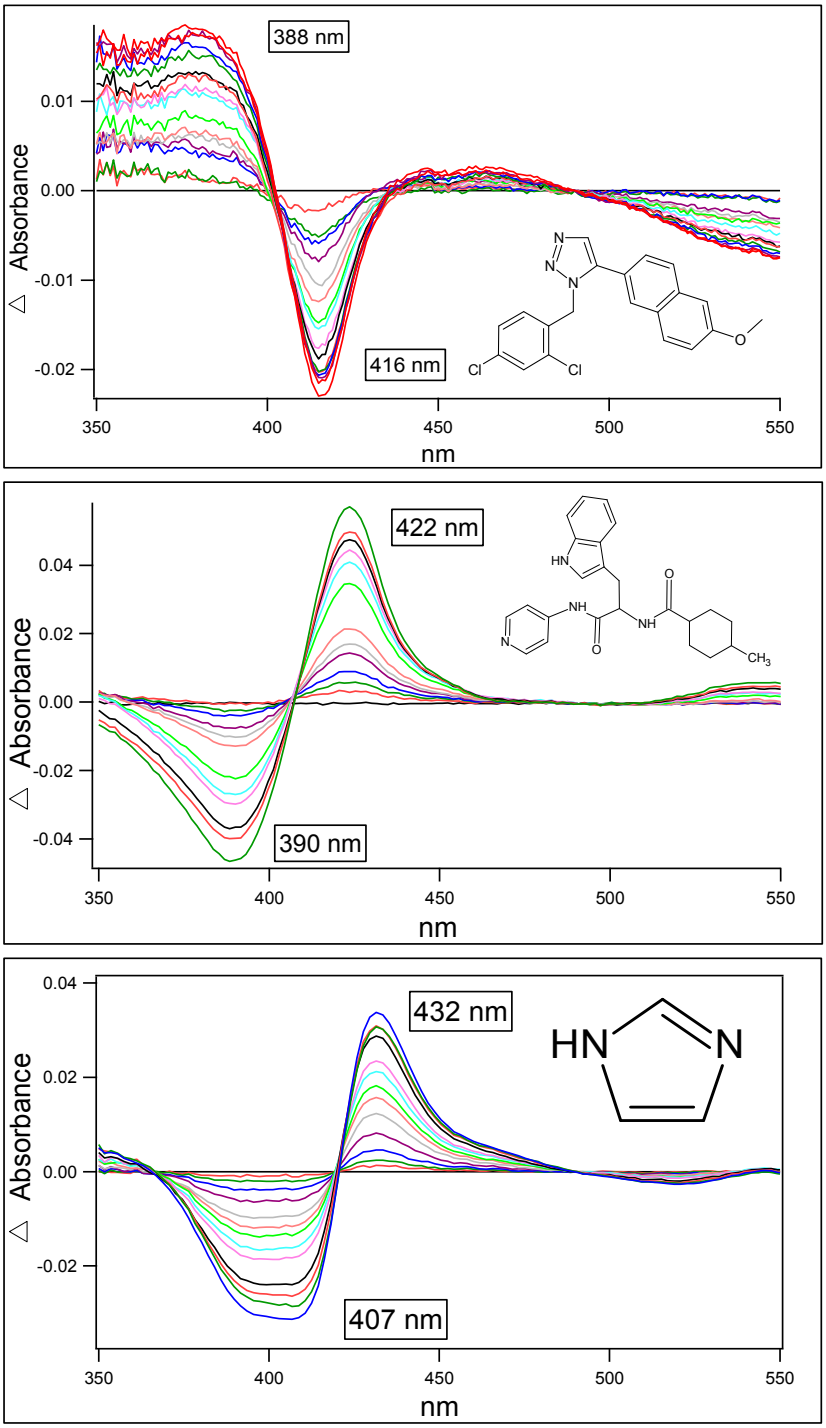

Figure 1.2 Representative UV/vis absorbance difference spectra for various CYP ligand categories. (Top) Type I spectrum of CYP19 (human aromatase) in complex with 1-(2,4-dichlorobenzyl)-5-(6-methoxynaphthyl)-1,2,3-triazole; (middle) Reverse type I spectrum of CYP125A1 in complex with pyridine-base inhibitor LP10; (bottom) Type II spectrum of CYP3A4 in complex with imidazole.

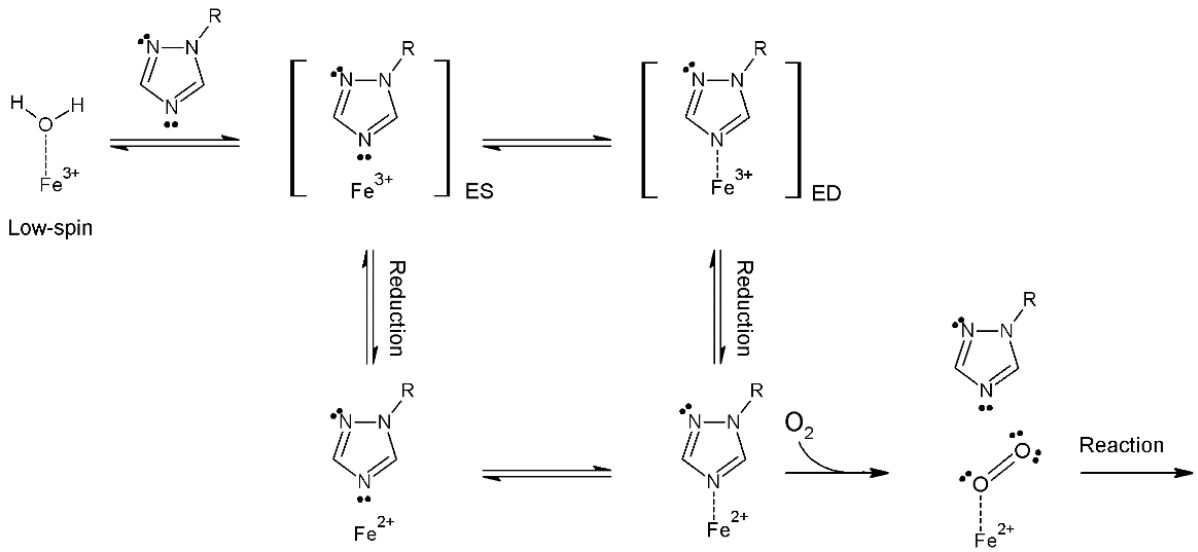

Figure 1.3: Schematic depicting possible kinetic mechanism of type II ligand binding and turnover. Both penta and hexacoordinate heme-iron states are shown, with direct reduction of hexacoordinate low-spin heme-ligand complex also depicted. ES = enzyme substrate complex; ED = dead-end complex.

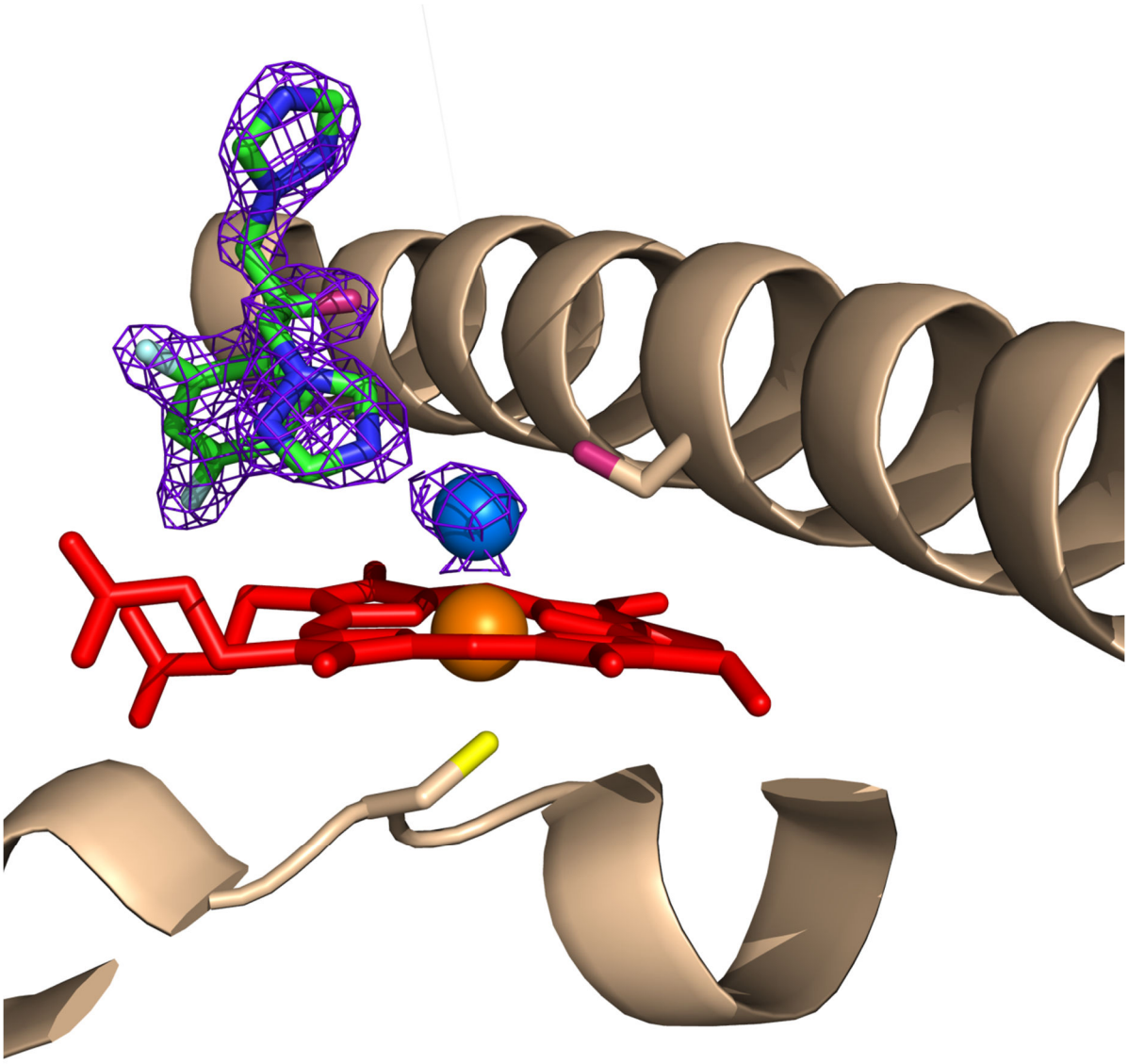

Figure 1.4: Low-spin ligands are not necessarily ligated directly to the heme. An alternate low-spin heme ligation mode is observed in the *Mtb* CYP121-fluconazole crystal complex (PDB ID: 2IJ7). For clarity only the I-Helix containing Ser237 side chain (*wheat*), the heme (*red*; *orange* iron), axial cysteinate (*yellow* sulfur) and associated secondary structure (*wheat*), distal water ligand (blue), and bound FLU (*green* carbon, *light blue* fluorine, *blue* nitrogen, *magenta* oxygen) are shown. Figure was rendered using PyMOL (The PyMOL Molecular Graphics System, Version 1.0r2, Schrödinger, LLC). Electron density maps for FLU and H_2O ligands were generated using the Uppsala Electron Density Server (*79*) and contoured at 1.5σ.

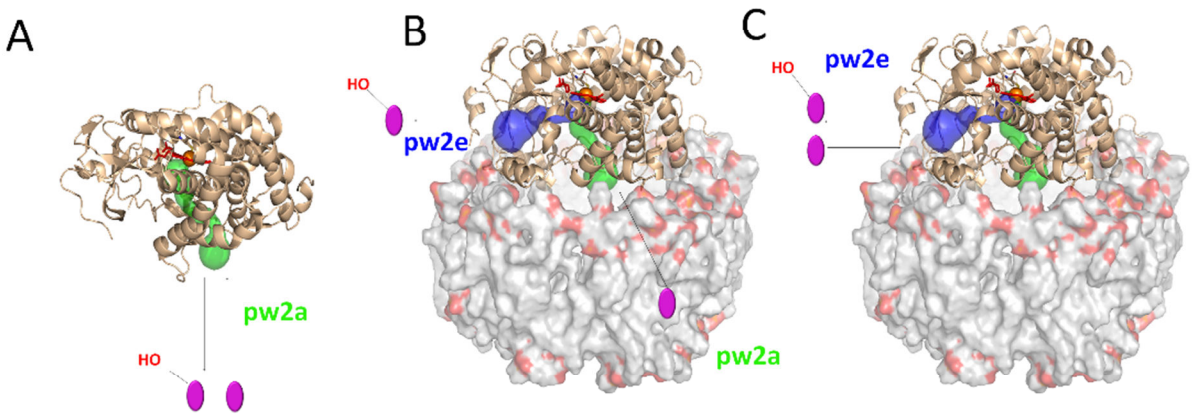

Figure 1.5: Proposed substrate access/egress channels for bacterial and mammalian CYPs. Channel nomenclature is consistent with that of Wade et al. (*69*). (A) Ligand access and egress in soluble CYPcam (PDB ID: 3L61) through pw2a (*green*). (B) Mammalian CYP3A4 (PDB ID: 1TQN) in model membrane illustrating active site access channel pw2a (*green*) through the membrane and egress of polar metabolite via pw2e (*blue*). (C) Alternatively, both access and egress may occur through channel pw2e. Figure was rendered using PyMOL (The PyMOL Molecular Graphics System, Version 1.0r2, Schrödinger, LLC). Tunnel calculation and visualization was conducted using the CAVER 1.0 plug-in (*80*).

Chapter 2:

Deconstruction of Low-Spin Heme Interactions in CYP450: Evidence for a Diverse Spectrum of Apparent Type II Binding States

2.1 General introduction

Biophysical study of CYP-ligand binding interactions has traditionally been grounded in a rigid spectral paradigm that distinguishes inhibitors from substrates on the basis of ligand-induced perturbations of the heme spin state equilibrium, measured optically as changes in heme absorbance (*16*). With this convenient method, compounds are categorized either as high-spin 'type I,' or one of two low-spin varieties, 'type II' and related 'reverse type I' (*18*). Both type II and reverse type I ligands favor ferric heme spin equilibrium shifts toward low-spin; however, the defining spectral hallmark of type II species is a significant redshift of the location of the heme Soret band measured by absorbance. As for reverse type I ligands, there is no consensus of ligand-bound structure with regards to ligand-heme interactions, although many have suggested replacement of ferric heme axial-H_2O ligand by alcohol functions when applicable, or simply retention of water in the presence of ligand as the source of spectral change (*19, 81*). For CYP101A1 (P450cam) of *Pseudomonas putida*, binding and spin state equilibrium are highly coupled with changes in heme redox potential, so the methodology works quite well for predicting functional outcomes in this enzyme. Structurally, type II ligands are believed to be better inhibitors than chemically similar type I analogues because they can form a coordinate bond to ferric heme iron that stabilizes a hexacoordinate heme geometry that is difficult to reduce, which obstructs the oxygen binding site necessary for catalytic turnover. However, despite multiple crystallographic examples (*82, 83*) that corroborate the structural expectations of

type II binding, there have been numerous inconsistencies reported in the recent literature that challenge our fundamental understanding of binding and catalytic turnover mechanisms for type II ligands. For example, Peng et al. recently reported that there exists no correlation between type II spectral behavior, affinity, and metabolic stability in CYP3A4 for several quinoline-4-carboxamide pyridine derivatives (*38*). Additionally, high affinity type II binding antifungal drugs such as itraconazole and ketoconazole are known to be slowly metabolized by CYP3A4 (*39, 84*). These results highlight the inherent risks of adopting any *generic* spectral classification paradigm to predict CYP-ligand structure/function. Importantly, these examples reveal that our knowledge of apparent type II/reverse type I ligand-heme interactions is incomplete and that a *range* of low-spin binding scenarios exists. Thus, there is a need for further exploration of the molecular details of type II binding so that an understanding of the complex interplay between heme binding, drug affinity, and functional outcome can be harnessed and potentially exploited by the medicinal chemist and/or DMPK scientist.

The azoles are a proven class of CYP inhibitors (Figure 2.1). Most commonly, azole drugs harbor 1,2,4-triazole (1,2,4-TRZ), or imidazole (IMZ) fragments capable of coordinate bonding with heme in CYPs as pharmacophores crucial for the drugs mechanism of action. Within the last decade, the synthetic strategy of 'click' chemistry has rendered the related 1,2,3-TRZ fragment ubiquitous, as evident by its incorporation into bona fide pharmaceuticals, peptide and carbohydrate mimetics, as well as nanotechnologies (*85, 86*). This chapter documents our efforts to characterize, via spectroscopy and functional assay, several apparent type II 123-TRZ-CYP complexes that showcase this moiety's ability to form novel ligand-heme structures, and their effects on CYP catalytic function. In addition, we validate our spectroscopic approach with a pyridine-based reverse type I species previously identified crystallographically by others (*87*)

to form a complex with CYP125A1 (*Mtb*) that is consistent with our own observations and extends them to other common drug-like heterocycles. This study combines traditional optical criteria with the techniques of continuous wave (CW) and pulsed electron paramagnetic resonance (EPR) spectroscopies, and magnetic circular dichroism (MCD) to provide a detailed structural analysis of these complexes. Finally, it should be emphasized that the range of atypical low-spin interactions that are characterized here occurred within diverse CYPs that include *Mtb* CYP51B1 and CYP125A1, and the detoxification CYP2C9. This enzymatic diversity further exemplifies the potential commonality of such interactions and the need to reassess the value of a simplified CYP-ligand classification paradigm.

2.1.1 CYP2C9 background

Mammalian CYP2C9 is the second most abundant CYP isoform found in human liver and is responsible for the hepatic-mediated clearance of about 15% of all pharmaceutical drugs that undergo phase I metabolism (*88*). Unlike the major hepatic drug metabolizing enzyme CYP3A4, CYP2C9 does appear to display some level of substrate selectivity, generally favoring small aryl acetic and aryl propionic acids, with non-steroidal anti-inflammatory drugs diclofenac, (S)-flurbiprofen, naproxen, and ibuprofen being representative examples. The CYP2C9 gene is subject to genetic polymorphism, and has been the focus of intense study in the field of pharmacogenomics due to the enzyme's key metabolic role in clearance of low therapeutic indices drugs such as the anticoagulant warfarin (*88, 89*). Additionally, CYP2C9 activity is subject to allosteric regulation by both substrates and inhibitors, where both heterotropic and homotropic cooperative steady-state kinetic behavior has been demonstrated *in vitro* (*90, 91*).

These facts highlight the importance of characterizing the molecular details of CYP2C9-ligand interactions.

2.1.2 CYP51B1 of *M. tuberculosis* background

With the recent unexpected discovery of up to twenty CYP genes residing in the genome of *Mycobacterium tuberculosis* (H37Rv strain) (*Mtb*) (*92*), there has been intense effort to characterize the structure and function of CYPs essential to this deadly pathogen with the aim of developing urgently needed tuberculosis drugs. Although not essential for the viability of the organism (*15, 93*), CYP51B1 has been speculated to play a role in host infectivity (*94*) because the enzyme exhibits 14α-demethylase acivity (*95*) for substrates lanosterol, 24,25-dihydrolanosterol, and obtusifoliol, with a moderate selectivity for C-4 methylated sterols, despite the fact that the *Mtb* organism lacks a complete sterol biosynthetic pathway (*92*). It has been demonstrated that CYP51B1 harbors a high affinity for existing azole drugs (*14, 82*) as evidenced by several crystallographic examples of type II binding (*82, 94*). However, CYP51B1 possesses unusual structural and biophysical properties that render study of ligand-heme interactions in this isoform essential. As was mentioned previously in chapter one, the heme of CYP51B1 is susceptible toward collapse to a penta-coordinate P420 species under reducing conditions, and the condition for this transition appears to be specifically regulated by the type of ligand-bound (*96*). The CYP51B1 spin state displays an unusual temperature dependence, as was demonstrated for CYP51B1 in complex with 2-phenylimidazole (*96*). Furthermore, CYP51B1 maintains an aberrantly low redox potential (-375 mV rel. SHE) that is variably affected by substrate binding (*96*). Interestingly, heme iron reduction has been demonstrated for CYP51B1

in complex with estriol despite a large thermodynamic barrier (+ 3.1 kcal/mol) for electron transfer between the heme cofactor and the organism's putative 3Fe-4S ferredoxin redox partner protein (*96*). Structurally, the heme of CYP51B1 is solvent exposed in both ligand-free and inhibitor-bound states by virtue of an open conformation of the BC loop region of the protein that normally behaves as a barrier between the active site and bulk solvent in most CYPs (*82*). Thus, our knowledge of ligand-heme interactions in CYP51B1 is limited and warrants further study.

2.1.3 CYP125A1 of *M. tuberculosis* background

Mtb requires host cholesterol for infection and persistence as demonstrated in mouse. In addition, cholesterol is believed to play a prominent role in *Mtb* lipid metabolism (*93, 97*). CYP125A1 was isolated as a gene element encoded in the *igr* operon on (Rv3540c-Rv3545c), and has since been characterized as a C-27 hydroxylase of cholesterol and related cholest-4-en-3-one substrates, rendering the enzyme an attractive drug target CYP to thwart *Mtb* infection (*13*). The crystal structure of CYP125A1 bound to androstenedione has proven a useful model to rationalize the C-27 regiospecificity, while the structure of CYP125A1 in complex with anti-tubercular drug econazole attests to the strict steric requirements at the level of the heme iron (*97*). In purified form, CYP125A1 is unusually rich in a high-spin enzyme fraction (Figure 2.2), and the heme spin state has proven highly sensitive to treatment by alcohols (*97*). Additionally, there appears to be a high degree of conformational regulation of the heme spin state equilibrium, with the carbonyl function of Val^{267} regulating the local water dynamics near the cofactor (*97*). Recently, CYP125A1 was co-crystallized with a pyridine-based reverse type I

inhibitor (LP10) revealing a highly ordered H_2O network that is critical for mediation of LP10-heme interactions (*87*). In this chapter we subject CYP125A1-LP10 complex to further spectroscopic characterization to validate our EPR-based approach by demonstrating that our structural conclusions with different isoforms are consistent with other methods, such as x-ray crystallography. Excitingly, our focus on CYP125A1 further exemplifies the diverse array of ligand-heme interactions that exist across the CYP family, while providing clarity to the ambiguous nature of reverse type I inhibitor structure.

2.1.4 Electron paramagnetic resonance (EPR) background: Rhombic EPR spectra of low-spin ferric CYP and the estimation of axial (Δ) and rhombic (V) crystal field parameters

Electron paramagnetic resonance (EPR) spectroscopy is useful for characterizing the electronic configuration and associated energy levels of the ferric heme coordination sphere (*8, 98, 99*), and can yield detailed structural information for low-spin CYP-ligand complexes. The CW EPR spectra of low-spin CYP contains three principal g-values (g_z, g_y, g_x) that are characteristic of a rhombic EPR spectrum—a designation that implies a specific electronic ground state (vide infra). In rhombic EPR spectra of hemoproteins, the principle axis system of the g-tensor depends on the local environment of the unpaired electron of ferric iron as observed from the molecular frame, which is defined with respect to the applied magnetic field by the three designated axes of the heme cofactor (i.e. xy-plane represents the porphyrin macrocycle, and axial ligands define the z-axis) (*98*). Thus, the three g-values (in particular g_z) are highly sensitive reporters on the axial ligation state of heme Fe(III) and on alterations of the heme field, in general, that occur during ligand binding.

Low-spin ferriheme, which is the predominant form present as cofactor in ligand-free CYPs, is characterized as a distorted octahedral coordination sphere about iron (III), the result of chemical mismatch between the two axial ligands (proximal cysteinate and distal H_2O, respectively) and four pyrrole nitrogen ligands that define the plane of the heme macrocycle (*98*). A distortion of the octahedral field induces non-degeneracy of the three lowest energy iron (III) d-orbitals (designated t_{2g}), the result of orbital mixing due to spin orbit coupling (SOC, λ) (*98, 100*). Thus, most low-spin ferrihemes are characterized by an $(d_{xy})^2(d_{xz},d_{yz})^3$ ground state electron configuration (Figure 2.3). The energy differences between the three lower d-orbitals can be defined by two energy parameters that characterize the splitting: the rhombic parameter, V, which is defined as the difference in energy between d_{xz} and d_{yz}; and the axial parameter, Δ, which represents the energy difference between the lowest energy d_{xy} orbital and the *average* energy of the d_{xz} and d_{yz} orbitals (Figure 2.3) (*98, 99*). Based on several assumptions including the possible values of V/Δ, and an implied 'proper axis' system for a $(d_{xy})^2(d_{xz},d_{yz})^3$ ground state electronic configuration, Taylor has derived expressions that relate the three g-values measured in a typical CYP EPR spectrum to the axial and rhombic crystal field parameters, expressed in units of the SOC (Δ/λ, V/λ, respectively) (*98*). Thus, EPR-measured g-values for a given CYP-ligand complex yield valuable information about how a given ligand-heme interaction in CYP influences the electronic makeup of the catalytic redox center of the enzyme. Importantly, depending on the relative magnitude of V/Δ, the heme can experience a range of intermediate 'axial' versus rhombic 'strained' states that dictate the heme geometry (*101, 102*). Therefore, EPR yields valuable electronic and structural information that can be useful when characterizing low-spin CYP-ligand complexes, including the potential for metabolism. As an important aside, it must be emphasized that the pioneering work of Peisach and Blumberg demonstrated the

utility of EPR-derived crystal field parameters for defining heme geometry and axial ligand identity for several hemoproteins prior to the availability of crystallographic structural information (*102-104*).

2.1.5 Magnetic Circular Dichroism (MCD) background: Paramagnetic systems

A chromophore in solution can be induced to exhibit dichroism—differential absorption of left and right circularly polarized light—at absorption wavelengths when placed within a longitudinally-aligned magnetic field (*105*). Magnetic circular dichroism (MCD) study of hemoproteins is an invaluable technique for determination of heme iron spin and redox states, as well as for defining the heme axial ligand sets in the absence of structural information (*106*). Additionally, variable temperature variable field MCD can be used to assign the polarization of a given optical transition, and this information combined with quantum mechanical calculations has been used to make formal orbital assignments for the numerous electronic transitions that comprise the complicated visible spectra of hemes (*107*). The paramagnetic nature of ferric CYPs, render their MCD spectra temperature dependent (*105*), which affords a great sensitivity enhancement at low temperatures. One additional advantage of low-temperature MCD of CYPs is that the sensitivity provided to the low-spin enzyme fraction can be up to one hundred times greater than the high-spin enzyme form, which is beneficial for characterizing the visible absorption properties of low-spin complexes exclusively. Additionally, MCD allows for detection of ligand-to-metal charge transfer (LMCT) transitions (Figure 2.4) that are located in the near infrared region of the electromagnetic spectrum. The significance of the LMCTs features, which result from excitation of an electron from the heme macrocycle HOMOs a_{1u} and

a_{2u}, to the vacant d_{yz} orbital on low-spin iron (Figure 2.4), is that the precise energy of this spectral feature is sensitive to the chemical nature of the axial ligands, and thus can be highly diagnostic of the axial ligand sets (*106*). In the absence of an applied magnetic field these transitions are normally far too weak to be detected by conventional absorbance spectroscopy; this is because the Zeeman splitting induced by the applied field strongly affects the electronic transitions and not the molecular vibrational overtones (e.g. H-O, H-N, H-C stretching) that normally obscure these features (*106*). These aspects of MCD, in addition to the resolution enhancement provided the visible absorbance spectrum over conventional absorbance, render the technique ideal for the study of CYP-ligand complexes.

2.2 Experimental Procedures

2.2.1 Materials

All small molecule reagents and/or synthetic precursors, organic solvents, as well as redox partner proteins and NADPH regenerating enzymes utilized during the reconstitution of CYP125A1 activity were obtained from Sigma-Aldrich (St. Louis, MO). Protein purification resins and media used for cell culture were obtained from Fisher-Scientific. Competent C41 (DE3) E. coli cells used during CYP gene transformation and protein expression were obtained from Lucigen. Deuterated solvents for NMR analysis were purchased from Cambridge Isotopes (Andover, MA, USA). Water employed during synthesis and in all buffers was of Milli-Q quality from a Barnstead nanopure UV dispenser. Recombinantly expressed and purified *M. tuberculosis* CYP125A1 was a generous gift from the lab of Dr. Paul Ortiz de Montellano. Purified *M. tuberculosis* CYP51B1 was a generous gift from the lab of Dr. Andrew Munro. CYP125A1 inhibitor, LP10, was a gift from the lab of Dr. Larissa Podust.

$^{1}H/^{15}N$ NMR. Characterization of synthesized TMZ-N_3, PhP-TRZ, and 17-click was performed on a Varian (Palo Alto, CA) Inova 500 (500 MHz) spectrometer equipped with a 5mm HCN z-axis PFG triple resonance probe.

2.2.2 Protein expression and purification

CYP2C9 (hepta mutant) was constructed as previously described (*108*) with the exception of a hexa His rather than a tetra His C-terminal sequence to facilitate purification. The enzyme was expressed in C41 (DE3) *E. coli* and purified as described previously for CYP3A4 (*109*). Details of the expression and purification of *Mtb* CYP51B1 and CYP125A1 can be found in references (*96*) and (*97*), respectively.

2.2.3 Organic synthesis

Synthesis of 17α-(2H-2,3,4-triazolyl)-estradiol (17-click)

17α-(2H-2,3,4-triazolyl)-estradiol (1) was obtained using a one-step click reaction between 17-α-ethynylestradiol and azidotrimethylsilane (TMS-N_3) using a published procedure for preparation of N-unsubstituted 1,2,3-triazoles (*110*). Purification was achieved using silica gel (0.035-0.07 mm, 6 nm pore dia.) chromatography with 8% CH_3OH in CH_2Cl_2 isocratic mobile phase to afford pure (1) in 60% yield. (1): NMR (δ ppm, DMSO, d_6): 0.93 (3H, s, 18-CH_3), 6.40 (1H, d, J = 2.4 Hz, 4-H), 6.46 (1H, dd, J = 8.4, 2.4 Hz, 2-H), 6.95 (1H, d, J= 8.4 Hz, 1H), 8.95 (1H, s, triazole –CH), 14.69 (1H, broad s, triazole –NH). MS: [M+H] (theoretical) = 340.203, [M+H] (observed) = 340.202.

Synthesis of 4-(3-phenylpropyl)-1H-1,2,3-triazole (PhP-TRZ)

To a 15 mL round bottom flask containing 2 mL DMF:H_2O (4:1) were added 144 µL of 5-phenyl-1-pentyne (0.95 mmol), 252 µL azidotrimethylsilane (1.89 mmol), and 95 mg sodium L-ascorbate (478 µmol). The reaction flask was sealed and placed under argon while stirring vigorously prior to the addition of 31 mg cuprous sulfate (58 µmol) dissolved in reaction solvent via syringe. The mixture was allowed to react overnight at 70 ºC. For initial workup of the reaction crude, ~ 1 g of florosil was added to the mixture to adhere the majority of the copper ion, prior to vacuum filtration. The resin was rinsed with ~2 volumes ethylacetate (EtOAc) prior to the addition of 10 volumes of water to the filtrate to remove the DMF. The organic layer was isolated and rinsed with an additional two volumes of water prior to treatment with brine and then dried over $MgSO_4$. The organic solvent was evaporated to dryness and the PhP-TRZ-containing residue purified using silica gel (0.035-0.07 mm, 6 nm pore dia.) chromatography with 5% CH_3OH in CH_2Cl_2 isocratic mobile phase to afford pure PhP-TRZ in 50% yield. For synthesis of isotopically-labeled PhP-^{15}N-TRZ containing nitrogen enrichment at either N1 and N3 in a 50:50 ratio, TMS-^{15}N=N=N/TMS-N=N=^{15}N was substituted for TMS-N_3. ^{1}H NMR (δ ppm, $CDCl_3$): 2.03 (2H, m), 2.69 (2H, d, J = 7.7 Hz), 2.78 (2H, d, J = 7.8 Hz), 7.16-7.22 (3H, m), 7.25-7.32 (2H, m), 7.51 (1H). MS: [M+H] = 188.2. PhP-^{15}N-TRZ: NMR ($CDCl_3$), 7.51 (1H, d, $J2_{HN}$ = 6.5 Hz), 7.52 (1H, d, $J3_{HN}$ = 4.9 Hz). ^{13}C NMR: 24.68, 30.85, 35.39, 126.09, 128.55, 128.61, 131.65, 141.74, 147.01. MS: [M+H] = 189.2.

Synthesis of ^{15}N-labeled trimethylsilyl-azide (TMS-^{15}N=N=N, TMS-N=N=^{15}N)

A three-neck 50 mL round-bottom flask was connected to a water-cooled reflux condenser and fitted with an inline desiccant-filled drying tube attached to an oil bubbler to

allow positive pressures to escape the reaction. The reaction vessel was purged with argon prior to charging with 1g of NaN_3 ($^{15}N(1)$) (14.8 mmol), and 10 mL of diglyme with vigorous stirring. The vessel was then sealed, set in an ice bath, and placed under positive pressure of argon prior to addition of 1.8 mL (14.2 mmol) trimethylsilyl chloride drop wise via syringe. The sealed reaction mixture was heated in an oil bath to 70 °C and allowed to react for 60 hours. The pure product was isolated from the resultant slurry in 90% yield by vacuum distillation (8 mmHg) without heating. ^1H NMR: (δ ppm; $CDCl_3$); 0.28 (9H, s).^{15}N NMR (δ rel. liquid NH_3): 169.2 (s), 206.7 (s).

2.2.4 CW/Pulsed EPR spectroscopy

EPR measurements were conducted at X-band on an ELEXSYS E680 EPR spectrometer (Bruker-Biospin, Billerica, MA) equipped with a Flexline ER 4118 CF cryostat and Flexline ER 4118X-MD4 ENDOR resonator. A two-dimensional pulsed EPR technique, hyperfine sublevel correlation spectroscopy (HYSCORE), was used to probe the interaction of nearby nuclei. The pulse sequence is $\pi/2-\tau-\pi/2\text{-}t_1\text{-}\pi\text{-}t_2\text{-}\pi/2-\tau$-echo where the τ, t_1 and t_2 indicate delays between pulses whose nominal turning angles are $\pi/2$ or π. A 16-step phase cycle was used to reject unwanted responses and correct the baseline as explained in (*111*). In HYSCORE, electron nuclear double resonance (ENDOR) frequencies (the hyperfine-shifted NMR frequencies) from the nearby nuclei are correlated with each other and dispersed in two dimensions, allowing resolution of peaks that overlap in simple 1D spectra. HYSCORE spectra were collected at the g_z (low field) peak of the EPR spectrum. HYSCORE spectra from protons are analyzed using the contour lineshape analysis (*112, 113*) to extract both isotropic and anisotropic components of the hyperfine interaction, followed by complete spectral simulation with orientation selection. Fe-H

distances were calculated from the anisotropic component of the hyperfine interaction using the standard formula for point dipoles as described previously (*114*).

Conventional continuous-wave (CW) EPR spectra were measured on a Bruker ELEXSYS E540 X-band spectrometer with ER 4102 ST resonator and either a liquid nitrogen quartz insertion dewar or a Bruker ER 4112 HV helium flow cryostat. EPR samples were prepared by mixing 50 μl of a buffered protein solution containing 20% glycerol with a saturating amount of ligand (usually 10 x K_D) suspended in the appropriate co-solvent when necessary. These samples were placed in 3mm OD (outer diameter) EPR tubes, frozen and stored in liquid nitrogen.

The spectral g-values were obtained by fitting the CW-EPR spectra using EasySpin software, a toolbox contained within the MATLAB environment (*115*). Briefly, the following parameters are associated with the Levenberg-Marquardt least squares fitting algorithm used to analyze the experimental spectra collected on frozen disordered 'powder' samples: (Sysn), which denotes the n^{th} unique species recovered from the fit and is described by a unique set of g-values (g_z,g_y,g_x); linewidth peak to peak (lwpp), in mT; g-strain (gStrain), which is responsible for line broadening of the spectra and relates to the magnetic distribution in the sample and/or the structural variation that comes from unresolved hyperfine interactions; (weight) describes the relative contribution of an individual species to the spectrum. During a typical fit analysis, the parameters are varied by an increment that is manually set in Easyfit. During fitting, minima or maxima are reached and the g-value is then manually incremented for another round of fitting and the process continues until error between the fit and experimental data is at a minimum. Polynomial baseline correction is employed when necessary due to quartz tube interference and/or contaminant trace metals in the sample.

Calculation of the axial (Δ/λ) and rhombic (V/λ) crystal field parameters expressed in units of the spin-orbit coupling constant for ferric ion was performed via the methods of Taylor (*98*). Briefly, the three g-values obtained for each spectral component via least-squares regression in EasySpin were applied to the following formalism:

(1) $A = g_x/(g_z + g_y) + g_y/(g_z - g_x)$
(2) $B = g_x/(g_z + g_y) + g_z/(g_y - g_x)$
(3) $\Delta/\lambda = B - (A/2)$
(4) $V/\lambda = A$

2.2.5 UV/vis absorbance analysis of ligand binding

Absorbance measurements were conducted on an Olis Modernized Aminco DW-2 (Olis,Inc., Bogart, GA) dual beam spectrophotometer equipped with a Julabo F30-C compact refrigerated circulator (Julabo USA, inc., Allentown, PA). Each binding experiment required 500 µL initial sample volume using a 0.1 x 1 cm path length quartz cuvette, and the typical sample consisted of 1-2 µM purified CYP in 100 mM KPi buffer + 20% glycerol. Spectra were recorded in the absolute mode (270 – 650 nm) in between 1 µL aliquots of the appropriate ligand stock solution added to the sample cuvette. For titrations of lipophilic species, organic stock solutions were used with a final concentration of organic kept below 2%/vol. Due to excessive absorbance of LP10 during titration of CYP125A1, difference spectra were collected directly using a split cuvette format. Briefly, 2 mL volume of protein solution was split into 1 mL volumes to fill one side of both the sample and reference cuvettes, while the remaining compartment of each was filled with 1 mL of buffer. For each titration point, 1 µL of ligand stock was added to the protein compartment of the sample cell, and the buffer compartment of the reference cell; the appropriate solvent was added to the buffer compartment and the protein compartment of the

sample and reference cuvettes, respectively. Affinity, K_s, and B_{max} parameters were estimated from non-linear regression analysis in IGOR pro 6.1 (Wavemetrics, Lake Oswego, OR, USA) using equation (1).

(1) $\Delta Abs. = [E \cdot L] = B_{max} \cdot [L]/(K_s + [L])$

2.2.6 MCD spectroscopy

MCD spectra were collected using an Aviv 40DS spectropolarimeter and a high-field superconducting magneto-optical cryostat (Cryo-Industries SMC-1659 OVT) equipped with a variable temperature sample compartment. MCD intensities are measured as differential absorbance of left (σ^-) and right (σ^+) circularly polarized light ($\Delta A = A_L - A_R$), following the sign convention of Piepho and Schatz (*116*). MCD spectra are measured in units of θ (mDeg) with the relationship θ (mDeg) = 32,982*ΔA. All spectra were baseline corrected via measurement and subtraction of a spectrum collected at zero field. For low temperature measurements, depolarization of the sample was checked via CD measurement of a solution standard of nickel (II) tartrate. Near infrared absorption was detected with a nitrogen-cooled 1x1 mm InGaAs detector (Sciencetech Inc., USA). Measurements at room temperature are expressed as $\Delta\varepsilon$ (M^{-1} cm^{-1} T^{-1}) to account for the field dependence, while measurements at cryogenic temperature are expressed as $\Delta\varepsilon$ (M^{-1} cm^{-1}). A typical MCD sample contained 20-400 µM protein dissolved in an appropriate buffer containing 55% glycerol as glassing agent. For all nIR measurements the samples were prepared in deuterated buffers containing d8 glycerol (Sigma-Aldrich). Preparation of a sample was performed by depositing 90 µL of protein solution (+/- added ligand stock, not to exceed 2% organic) upon a 1.5 cm dia. circular quartz plate placed on

an in-house fabricated aluminum sample mount fitted with a 0.1 cm thick Teflon spacer. The solution was sealed between a second quartz plate and sandwiched between a second aluminum housing with hand-tightened screws. The sample mount was secured to a rod containing a temperature sensor and fit for the appropriate optical cryostat before being introduced in between the poles of the superconducting magnet.

2.2.7 Reconstitution of CYP2C9 activity and substrate depletion analysis of PhP-TRZ

The diclofenac 4-hydroxylase activity of the mutant CYP2C9 was reconstituted in vitro using the lipid pre-mix protocol of Shaw et al. (*117*). Briefly, liposomes were prepared via combination of buffered premix (5X) with a concentrated (100X) lipid mixture consisting of L-α-dilauroyl-sn-glycero-3-phosphocholine, L-α-diloleoyl-*sn*-glycero-3-phosphocholine, and L-α-dilauroyl-sn-glycero-3-phosphoserine prior to the addition of 50 nM CYP2C9, cytochrome P450 reductase (rat ortholog, CPR), and cytochrome b5 in a ratio of 1:2:1, and allowed to sit on ice for 10 min. The liposome mixture was then diluted to volume and aliquot (178.2 µL to row A, 90 µL to all remaining rows) in triplicate to a 96-well assay plate. 1.8 µL of concentrated diclofenac stock (10 mM) was added to row A (100 µM final) prior to serial dilution (1:2). A zero concentration point was also prepared for use as a control. The plate was allowed to equilibrate at 37 ℃ with moderate agitation for 5 min prior to the addition of 1 mM NADPH to initiate the reaction (or buffer for no NADPH control series). After 5 min reaction time the reaction was terminated by the addition of acetonitrile:acetic acid (16:1) quench solution containing authentic d4, 4-hydroxy diclofenac internal standard (IS). The plates were centrifuged at 4100 g to sediment the solids prior to direct UPLC/MSMS analysis using a Waters Acquity UPLC

(Milford, MA, USA) interfaced with an AB-Sciex (Framingham, MA, USA) API4000 QTQ tandem quadrupole MS operated in positive electrospray mode. For detection of the metabolite and IS, MRM methods were tuned and optimized automatically in Analyst 4.2 software (MRM, 4-OH diclofenac: m/z = 312.0/231.0 Q1/Q3; d4, 4-OH diclofenac: m/z = 316.0/234.0 Q1/Q3). Quantification of the 4-OH diclofenac metabolite produced in the reaction was conducted using a previously constructed standard curve. K_M and V_{max} parameters were obtained for the reaction by fitting the velocity vs. diclofenac concentration data to the Michaelis-Menten equation via non-linear regression analysis in IGOR Pro (Lake Oswego, OR, USA).

For substrate depletion analysis of 4-(3-phenylpropyl)-1H-1,2,3-triazole (PhP-TRZ), CYP2C9 activity was reconstituted as described above. Concentrations of PhP-TRZ ranged from 300 µM – 50 nM. Briefly, the reconstituted protein mix containing 50 nM CYP2C9 was aliquoted into nine 1.17 mL aliquots prior to the addition of 17.8 µL of the appropriate concentration of PhP-TRZ (66.7 X; 1.5% organic v/v) stock in methanol. Each solution was then dispensed into 3 x 396 µL aliquots in epi tubes and pre-incubated at 37 ℃ for 5 min. Prior to initiation of the reactions by addition of 1 mM NADPH, 50 µL aliquots were removed and quenched in a 96-well plate with two volumes acetonitrile:acetic acid (16:1) quench solution containing 4-benzyl-1H-1,2,3-triazole internal standard (IS) for use as minus NADPH control. Time points were taken every 30 seconds up to 180 seconds, followed by two additional time points at 300 and 600 seconds. Depletion of 1 µM diclofenac was used as a control reaction. The plates were subjected to centrifugation as before to remove the solids prior to analysis by UPLC/MSMS (MRM: PhP-TRZ, m/z = 188.1/109.8 Q1/Q3; IS, m/z = 160.0/53.9 Q1/Q3). For PhP-TRZ concentration series higher than 5 µM, the reactions were diluted prior to analysis to

stay within the linear range of the MSMS detector. Depletion of the PhP-TRZ parent over time was quantified via MS/MS area ratios.

2.2.8 Reconstitution of CYP125A1 activity and substrate depletion analysis of LP10

Reconstitution of C27-cholesterol hydroxylase activity and substrate depletion analysis of LP10 inhibitor was achieved using a previously published protocol (*87*). Briefly, 1 μM purified CYP125A1, 500 nM ferredoxin (spinach), 100 μU/μL ferredoxin reductase (spinach), 10 μg/mL catalase (bovine pancreas), 4.8 mU/μL glucose-6-phosphate dehydrogenase (S. cerevisiae), and 1 mM glucose-6-phosphate were brought to volume in 50 mM KPi (pH = 7.5) containing 0.45 % (w/v) β-methylcyclodextrin (βMCD). The reaction mixture was split into two aliquots prior to addition of either cholesterol (CHO) or LP10 inhibitor prepared in 10% βMCD solution: DMSO solution (1:1; final DMSO 1% v/v). Each ligand-containing solution was split into three aliquots (triplicate) and allowed to incubate in epi tubes at 37°C for 5 min. Prior to initiation of the reactions with 500 μM $NADP^+$, zero time control aliquots (50 μL) were quenched into two volumes of acetonitrile:acetic acid (16:1) quench solution containing carbamazepine (CBZ) internal standard (IS). Time points were taken over the course of 2 hrs. reaction time. The quenched reaction mixtures were centrifuged (4100 g) to sediment the solids prior to UPLC-MSMS analysis (API4000 QTQ) in positive atmospheric pressure chemical ionization (APCI) mode. Depletion of CHO and LP10 parent was quantified via MSMS peak area ratios relative to the signal at t = 0. For detection of parent CHO and LP10 analytes and IS, MRM methods were tuned and optimized automatically in Analyst 4.2 software (MRM, CHO: m/z = 369.1/161.1 Q1/Q3; LP10: m/z = 405.1/159.1 Q1/Q3; CBZ: m/z = 237.1/193.1 Q1/Q3).

2.2.9 NADPH depletion assay

To assess the effect of inhibitor binding on NADPH consumption, a UV/vis spectrophotometric assay was employed. Reconstitution of enzyme activity in both CYP2C9 and CYP125A1 systems was conducted as described above with the exception that NADPH regenerating system was excluded for the CYP125A1 reconstitution and the protein concentration was lowered from 1 μM to 250 nM. For a typical NADPH depletion experiment, 1350 μL of reconstitution mixture containing protein and the appropriate ligand (or ligand-free control) were equilibrated at 30°C for 5 min. in a 1x1 cm cuvette containing a magnetic stir bar. The instrument was zeroed with buffer in the reference cuvette position prior to the initiation of data collection at 340 nm wavelength. After baseline stabilization was observed (~ 30s), the acquisition was paused and 150 μL of 1.5 mM NADPH solution was rapidly introduced via pipette. Data collection at 340 nm was immediately resumed and the depletion of the absorbance signal was monitored for 8 min. To quantify NADPH concentration a molar extinction coefficient of 6.22 $mM^{-1}cm^{-1}$ was used (*118*). Rates were determined by linear regression to the initial portion of the depletion curve and represent the average of at least two measurements.

2.3 Results

2.3.1 Heme binding complexity detected by EPR for un-substituted azole fragments in complex with CYP2C9

A fragment-based comparative binding analysis was conducted by EPR of small azole compounds binding CYP2C9 (n-terminal truncation, hepta mutant; see Chapter 2.2.2) to characterize type II interactions more thoroughly with a detoxification CYP. CW EPR spectra of ligand-free CYP2C9 as well as low-spin complexes of imidazole (IMZ), 1-H-1,2,4-triazole (124-TRZ), and 1H-1,2,3-triazole (123-TRZ) were obtained between 15-77 K, and are shown in Figure 2.5 with the best fit obtained via least squares regression analysis in EasySpin software (Chapter 2.2.4) to provide accurate g-values (Table 2.1) for the multiple species detected in each spectrum. Ligand-free CYP2C9 contains at least two low-spin species detectable by EPR: a major species (with high axial character) with g-values 2.429, 2.252, and 1.917 (g_z, g_y, g_x, respectively), and a minor species (more rhombic character) with g-values 2.392, 2.244, and 1.929. Importantly, no heterogeneity is evident in the ligand-free EPR spectra of other CYPs studied by us (Figure 2.6). Such heterogeneity implies structural heterogeneity of the isoform in frozen solution. Interestingly, the spectra of all three CYP2C9-azole fragment complexes also display heterogeneity, with at least two species present at enzyme saturation that could reflect the fact that each ligand-free species yields a distinct azole-ligated species when fragment binds (Table 2.1). The minor species observed in the spectrum of the 123-TRZ complex exhibits remarkable similarity in g_z (2.399) to the minor species of ligand-free enzyme, suggesting that oxygen remains bound to a small fraction of CYP2C9 in the presence of 123-TRZ. Also unusual is the fact that 123-TRZ binding exhibited a distinct increase in g_y not observed for the other azoles studied. Both species detected in the spectra of CYP2C9 in complex with 124-TRZ and IMZ are consistent with direct nitrogen ligation (*119*). These results may be indicative of a heterogeneous enzyme population with differential affinity for azoles, or possibly reflect the fact that multiple coordination modes for each fragment are possible. Curiously, similar

heterogeneity was reported by Peng et al. during EPR analysis of wild-type CYP2C9 in complex with several pyridine containing molecules (*44*) that contain a single nitrogen coordination site. These results suggest that type II binding interactions with CYP2C9 are inherently complex for the range of type II binding heterocycles studied here and it is anticipated that such structural heterogeneity may go unnoticed by less discriminating absorbance-based methods during type II binding analysis.

2.3.2 Identification and characterization of apparent 'type II' heme-H_2O-triazole ternary complex in CYP2C9 by EPR

4-(3-phenylpropyl)-1H-1,2,3-triazole (PhP-TRZ) was observed to induce apparent type II spectral behavior in CYP2C9 during a previous 123-TRZ-based inhibitor screen. We compared the CYP2C9 binding spectra of PhP-TRZ to that measured for 123-TRZ binding because the fragment is assumed not to participate in additional binding interactions with CYP2C9 active site architecture and thus serves as a 'complete' type II heme binding spectral reference ligand for this moiety. Both 123-TRZ fragment and PhP-TRZ binding induced similar minor redshifts in the heme Soret (3 nm vs. 4 nm, respectively), and similar trough wavelength in their respective calculated difference spectra; although, due to the overwhelming low-spin nature of ligand-free CYP2C9, differences in spectral trough behavior are anticipated to be less pronounced than in isoforms that maintain significant high-spin content in the resting state (e.g. CYP3A4). Interestingly, the molar extinction of the Soret for the PhP-TRZ complex appeared lower than the corresponding Soret for 123-TRZ reference complex as evidenced by the lack of peak in the difference spectrum (Figure 2.8).

To gain a more detailed understanding about differences in the CYP2C9 complexes with 123-TRZ vs. PhP-TRZ, both were analyzed by continuous wave electron paramagnetic

resonance (CW EPR). Figure 2.9 shows the overlay of EPR spectra collected at 15 K corresponding to low-spin ligand-free CYP2C9 (black), and in complex with PhP-TRZ (blue), and 123-TRZ (green). Remarkably, despite yielding very similar optical spectra during binding analysis, the two ligands affect the g-values in dramatically different ways. Compared to ligand-free CYP2C9 (g-values 2.429/2.392 (g_z), 2.252/2.244 (g_y), 1.917/1.929 (g_x)), the 123-TRZ complex has shifted g-values (2.513/2.473 (g_z), 2.275/2.270 (g_y), 1.875/1.892 (g_x)) and broadening of the spectral linewidth (g_z and g_x) consistent with direct nitrogen ligation (*119*) to ferric heme iron, although a third minor species is also observed (2.397/2.252/1.922) that appears similar to the ligand-free enzyme. In stark contrast, CYP2C9 in complex with PhP-TRZ yields g-values (2.387/2.254/1.933) that shift in opposite directions (g_z to higher field (lower g-value) and g_x to lower field (higher g-value)) compared with the g-value shifts exhibited during complexation with 123-TRZ. In addition, binding of PhP-TRZ causes a noticable *decrease* in linewidth for g_z and g_x that sharpen the signals significantly. There does, however, appear to be a minor fraction of CYP2C9-(PhP-TRZ) complex that is similar in structure to the major species observed in CYP2C9-(123-TRZ) complex based on the small shoulders developing to low field in g_z and high field in g_x. Table 2.1 lists all g-values for each species in order of their apparent contribution to the spectrum as determined from the spectral fits in EasySpin (see Chapter 2.2.4). The EPR results suggest that distinct perturbations of the heme field occur upon binding 123-TRZ and PhP-TRZ in CYP2C9 despite both ligands yielding an apparent type II optical response.

Further spectroscopic analysis of PhP-TRZ and 123-TRZ in complex with CYP2C9 was conducted by pulsed EPR methods. Specifically, a two-dimensional 4-pulse (Figure 2.7) electron spin echo-envelope modulation (ESEEM) experiment known as hyperfine sublevel correlation

spectroscopy (HYSCORE), was used to probe the radial distribution of magnetically-active nuclear spins located within the immediate environment of low-spin ferric heme iron (*120*). This technique allows for detection of nuclei constructing ligands bound to or near the heme iron of CYP (*121, 122*) with the additional possibility of obtaining structural information about the heme coordination sphere. As a further aid toward more detailed characterization of the unusual heme interaction that occurs in CYP2C9-(PhP-TRZ) complex, ^{15}N-enriched PhP-TRZ (PhP-^{15}N-TRZ) was synthesized to contain a heavy isotope at either position N1 (50%) or N3 (50%) (see Chapter 2.2.3). Figure 2.10 shows the (+,+) quadrant of the HYSCORE spectrum of ligand-free CYP2C9 within the frequency range containing hydrogen features (> 8 MHz), acquired at a field strength corresponding to g_z. Two sets of broad arcs are resolved and have been assigned to the protons of the heme axial 6th-position water molecule (*114*) (outer, frequency 10.1, 15.6 MHz) and the proximal cysteinate β-protons (inner, frequency 11.2, 13.8 MHz) that reside at distances of 2.6 Å and 3.1 Å from the unpaired electron on ferric heme iron, respectively, as determined via proton arc analysis that assumes a point dipole approximation (i.e. negligible spin delocalization) (see Chapter 2.2.4) (*121, 122*). Also shown in Figure 2.10 are the HYSCORE spectra for CYP2C9 complexes of 123-TRZ (middle) and PhP-TRZ (right), again taken at field strength corresponding to g_z. In the spectrum of the 123-TRZ complex, a complete disappearance of the axial H_2O proton arcs is observed. This suggests that 123-TRZ replaces heme axial H_2O ligand via direct nitrogen coordination of the fragment, consistent with type II binding. Further corroborating this fact are the appearance of new nitrogen signals in the low frequency (0-8 MHz) portion of the spectrum (data not shown). The HYSCORE spectrum obtained for CYP2C9-(PhP-TRZ) complex is profoundly different from that observed for CYP2C9 in complex with 123-TRZ. In the HYSCORE spectrum of CYP2C9-(PhP-TRZ) the proton arcs

from axial H_2O ligand remain at frequencies 10.9, 15.1 MHz. In addition, an increased distance of the axial H_2O protons to heme iron (2.7 Å, + 0.1 Å) is discernable based on proton arc analysis. These observations suggest that the axial H_2O ligand is not displaced/replaced, but is perturbed, despite the apparent type II binding of PhP-TRZ observed optically. This result coincides with the large g-value shifts observed by EPR for CYP2C9-(PhP-TRZ) complex that suggest ligand binding alters the heme field significantly, but in a manner consistent with oxygen ligation (*119*) at the axial heme position. With these results, we propose a water-mediated azole-heme interaction exists in the CYP2C9-(PhP-TRZ) complex, consistent with hydrogen-bonding to the H_2O axial ligand *without* displacement.

Additional support for our conclusion that PhP-TRZ forms a heme-H_2O-(PhP-TRZ) ternary complex with CYP2C9 comes from HYSCORE analysis of the equivalent complex with isotopically-enriched ^{15}N-PhP-TRZ. Figure 2.11, compares the HYSCORE spectra at 2935 Gauss field of CYP2C9 complexes of natural abundance PhP-TRZ (left) and isotopically-enriched PhP-^{15}N-TRZ spanning a frequency range that includes nitrogen features (0-8 MHz). Comparison of the HYSCORE spectra reveals the appearance of two new intense nitrogen peaks for the CYP2C9-(PhP-^{15}N-TRZ) complex that appear to be only weakly interacting with the heme iron based on the small hyperfine coupling (~ 1.5 MHz). Concomitant with the appearance of these new nitrogen features is the disappearance of two unique sets of peaks observed at 1.6, 2.8 MHz, and 2.1, 3.6 MHz in the spectrum of unlabeled CYP2C9-(PhP-TRZ) that likely arise from coupling between ^{14}N of the unlabeled triazole moiety to the iron(III) spin. These results are entirely consistent with the existence of a heme-H_2O-(PhP-TRZ), (123-TRZ)-bridged, low-spin ternary complex in CYP2C9. Taken together, these results demonstrate, unequivocally, that 123-TRZ based azoles are competent for a previously unrecognized, novel form of type II

binding. These results were the basis of our follow up study with additional ligands and CYP isoforms (vide infra).

2.3.3 Characterization of apparent type II binding heme-H_2O-(PhP-TRZ) ternary complex in CYP2C9 by MCD

The complexes of CYP2C9 with 123-TRZ and PhP-TRZ were analyzed in more detail by magnetic circular dichroism (MCD) to determine whether the atypical heme binding structure already detected via EPR-based methods is readily distinguishable by optical measures. MCD provides enhanced spectral resolution of heme electronic transitions through magnetically-induced circular dichroism. This occurs due to differential absorption of left and right circularly polarized light by a sample suspended within a longitudinally-aligned magnetic field (*105*). Because MCD is a signed quantity, in that differential absorption can be either positive or negative, overlapping electronic transitions that comprise the conventional absorbance spectrum can often be resolved individually, allowing observation of the spectral fingerprint at a greater level of detail for a given CYP-ligand complex. It is of considerable mention that this is the first example of MCD study of a drug metabolizing CYP, so the spectral data provide a reference for ligand-free CYP2C9 and in complex with low-spin ligands that are structurally distinct at the level of the heme. Figure 2.12 shows the MCD spectrum collected at 4.7 K between 495-750 nm for ligand-free CYP2C9 (blue), and in complex with 123-TRZ (black) and PhP-TRZ (green). The spectral region between 495 - 750 nm, which is typically referred to as the alpha/beta region, is known to contain several overlapping electronic transitions, of which many are unique to either the low-spin or high-spin heme states (*123*), although at liquid helium temperatures a

significant sensitivity enhancement is provided the low-spin species (*106*) that can obscure detection of high-spin transitions. The spectral complexity in this region has been ascribed to the presence of several overlapping ligand-to-metal charge transfer (LMCT) bands with various degrees of xy and/or z molecular orbital polarization (*123*), referring specifically to the directionality of the orbitals that are associated with each transition with respect to the molecular frame defined by the heme cofactor (i.e. heme macrocycle defines xy plane, axial ligands, z-axis). It is not surprising then that both the energy and the intensity of these bands appear to be dramatically affected by the presence of apparent type II binding ligands. The heterogeneity of the spectra in the region 640-720 nm is magnified as an inset to Figure 2.12, and is comprised of several thiolate(π)-to-iron(III) CT transitions that have varying degrees of z-polarization (*123, 124*). Shown at the top of Figure 2.12 are the corresponding absorbance spectra taken at 298 K in the same spectral region (α/β band absorbance region) for comparison. The tabulated MCD peak/trough wavelengths and crossover points are given in Table 2.3 along with associated molar extinction coefficients. Some key observations are as follows: First, clearly much more spectral detail is resolved in the MCD spectrum compared with the absorbance spectrum in this same region. The α/β bands each split into pseudo A-term derivative features that allow at least four electronic transitions to be examined. On close inspection CYP2C9-(PhP-TRZ) exhibits pronounced differences in peak location and amplitude compared with directly N-ligated fragment complex CYP2C9-(123-TRZ) (Table 2.3). Although similar decreases in differential absorption are observed for the two complexes at 530 nm and 572 nm, the bands do not appear to shift for the axial-H_2O bound complex. Several other marked differences in peak position and band shape exist throughout the spectrum, and are especially noticeable within the CT region highlighted as inset between 640 - 720 nm. The spectral disagreement between CYP2C9

complexes that harbor identical 123-TRZ moieties is entirely consistent with distinct heme binding motifs, as previously determined by EPR. Although the relationship between axial Fe(III) ligand identity and heme electronic transitions in this spectral region is complex, direct coordinate bonding of nitrogen to a heme center is anticipated to induce fundamentally distinct perturbations of the heme molecular orbitals that govern absorbance, compared with those caused by mere hydrogen bond effects or local active site polarity changes affecting a resident H_2O ligand (*119, 125-127*). In conclusion, MCD has amplified differences between the spectral fingerprints of CYP2C9 in complex with PhP-TRZ and 123-TRZ, suggesting that atypical, or azole-H_2O-heme binding behavior can be detected optically.

2.3.4 Assessment of the metabolic stability of PhP-TRZ in complex with CYP2C9 and effects upon NADPH consumption

The metabolic stability of PhP-TRZ was assessed in the presence of reconstituted CYP2C9 activity to determine whether low-spin heme-H_2O-TRZ complexes are catalytically competent in this isoform. CYP2C9 activity was reconstituted with cytochrome P450 reductase (CPR) and Cytb5 using a standard three lipid premix protocol of Shaw et al. (*117*). Steady-state kinetic parameters for diclofenac 4-hydroxylation were measured by LC-MSMS assay (K_M = 13.5 ± 9.4 μM, V_m= 1.2 ± 0.1 μM/min, k_{cat} = 47.5 min^{-1}; data not shown) to verify that catalytic behavior of the mutant CYP2C9 studied here (hepta mutant, see Chapter 2.2.2) was similar to the wild-type. Metabolic stability of PhP-TRZ was assessed by the methods of substrate depletion LC-MSMS assay (see Chapter 2.2.7). No significant depletion of PhP-TRZ was observed during the analysis conducted at several concentrations of PhP-TRZ ranging between 0.050 – 100 μM

substrate in the presence of 45 nM CYP2C9 over the course of 10 min assay time. Figure 2.13 shows a representative depletion plot for PhP-TRZ compared with diclofenac control.

Next we considered the possibility that interactions between axial H_2O and PhP-TRZ could influence catalytic uncoupling in CYP2C9. Specifically, rates of NADPH consumption measured by optical absorbance (see Chapter 2.2.9) were compared for ligand-free reconstituted CYP2C9 to rates measured in the presence of PhP-TRZ and the two probe CYP2C9 substrates (S)-flurbiprofen and diclofenac. Figure 2.14 compares the rates measured for each system including protein-free control (background NADPH depletion), and these values are given in Table 2.4. Probe CYP2C9 substrates (S)-flurbiprofen, and diclofenac stimulated NADPH consumption significantly above basal levels, with measured rates of 59.9 ± 1.0 min^{-1} (+ 24%) and 60.7 ± 0.6 min^{-1} (+ 26%), respectively, compared with 48.2 ± 0.9 min^{-1} measured in the absence of substrate. Interestingly, despite the metabolic stability of PhP-TRZ in the presence of reconstituted CYP2C9 activity, a moderate increase in NADPH consumption was observed, with a measured rate of 52.2 ± 0.8 min^{-1} (+ 8.3%). The results suggest that PhP-TRZ interactions with axial H_2O may affect unproductive catalytic uncoupling in the absence of productive turnover. Interestingly, previously reported values by Locuson et al. for both the basal rate of NADPH consumption (9.7 ± 8 min^{-1}) and (S)-flurbiprofen-stimulated rate (114 ± 13 min^{-1}) are drastically different than the rates measured here, and highlight the dependence of the reconstitution strategy and detection methods employed (*40*).

2.3.5 Identification and characterization of apparent ‘type II’ heme-H_2O-triazole ternary complexes in CYP51B1 (*M. tuberculosis*) by EPR

To further explore the range of CYP isoforms that form triazole-water-heme complexes, the bacterial CYP51B1 from *M. tuberculosis* was studied (*Mtb*; strain H37Rv). Several mono-substituted 123-TRZ-based compounds were screened for binding to CYP51B1 via UV/vis absorbance. Two molecules that induced apparent type II optical responses were identified: PhP-TRZ and the estrogen-derivative 17α-1H-1,2,3-triazolyl-estradiol (17-click). The absorbance spectra of the two complexes were similar—both redshifted the Soret by ~4 nm and induced similar perturbations of the α:β spectral region. Figure 2.15 shows the measured calculated difference spectra from the titrations along with measured affinity parameters, $K_{s,}$ obtained from constructed binding isotherms. The spectral trough behavior was also conserved for the two ligands, indicating similar effects on the ferric heme iron spin equilibrium toward low-spin. However, the larger 17-click displays considerably higher affinity for CYP51B1, possibly the result of its steroid-like structure because this bacterial isoform is known to prefer sterol substrates (*95*). Interestingly, although a type II spectral perturbation could be induced by 123-TRZ fragment binding, the affinity for CYP51B1 was dramatically lower (>> 10 mM) (data not shown) than that measured in mammalian drug metabolizing isoforms CYP2C9 (10 mM) and CYP3A4 (14 mM; Chapter 3.3.3) and demonstrates that the energetics of heme-(123-TRZ) interactions are altered in CYP51B1.

The apparent type II binding of 123-TRZ, PhP-TRZ, and 17-click to CYP51B1 observed by optical spectroscopy was scrutinized further by CW EPR. The EPR spectral results obtained at 15 K for ligand-free enzyme are compared with complexes of 123-TRZ, PhP-TRZ, and 17-click in Figure 2.16, and the tabulated g-values obtained from fits of the spectra are given in Table 2.5. The EPR spectrum of ligand-free CYP51B1 shows a typical rhombic EPR pattern, with three g-values at 2.436 (g_z), 2.260 (g_y), and 2.191 (g_x), similar to what has been reported by

others (*96*). When 123-TRZ binds CYP51B1, the g-values are shifted (2.498 (g_z), 2.272 (g_y), and 1.872 (g_x)) and the line shape broadened in a manner consistent with direct-nitrogen ligation to the ferric heme iron. Notably, the low CYP51B1 affinity of 123-TRZ is evident from the presence of a second low-spin species in the EPR spectrum with g-values indicating unbound enzyme in the presence of 80 mM 123-TRZ. In dramatic contrast, the EPR spectra for *both* PhP-TRZ and 17-click in complex with CYP51B1 display g-value shifts and sharpened linewidth in a manner similar to what was observed for PhP-TRZ in complex with CYP2C9, where it was demonstrated unequivocally via HYSCORE that ligand interactions with heme iron are indirect, presumably via a heme axial H_2O ligand intermediary. The g-values for CYP51B1-(PhP-TRZ) are 2.408 (g_z), 2.253 (g_y), and 1.926 (g_x), and are nearly identical to those observed for CYP51B1-(17-click) complex at 2.409 (g_z), 2.253 (g_y), and 1.925 (g_x). The EPR results suggest that mono-substituted 123-TRZs, PhP-TRZ and 17-click, induce total conversion of low-spin, ligand-free enzyme to a ligand-bound state with very similar heme environments in CYP51B1. Importantly, the EPR spectra are not consistent with replacement of axial H_2O by nitrogen on 123-TRZ moiety. However, a small fraction of CYP51B1-(17-click) exists as a species with g-values consistent with direct ligation of the heme iron (III), and is observed in the spectra as small shoulders emanating from g_z to low field and from g_x to high field.

The similarity of EPR spectral behavior observed between CYP2C9-(PhP-TRZ), and CYP51B1 complexes of PhP-TRZ and 17-click was assessed in more detail via HYSCORE analysis. Figure 2.16 shows the HYSCORE spectra taken at g_z for ligand-free CYP51B1 (left), bound to 17-click (middle), and bound to PhP-TRZ (right) in the frequency range containing hydrogen features. In the ligand-free CYP51B1 spectrum, the outer set of arcs at (10.2, 15.2 MHz) lie at similar frequency to those detected in CYP2C9 and are again assigned to the heme

axial ligand H_2O protons. Proton arc analysis defines a Fe(III)--H distance of 2.57 Å for these protons, also similar to that measured by HYSCORE in CYP2C9. The inner set of arcs (11.5, 13.3 MHz) are assigned to the beta protons of proximal heme ligand, thiolate, as was already assigned in CYP2C9, and reside at a calculated distance of 3.31 Å. Notably, the axial heme-ligand H_2O proton signals remain present in the HYSCORE spectra of both 17-click and PhP-TRZ bound CYP51B1 complexes (10.4, 15.2 MHz; and 10.5, 15.2 MHz for CYP51B1-(17-click) and CYP51B1-(PhP-TRZ), respectively). This result is consistent with the CW EPR behavior observed for the individual complexes of CYP51B1, and with the behavior observed in the CW EPR spectra of CYP2C9-(PhP-TRZ), for which HYSCORE revealed H_2O remained bound to heme iron despite an apparent type II binding response measured optically. Thus, the HYSCORE and EPR data are consistent with two very similar examples of atypical heme binding in CYP51B1; the similarity of the spectra of each suggests a conserved structure at the level of the heme, one involving heme axial H_2O ligand intermediary as transducer of local changes in the heme field that affects shifts in the heme spin state equilibrium normally categorized as type II binding.

Taken together, the EPR and HYSCORE results suggest that two structurally distinct 123-TRZ-based ligands, PhP-TRZ and 17-click, participate in similar bound state structures at the level of the heme, putatively, with axial-H_2O heme ligand acting as an intermediary toward alterations in the heme field. It is important to highlight that apparent type II binding interactions involving axial H_2O and 123-TRZ moiety were observed in two diverse CYP isoforms binding a common ligand, and in the case of CYP51B1, with multiple ligands. Thus, this interaction is CYP isoform dependent and ligand dependent. These results suggests that substituted 123-TRZs

favor non-canonical heme interactions involving water. This phenomenon has not been considered in the context of the historical CYP-ligand spectral paradigm.

2.3.6 Characterization of apparent type II binding heme-H_2O-triazole complexes in CYP51B1 by MCD

The MCD spectra of CYP51B1-(PhP-TRZ) and CYP51B1-(17-click) were contrasted with spectra obtained from CYP51B1-(123-TRZ) and ligand-free enzyme to determine whether the unusual heme ligation state detected by EPR and HYSCORE could be discerned optically, as was previously demonstrated at low temperature (4.7 K) for CYP2C9 in complex with 123-TRZ and PhP-TRZ. The MCD measurements of CYP51B1 complexes were taken at room temperature as an additional check against whether the unique apparent type II binding mode exhibited by PhP-TRZ and 17-click in CYP51B1 during low temperature EPR measurements was an artifact of the freezing process.

An additional advantage of MCD that was exploited during optical measurements of CYP51B1 is that near infrared (nIR) transitions associated with exclusively low-spin enzyme could be detected at the high concentrations used here, and were extremely informative for assessing the chemical nature of the axial ligand (*105, 106*). Figure 2.18 shows the MCD spectra acquired between 490-750 nm (α/β) for ligand-free CYP51B1 (black), and saturated with 123-TRZ (green), 17-click (pink), and PhP-TRZ (blue). The corresponding absorbance spectra (taken in 50 mM KPi (pH =7.5) +10% glycerol-containing buffer) of CYP51B1 and in complex with 17-click and PhP-TRZ are shown at the top for comparison. The inset of Figure 2.18 shows the region of the spectrum known to contain a ligand to metal charge transfer (LMCT) feature of

negative intensity centered at ~650 nm arising from the high-spin enzyme fraction, and this can be used to gauge the relative efficiency of binding-induced low-spin conversion (*106, 123*). The tabulated spectral data are given in Table 2.5. Some key observations are as follows: First, while binding of all three 123-TRZ species attenuates the spectral intensity at prominent transitions, shifts in wavelength for several peak/trough/crossover features are unique or non-existent for PhP-TRZ complex (Table 2.5). In particular, the pseudo A-term derivative MCD feature at ~565 nm that comprises the α band in the absorbance spectrum reveals that PhP-TRZ complex does not shift to longer wavelengths; this is not observed in the absorbance spectrum as the band intensity drops off sharply thereby eliminating a clear peak of reference. In contrast, the CYP51B-(17-click) complex has more spectral similarity to the 123-TRZ bound species. The dissimilarity between CYP51B1 complexes of PhP-TRZ and 17-click observed by MCD was surprising given their very similar absorbance (and EPR) spectra. It was hypothesized that the high glycerol content (55%) employed in the protein samples during the MCD measurements affected the active site hydration state enough to encourage direct ligation to heme iron (III) in CYP51B1-(17-click), which was observed to contain a small fraction of a second species in the EPR spectrum with g-values consistent with type II binding. To aid in this assessment, the nIR spectra of the low-spin complexes were scrutinized and are shown in Figure 2.19. The ligand-free enzyme displays a peak at 1095 nm that is typical in location and intensity for heme thiolate-containing proteins coordinated by an axial H_2O molecule. In contrast, the nIR band for CYP51B1-(123-TRZ) exhibits relatively low intensity and altered line shape concomitant with a pronounced redshift. Similar nIR band behavior has been reported for CYP51B1 in complex with azole antifungal fluconazole (FLU), and was shown by crystallography to be directly coordinated to heme iron (*82*). The nIR MCD spectrum of CYP51B1-(17-click) is similar to the 123-TRZ

complex, and would suggest that our hypothesis that glycerol has encouraged direct ligation of 17-click to the ferric heme iron is correct. In contrast, the nIR feature for PhP-TRZ complex is unique, compared with 17-click and 123-TRZ CYP51B1 complexes, and is consistent with the differential spectral behavior observed by visible MCD. The CYP51B1-(PhP-TRZ) nIR band line shape and position is similar to the ligand-free enzyme that has a water molecule bound to the axial 6th position of the heme, although it is redshifted by 5 nm and broadened. This nIR signature is consistent with axial H_2O ligand remaining bound to heme at the axial 6th position in the presence of PhP-TRZ.

2.3.7 H_2O-bridged heme interactions in CYP125A1: Corroboration of the EPR and HYSCORE technique via analysis of previously identified reverse type I ligand LP10

There are no crystal structures available for the complexes that contain water-bridged triazoles based on spectroscopy described above. Therefore, we sought to validate our approach using a ligand-CYP pair that had been previously characterized crystallographically and shown to retain axial water in the ligand-bound state. Therefore, we obtained CYP125A1 (*Mtb*) from the laboratory of Paul Ortiz de Montellano that had previously characterized by x-ray crystallography a pyridine-based reverse type I inhibitor, LP10 (structure given in Figure 2.22), that retained multiple waters including heme axial H_2O in the low-spin complex (PDB ID: 2XC3) (*87*). Interestingly, because the CYP125A1-(LP10) complex includes a *network* of hydrogen-bonded water molecules that communicate heme interactions between LP10 and axial H_2O heme ligand, in the crystal form, the detection of these effects by CW EPR and HYSCORE

suggests that these methods are not limited to first coordination sphere effects. This makes possible the study of a much larger range of atypical apparent type II structures.

CW EPR spectra acquired at 77 K for ligand-free CYP125A1 and in complex with LP10 are shown in Figure 2.21. The ligand-free enzyme has g-values at 2.401 (g_z), 2.243 (g_y), and 1.926 (g_z). The g-values for CYP125A1-(LP10) complex are only slightly shifted to 2.395 (g_z), 2.242 (g_y), and 1.927 (g_x), but the direction of the shifts as well as the sharpened linewidth of g_z is consistent with previous results with CYP2C9/51B1-(PhP-TRZ) and CYP51B1-(17-click). The diminished magnitude of heme field perturbation due to LP10 binding compared to PhP-TRZ or 17-click may be related to the second sphere vs. first sphere interactions of ligand with axial heme water in the low-spin complex. Regardless, the EPR suggests that oxygen is still coordinated to the heme axial 6th position; this assessment is further supported by the typical type II g-value shifts reported for imidazole bound to CYP125A1: 2.53 (g_z), 2.26 (g_y), and 1.89 (g_x) (*97*). The HYSCORE spectrum of both ligand-free and LP10 bound CYP125A1 acquired at field corresponding to g_z are given in Figure 2.21 and show conclusively that the proton signals from axial H_2O remain (10.8, 15.5 MHz; 10.8, 15.4 MHz for ligand-free and LP10, respectively), which is consistent with the crystal structure reported earlier (*87*). Additionally, a detectable increase in H—Fe(III) distance (2.6Å → 2.7Å) is suggested by proton arc analysis of the HYSCORE signals for axial H_2O in the LP10-bound complex, consistent with H-bonding effects.

2.3.8 Assessment of the metabolic stability of LP10 in complex with CYP125A1 and effects upon NADPH consumption

The susceptibility of LP10 to CYP125A1-mediated oxidative turnover was assessed by reconstitution of enzyme activity using spinach ferredoxin/ferredoxin reductase surrogate redox couple in the presence of NADPH regenerating system as described previously by others (*87, 97*). Depletion of probe substrate cholesterol was monitored by APCI MS/MS to assess successful reconstitution. Figure 2.22 shows the time course run for LP10 compared with the cholesterol probe reaction. Despite facile depletion of the substrate cholesterol at 1 μM CYP125A1 ($t_{1/2}$ = 17.4 min) over the course of two hours, LP10 appeared stable under the conditions of reconstitution employed here (see Chapter 2.2.8).

The effects of LP10 binding upon CYP125A1 uncoupling were assessed by monitoring NADPH consumption spectrophotometrically, and Figure 2.23 summarizes the results. The probe substrates cholesterol and cholest-4-en-3-one (C-26 monooxygenase activity previously demonstrated (*87, 97*)) were used to assess the magnitude of stimulated NADPH consumption, and rates of 4.6 min^{-1} (71% increase rel. ligand-free) and 8.2 min^{-1} (203% increase) were measured for the two probes, respectively. Despite the metabolic stability of LP10, it does appear to stimulate NADPH consumption in CYP125A1, with a measured rate of 3.6 min^{-1} representing a 33% increase from the basal rate of NADPH consumption measured in the absence of ligand. These results suggest that interactions between LP10 and active site water may perturb the redox properties of the enzyme and affect unproductive redox cycling.

2.4 Discussion

This chapter characterizes several examples of atypical low-spin azole-ligand binding interactions in diverse CYP isoforms from different species. These results document a previously

unappreciated structural role of CYP active site water networks for low-spin inhibitor binding—an added layer of structural complexity that must be considered in the context of ligand-induced heme spin state perturbations, and ultimately, the catalytic competency of a given low-spin CYP complex. These results expose the limitations of a rigid CYP-ligand classification paradigm in which type II ligands are assumed to behave identically at the level of the heme. It is clear from this study that an exciting avenue of further exploration exists for understanding the range of low-spin structures that are possible, and the range of low-spin inhibitor moieties that are prone to such structural diversity. Details of how these novel structures influence the complicated redox and catalytic properties of CYPs will likely lead to a better understanding of mechanisms of type II ligand turnover.

The novel low-spin binding mode identified in this study for CYP2C9-(PhP-TRZ) complex may hold important implications for CYP-dependent drug metabolism. Given the structural simplicity of PhP-TRZ, we find it unlikely that this heme-H_2O-(PhP-TRZ) structure has been driven by steric clash within the active site, and therefore does not represent a 'compromised' type II binding structure due to inaccessibility of the heme iron. On the contrary, the fact that we observed similar binding behavior for PhP-TRZ in a structurally disparate isoform, CYP51B1, would argue that PhP-TRZ *prefers* to incorporate into active site H_2O networks within the hydrophobic confines of the CYP active. Thus, it is not unlikely that a range of similar apparent type II binding structures readily form in drug metabolizing CYP2C9, especially if one considers the ubiquity of drug moieties that harbor Lewis base functionality competent for iron coordination and/or H-bonding with other species. Although CYP2C9-(PhP-TRZ) proved metabolically stable, we did detect potentially significant effects upon NADPH consumption, which suggests that H_2O-heme low-spin complexes are distinct, catalytically, from

the resting state. These results warrant further study to determine how type II interactions influence catalysis in this important CYP isoform.

A great advantage of EPR over the use of UV/vis optical absorbance to glean structural information for CYP complexes is that EPR allows one to focus on the low-spin enzyme fraction exclusively. An unexpected observation during our EPR measurements of CYP2C9 was the apparent structural heterogeneity present for the ligand-free H_2O-bound state that was not observed for other isoforms measured here (CYP51B1, CYP125A1, CYP3A4 (Chapter 3)). Distinct species detected by EPR in purified CYP samples could indicate several things, including co-purified substrates/ligands, denatured enzyme, or the coexistence of distinct conformations that could potentially harbor differential affinity for ligands, and/or possess unique catalytic properties. A related possibility is that the heterogeneity observed is the result of several surface mutations introduced to the CYP2C9 form (*108*) used here. However, Peng et al. report (*44*) similar heterogeneity observed by EPR using a form of CYP2C9 without these surface modifications, so this is unlikely to be the cause. Importantly, pronounced heterogeneity is also observed in EPR spectra of CYP2C9 in complex with small type II binding fragments. Although each species observed by EPR must be considered distinct from one another, it is tempting to speculate that small azole ligands are binding structurally unique enzymatic forms; furthermore, it is not implausible that what we observe are distinct type II binding modes that vary in orientation and proximity relative to the unpaired electron of ferric iron.

We initially categorized PhP-TRZ as a type II ligand when bound to CYP2C9 based on conventional optical criteria; only after detailed EPR analysis was the unique ligation state appreciated. The unique g-value shifts and sharpened linewidth observed in the EPR spectrum of CYP2C9-(PhP-TRZ) compared with the EPR spectrum of CYP2C9-(123-TRZ) were unexpected

because both molecules contain an identical triazole moiety. Intriguingly, upon review of the older CYP literature we found obvious similarities between our data and the EPR signatures reported by Dawson (*119*) for a series of sterically-hindered nitrogen heterocycles (indole, benzimidazole, 2-phenylimidazole (2-PI)) in complex with P450cam, which were at the time categorized simply as "abnormal" N-donors (*119*). We turned next to pulsed EPR approaches to uncover the molecular details of how the two 123-TRZ interactions were unique. HYSCORE proved invaluable because the analysis clearly revealed that PhP-TRZ binding does not displace/replace axial H_2O ligand in CYP2C9, while 123-TRZ binding does. This is an intriguing result. It implies that the pronounced effects upon the heme-field observed by EPR (and by extension, optically) are the result of *non-local* changes in the environment of ferric heme iron. Importantly, our conclusion based on EPR and HYSCORE is supported by the findings of Poulos et al. who reported a crystal structure (PDBID: 1PHE (*23*)) of P450cam-(2-PI) containing axial water in a follow up study to Dawson's previously mentioned EPR work. Surprisingly, in that study it was found that it is the phenyl moiety of 2-PI, not the imidazole moiety, that is closest to heme axial H_2O. For our purposes, in the absence of crystallographic information, the most crucial piece of information that allow us to conclude with confidence that the heme-H_2O-(PhP-TRZ) interaction in CYP2C9 involves the triazole moiety of bound PhP-TRZ, comes from the HYSCORE results after PhP-^{15}N-TRZ isotopic enrichment. A strong signal from the nitrogen label on the ligand was observed with weak hyperfine coupling that is consistent with the interaction between a somewhat distant azole nitrogen and low-spin ferric heme iron (*120*). These results clearly support our conclusion that PhP-TRZ is oriented towards heme and interacting via H-bonds with heme axial H_2O.

Optical absorbance difference analysis of type II ligands binding CYP2C9 is historically difficult because redshifts of the heme Soret often coincide with decreases in molar extinction, combined with the fact that it exists in a predominantly low-spin form rendering equilibrium shifts toward low-spin difficult to detect (*7, 40*). In this study, we applied MCD spectroscopy to resolve differences in the visible absorbance spectra of water-bridged CYP2C9-(PhP-TRZ) and the directly N-ligated 123-TRZ fragment complex. The visible absorbance spectrum includes contributions from both high and low-spin enzyme, but at the low temperature used during MCD analysis of CYP2C9, the spectrum is dominated by the low-spin fraction (*123*). We observe clear differences in intensity and band location between the two complexes that are not obvious from the absorbance spectrum in this region. Notably, the MCD spectral behavior of CYP2C9-(PhP-TRZ) appears consistent with results of Dawson et al. for several 'abnormal' N-donor ligands in complex with P450cam (*119*) already discussed. These result suggest that the optical spectra of CYP-azole complexes can be useful for identifying 'incomplete' heme ligation, a structural concept that has been proposed by others (*40*).

Our discovery that heme-H_2O-triazole low-spin interactions also occur in the structurally diverse CYP51B1 of *Mtb* eliminates any doubt that the structure identified in CYP2C9-(PhP-TRZ) is an isoform and ligand specific anomaly. As observed for PhP-TRZ interactions with CYP2C9, both PhP-TRZ and 17-click were shown to bind CYP51B1 in an apparent type II fashion based on classic optical criteria, yet their EPR behavior is consistent with indirect perturbations of the heme field. Interestingly, PhP-TRZ and 17-click share similar absorbance spectral fingerprints in complex with CYP51B1 that are very convincing type II signatures; this is in contrast to the difference spectrum measured for CYP2C9-(PhP-TRZ) which showed signs of 'incomplete' heme coordination (*40*). These observations support the proposal that the

spectral paradigm is insufficient for inference of type II and reverse type I ligand structure. Furthermore, the similarity of these 123-TRZ-heme interactions in CYP51B1 was clear from the EPR spectra, which were nearly identical except for a minor amount of a second species appearing in the spectrum of CYP51B1-(17-click) with g-values consistent with direct coordination to the heme. As expected based on the EPR signatures, HYSCORE revealed that H_2O remained bound to the iron despite ligand binding. It must be emphasized that PhP-TRZ was observed to bind in a similar indirect manner in two *structurally diverse* CYPs, while a second mono-substituted 123-TRZ, 17-click behaves similarly in CYP51B1. These observations argue for a preferred indirect ligation mode for mono-substituted 123-TRZs. It is speculated that the low basicity of 123-TRZ (pKa = 1.15) results in relatively inferior coordinate bonding potential with ferric heme iron, and as a result, interactions between active site residues and the triazole periphery are comparable, energetically, so the ligand takes on a much broader range of low-spin structures than related IMZ and 124-TRZ-based type II inhibitor ligands. These observations suggest that 123-TRZ-based libraries may be ideal for characterizing and studying unusual azole-H_2O-heme interactions, as the moiety appears prone to interactions with active site H_2O.

Although little is known about the physicochemical differences between five-member azole isosteres 123-TRZ, 124-TRZ, and IMZ *relevant to CYP binding*, there exists an abundance of literature documenting their physical properties, so some generalizations can be stated: First, 123-TRZ is more acidic than its 124-TRZ isomer, and in turn IMZ (Figure 2.1). Basicity is an important physicochemical determinant of heme iron ligation, and a causal relationship between basicity and nucleophilicity is generally anticipated. Second, while there is currently no consensus on how best to quantify aromaticity, several studies that employed both

computationally and empirically-derived (NMR) indices suggest that 123-TRZ is more aromatic than 124-TRZ, while both are more so than IMZ. However, it is unclear how aromaticity influences imino-nitrogen *lone-pair* electrons involved in metal complexation in these systems, which are not formally part of the aromatic network (*128-131*). Furthermore, with regard to triazoles, although tautomeric equilibria exist in both triazole species, it is far more important in 1,2,3-triazole, which favors a statistical population of 1NH and 2NH tautomers in dilute aqueous conditions (*128*). In fact, 123-TRZ tautomeric equilibria behavior is so complex that numerous discordant results have been published on the topic due to a dependence of the equilibrium on solvent polarity, temperature, and triazole concentration (*132*). Finally, evidence exists that 123-TRZs can coordinate several transition metals, including ferrous and ferric iron, at all three nitrogen positions (*133*), which could be an attractive advantage from a medicinal chemistry standpoint. One, or any combination of these chemical differences between these species may render the heterocycles more or less prone to water bridging interactions in CYPs.

The results of room temperature MCD measurements for CYP51B1-(17-click) support the idea that there exists a delicate balance, influenced by the hydration state of a given CYP active site, between the tendency for a triazole-based ligand to form heme-H_2O-azole complexes, or directly ligate heme iron. Near IR MCD spectra of 17-click bound to CYP51B1 appear to conflict with the EPR and HYSCORE results obtained at 15K. This assessment is based upon the apparent similarity of the nIR LMCT bands exhibited by 17-click and 123-TRZ fragment, which suggests both are directly ligating heme iron. The nIR LMCT is unique to low-spin enzyme, and can be highly diagnostic of the axial ligand sets in hemoproteins (*106*). To rationalize this apparent disagreement one must take into account effects that 55% glycerol may have on the hydration state of the CYP active site, compared with only 10% used during the EPR measures.

Glycerol is a non-ionic kosmotrope, meaning it greatly enhances water structure in solution (*134*). This aspect of glycerol makes it a useful additive to improve solubility of biomolecules by enhancing intramolecular interactions within the protein at the expense of intermolecular interactions with the solvent (*135*). Thus, at concentration of 55% glycerol, the active site water dynamics may be altered significantly, either directly via alteration of structural water dynamics, or indirectly via changed behavior of protein secondary structure (*136*). Interestingly, a minor species consistent with direct heme coordination was observed by EPR for CYP51B1-(17-click), so it is tempting to speculate that an equilibrium of ligation states exists for this complex, one that can be perturbed by affectedly 'wetting' or dehydrating the CYP51 active site. Notably, the CYP51B1 crystal structure reveals a large active site that is bulk-solvent exposed (*82*), and this may render the local water dynamics of the heme highly susceptible to additives in solution. High glycerol was observed to influence the equilibrium between two distinct low-spin forms of antifungal drug fluconazole in complex with CYP121 of *Mtb* (*33*). In contrast, a distinct low-spin species that we assign as water-bridged CYP51B1-(PhP-TRZ) complex was observed by nIR MCD, in agreement with only a single species detected by EPR. Interestingly, it has been shown for several low-spin hemoprotein types that a correlation exists between the axial, Δ, and rhombic, V, crystal field parameters (see EPR Background, Chapter 2.1.4) calculated from the g-values measured by EPR, and the location of the LMCT transition measured by MCD (*137*), yet this correlation failed to accurately predict the location of the nIR band for CYP51B1-(PhP-TRZ) complex. One possible reason for a lack of correlation in complexes of CYP51B1 could be the high ratio of V/Δ (= 0.934 for ligand-free) which results in reclassification of CYP51B1 as possessing an 'improper axis' that can result in an alternate electronic ground state for ferric heme iron $(d_{xz}, d_{yz})^4(d_{xy})^1$ as is described elsewhere (*99*). Additionally, it is worthy of mention

that the experimental data used to derive the original nIR MCD-EPR correlation was collected from a series of globins and electron transfer cytochromes all possessing proximal histidine 5th-axial ligand in contrast to the cysteinyl ligand of these CYPs.

While the results presented here are the first documented examples of low-spin heme-H_2O-azole ternary complexes in CYP2C9 and CYP51B1, the structural motif that is proposed is not unprecedented. Seward et al. published a crystal structure along with supporting nIR MCD and CW EPR evidence for apparently similar heme interactions occurring between azole antifungal drug fluconazole (FLU) and CYP121, also from *Mtb* (*33*). In that study the CW EPR behavior is very close to what we report here for both CYP2C9 and CYP51B1. In addition, the extremely high resolution crystal structure obtained (1.9 Å) showed unequivocally that axial water remained bound while in direct H-bonding contact with the 1,2,4-triazole moiety of FLU (Figure 1.4, Chapter 1). These finding support our extension of the CW EPR and HYSCORE results reported here to inferences for ligand-bound structure at the level of the heme iron. Importantly, the CYP121-FLU result demonstrates that expectations for this type of apparent type II binding behavior can be extended to other heterocycles, including type II binding moieties that are commonly found in CYP-targeted drugs. An additional crystallographic example from CYP121 in complex with cyclo di-tyrosyl substrate (PDB ID: 3G5H (*138*)), cYY, highlights an even more complex heme-H_2O-ligand structure involving as many as three structural waters in H-bonding contact with ligand and axial-H_2O ligand. That same study presented EPR data that is also consistent with what we observe for our complexes. Finally, as was mentioned in the results, water bridged complexes have been found in P450cam that are apparently similar to those reported here, although the link between EPR spectral behavior and CYP101A1-(2-PI) structure (in addition to several other 'abnormal' nitrogen donor ligands) was

never expounded upon by Dawson or others. Thus it is rather curious, if not a bit ironic, that the very same enzyme of which the spectral ligand classification paradigm was based also appears susceptible to the atypical heme-ligand binding behavior documented here for CYP2C9, and CYP51B1 complexes.

Our ability to identify increasingly complex low-spin CYP-ligand structures involving intermediary molecules by CW EPR and HYSCORE is demonstrated via analysis of CYP125A1-LP10. We chose to study reverse type I inhibitor LP10 by EPR specifically because of the intricate water network that was demonstrated in the crystal structure of this complex. It was not clear whether EPR would be useful for detecting such long-range heme interactions, i.e. those that appear to transduce alterations of the heme field via participation of secondary 'shells' of active site water. Indeed, the EPR behavior of this complex is entirely consistent with what was observed for the other examples in this chapter, albeit the magnitude of the effects on g-values appeared diminished relative to CYP2C9-(PhP-TRZ) and 17-click/PhP-TRZ in complex with CYP51B1, which is, however, consistent with the more remote nature of the interaction with iron. Intriguingly, the fact that LP10 binding induces a classic reverse type I spectrum in CYP125A1 warrants EPR characterization of the numerous examples of reverse type I ligands documented in the literature so as to shed light on the structure of this rather anomalous historical categorization. Finally, it is important to highlight that LP10 is a pyridine-containing low-spin inhibitor, which suggests that more basic, 'drug-like' moieties are also prone to atypical heme binding behavior.

Functionally, the water bridged low-spin CYP2C9-(PhP-TRZ) and CYP125A1-(LP10) complexes studied here are metabolically stable. However, these low-spin structures appear to have altered catalytic properties from the H_2O-ligated heme resting state. A significant increase

in NADPH consumption was observed for both complexes relative to the resting state enzyme, and this suggests that the CYP catalytic cycle is stimulated by ligand binding, but that unproductive redox cycling (H_2O_2, O_2^-, or H_2O formation) dominates. These results are intriguing because they suggests H-bonding interactions with heme axial water in CYPs can alter the redox potential of the heme Fe(III) and/or disrupt productive oxygen binding and proton transfer mechanisms during catalytic turnover. The potential for alterations of the heme spin state, and by extension possible effects upon heme redox potential, as the result of H-bonding to the axial 6th heme-ligand are significant. Smulevich et al. has demonstrated large H-bonding effects on heme iron spin state in several heme-containing peroxidases, as well as the alkaline form of metmyoglobin (Mb) (*125-127*). Notably, alkaline forms of both horseradish peroxidase (HRP) and Mb contain identical axial ligand sets (His-Fe(III)-OH^-), yet only Mb contains a significant fraction (~ 70%) of hexacoordinate *high-spin* heme (*127*). This phenomenon in HRP was rationalized by the authors' to be the result of H-bond donation from a neighboring arginine residue (R38) to the resident 6th-axial hydroxide ligand, resulting in more water-like character for the heme ligand. The importance of this residue for both spin state control and axial ligand affinity was later demonstrated by mutagenesis (*126*). As an extension of this observation to our system, it is not unreasonable to suggest that H-bond donation *from* the axial-H_2O in CYP to an azole ligand may impart more hydroxide-like (high-spin) character to the heme iron—a condition that may encourage more facile reduction of the cofactor. Such a direct reduction mechanism has been suggested by Jones et al. (*139*) to explain facile turnover of several type II binding pyridines; however, the alternate low-spin structures described in this chapter were not considered. Lastly, with regards to catalytic uncoupling, we propose that atypical heme binders such as those documented here encourage the retention of active site water, which in turn

disrupts normal proton-transfer conduits and local water concentration near the oxygen binding site. The importance of local water concentration to the precise orchestration of proton transfer pathways in CYP has been suggested by Raag et al. (*140*) to explain the marked increase in catalytic uncoupling in the Thr252 P450cam mutant, as documented by Sligar et al. (*141*).

This aim of this chapter is to emphasize the range of unusual, and often unanticipated, low-spin CYP-ligand complex structures that exist—structures that have not been considered in the traditional spectral paradigm that classify CYP ligands as substrates or inhibitors solely on the basis of qualitative optical measures of heme spin state. The results suggest additional complexity for low-spin heme interactions and warrant further consideration during any mechanistic interpretation of type II and reverse type I inhibitor metabolism. Furthermore, the results demonstrate the advantages of sensitive spectroscopic techniques such as EPR and MCD to probe the local heme environment in complex with azole ligands, and the data serve as a foundation for understanding the elusive structural and functional nature of apparent type II and reverse type I inhibitor interactions in CYPs.

Figures

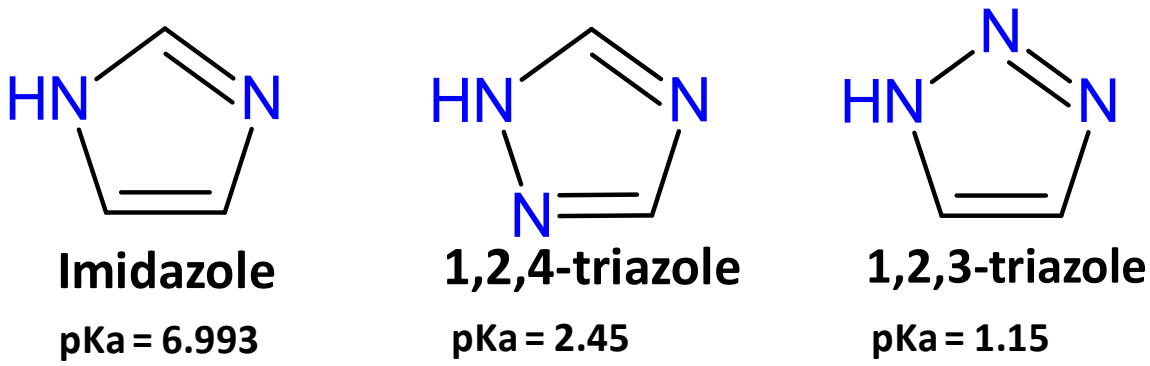

Figure 2.1 Structure and acidity of common azole fragments found in drugs. Interestingly, 1,2,3-triazole (123-TRZ) is absent from existing CYP-targeted therapeutics. This work demonstrates 123-TRZs harbor a propensity to participate in novel heme-ligation modes that often masquerade as traditional 'type II' binding species based on optical criterion. Similar atypical type II binding structural behavior has also been observed for 1,2,4-triazole. 123-TRZ may be an attractive moiety for systematic study aimed at understanding functional and structural anomalies related to type II binding.

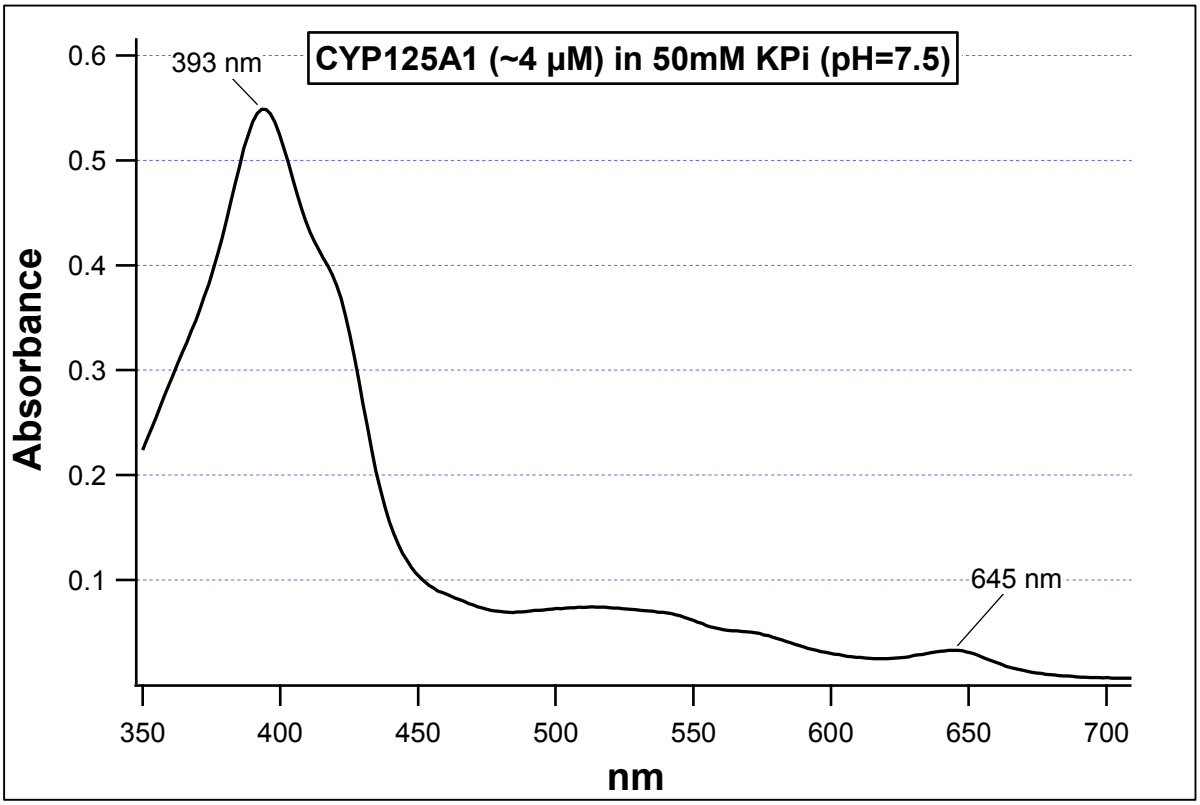

Figure 2.2 Ligand-free CYP125A1 (*M. tuberculosis*) absorbance spectrum. The purified isoform exists in a predominantly high-spin heme form that is evident in the spectrum by the relatively blueshifted maximum wavelength of the heme Soret, the lack of well-defined α/β band structure between 500-600 nm, and the prominent heme ligand to metal charge transfer feature at 645 nm that is unique to high-spin enzyme (*87, 123*).

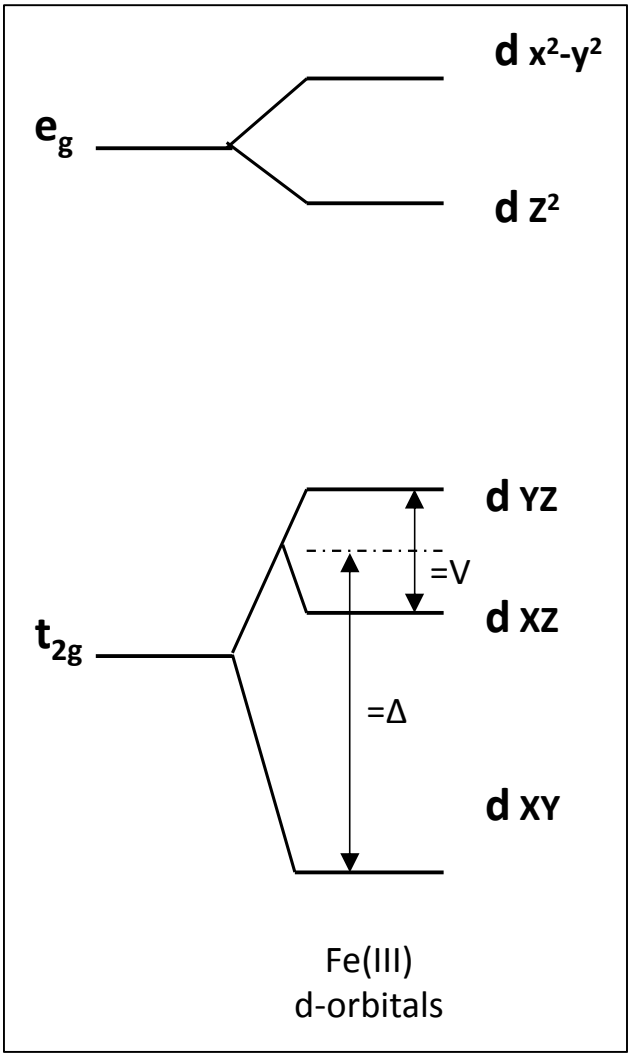

Figure 2.3 Orbital diagram depicting the non-degeneracy of d-orbital energies of ferric low-spin (S = 1/2) heme iron. The lower three t_{2g} orbitals are non-degenerate in CYP heme, and the energy separation of the three orbitals can be described by the axial (Δ) and rhombic (V) crystal field parameters, expressed in this study in terms of the spin orbit coupling constant (SOC, λ) for ferric ion. Taylor has derived expressions (*98*) relating the measured EPR g-values in certain ferriheme systems such as CYPs to these energy parameters, which allow for an energetic metric of heme field effects associated with ligand binding. The formalism derived by Taylor assumes $V/\Delta < 2/3$, which normally indicates an $(d_{xy})^2(d_{xz},d_{yz})^3$ ground state electronic configuration. Note that the e_g orbitals are occupied when high-spin (S = 5/2) or intermediate (e.g. S=3/2) spin states are present in the system.

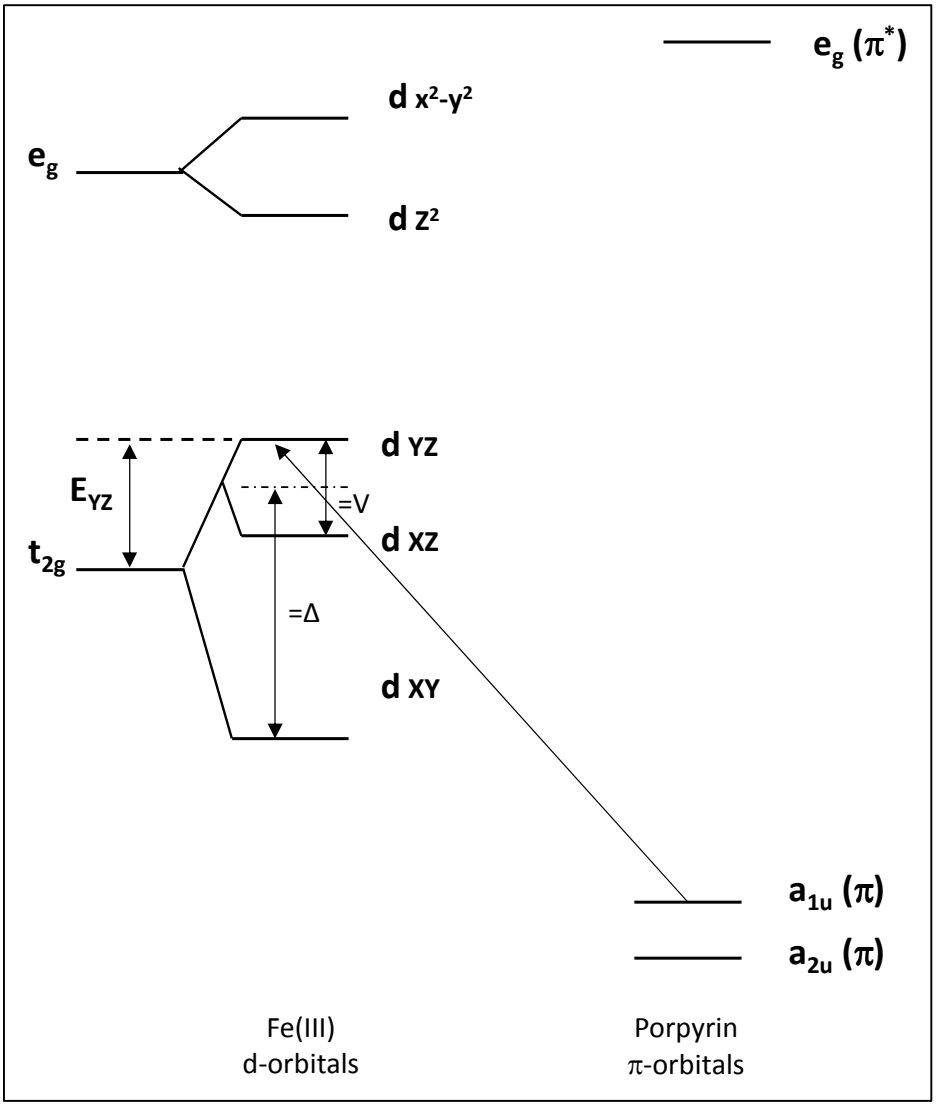

Figure 2.4 Orbital diagram depicting ligand to metal charge transfer transitions (LMCT) that occur between the heme porphyrin macrocycle HOMOs (a_{1u} and a_{2u}) and the d_{yz} hole on low-spin ferric iron ($a_{1u}/a_{2u} \rightarrow d_{yz}$). These transitions can be detected by near infrared magnetic circular dichroism spectroscopy (nIR MCD) and are their location is often highly diagnostic of the chemical nature of the axial ligand ligands in hemoproteins. The precise energy of the transition is determined by the axial and rhombic crystal field splitting parameters (Δ & V, respectively) that describe the energy separation between the iron t_{2g} d-orbitals and are sensitive to the chemical nature of the axial ligands, among other factors. The figure has been reproduced from that presented by Gadsby et al. (*137*). Note that the e_g orbitals of iron are occupied when high-spin (S = 5/2) or intermediate (e.g. S = 3/2) spin states are present in the system.

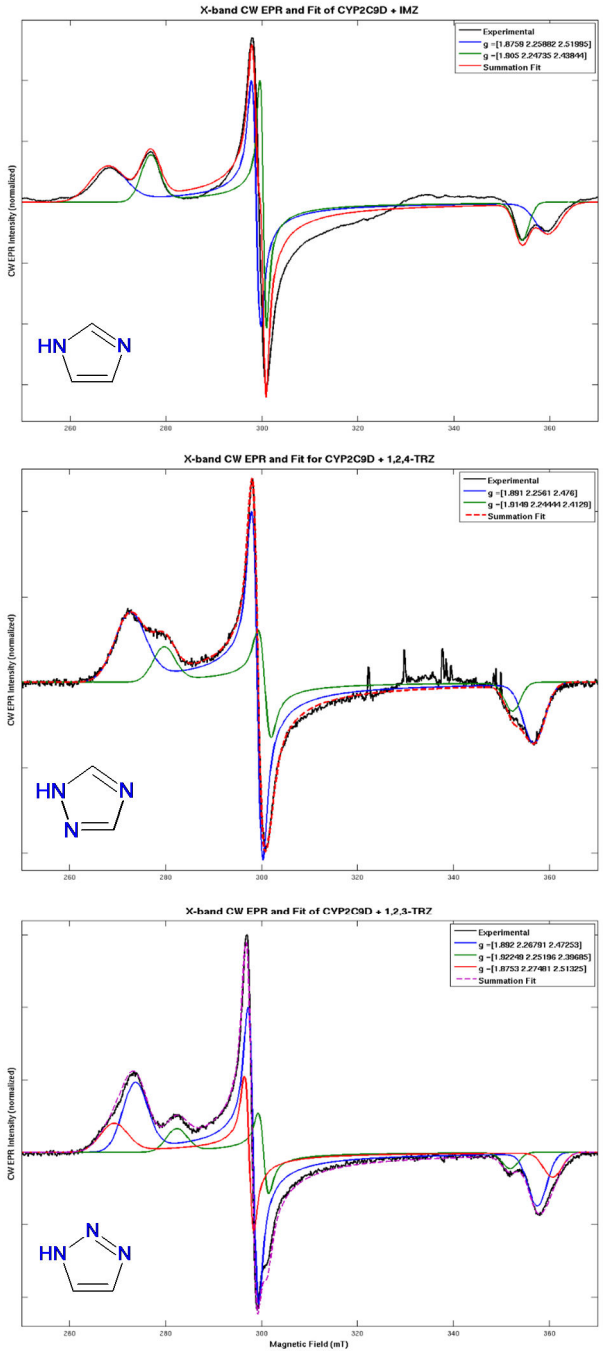

Figure 2.5 EPR spectra (77 K) of CYP2C9 (hepta mutant) in complex with small azole fragments IMZ (top), 124-TRZ (middle), and 123-TRZ (bottom). These azole fragments exhibit a large range of affinities for CYP2C9 (98 - 10000 µM; Chapter 3.3.4), yet there exists multiple, magnetically-distinguishable low-spin species at enzyme saturation in each case. The results of the best fit (Easyspin; Chapter 2.2.4) of each component of the heterogeneous spectra are included along with associated g-values in the legend (also tabulated in Table 2.1).

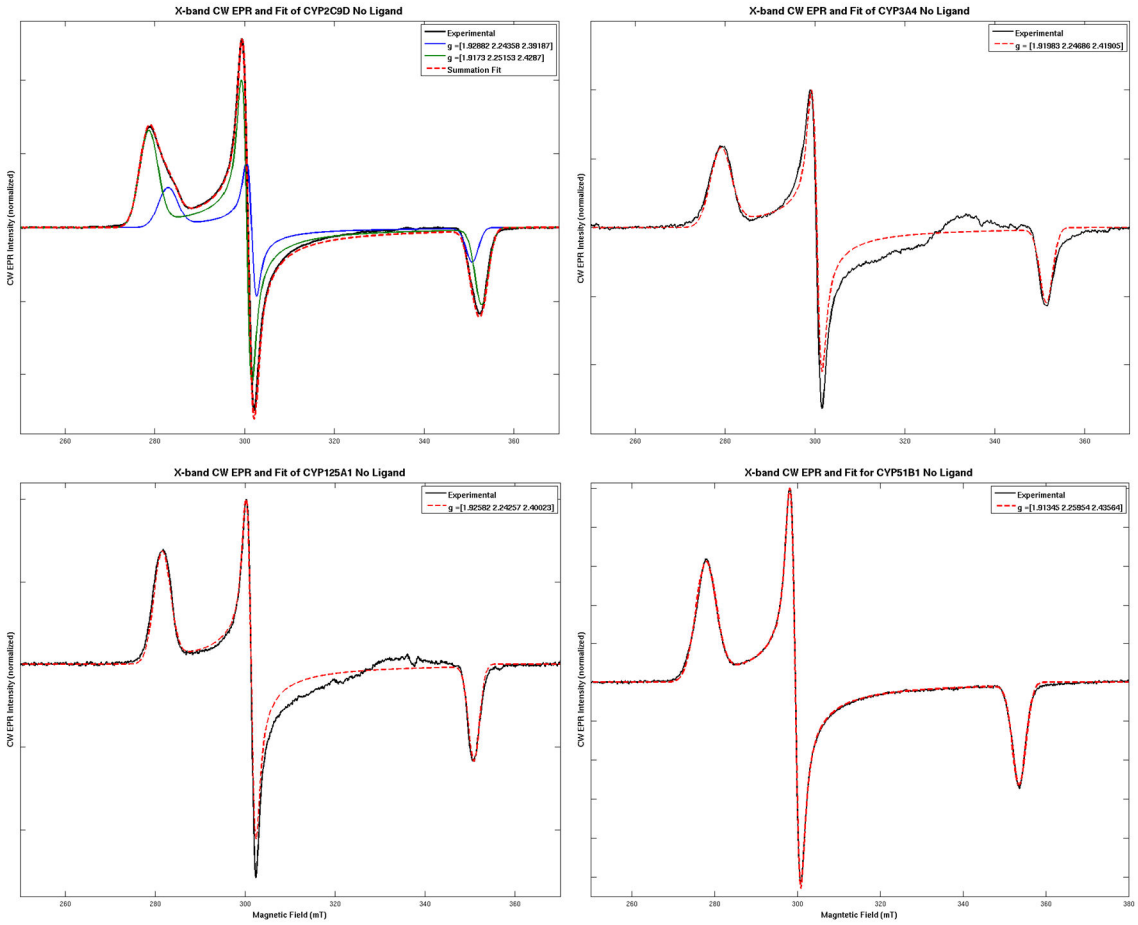

Figure 2.6 Comparison of low-spin EPR spectra of various heterologously expressed, purified CYPs. (Top left) CYP2C9 (hepta mutant, (*108*)) obtained at 15K; (Top right) CYP3A4 (NF14 construct (*142*)) obtained at 77K; (Bottom left) CYP125A1 (*Mtb*, (*97*)) obtained at 77K; (Bottom right) CYP51B1 (*Mtb*, (*96*)) obtained at 15K. The spectra were fit via least squares non-linear regression analysis in EasySpin (*115*). Note the heterogeneity detected by EPR for the low-spin enzyme fraction of CYP2C9 indicating at least two distinct species present for this isoform. In contrast, the other CYPs studied here did not exhibit similar ligand-free heterogeneity.

Table 2.1 EPR data and calculated crystal field parameters for ligand-free CYP2C9 (hepta mutant) and in complex with small azole fragments and PhP-TRZ ligand. Axial (Δ) and rhombic (V) crystal field parameters expressed in terms of the spin-orbit coupling constant for ferric ion were calculated from the g-values for each species using the methods of Taylor (*98*). The individual species are listed in order of their weight (based on double integrated intensity) to the overall EPR spectrum.

Species	Ligand	gz	gy	gx	Δ/λ	V/λ	V/Δ
0.73	CYP2C9	**2.429**	**2.252**	**1.917**	**5.256**	**4.808**	**0.915**
0.27	CYP2C9	**2.392**	**2.244**	**1.929**	**5.378**	**5.263**	**0.979**
0.63	123-TRZ	2.473	2.268	1.892	4.825	4.303	0.892
0.26	123-TRZ	2.513	2.275	1.875	4.695	3.957	0.843
0.11	123-TRZ	2.397	2.252	1.922	5.100	5.154	1.011
0.64	IMZ	2.52	2.259	1.876	5.022	3.900	0.777
0.36	IMZ	2.438	2.247	1.905	5.224	4.622	0.885
0.77	124-TRZ	2.476	2.256	1.891	5.055	4.256	0.842
0.23	124-TRZ	2.413	2.244	1.915	5.287	4.917	0.930
0.70	PhP	2.387	2.254	1.932	5.144	5.370	1.044
0.30	PhP	2.472	2.253	1.894	5.137	4.299	0.837

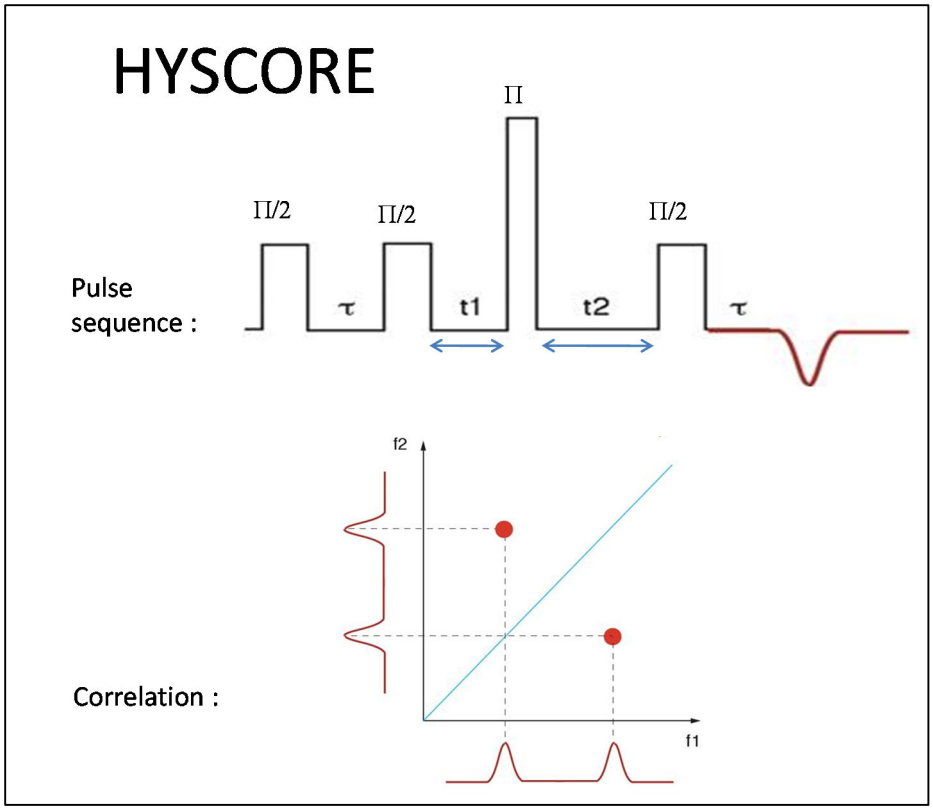

Figure 2.7 Diagrammatic representation of the HYSCORE approach. The EPR pulse sequence is shown in the top left (for a detailed pulse sequence see Chapter 3.2.12). Data is acquired while holding a fixed tau between the first and second pulse while varying the t1 (between second and third pulse) in one dimension with fixed t2 (between third and fourth pulse) in the second dimension. The acquisition is repeated with variable t2 and fixed t1. In HYSCORE the ENDOR frequencies (Hyperfine-shifted NMR frequencies) from nuclei in the vicinity of the unpaired electron spin are correlated with one another and dispersed in two dimensions to improve resolution. The HYSCORE spectra are taken at a magnetic field strength corresponding to g_z in the EPR spectrum; thus, the HYSCORE spectrum at a given field strength detects a specific distribution of molecular orientations within the sample.

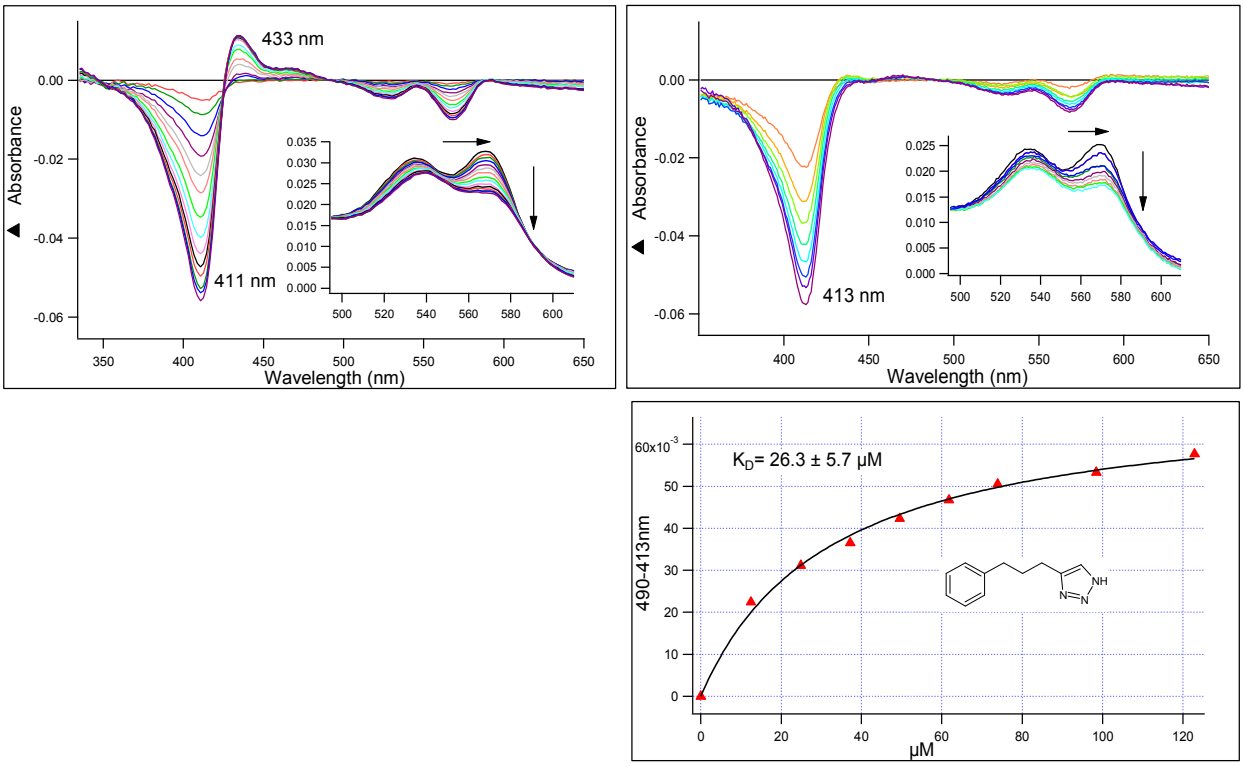

Figure 2.8 CYP2C9 (hepta mutant) UV/vis absorbance difference binding spectra for 123-TRZ (left) and apparent type II binding 4-(3-phenylpropyl)-1H-1,2,3-triazole (PhP-TRZ) (right). The α and β band region of the absolute absorbance spectra are given as insets as further confirmation of apparent type II binding. Note the lack of peak in the difference spectrum for PhP-TRZ binding due to a decrease molar extinction for the Soret band. The K_s determined from non-linear regression of the calculated binding isotherm (botttom right) for PhP-TRZ was 26 ± 6 µM. Protein concentration was 2 µM; 100 mM KPi (pH = 7.4) + 20% glycerol; 20°C.

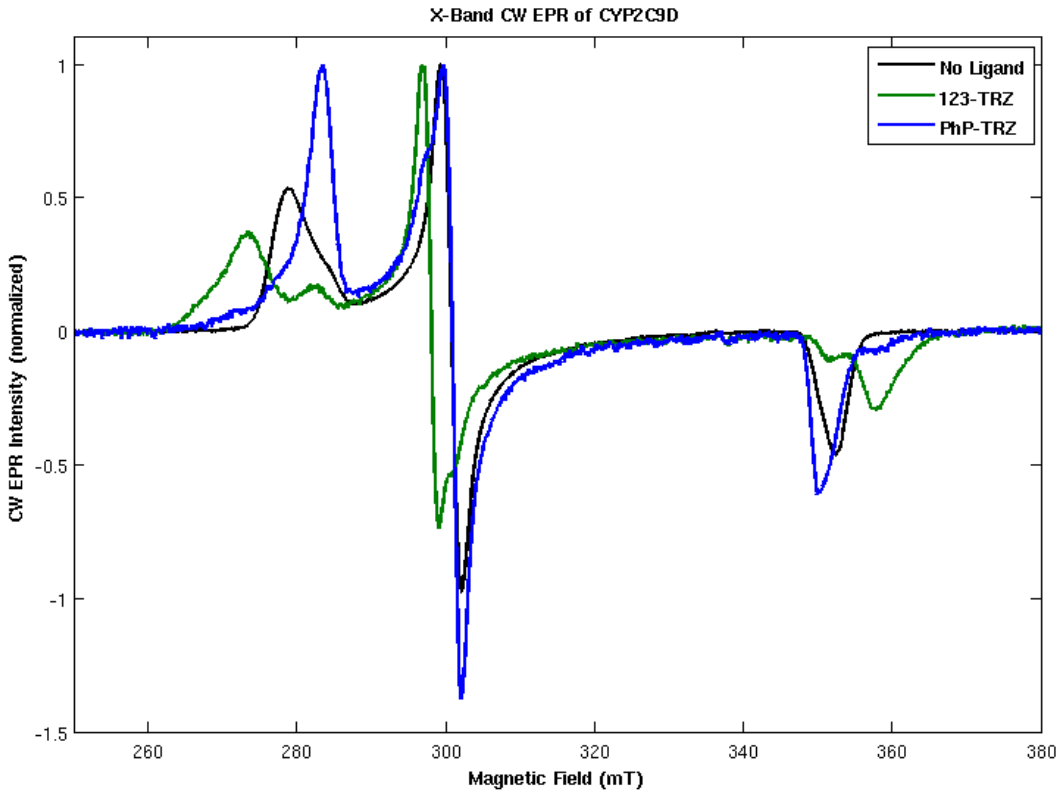

Figure 2.9 CW EPR spectra of CYP2C9 (hepta mutant) and in complex with 123-TRZ and PhP-TRZ collected at 15 K. Ligand-free (black), + 123-TRZ (green), + PhP-TRZ (blue) all normalized to g_y. The shifts in g-values for CYP2C9-(PhP-TRZ) complex relative to ligand-free enzyme are distinct from that observed for 123-TRZ fragment binding, and are not consistent with direct nitrogen ligation. Note the shifts in g_z and g_x induced by PhP-TRZ binding are in opposing directions to the shifts observed upon 123-TRZ binding, and have dramatically different linewidths. All spectra were normalized in intensity to the signal at g_y. Samples prepared with 200µM protein, 100 mM KPi (pH=7.4), + 20% glycerol.

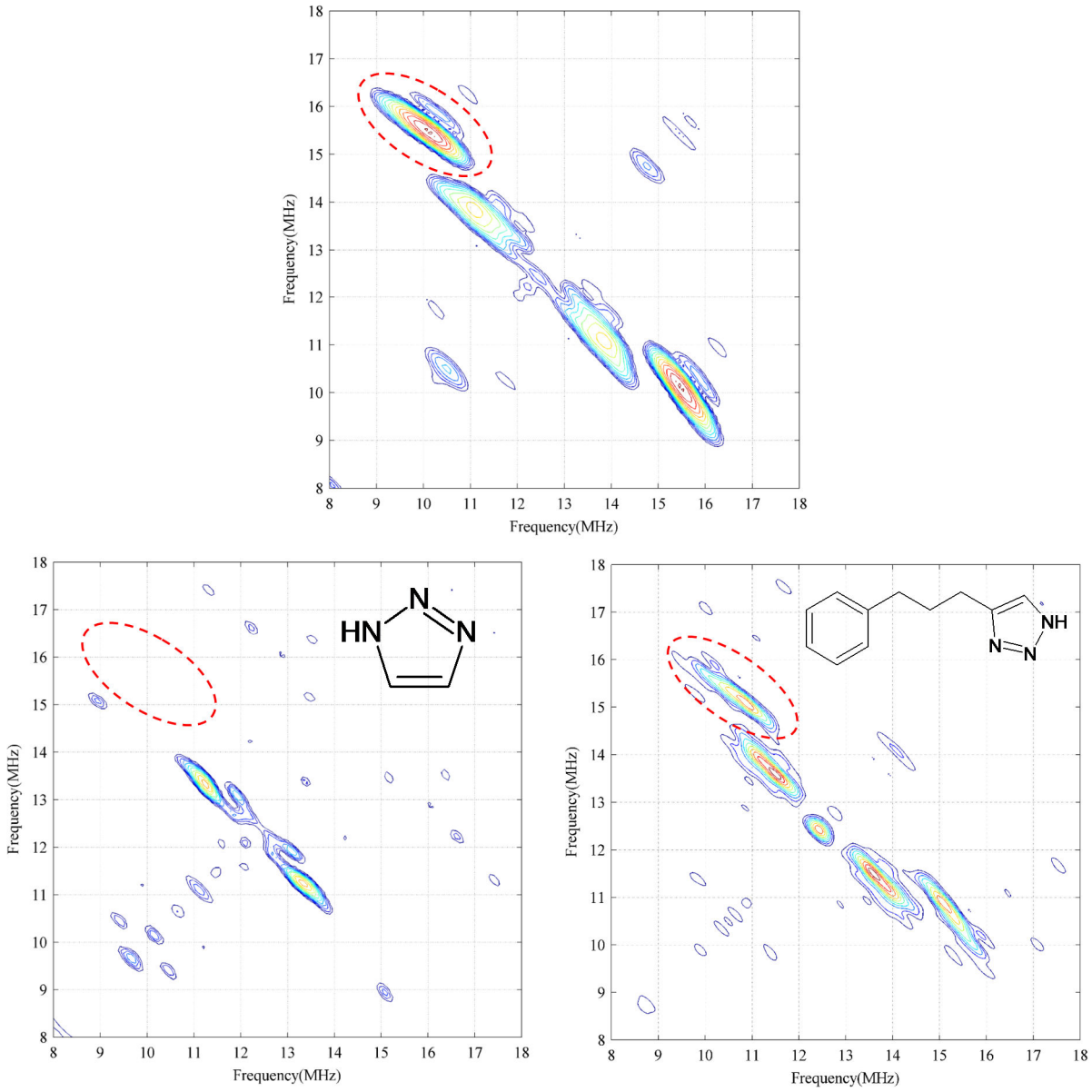

Figure 2.10 HYSCORE spectrum (+,+ quadrant) acquired at 15 K corresponding to proton features for ligand-free CYP2C9 (hepta mutant, top), in complex with 123-TRZ (bottom left), and in complex with PhP-TRZ (bottom right) taken at field strength corresponding to g_z (2870 G, 2837 G, and 2910 G, repectively). The frequecy axis are representative of the *nuclear* frequencies at the magnetic field strength employed during the experiment. The outer set of arcs in the ligand-free spectrum highlighted in red ellipsoid are assigned to axial-H_2O heme ligand protons; the inner set of arcs are assigned to the β protons on the proximal heme ligand, thiolate. Binding of 123-TRZ fragment causes the water proton signals to disappear from the HYSCORE spectrum, consistent with direct nitrogen coordination to heme iron (type II binding). Profoundly, despite apparent type II binding measured optically, PhP-TRZ bound to CYP2C9 retains axially-ligated H_2O. This result is consistent with the differential affect upon the heme field induced by ligand binding as determined by distinct shifts of g-values measured by CW EPR for the two apparent type II complexes.

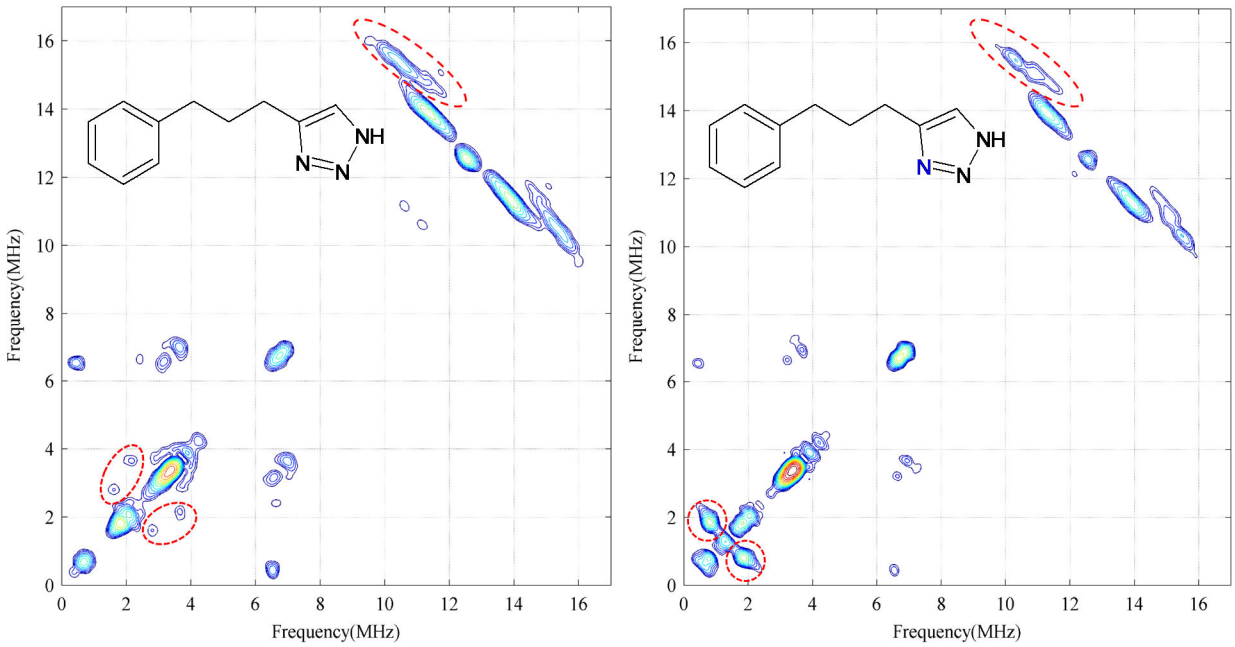

Figure 2.11 HYSCORE detection of ^{15}N-label in CYP2C9-(PhP-^{15}N-TRZ) complex. (Left) HYSCORE spectrum taken at 2935 Gauss corresponding to g_z of PhP-TRZ in complex with CYP2C9 (hepta mutant). Proton arcs from axial H_2O heme ligand are highlighted by red ellipsoid in the upper right corner (> 8 MHZ), where they reside at their larmor frequency, separated by their hyperfine coupling to the lone electron on low-spin iron (III). The signals circumscribed on the lower left (< 6 MHz) correspond to faint ^{14}N couplings between nitrogen of the 123-TRZ moiety of PhP-TRZ and the electron on iron (III). (Right) HYSCORE spectrum taken at 2935 Gauss of ^{15}N-enriched PhP-^{15}N-TRZ (N1:N3, 50:50) in complex with CYP2C9. The axial H_2O protons are again highlighted by red ellipsoid in the upper right. Clearly, there are two additional intense nitrogen peaks at ~1.6 MHz that arise from the isotopic label (hyperfine coupling ~1.5 MHz). The HYSCORE results demonstrate, unequivocally, that axial H_2O is *not* displaced upon binding of PhP-TRZ ligand, *and* that PhP-TRZ resides in close proximity to, and interacts with heme iron, most probably through an intervening water molecule.

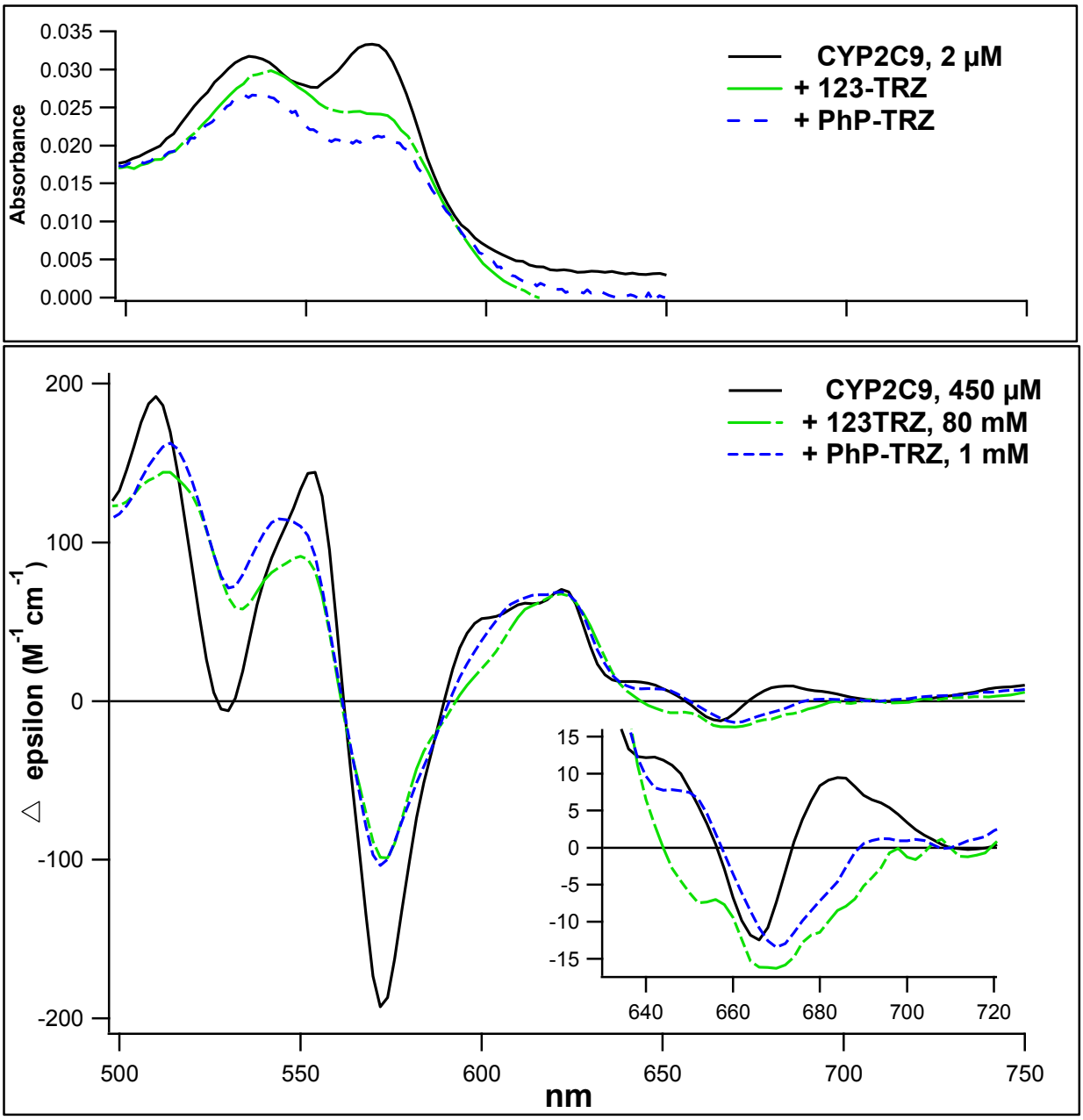

Figure 2.12 Comparison of the CYP2C9 (hepta mutant) absorbance spectrum (top; 298K) and corresponding MCD spectrum (bottom; 4.7K, 6 Tesla field) of CYP2C9 in complex with direct nitrogen coordinated 123-TRZ fragment, and indirectly-ligated (H_2O ligand intermediary) PhP-TRZ. The spectral range shown highlights the α/β region. Although differences between PhP-TRZ and 123-TRZ complex at saturation are evident in the absorbance spectrum, suggesting altered interactions with the heme iron, the MCD spectrum provides much higher resolution of these features. This result suggests that differences in low-spin CYP-ligand complex structure can be scrutinized by optical methods. The absorbance spectrum is for CYP2C9 solubilized in 100 mM KPi (pH=7.4) buffer containing 20% glycerol, while the MCD spectrum required the addition of 55% glycerol as glassing agent for low temperature work.

Table 2.2 visible (495-750 nm) CYP2C9 MCD spectra (4.7 K) taken at 6 Tesla for select 123-TRZ complexes

Ligand	Peak (nm)	Δε ($M^{-1}cm^{-1}$)	Trough (nm)	Δε ($M^{-1}cm^{-1}$)	Peak (nm)	Δε ($M^{-1}cm^{-1}$)	Crossover (nm)	Trough (nm)	Δε ($M^{-1}cm^{-1}$)	Crossover (nm)	Peak (nm)	Δε ($M^{-1}cm^{-1}$)	Crossover (nm)	Minima (nm)	Δε ($M^{-1}cm^{-1}$)
none	510	192.1	530	-6.1	554	144.3	562	572	-192.9	590	622	70.3	656	666	-12.5
123-TRZ	514	144.3	534	57.9	550	91.3	561	574	-99.0	593	622	67.5	644	668	-16.2
PhP-TRZ	514	162.6	530	71.2	544	114.8	561	572	-103.8	591	622	68.9	656	670	-13.4

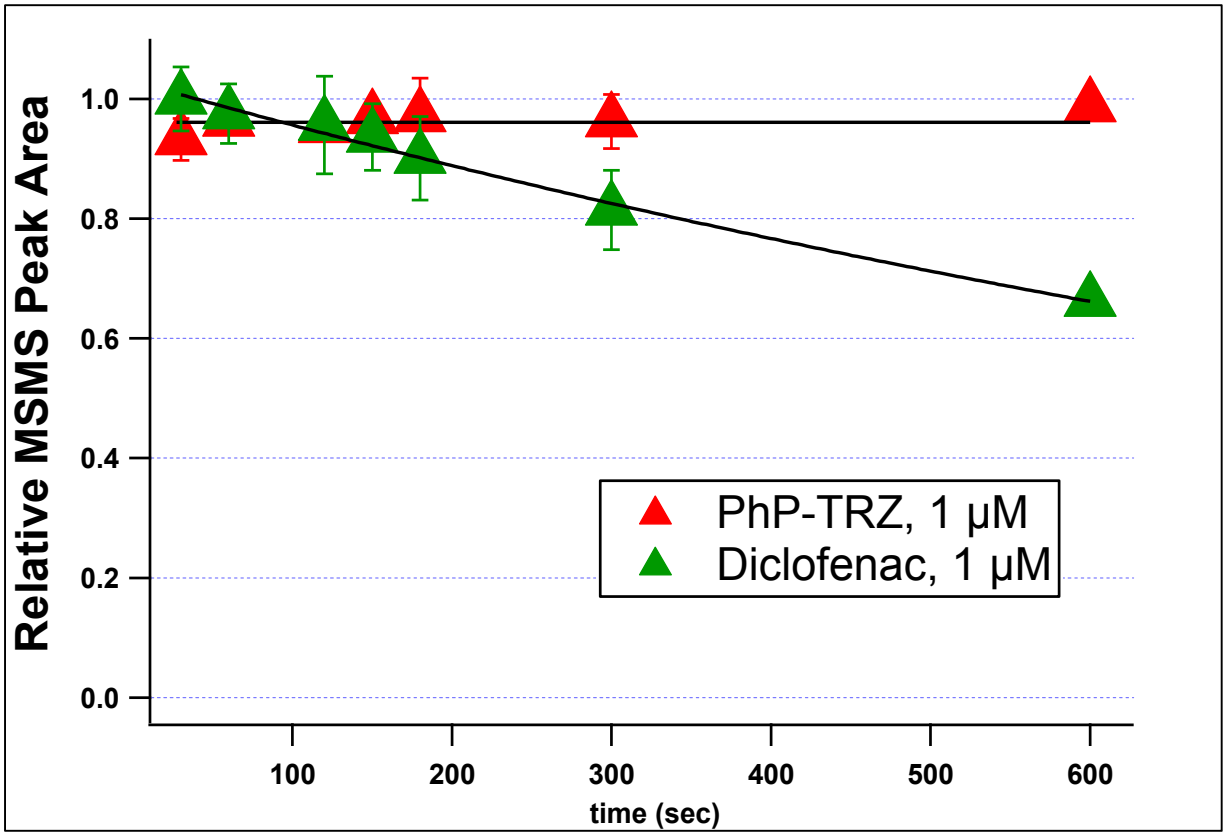

Figure 2.13 Represetative CYP2C9-mediated substrate depletion analysis conducted for H_2O-bridged apparent type II ligand PhP-TRZ (red), compared with control CYP2C9 substrate diclofenac (green). Enzyme and substrate concentrations were 45 nM and 1 µM, respectively. PhP-TRZ is metabolically stable.

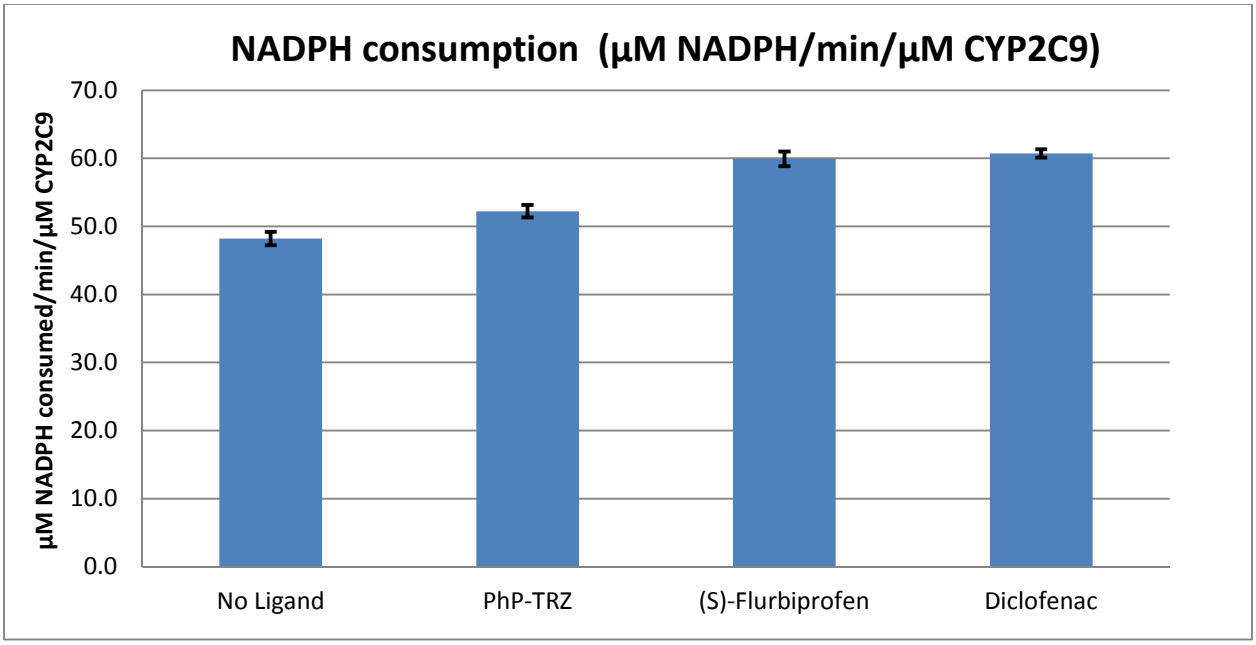

Figure 2.14 NADPH depletion rates (± standard deviation) measured for reconstituted CYP2C9 (hepta mutant, 100 nM) in the presence of probe substrates and H_2O-bridged PhP-TRZ inhibitor. The background rate of NADPH depletion (4.8 min^{-1}) has been subtracted from each experiment. Rates of NADPH depletion (expressed as µM NADPH/min/µM CYP2C9) in the presence of PhP-TRZ were less than that observed in the presence of probe CYP2C9 substrates (S)-flurbiprofen and diclofenac, but slightly elevated relative to the ligand-free reconstitution. The results suggest that low-spin interactions between axial H_2O and PhP-TRZ ligand may increase catalytic uncoupling in CYP2C9.

Table 2.4 Rates of NADPH depletion in reconstituted CYP2C9 activity assays. NADPH depletion was monitored by absorbance at 340 nm and quantified using a molar extinction of 6.22 $mM^{-1}cm^{-1}$. All rates were corrected for background NADPH depletion (No protein control).

	Fit result (µM/min)	+/-	µM/min/µM CYP	+/-	% change from ligand free	+/-
No Ligand	4.82	0.10	48.2	1.0	**0.0**	
PhP-TRZ	5.22	0.09	52.2	0.9	**8.3**	**2.2**
(S)-Flurbiprofen	5.99	0.11	59.9	1.1	**24.3**	**2.1**
Diclofenac	6.07	0.06	60.7	0.6	**25.9**	**2.1**

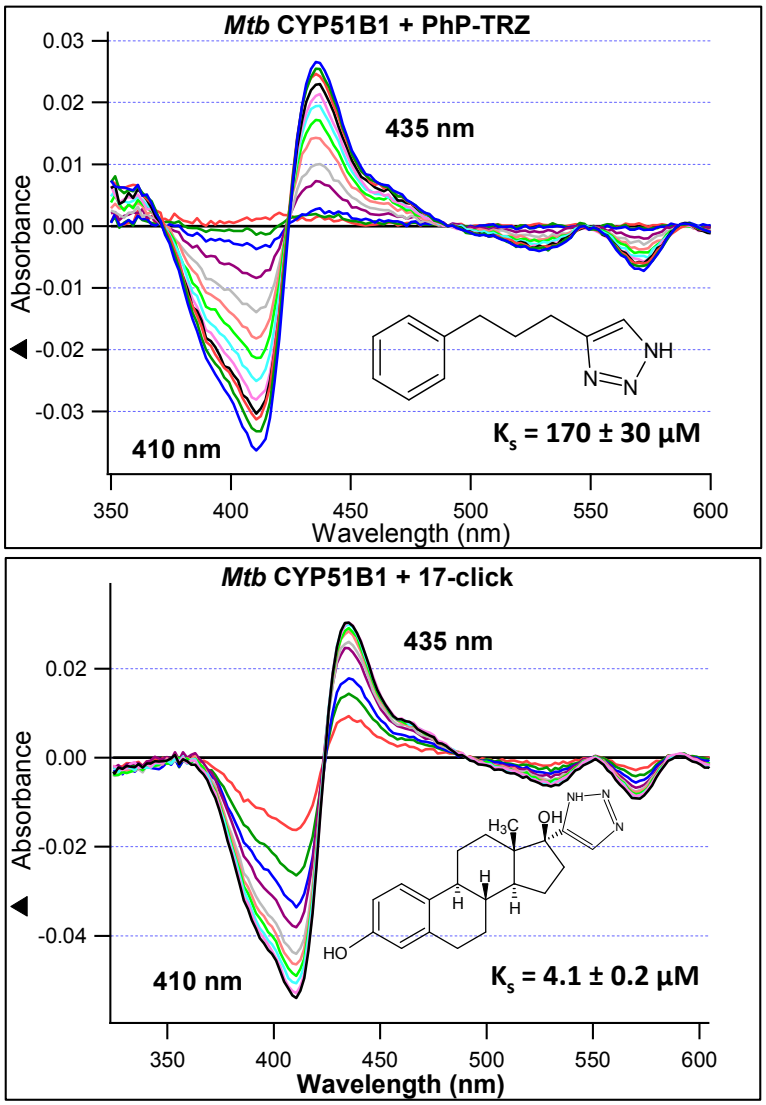

Figure 2.15 UV/vis absorbance difference spectra measured during CYP51B1 (*M. tuberculosis*) binding analysis of 4-(3-phenylpropyl)-1H-1,2,3-triazole (tof), and 17α-1H-1,2,3-triazolyl-estradiol (17-click). Both molecules induce an apparent type II binding response favoring low-spin enzyme. The K_s values determined from the best fit to the calculated hyperbolic binding isotherm are given in the figure.

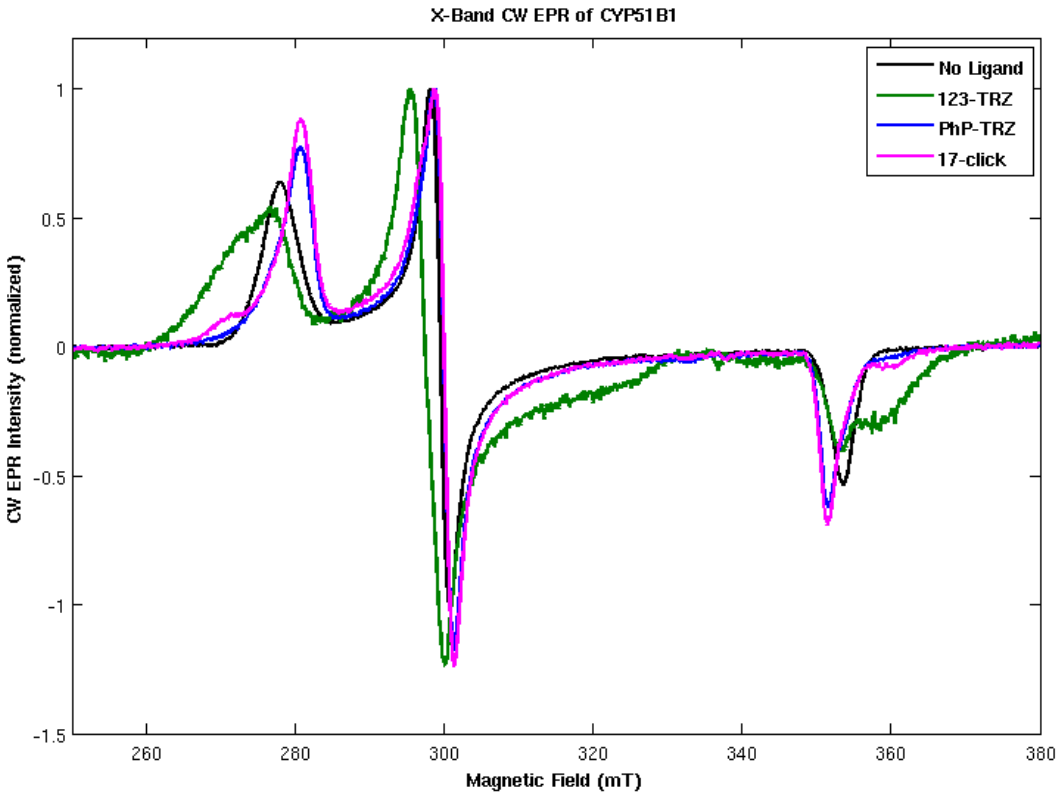

Figure 2.16 CW EPR spectra of CYP51B1 (*M. tuberculosis*) and 123-TRZ complexes normalized to g_y. Spectra were acquired at 15 K (77 K, 123-TRZ) in 50 mM KPi (pH = 7.5) + 10% glycerol, + 100 mM KCl. The ligand-free spectrum of CYP51B1 (200 μM) is shown in black, + 123-TRZ (green), + 17-click (pink), and + PhP-TRZ (blue). The ligands were added to to saturation of the enzyme (~10 x K_D). CYP51B1-(123-TRZ) fragment complex exhibited shifts in g-values and linewidth broadening consistent with direct nitrogen ligation (i.e. type II binding). In dramatic contrast, despite apparent type II binding observed optically, both PhP-TRZ and 17-click bound CYP51B1 complexes induce distinct spectral shifts in both g_z and g_y relative to the 123-TRZ complex, and significant *decreases* of spectral linewidth for those g-values. The EPR g-values are consistent with oxygen coordination to theme iron with dramatic alteration of the heme field relative to the ligand-free state. Interestingly, both atypical type II complexes yield similar g-values for the major component (2.408/2.253/1.926, for PhP-TRZ vs. 2.409/2.253/1.925 for 17-click; g_z, g_y, g_x, respectively), but there clearly exists an additional species in the spectrum of 17-click complex (shoulders of g_z and g_x) consitent with direct nitrogen-coordination.

Table 2.5 EPR data and calculated crystal field parameters for CYP51B1 (*M. tuberculosis*) and in complex with 123-TRZs. Axial (Δ) and rhombic (V) crystal field parameters expressed in terms of the spin-orbit coupling constant for ferric ion were calculated using the methods of Taylor (*98*). The individual species recovered from the EPR spectral fits are listed in decreasing order of their weighted contribution (double integrated intensity) to the EPR spectrum.

Species	Ligand	gz	gy	gx	Δ/λ	V/λ	V/Δ
1.0	**CYP51B1**	**2.436**	**2.26**	**1.913**	**5.063**	**4.729**	**0.934**
0.58	PhP-TRZ	2.43	2.259	1.916	5.091	4.804	0.943
0.42	PhP-TRZ	2.408	2.253	1.926	5.233	5.087	0.972
0.48	17-click	2.427	2.256	1.916	2.427	2.256	1.916
0.35	17-click	2.409	2.253	1.925	5.223	5.068	0.970
0.17	17-click	2.495	2.272	1.88	4.715	4.089	0.867
0.62	123-TRZ	2.498	2.272	1.872	4.627	4.022	0.869
0.22	123-TRZ	2.464	2.266	1.888	4.751	4.333	0.912
0.16	123-TRZ	2.43	2.255	1.911	5.095	4.753	0.933

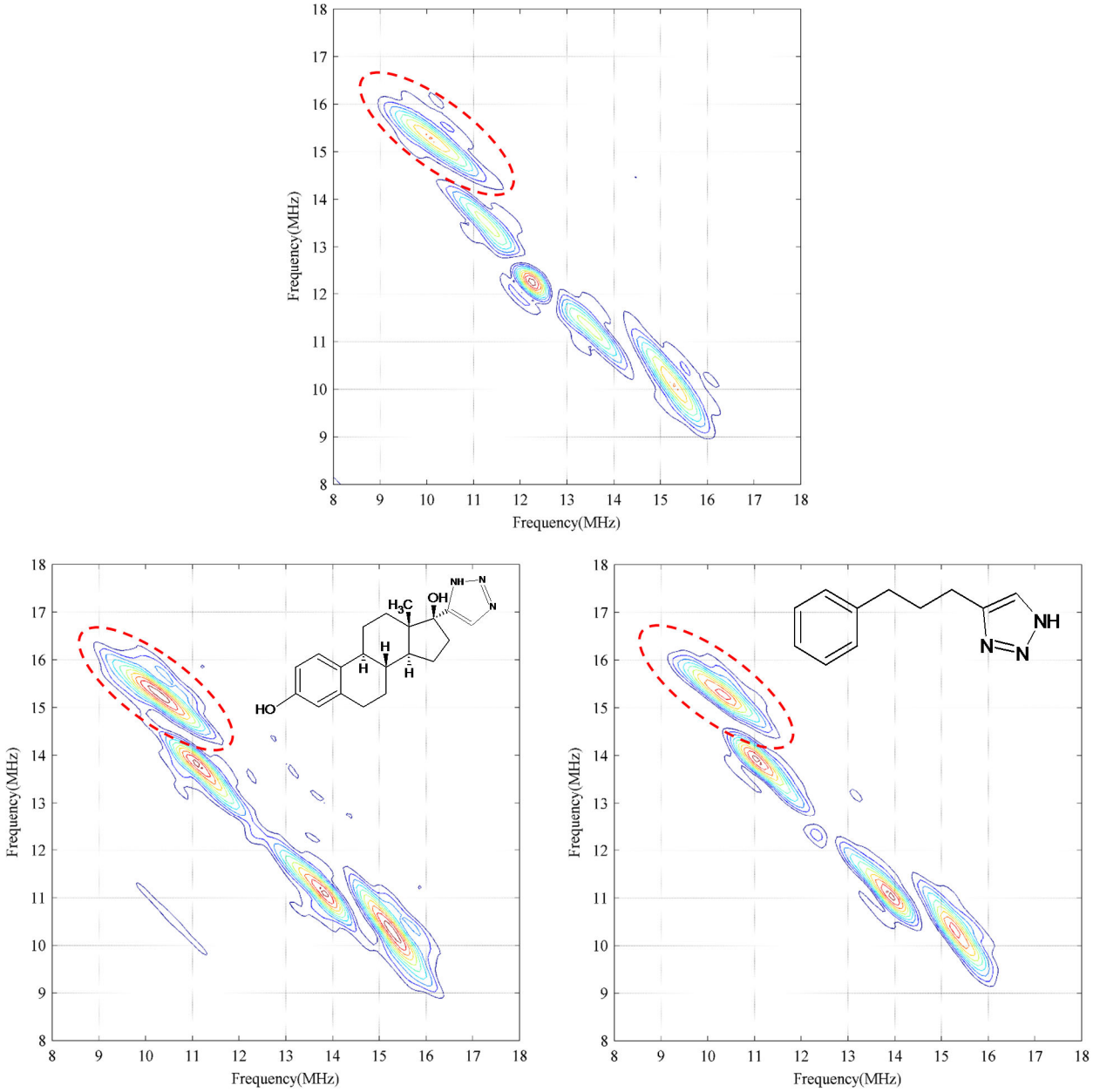

Figure 2.17 HYSCORE spectra obtained at 15 K for ligand-free *Mtb* CYP51B1 (left), and in complex with 17-click (middle), and PhP-TRZ (right) at field strength corresponding to g_z (2865 G 2890 G, and 2880G respectively). In the proton frequency region (> 8 MHz) The outer set of arcs (red ellipsoid) in the ligand-free spectrum are assigned to axial H_2O heme ligand (calculated 2.6 Å H—Fe(III) distance; Chapter 2.2.4); the inner set of arcs are assigned to the β protons of the proximal heme thiolate ligand (3.1 Å). Both apparent type II binding complexes contain signals from heme axial-H_2O ligand in HYSCORE, suggesting that binding of the ligands does not replace the distal heme-ligand dispite large changes in the heme crystal field observed by CW EPR. Taken together with the results of optical analysis and EPR, this suggests that both ligands favor the low-spin heme state via *indrect* interactions with the heme iron mediated through a water molecule.

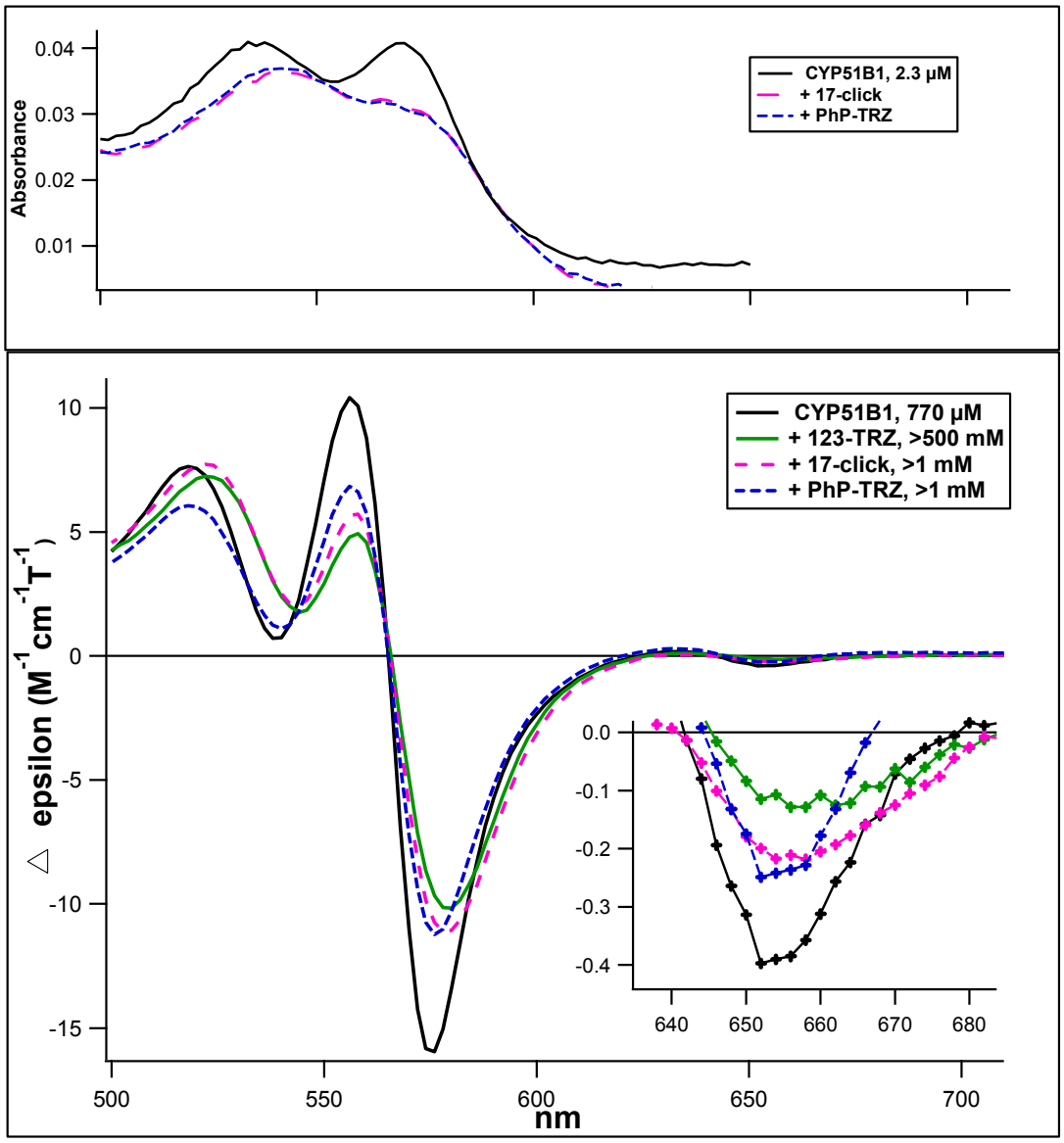

Figure 2.18 298 K MCD spectrum (bottom) of CYP51B1 and in complex with 123-TRZs collected at 6 Tesla field (path length 0.1cm, in 50 mM KPi (pH=7.4), +100mM KCl, + 55% glycerol). The spectral region highlighted as inset includes CT features dominated by the high-spin enzyme fraction that decrease in intensity upon binding type II and apparent type II ligands. The spectra of CYP51B1 complexes of PhP-TRZ and 17-click appear unique in high glycerol buffer, in contrast to the spectral similarity observed for these complexes by absorbance analysis and CW EPR and HYSCORE. (Top) Corresponding UV/vis absorbance spectrum of the same spectral region shown for comparison of the spectal features. The absorbance spectrum was obtained in the same buffer but with only 10% glycerol.

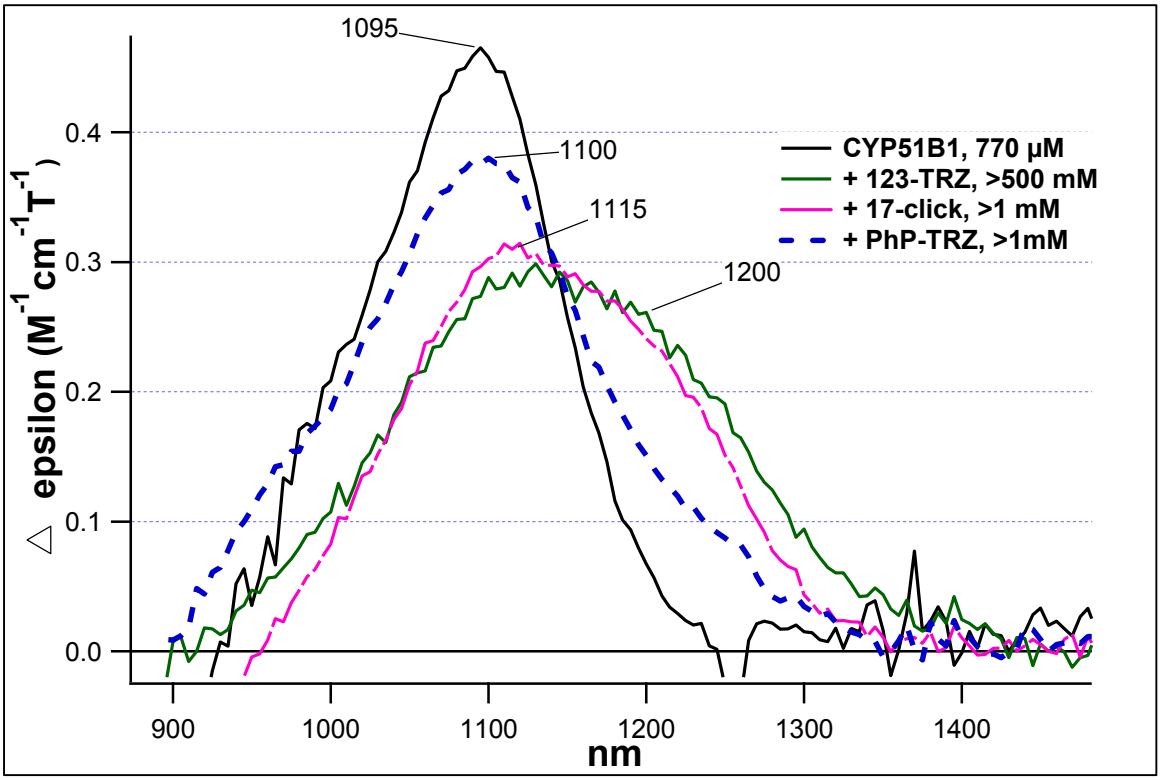

Figure 2.19 Near infrared (nIR) MCD spectra acquired at 298 K and 6 Tesla field for CYP51B1 and associated 123-TRZ complexes. The MCD spectrum in this wavelength range is dominated by two overlapping ligand to metal charge transfer (LMCT) electronic transitions (a_{1u} (π) → d_{yz} and a_{2u} (π) → d_{yz}) that are exclusively low-spin enzyme (*106*). The behavior of these LMCT bands can be a diagnostic reporter of the axial ligand type. Compared with ligand-free enzyme (black), 123-TRZ fragment (green) has altered band shape and a shoulder out to lower energy (~ 1200nm), consistent with significant distortions of the crystal field as the result of direct nitrogen coordination to heme iron. CYP51-(17-click) (pink) appears to behave similar to 123-TRZ and suggest that in the presence of 55% glycerol this ligand is capable of replacing water as axial 6th heme ligand. This result is consistent with two possible low-spin binding modes for 17-click observed by CW EPR: the equilibrium favors hydrogen bonding with retention of axial-H_2O under the low glycerol (10%) and low temperature (15 K) conditions used during EPR and HYSCORE analysis, but appears to favor direct nitrogen heme-ligation in the presence of elevated glycerol (55%). In contrast, the MCD results for CYP51-(PhP-TRZ) complex appear to agree with the EPR data in that oxygen remains bound to iron in the presence of PhP-TRZ, yet the field is distorted, evidenced here by the slight redshift and broadening of the nIR band.

Table 2.5 visible (495 - 750 nm) CYP51B1 MCD spectra (298K) taken at 6 Tesla for select 123-TRZ complexes

Ligand	Peak (nm)	Δε ($M^{-1}cm^{-1}T^{-1}$)	Trough (nm)	Δε ($M^{-1}cm^{-1}T^{-1}$)	Peak (nm)	Δε ($M^{-1}cm^{-1}T^{-1}$)	Crossover (nm)	Trough (nm)	Δε ($M^{-1}cm^{-1}T^{-1}$)	Crossover (nm)	Peak (nm)	Δε ($M^{-1}cm^{-1}T^{-1}$)	Crossover (nm)	Minima* (nm)	Δε ($M^{-1}cm^{-1}T^{-1}$)
none	518	7.6	538	0.7	556	10.4	565	576	-16.0	624	634	0.2	642	652	-0.4
123-TRZ	522	7.3	544	1.7	558	4.9	566	578	-10.1	626	636	0.1	645	658	-0.1
PhP-TRZ	518	6.1	540	1.1	556	6.8	565	576	-11.2	620	632	0.3	644	652	-0.2
17-click	522	7.7	544	2.1	558	5.72	566	578	-11.1	628.0	636	0.1	640	658	-0.2

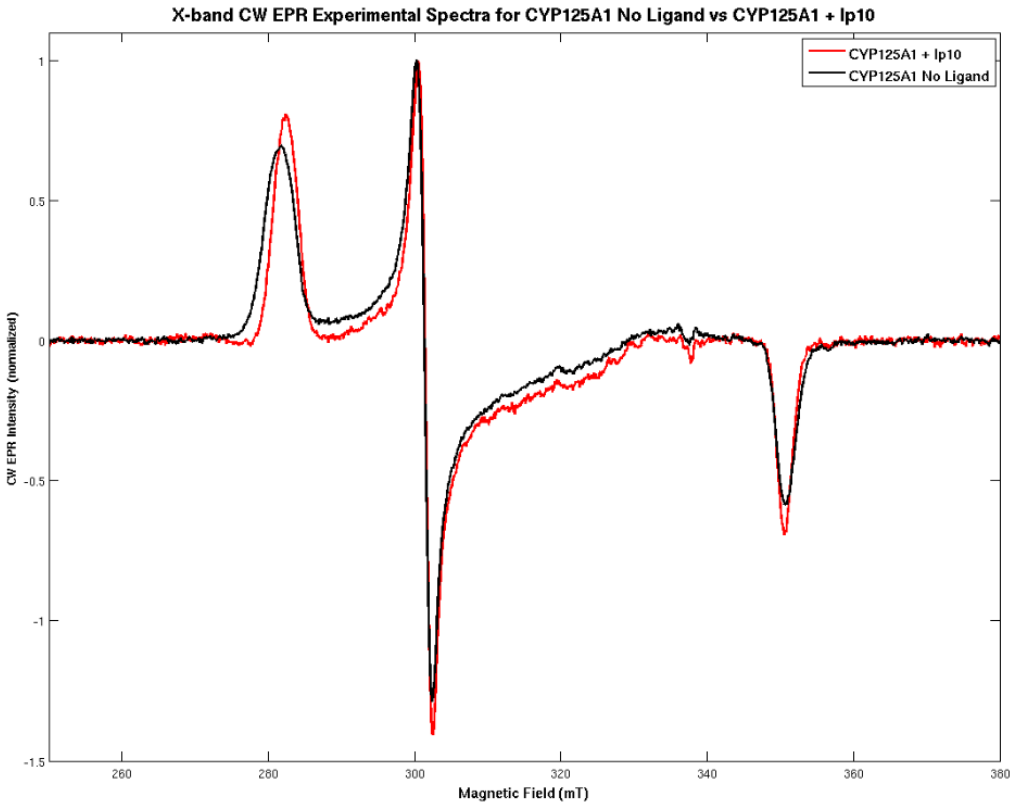

Figure 2.20 CW EPR spectra taken at 77 K of CYP125 (*Mtb*) (blue) and in complex with reverse type I inhibitor LP10. LP10 binding induces shifts to higher field (lower g) for g_z, concomitant with sharpened linewidth for both g_z and g_x, which is consistent with the several other examples of heme-H_2O-ligand ternary interactions documented in this chapter. This EPR result agrees with a previous crystallographic study by Podust et al. (*87*) that found at least two H_2O molecules involved in H-bonding interactions with LP10 while axial-H_2O ligand remained bound. This result demonstrates that second-coordination sphere effects can be detected by EPR-based methods and highlights the range of water-bound apparent type II and reverse type I complexes that are possible for nitrogenous inhibitors.

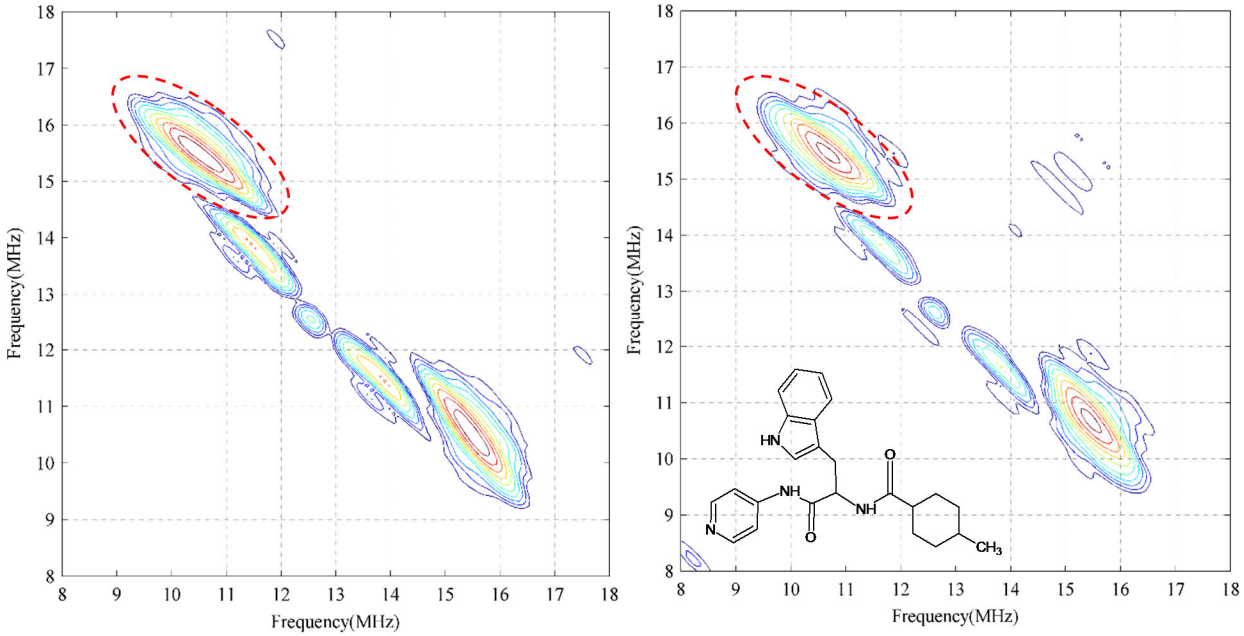

Figure 2.21 HYSCORE spectra of CYP125A1 (*Mtb*) (left) and bound to reverse type I inhibitor LP10 (right) taken at 15 K at field strength corresponding to g_z (2930 G and 2945 G, respectively). Axial water is clearly present in complex with LP10, which is consistent with g-value shift behavior observed by CW EPR and previously the published X-ray structure (PDB ID: 2XC3, (*87*)) showing multiple intervening H_2O molecules in remain during low-spin interactions of this inhibitor with heme iron.

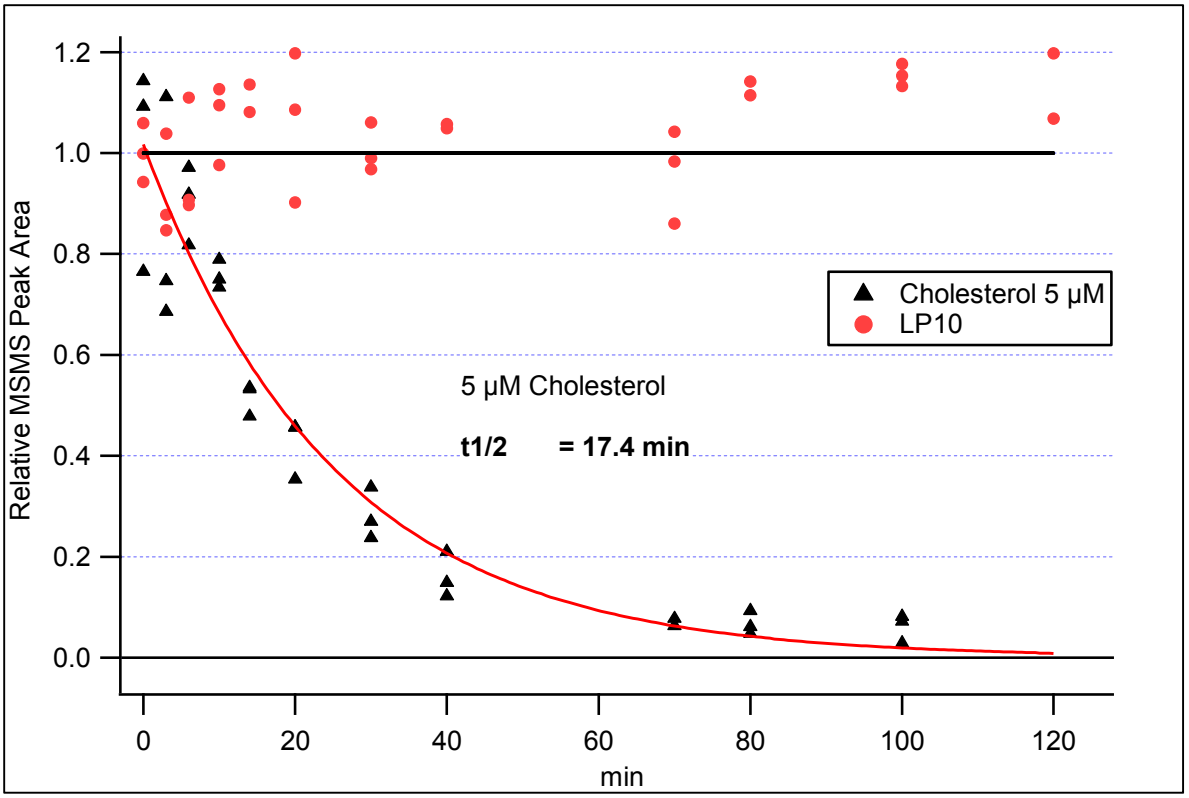

Figure 2.22 Substrate depletion monitored by APCI MSMS for cholesterol (5µM) and LP10 (2 µM) in the presence of 1 µM CYP125A1. Reverse type I inhibitor LP10 is metabolically stable despite an inability to coordinate bond with heme directly. CYP125A1 activity was reconstituted with ferredoxin reductase/ferredoxin (spinach) redox couple in the presence of NADPH regenerating system as described by others (*97*).

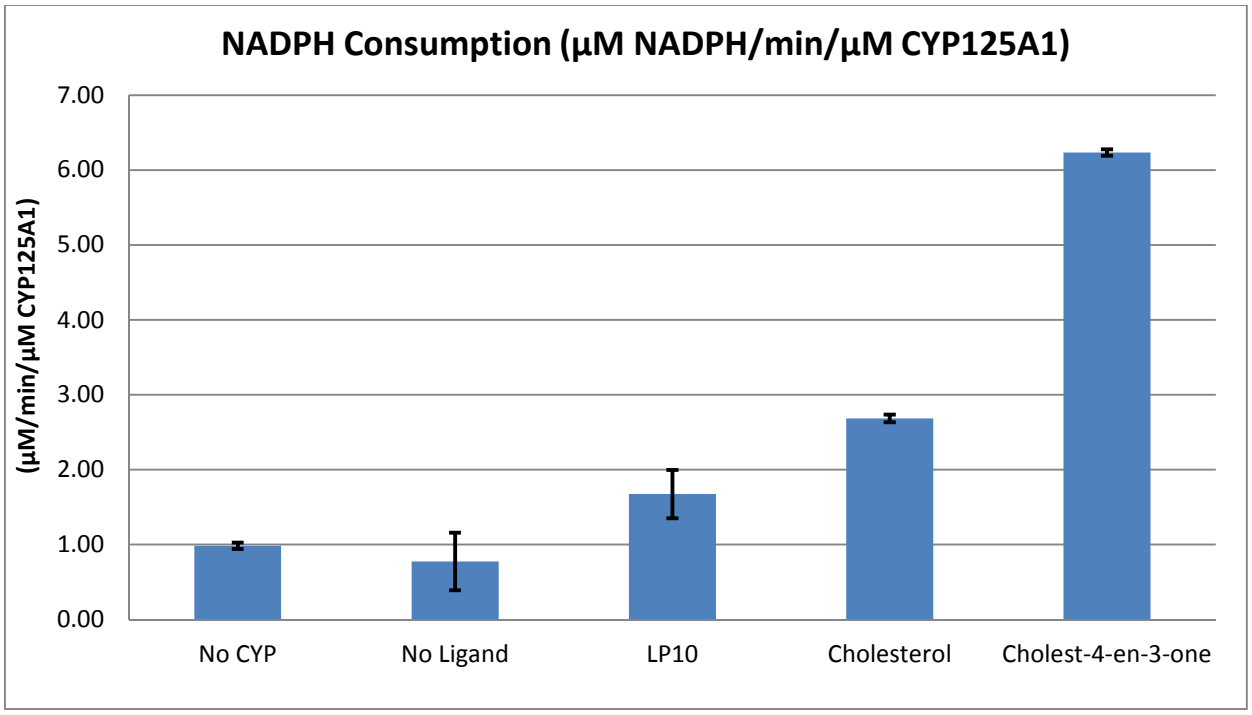

Figure 2.23 NADPH depletion rates (± std. error) for CYP125A1 (*Mtb*) reconstitution assays in the presence of H_2O-bridged inhibitor LP10 and sterol substrates. All rates were corrected for background NADPH depletion (0.48 µM/min) in the absence of protein. The results suggest that the while reverse type I inhibitor LP10 is metabolically stable, it increases catalytic uncoupling inferred on the basis of elevated NADPH consumption. Enzyme activity was reconstituted in the presence of ferrodoxin/ferrodoxin reductase from *Spinacia oleracea* and glucose regenerating system (Chapter 2.2.8).

Table 2.6 Results of NADPH depletion kinetics measurements via reconstitution of enzyme activity in Spinach ferrodoxin/ferrodoxin reductase redox couple. Mean rates are listed ± std. error and were corrected for background NADPH depletion in the absence of protein (0.48 µ/min)

	Fit result (µM/min)	+/-	µM/min/µM CYP	+/-	% change rel to ligand free
No CYP	0.25	0.01	0.98	0.04	
No Ligand	0.19	0.10	0.77	0.38	
LP10	0.42	0.08	1.68	0.32	116
Cholesterol	0.67	0.01	2.68	0.05	247
Cholest-4-en-3-one	1.56	0.01	6.23	0.04	705

Chapter 3:

1,2,3-Triazole-Heme Interactions in Cytochrome P450:Functionally Competent Triazole-Water-Heme Complexes

Note: portions of this chapter have been taken from published manuscript:

Conner, K. P, Vennam P., Woods CM., Krzyaniak MD., Bowman MK., and Atkins WM. 1,2,3-triazole interactions in cytochrome P450: functionally competent water-triazole-heme complexes, (2012) *Biochemistry 51, 6441*.

3.1 Introduction

Cytochrome P450 (CYP)-heme interactions with nitrogenous drugs contribute to the pharmacology of a wide range of therapeutic agents. Collectively, CYPs represent both therapeutic targets and critical determinants of drug metabolism and drug-drug interactions. For example, drugs targeted to aromatase (CYP19) for use in breast cancer (*11*), to lanosterol demethylase (CYP51A1) for antifungal therapy (*12*), or to other CYPs expressed in infectious pathogens (*92*), exploit heme-imidazole or heme-triazole interactions. Similar heme-nitrogen interactions are often considered to be a component of inhibition of the drug-metabolizing CYPs, and such inhibitors can alter the clearance of other drugs (*143*). However, recent studies (*38, 84, 139*) demonstrate that the heme-nitrogen interactions are not exclusively 'inhibitory,' and our fundamental understanding of the interaction between nitrogenous drugs and the heme group of CYPs is incomplete.

Surprisingly, all marketed azole drugs designed to exploit heme-nitrogen interactions with CYPs are either imidazole (IMZ), 1,2,4-triazole (1,2,4-TRZ), or thiazole-based despite the extraordinary synthetic advantages of 1,2,3-triazoles (123-TRZs) (*85, 86*). Although several studies have suggested (*133, 144*) that, despite their lower basicity, the 123-TRZs can ligate to

the heme iron of CYPs, they are conspicuously absent among marketed CYP inhibitors. In the absence of significant confounding problems, 123-TRZs, in principle, could be a powerful element of fragment-based anti-CYP drug discovery. In order to determine whether 123-TRZs have unique properties among isosteric nitrogen heterocycles, we have compared the spectroscopic and thermodynamic behavior of 123-TRZ binding to CYPs with that of IMZ and 1,2,4-TRZ. We also provide a spectral and functional characterization of a well-established CYP3A4 inhibitor after installation of a 123-TRZ on its molecular framework. This chapter expands the scope of the novel low-spin CYP-(123-TRZ) structures identified and characterized in Chapter 2 to include an additional drug-metabolizing isoform, CYP3A4. Additionally, in contrast to the metabolically-stable examples of H_2O-bridged complexes that have already been presented, we demonstrate in this chapter their potential to be both functionally competent and capable of influencing the oxidative regioselectivity. The results indicate that heme interactions with 123-TRZs include unusual structural features that could explain the limitations of this fragment in CYP inhibitor discovery, but which could be exploited to 'steer' regiospecific metabolism of other drugs. They further emphasize that ligands that yield apparent type II optical spectra are not necessarily directly ligated to the heme iron nor are they necessarily inhibitory, as recently revealed by Jones and co-workers (*38, 139*).

3.2 Experimental procedures

3.2.1 Materials

1H-1,2,3-triazole, imidazole, 1H-1,2,4-triazole, and 17α-ethynylestradiol used during binding and turnover analysis were obtained from Sigma Chemical Co. (St. Louis, MO, USA) and used without further purification. All reagents, purification solvents, and chemical precursors

used during synthesis of 17-click and 2-OH/4-OH 17-click were also obtained from Sigma. Deuterated solvents for NMR analysis were purchased from Cambridge Isotopes (Andover, MA, USA). Solvents for LC-MS were of Optima grade from Fisher. Water not employed as LC-MS solvent was of Milli-Q quality from a Barnstead nanopure UV dispenser. Supersomes co-expressing cytochrome *b5* and P450 reductase, were purchased from BD Biosciences (San Jose, CA).

^{1}H NMR. Characterization of synthesized 17-click and 2-OH/4-OH 17-click by NMR was performed on a Varian (Palo Alto, CA) Inova 500 (500 MHz) spectrometer equipped with a 5mm HCN z-axis PFG triple resonance probe.

3.2.2 Protein expression and purification

CYP3A4 was expressed and purified as previously described (*109*). CYP2C9 (hepta mutant) was constructed as previously described (*108*) with the exeption of a hexa His rather than a tetra His C-terminal sequence to facilitate purification. The enzyme was expressed in DL39 *E. coli* and purified as described for CYP3A4.

3.2.3 Organic synthesis

Synthesis of 17α-(2H-2,3,4-triazolyl)-estradiol (17-click)

As described in Chapter 2.2.3

Synthesis of 2-OH and 4-OH 17-click

19-Nor-*17α*-pregna-*1,3*,5(10)-trien-20-yne-2,3,17β-triol (2), and 19-nor-17α-pregna-1,3,5(10)-trien-20-yne-3,4,17β-triol (3), were synthesized using the protocol of Xie et al.(*145*) with minor modifications. Notably, during electrophilic aromatic substitution (formylation

reaction, step 1), the Grignard reagent, EtMgBr, was used as a 1 M solution in THF delivered to the reaction after 1:6 dilution in anhydrous diethylether. For successful acylation reaction, triethylphosphate was used as suggested. It was observed during the Dakin oxidation (step 2), that the molar ratio of NaOH and H_2O_2 is critical to limiting the formation of unwanted byproducts. Therefore, standardized 1M NaOH (0.75 equiv.) and 3% H_2O_2 (1.1 equiv.; ε_{240nm} = 43.6 M^{-1} cm^{-1} (*146*)) solutions were prepared and added to an argon purged THF solution of the 2-formyl and 4-formyl intermediates for a final aqueous concentration of 8.6% v/v. The catechol products were separated on silica gel (0.035-0.07 mm, 6nm pore dia.) with 2% CH_3OH in CH_2Cl_2 mobile phase under isocratic conditions: (2) was isolated in 48% overall yield and (3) isolated in 8% overall yield, both were off-white solids; NMR chemical shifts and MS data for all intermediates conformed to that published previously (*145*). To generate the 2-OH (4) and 4-OH (5) 17-click, click reactions were conducted in microscale using a slightly modified procedure to that used to obtain (1; 17-click): To a small conical pressure vial were added 400 µL DMF:H_2O (4:1) solution containing 11 mg (35 µmol) of intermediate (2) or (3), followed by addition of 7 mg of sodium ascorbate (35 µmol), and 1 mg of $CuSO_4 \cdot 5H_2O$ (4 µmol Cu(II)). The solution was purged with argon while stirring at room temperature before initiation of the reaction with 7.5 µL (57 µmol) of azidotrimethylsilane. The reaction was heated (100°C) overnight with vigorous stirring. The mixture was diluted with water prior to extraction with ethylacetate. The organic layer was washed with several equivalents of water prior to treatment with brine and anhydrous $MgSO_4$. The organic layer was evaporated to dryness and the residue purified over silica gel (70-230 mesh, 100 Å pore) using a 5" disposable glass pipette with 5 - 8 % CH_3OH in CH_2Cl_2 mobile phase. Both (4) and (5) were isolated as slightly yellow solids in ~30% yield. (4): NMR (δ ppm, CD_3OD): 1.05 (3H, s, 18-CH_3), 6.43 (1H, s, 4-H), 6.61 (1H, s, 1-

H), 7.65 (1H, broad s, triazole –CH). MS: [M+H] (theoretical) = 356.197, [M+H] (observed) = 356.196. (5) 6.55 (1H, d, J = 8.8Hz 1-H), 7.64 (1H, broad s, triazole –CH). MS: [M+H] (theoretical) = 356.197, [M+H] (observed) = 356.197.

3.2.4 Kinetic assay

Kinetic parameters k_{cat} and K_M for total 17-click turnover were estimated by LC-MS/MS using the methods of substrate depletion (*147, 148*). Briefly, typical incubation mixtures were prepared by combining 198 pmol of rCYP3A4 in Supersomes co-expressing P450 reductase and *b5* (198 µL; 50 nM working P450 concentration based on 0.5 nmol P450/0.5 mL as determined by the manufacturer), 79.2 µL of appropriate 50X 17-click stock solution (0.005 – 10 mM) in ethanol (2 % v/v final EtOH), and 3286.8 µL KPi (0.1 M, pH =7.4; 6 mM $MgCl_2$) buffer. Triplicate 90 µL aliquots were dispensed in 96 well plate format prior to pre-incubation of the plates at 37 °C for 5 min. Wells representing the t = 0 time point received 10 µL of KPi buffer while the reactions were initiated by addition of 10 µL of 10 mM NADPH solution (1 mM final). Reactions were quenched every 30 seconds up to 3.5 minutes, and then every 1-2 minutes up to 16 min with 150 µL of acetonitrile containing 1 µM carbamazepine (CBZ) as internal standard (IS). The quenched reactions were centrifuged at 3480 x g at 4 °C for 10 min. to remove precipitated protein. LC-MS/MS analysis of the samples was conducted on an API 4000 triple quadrupole mass spectrometer in positive electrospray mode (MDS SCIEX, Concord, ON), coupled to LC-10ADvp pumps and a SCL-10ADvp controller (Shimadzu, Columbia, MD) with a CTC PAL (Leap Technologies, Carrboro, NC) autosampler. For LC, an Aquasil (Thermo Scientific) C18, 30 x 2.1 mm I.D. (3 µm pore size) was used with water (solvent A) and acetonitrile (solvent B) mobile phases containing 0.1 % formic acid. Data acquisition was

conducted in multiple reaction monitoring (MRM) mode monitoring the transitions m/z 340.2/159.1 (Q1/Q3) for the 17-click parent, and m/z 237.2/193.1 (Q1/Q3) for the CBZ internal standard. The desolvation temperature was 650 °C, the spray voltage was 2.5 kV, declustering potential 55 V, a collision energy of 38 V, entrance potential was 10 V, and the exit potential was 13 V. Data analysis was conducted with analyte:IS peak area ratios determined using Analyst software (AB SCIEX, Framingham, MA) as described previously (*147*).

Incubation mixtures for measurement of 17EE depletion were prepared in an identical fashion to that described for 17-click. 17EE reactions were quenched every 30 seconds (up to four minutes) with 200 µL of ethyl acetate containing 0.1 µM β-estradiol IS. The quenched plates were placed in a dry ice/acetone bath to separate the aqueous layer and the organic layer was removed and evaporated to dryness in a new plate under a gentle stream of nitrogen at 45°C. To facilitate detection of 17EE by ESI-MS/MS, the reaction residue was resuspended in 100 µL 50 mM sodium carbonate buffer (pH = 11.0) and 100 µL of 1 mg/mL dansyl chloride in acetone solution. The derivatization reactions were heated (50 °C) for up to 40 minutes. The derivatized reaction mixtures were assayed directly by MRM after automatic tune optimization with infused standards in the positive ion mode: m/z 530.4/171.1 (Q1/Q3) to detect parent 17EE, and m/z 506.4/171.1 (Q1/Q3) for β-estradiol IS.

3.2.5 Measurement of 17-click IC_{50}

Median inhibitory concentration (IC_{50}) values of 17-click were determined against testosterone 6β-hydroxylation by CYP3A4 in Supersomes co-expressing P450 reductase and *b5*. Incubations in 100mM KPi (pH = 7.4) contained varying concentrations of 17-click (0-60 µM), 10 nM enzyme, and 50 µM testosterone, and were preincubated for 5 min. prior to initiation of

the reaction with NADPH (10 mM; 1 mM final). Triplicate reactions were quenched after 20 min using an equal volume (100 µL) of 1 µM tolbutamide (IS) in acetonitrile. Quantitation of percent remaining activity was conducted using the MRM scan mode of a 4000Q-Trap (MDS SCIEX, Concord, ON) connected to a Shimadzu HPLC system. 6β-hydroxy testosterone was monitored using m/z 305.0 and m/z 269.0 (Q1/Q3) with a declustering potential of 55 and collision energy of 25. Tolbutamide was monitored using m/z 271.2 and m/z 91.1 (Q1/Q3), using a declustering potential of 66 and collision energy of 39. The following instrument settings were applied: dwell time, 500 ms; curtain gas, 10; spray voltage, 4.5 kV; source, 400 °C; ion spray gas 1 and 2, 40.

3.2.6 HPLC-qTOF MS analysis of 17-click metabolites

Liquid chromatography was performed using a Waters (Milford, MA) ACQUITY UPLC coupled to a SYNAPT High Resolution Quadrupole TOF mass spectrometer via an ESI interface. Chromatographic separation was achieved on a Hypersil GOLD (ThermoFisher) UPLC column (150 x 2.1 mm, 1.9 µm particle). A gradient program consisting of Solvent A (H_2O containing 0.1% formic acid (v/v) and Solvent B (ACN containing 0.1% (v/v) formic acid) was used. Solvent A was held at 90% for 3 min, followed by a linear gradient to 48% B over 12 min. Solvent B was then increased using a linear gradient to 95% B at 17 min and held for 5 min. Pre-equilibration of the column at 90% A was conducted for 5 min prior to each injection. The parent ions were detected in full scan mode (50-800 m/z) with a cone voltage of 17 eV, a collision energy of 6 eV, and transfer cell energy set 4 eV. For fragmentation analysis, data were acquired in MS expression (MS^E) mode, with the cone voltage set to 17 eV, the collision cell set to 4 eV, and trap cell set to 6 eV. Fragmentation in the MS^E mode was induced using a collision energy ramp of 15-45 eV. In both modes, the capillary voltage was set to 3.5 kV with a source

temperature of 120 °C and desolvation temperature of 350 °C. Calibration of the instrument was performed using sodium formate over a range of 50-800 prior to use. Leucine enkephalin was used as a lockspray reference with a sampling interval of 30 s and scan rate of 1.0 s. Spectra were averaged for the FWHM of the metabolite peaks using Masslynx software and subjected to mass defect filtering with Metabolynx software using a parent mass tolerance of 50 mDa. All elemental compositions were determined using Masslynx. The Masslynx software MassFragment was used to obtain structural proposals for the fragments.

3.2.7 Ion trap LC-MS^n analysis of 17-click metabolites

Further characterization of the primary 17-click metabolite (M4) was conducted using a Finnigan LTQ ion trap instrument (Thermo Electron Corp., San Jose, CA, USA) connected to an Agilent 1100 series HPLC system equipped with autoinjector. Ionization of the metabolites was achieved by ESI in the positive ion mode. The capillary temperature was 300 °C; sheath gas flow, 40; auxiliary gas flow, 10; source voltage, 3 kV. MS^4 was conducted using two distinct normalized collision energy sequences: (1) m/z 356 @ 8 %, m/z 338 @ 15 %, and m/z 213 @ 20 %; (2) m/z 356 @ 8 % , m/z 338 @ 15 %, and m/z 320 @ 20%; activation time of 30 ms was used throughout both sequences. LC conditions were as described above for qTOF analysis.

3.2.8 Computational methods

Density Functional Theory (DFT) calculations were performed on a simplified heme macrocycle consisting of an unsubstituted porphine, ferric iron, thiolate (-SH) proximal ligand complex with a variable neutral sixth distal ligand (e.g. water, IMZ, 123-TRZ, or 1,2,4-TRZ). Structures were initially built in Avagadro. DFT calculations were performed with GAMESS

(version number 1 October, 2010 (R1)). Calculations used unrestricted DFT (M06) methods (*149*). We chose the charge of the molecule to be zero; Fe(III) with balancing negative charges on the macrocycle (-2) and thiolate (-1); and the Fe(III) spin to be S = ½ corresponding to a single unpaired electronic configuration. GAMESS implemented DFT used a Euler-Maclaurin quadrature with 96 radial points, with theta and phi set to 12 and 24 for the number of angle grids in the Gauss-Legendre quadrature. The molecular coordinates used were systematically generated delocalized internal coordinates generated from Cartesian coordinates in the GAMESS input file. Basis sets for geometry optimization and energy calculations were s6-31G(d)(*150*), implemented as spherical harmonics unless indicated otherwise. Convergence criteria were loosened in all heme calculations. All calculation parameters used GAMESS default settings unless otherwise mentioned. GAMESS output was visualized using MacMolPlt (*151*). The relative binding energy of the fragment azoles was evaluated *in silico* by assessing the equilibrium between resting state heme complex (Fe(III)-H_2O) and free azole fragment on the reactant side of the equilibrium and azole bound heme (Fe(III)-azole) and free H_2O on the product side of the equilibrium. The differences in the sum of energies on the product and reactant side were used to calculate $\Delta E_{binding}$ for each azole fragment, which corresponds to the difference in energy between the water-ligated and azole-ligated model heme. Bond orders were calculated using Mullikan population analysis of the canonical Kohn-Sham orbitals.

3.2.9 UV/vis absorbance analysis of ligand binding

Absorbance measurements were conducted on an Olis Modernized Aminco DW-2 (Olis,Inc., Bogart, GA) dual beam spectrophotometer equipped with a Julabo F30-C compact refrigerated circulator (Julabo USA, inc., Allentown, PA). Each binding experiment required 500

μL initial sample volume using a 0.1 x 1 cm path length quartz cuvette, and the typical sample consisted of 1-2 μM purified CYP in 100 mM KPi buffer + 20% glycerol. Spectra were recorded in the absolute mode (270 – 650 nm) in between 1 μL aliquots of the appropriate ligand stock solution added to the sample cuvette. For titrations of lipophilic species 17EE and 17-click, ethanol stock solutions were used with a final concentration of organic kept below 2%/vol. During temperature dependent measurements (van 't Hoff analysis), the protein samples were allowed to equilibrate at the desired temperature for a minimum of ten minutes prior to initiation of the experiment, and the sample was allowed to equilibrate for 5 minutes between ligand aliquots prior to data acquisition. The temperature was precisely monitored inside the cuvette by thermocouple and fluctuations larger than ± 0.4 °C during the course of the experiment resulted in a discarding of the data. Corrections were applied to the data to account for baseline drift and sample dilution over the course of the binding experiments. Difference spectra were generated by subtracting the ligand-free spectrum from all ligand-containing spectra containing, and binding isotherms were constructed using the spectral peak minus spectral trough intensity values plotted as a function of ligand concentration. Affinity, K_D, and Bmax parameters were estimated from non-linear regression analysis in IGOR pro 6.1 (Wavemetrics, Lake Oswego, OR, USA) using equation (1). Equations (2), (3), and (4) were used when curvature was observed in the Eadie-Hofstee transform of the data.

(1) $\Delta Abs. = [E \cdot L] = B_{max} \cdot [L]/(K_D + [L])$

(2) $\Delta Abs. = [E \cdot L] = B_{max} \cdot [L]^n/(K_s^n + [L]^n)$

(3) $\Delta Abs. = [E \cdot L] = B_{max1} \cdot [L]/(K_{D1} + [L]) + B_{max2} \cdot [L]/(K_{D2} + [L])$

(4) $\Delta Abs. = [E \cdot L] = [B_{max1} \cdot [L]/K_{D1} + B_{max2} \cdot [L]^2/K_{D1} \cdot K_{D2}]/[1 + [L]/K_{D1} + \cdot [L]^2/K_{D1} \cdot K_{D2}]$

To accurately compare UV/vis binding spectral characteristics for azole fragments and for 17-click, the spectra for a given titration were normalized to 1 μM CYP concentration using the Soret band absorbance measured in the absence of ligand (CYP3A4 ε_{417nm} = 115 $mM^{-1} \cdot cm^{-1}$(*152*); and estimated for CYP2C9 ε_{417nm} ~ 133 $mM^{-1} \cdot cm^{-1}$). For CYP3A4 binding spectra, comparison of trough intensity at 390 nm in calculated difference spectra was used as an estimate of type IIa character (*17, 40*). In cases where complete saturation had not been achieved at the highest experimental ligand concentration, principal component analysis (PCA) was conducted as described previously (*153-155*) using software written in the Python programming language (version 2.6) and adapted to IGOR Pro 6.1 (Wavemetrics, Lake Oswego, OR, USA) to obtain the 'saturated' type II binding spectrum and facilitate more accurate spectral comparisons.

3.2.10 van 't Hoff data analysis

The natural logarithm of the equilibrium association constant ($\ln K_a = \ln K_D^{-1}$) obtained by non-linear regression analysis of the UV/vis generated binding isotherms, was plotted as a function of inverse experimental temperature (Kelvin). At each temperature K_a was measured in duplicate and the associated standard error from the fit was assigned to each point in the van 't Hoff plot to be weighted during regression analysis using the linear form of the van 't Hoff equation: $\ln K_a = - \Delta H°/R(1/T) + \Delta S°/R$. $\Delta H°$ and $\Delta S°$ were calculated from the best fit slope and intercept, respectively, using a value R = 1.9859 cal/mol/K.

3.2.11 Corrections to [IMZ] during van 't Hoff analysis.

Due to the mixture of charge states anticipated at pH = 7.4 for basic IMZ, a correction procedure was applied to the absolute IMZ concentration when determining K_a and is based on

several assumptions: 1) Only the neutral fraction of IMZ fragment is involved in CYP binding; 2) The temperature dependence of pK_a for the IMZ ionization reaction is accurately described by published values for the thermodynamic parameters ΔH° and ΔC°p measured under dilute aqueous conditions (*156*); and 3) The $IMZ{\cdot}H^+$ activity coefficient ($\gamma_{IMZ{\cdot}H^+}$) can be calculated at constant ionic strength determined by the buffer (I ≈ 240 mM [KPi]) without accounting for short-range non-electrostatic interactions using the extended Debye-Hückel expression, equation (5): $\ln\gamma i = -A_m z_i^2 I^{1/2}/(1 + BI^{1/2})$. Here, A_m represents the Debye-Hückel constant (temperature dependent values between 0.494 – 0.513 $(kg{\cdot}mol^{-1})^{1/2}$ taken from (*157*)), z_i, the charge of the ith ion, I, the ionic strength of the solution, and B, the so-called 'ion size' parameter (set equal to 1.6 $kg^{1/2}mol^{-1/2}$ as described in ref. (*158*)). First, published values for pKa_{298K} = 7.09 ± 0.1, ΔH° = 36.59 ± 0.06 kJ/mol, and $\Delta C°_p$ = -16 ± 5 J/mol/K, reported in the study by Fukawa and Takahashi (*156*) for the IMZ proton dissociation reaction (K_a) occurring in the presence of 100 mM potassium chloride, were used to calculate pKa within the range of experimental temperatures used in this study via the methods of Clarke and Glew (equation 6) (*159*).

(6) $\log K\,(T) = \log K°_{298} + \Delta H°_{298}/R{\cdot}\ln 10(1/298 - 1/T) + \Delta C_P°_{298}/R{\cdot}\ln 10(298/T + \ln(T/298) - 1)$

From the expression: $(10^{pH - pKa} \cdot \gamma_{IMZ{\bullet}H^+}) = [IMZ]/[IMZ{\cdot}H+]$, the molar [IMZ] fraction was obtained using calculated values for pKa and $\gamma_{IMZ{\cdot}H^+}$, along with the initial measured buffer pH. The [IMZ] concentrations were then corrected accordingly prior to non-linear regression analysis of the binding isotherms to estimate IMZ affinity (K_D). It was observed that addition of up to 6 mM IMZ to the buffered solutions only minimally effected the final solution pH (+ 0.03 units). It is noted that ionic strength corrections to ΔH°, and $\Delta C°_p$ parameters describing deprotonation

reactions for charge symmetric systems, such as the case of the deprotonation of amines, are zero at this level of theory (*158*).

3.2.12 Pulsed/CW EPR

As described in Chapter 2.2.4

3.3 Results

3.3.1 Models for type II CYP binding: 123-TRZ-heme energetics calculated by DFT

Gas phase DFT calculations (s6-31G(d) basis set; U-M06 functional (*149, 150, 160*)) were conducted to examine the binding of a model Fe(III) heme with 123-TRZ, 1,2,4-TRZ, and IMZ fragments to assess the potential for 123-TRZ-based ligands to form type II complexes with CYPs (Table 3.1). The M06 functional was chosen, in part, because it has been parameterized using transition metals in the training set and correctly predicts the Fe-azole vs. Fe-H_2O bond energies whereas the popular B3LYP hybrid functional fails (data not shown) (*149*). This non-isodesmic comparison is necessary because the resting state of the enzyme is six-coordinate with water as the distal axial ligand, although the isodesmic comparisons within the different N-Fe cases should show better correlation with experiment. All computational comparisons are isogyric as the water-ligated and azole-ligated heme structures are both low-spin with S = 1/2. The energies for the gas phase reaction between H_2O-ligated low-spin model heme-thiolate and the free azole fragments (see Chapter 3.2.8) are presented in Table 3.1 with IMZ (-5.3 kcal/mol) > 1,2,4-TRZ (-3.2 kcal/mol) > 123-TRZ (-1.7 kcal/mol). This result suggests that 123-TRZ-heme interactions are slightly weaker energetically than the other azole complexes but still favorable

relative to the H_2O-ligated state. Our results correlate with the solution pKa of the fragments: 6.99 (IMZ) > 2.45 (1,2,4-TRZ) > 1.15 (123-TRZ)(*161*), suggesting basicity is a major determinant for heme coordination. Thus, 123-TRZ was anticipated to induce similar type II optical signatures in CYP, albeit with lower affinity (K_D) relative to IMZ and 1,2,4-TRZ. Interestingly, interactions with the heme of both N1 and N2 of 123-TRZ are comparable.

3.3.2 Apparent type II binding of 123-TRZ fragment to multiple CYPs

Despite the DFT results, which indicate that 123-TRZs could interact with heme, an extensive analysis of the literature revealed no CYP-targeted azole drugs that possess the fragment. Therefore we explored experimentally the possibility that 123-TRZ can form type II complexes, and how these complexes compare spectrally with established drug-like azole fragments, 1,2,4-TRZ, and IMZ. Two mammalian CYP isoforms, CYP3A4 and a CYP2C9 variant (N-terminal truncation and hepta mutant (*108*), CYP2C9dh; hereafter referred to as CYP2C9), were expressed and purified (*108, 142*). Figures 3.1 & 3.2 display the calculated difference spectra and resultant binding isotherms obtained from UV/vis absorbance titration of CYP3A4 and CYP2C9, respectively, with 123-TRZ, 1,2,4-TRZ, and IMZ at 20°C in 100 mM KPi (pH = 7.4, + 20% glycerol). The pertinent spectral features of each titration are summarized in Table 3.2. All three fragments yield type II spectral complexes, which suggest that they displace the axial-H_2O molecule from resting state heme and coordinate to ferric iron (*44*). The magnitude of the Soret band redshift varies in CYP3A4: IMZ (8 nm) > 1,2,4-TRZ (6 nm) = 123-TRZ (6 nm), with similar shifts observed in the alpha/beta region. In CYP2C9 the Soret shifts vary: IMZ (9 nm) > 1,2,4-TRZ (5 nm) > 123-TRZ (2 nm), also with similar shifts in the alpha/beta spectral region. The affinity was markedly lower for 123-TRZ fragment binding both CYP3A4 (K_D = 14.3 ± 0.5 mM; ~38 fold lower vs. IMZ and up to ~367 fold lower vs. 1,2,4-

TRZ; Table 3.2) and CYP2C9 (K_D = 10.0 ± 0.4 mM; ~up to 50 fold lower vs. 1,2,4-TRZ, and ~101 fold lower vs. IMZ; Table 3.2). Curiously, these results corroborate a previous report (*40*) of complexity inherent in the binding of 1,2,4-TRZ to CYP3A4 and CYP2C9, which manifests as pronounced curvature in Eadie-Hofstee plots (Figures 3.1 & 3.2, inset). In both cases, the data fit best to a two site binding model (see Chapter 3.2.9, equation 4): the first molecule of 1,2,4-TRZ binds CYP3A4 with K_{D1} = 0.039 ± 0.007 mM and is responsible for 13% of the total absorbance change observed at saturation, followed by binding of a second low affinity equivalent with K_{D2} = 4.80 ± 0.21 mM; in CYP2C9, both 1,2,4-TRZ binding sites are responsible for nearly equal shift toward the low-spin azole-ligated spectrum (51% vs. 49% total spectral shift at saturation for high affinity and low affinity site, respectively), and the first molecule of 1,2,4-TRZ binds with K_{D1} = 0.198 ± 0.040 mM followed by a second low affinity equivalent with K_{D2} = 2.85 ± 0.82 mM. In contrast to a previous report (*40*), multiple binding of IMZ was not observed in our titrations with CYP2C9. Possibly, the difference lies in the use of the wild type enzyme vs. the variant used in our studies.

Regardless of these system-dependent differences, the binding studies and DFT calculations demonstrate that type II binding is favorable in the case of 123-TRZ. The DFT calculations correctly predict the rank order affinity of the three ligands for CYP2C9, but they fail to correctly predict the rank order affinity for CYP3A4 binding (1,2,4-TRZ > IMZ > 123-TRZ). This is not an altogether surprising result, as the DFT calculations do not include zero point energy, solvent interactions, and possible contribution of the protein itself to binding free energies.

3.3.3 Comparative van ’t Hoff analysis of 123-TRZ and IMZ binding CYP3A4

The thermodynamic basis for the inferior CYP3A4 binding energetics of 123-TRZ relative to IMZ was investigated by van 't Hoff analysis to estimate $\Delta H°_{binding}$ and $\Delta S°_{binding}$. 1,2,4-TRZ was excluded from the analysis due to the additional binding complexity observed during the initial binding screen. The temperature dependence of the equilibrium association constant (K_a) for azole binding to CYP3A4 was measured via UV/vis absorbance titration within a temperature range of 5-30 °C in 100 mM KPi (pH = 7.4, +20% glycerol) and the results are shown in Figure 3.3. In order to account for the relatively high basicity of IMZ and accurately define its thermodynamic quantities for CYP binding, an additional correction procedure (see Chapter 3.2.10) was used to calculate the effective IMZ concentration present during binding analysis, with the assumption that only neutral IMZ species binds CYP. Similar corrections were unnecessary for 123-TRZ due to the fact that it is expected to exist in essentially 100% neutral form at pH = 7.4 (pKa = 1.15(*161*)). From the fits to the linear form of the van 't Hoff equation (See Chapter 3.2.10) estimates of $\Delta H°_{binding}$ and $\Delta S°_{binding}$ for both species were calculated from the slope and y-intercept, respectively. In 100 mM KPi, binding of both fragments is enthalpically favorable, as would be expected for azole fragments that directly coordinate heme iron and presumably make little or no contact with active site residues. Values of $\Delta H°_{binding}$ were similar for IMZ (-8.1 ± 0.3 kcal/mol) and 123-TRZ (-8.8 ± 0.1 kcal/mol), clearly demonstrating that the main determinant for the low $\Delta G°_{binding}$ for 123-TRZ relative to IMZ is entropy, which is much more unfavorable for 123-TRZ (123-TRZ : $\Delta S°_{binding}$ = -22 ± 0.4 cal/mol/K; IMZ: $\Delta S°_{binding}$ = -10 ± 1 cal/mol/K). It is speculated here that this discrepancy for $\Delta S°_{binding}$ between IMZ and 123-TRZ may be due, in part, to the unusual nature of 123-TRZ tautomeric equilibria. Specifically, the well-documented dependencies of these equilibria on solvent polarity, solute concentration, and temperature (*132*) (see Discussion) suggest that protein binding and heme

ligation may further influence the distribution of 123-TRZ tautomers, which have unique electronic properties such as differing dipole moments (*128*) and NMR chemical shifts (*132*).

3.3.4 Influence of 1H-1,2,3-triazole fragment on CYP-inhibitor/substrate interactions: the case of 17α-ethynylestradiol.

Equilibrium Binding. The results above demonstrate the potential for the isolated 123-TRZ fragment to form a type II complex with multiple CYPs, albeit with lower affinity than other nitrogenous isosteres. Thus, it remains unclear whether the interactions between this fragment and the heme could be strong enough to influence binding of a well-characterized CYP3A4 substrate. To investigate this possibility, 17α-ethynylestradiol (17EE), a type I substrate/mechanism based inhibitor was chosen for derivatization due to its well-characterized metabolic profile, which suggests the molecule prefers to dock with its steroid A-ring nearest heme (see Discussion), and thus provides an opportunity to test the energetics of 123-TRZ-heme interactions by installing the fragment on the opposing end (D-ring) of the core steroid structure. 17EE was successfully derivatized to 17α-(2H-2,3,4-triazolyl)-estradiol (17-click) and isolated in 60% yield using a one step click reaction (see Chapter 2.2.3). Equilibrium binding of 17EE and 17-click to purified CYP3A4 in 100 mM KPi (pH = 7.4, + 20% glycerol) were measured by UV/vis absorbance at 25°C (Figure 3.4). 17EE binding induced a type I spectrum, typical of efficiently oxidized CYP substrates that are thought to displace the water molecule at the 6th axial position and favor the high-spin enzyme species (*44*). The calculated 17EE binding isotherm displayed obvious sigmoidal behavior that is corroborated by pronounced curvature observed in an Eadie-Hofstee transformation of the data (not shown), suggesting the stoichiometry of binding is greater than unity (Figure 3.4). A simple Hill plot (not shown) was used for non-linear regression analysis and exhibited a Ks = 37.7 ± 1.7 μM and Hill coefficient

of 1.75. The 17EE binding data were also fit to a two site sequential binding model (Figure 3.4) (Materials an Methods, equation 4) and the best fit yielded K_{D1} = 50 ± 25 μM for the first 17EE equivalent, which did not induce a significant heme spin state change, followed by binding of a second equivalent that perturbs the spin state with K_{D2} = 19 ± 8 μM. This was not entirely unexpected, as similar CYP3A4-steroid spin-silent binding interactions have already been documented in our lab for testosterone (*28*), and are suggested by crystallographic results with progesterone bound to CYP3A4 at a peripheral site (*29*).

In contrast, 17-click binding to CYP3A4 displays a dramatic reversal of the spin state towards low-spin heme, as evidenced by the type II difference spectrum shown in Figure 3.4. This result suggests that despite the inferior azole-heme binding energetics of 123-TRZ compared with similar azole heterocycles IMZ and 1,2,4-TRZ, the 123-TRZ fragment is still capable of weighting the preferred 17EE binding poses to accommodate an additional type II binding interaction with heme iron. 17-click binding was best described using a hyperbolic binding model with K_D = 45.8 ± 3.1 μM. Interestingly, further inspection of the type II optical signature at near protein saturation reveals that the interaction may be ‘strained’ or ‘incomplete’ (Table 3.3). This assessment is based on the sub-maximal Soret redshift (2 nm) and decrease in CYP3A4 high-spin fraction (ΔAbs_{390nm}) observed in the absolute absorbance spectrum, and most evident by the diminished peak to trough intensity difference observed in the calculated difference spectrum relative to what is observed for the 123-TRZ heme complex. Others have suggested that UV/vis absorbance spectra for azole fragment-CYP complexes can be useful references for detecting sub-optimal heme ligation for type II species bearing similar fragments (*40*).

3.3.5 Structural analysis of CYP3A4·17-click low-spin complex by CW-EPR and HYSCORE spectroscopy

On the basis of DFT calculations and equilibrium binding studies conducted here, 123-TRZ fragment-heme interactions are anticipated to be weaker than imidazole-heme and 1,2,4-TRZ-heme interactions, but sufficient to modulate substrate orientation, at least in the case of 17-click. However, the incomplete spectral conversion with 17-click, compared to the larger spin state conversion with the fragment 123-TRZ, suggested the possibility that the heme ligation is not complete in the former case. Speculatively, the incomplete difference spectrum described above for 17-click could be due to conformational heterogeneity or axial ligand heterogeneity on the heme.

Therefore, to test this hypothesis, CW and pulsed EPR techniques were used to examine the type II CYP3A4 complexes of 123-TRZ and 17-click. For these experiments, the concentration of KPi was increased to 200 mM to achieve the high CYP3A4 concentration necessary for detectable EPR signals. Binding affinity of 17-click was demonstrated to be minimally affected by this change in ionic strength (K_{D100mM} = 46 μM, vs. K_{D200mM} = 78 μM) and the UV/vis absorbance spectra at saturation were identical to that observed previously (Data not shown). Figure 3.5 shows the CW EPR spectra for ligand-free CYP3A4, and CYP3A4 with 123-TRZ and 17-click. The EPR spectra for ligand-free CYP3A4 have g-values 2.421 (g_z), 2.249 (g_y) and 1.921 (g_x). 123-TRZ shifted the EPR g-values of this complex, with two unique sets identified by fitting the CW-EPR spectrum (see Chapter 2.2.4): 2.505 (g_z), 2.259 (g_y) and 1.874 (g_x); and 2.459 (g_z), 2.261 (g_y), and 1.890 (g_x). Both species of 123-TRZ-bound CYP3A4 detected from the fit of the data have larger g_z values than ligand-free enzyme. It is speculated here that two unique sets of g-values for the [123-TRZ • CYP3A4] complex might correspond to two possible heme-ligation states of 123-TRZ involving either N1(3) or N2, each producing distinct EPR spectra. Interestingly, 17-click produced rather small shifts in EPR g-values from

those of the ligand-free protein: 2.415 (g_z), 2.249(g_y) and 1.922(g_x), with g_z being shifted to a smaller value than the ligand-free enzyme. The results suggest that 123-TRZ and 17-click, both of which form low-spin CYP3A4 complexes based on optical spectra, do so with distinctly different interactions with the heme-iron.

Hyperfine sublevel correlation spectroscopy (HYSCORE) was used to probe further the environment of heme-Fe(III) with different ligands using the hyperfine interaction between the unpaired spin on heme iron and nearby nuclei. HYSCORE is a two-dimensional EPR method that allows for detection of the effects of neighboring nuclei on EPR electronic transitions. Specifically, we investigated the protons of the axial H_2O coordinated to the heme that were assigned in previous studies of ligand-free CYP2C9 and CYP101A1 (P450cam) (*114, 162*). Figure 3.6 shows the HYSCORE spectra of CYP3A4 with no ligand at the magnetic field corresponding to g_z for 17-click complex. The peaks/arcs extending between frequencies [(9.3, 16.0) and (10.7, 14.5)], and [(16.0, 9.5) and (14.5, 10.9)] MHz indicated by arrows have isotropic hyperfine splitting values of 4.31 MHz, estimated from the spectral simulation, that are similar to values reported for protons of the axial-H_2O in Fe(III) CYP2C9 and CYP101 (*114, 162*). Detailed analysis of the spectral line shapes (*112, 113*) show that these signals arise from protons at a distance of 2.65 Å from the heme Fe(III). The remaining signals arise from other protons near the heme. A second set of peaks/arcs extending between frequencies [(10.5, 14.0) and (12.2, 12.5)] and [(12.8, 11.8) and (14.0, 10.8)] MHz has isotropic hyperfine splitting value of -3.82 MHz, and lies at a distance of 3.05 Å from the heme Fe(III). These signals are tentatively assigned to the thiolate β-protons (Fe(III)-S-CH_2-R) of the cysteine residue axially bound to the heme Fe(III). As a positive type II binding control, the HYSCORE spectrum for CYP3A4·123-TRZ complex was obtained, and the proton frequency region of the HYSCORE spectrum at

magnetic field strength corresponding to g_z for this complex is also depicted in Figure 3.6. The HYSCORE spectrum clearly demonstrates displacement of the axial 6th water molecule by 123-TRZ fragment by the disappearance of the previously characterized proton peaks/arcs. Unexpectedly, the HYSCORE spectra of CYP3A4 with saturating concentration of 17-click retain the axial-H_2O proton peaks/arcs, with only slight frequency shifts [(9.3, 16.0) and (10.5, 15.0)] and [(15.0, 10.3) and (16.0, 9.5)]. In addition, no new nitrogen interactions were detected by comparison with the ligand-free control spectra. The isotropic hyperfine coupling value obtained from spectral simulation of the shifted proton arcs is -4.02 MHz, which correspond to axially bound water protons at a distance of 2.75 Å from heme Fe(III), a slight increase from the ligand-free state.

These experimental results present a paradox. On one hand, 17-click induces a type II optical spectrum suggestive of direct interaction with the heme iron and displacement of the axial water. Yet, HYSCORE shows that the protons of the axial water (and the cysteine) are retained when 17-click binds, with small but readily detectable perturbation of both the protons and the EPR g-values. 17-click causes changes in electronic interactions of the heme while the axial water and cysteine remain. It is likely that the field strength of the axial water ligand is altered by hydrogen bonding interactions with the 123-TRZ moiety of 17-click, which is supported by the lengthening of the $OH_2\cdots$Fe(III) distance in the 17-click-bound HYSCORE spectra. Possible structural interpretations of this are suggested in the Discussion.

3.3.6 17-click functional inhibition of CYP3A4 and metabolic stability

17-click inhibited CYP3A4-mediated 6β-hydroxylation of testosterone in Supersomes with an $IC_{50} = 17 \pm 6$ μM as determined by LC-MS/MS assay (Figure 3.10). To assess metabolic

stability, substrate depletion of 2.5 μM 17-click was also monitored, and demonstrated facile turnover of the type II ligand with only ~50% of the compound remaining after 25 min incubation in the presence of 100 nM CYP3A4 in Supersomes (Data not shown). A representative ion current chromatogram for m/z = 340 + 16 (O) = 356 from LC-MS/MS analysis of a larger scale incubation is shown in Figure 7 and clearly shows formation of at least four NADPH-dependent metabolites.

To assess the rate of CYP3A4-mediated 17-click turnover, K_M and k_{cat} for *total* 17-click metabolism were measured by LC-MS/MS using the methods of substrate depletion (*148*) and found to be 2.5 ± 0.4 μM, and 2.1 ± 0.3 min^{-1}, respectively (Figure 3.11). Our attempts to quantify kinetic parameters for 17EE using the substrate depletion approach were unsuccessful; however, it was observed that depletion rates were between 3-10 fold faster for 17EE relative to 17-click at low substrate concentrations, and that significant depletion was still evident for 17EE at high concentrations that render depletion of 17-click negligible (Figure 3.12). Wang et al. have reported a K_M = 2.5 ± 1.1 μM and k_{cat} = 0.052 ± 0.007 min^{-1} for CYP3A4-mediated formation of 2-OH 17EE in Supersomes under conditions determined to be linear with respect to both assay time and enzyme concentration (*163*). In that study it was stated that 2-OH 17EE represents greater than 90% of total metabolism under the conditions employed. Our results suggest that induction of type II binding by the addition of a 123-TRZ fragment to 17EE has most likely slowed metabolism relative to the parent molecule by 3 – 10 fold, but that 17-click remains highly susceptible to oxidative turnover by CYP3A4.

3.3.7 Metabolic tailoring: 123-TRZ influence on oxidative regioselectivity in CYP3A4

Qualitatively, the number and relative abundance of CYP3A4-mediated 17-click metabolites are similar to that reported by both Lin et al. (*164*) and Geungerich (*165*) for 17EE. In order to compare the regioselectivity of 17EE oxidation with 17-click oxidation, authentic 2-OH and 4-OH 17-click metabolite standards (primary oxidation products for CYP3A4-mediated 17EE turnover(*163, 164, 166*)) were synthesized and isolated in 15% (2-OH) and 3% (4-OH) overall yield using procedures adapted from the literature (See Chapter 3.2.3) (*110, 145*). The retention times for the 2-OH and 4-OH 17-click standards did not match that for any of the metabolites during LC-qTOF MS anlaysis (Data not shown). Thus, metabolism at the preferred 2 and 4 positions of the 17EE steroid A-ring (Figure 3.8) is abolished by addition of 123-TRZ to the drug's scaffold. Representative mass spectra obtained from MS^E analysis (see Chapter 3.2.6) of m/z = 356.1974 for the 2-OH standard (similar to 4-OH 17-click spectrum, data not shown), and predominant oxidized metabolite, M4, observed in the Supersome incubation extract are shown in figure 9. Also shown for comparison in figure 3.9 is the MS^E spectrum for the remaining 17-click parent from the incubation, corresponding to m/z = 340.2025. Table 3.4 lists the elemental composition determined from the observed mass of important fragments from each spectrum (vide infra). The spectra for M1, M2 and M3 were similar (Figure 3.13) to that shown for the most abundant metabolite, M4, with the exception of a prominent fragment ion unique to M4 at m/z = 213.1277, consistent with the molecular formula $C_{15}H_{17}O$ (calculated m/z = 213.1279, -0.94 ppm).

The MS fragment data allow for some additional conclusions to be drawn regarding the structure of the 17-click metabolites. First, while all species investigated (including 17-click) were observed to dehydrate readily (ion at m/z = 356 (340) – 18 = 338 (322)), a second facile dehydration step was observed only for the metabolites (Figure S4) for M1, M2, and M3

spectra), and indicated by a prominent ion at m/z = 320 (20-100 rel. abundance), which is completely absent from the MS^E spectrum of both 2-OH (Figure 3.9) and 4-OH (Data not shown) 17-click. Fragmentation of the metabolites favors two facile water losses and loss of N_2 (m/z = 292), in stark contrast to fragmentation of the 2-OH/4-OH 17-click (and 17-click) that undergo a single dehydration and loss of N_2 (m/z = 310 (M1-M4), m/z = 294 (17-click)), a species nearly absent from all metabolite fragment ion spectra. In addition, there are spectral shifts from m/z = 157.0657 ($C_{11}H_9O$, +2.5 ppm) and m/z = 159.0809 ($C_{11}H_{11}O$, -0.6 ppm) present in spectra of 17-click, to m/z = 173.0602 ($C_{11}H_9O_2$, -0.6 ppm) and 175.0759 ($C_{11}H_{11}O_2$, 0 ppm) observed in spectrum of the 2-OH (and 4-OH) 17-click. These observations suggest that hydroxyl groups are retained at estrogen A-ring positions during fragmentation under the experimental conditions used here. Thus, we conclude that CYP3A4-mediated oxidation of 17-click does not occur at the remaining A-ring position to form 1-OH 17-click, a species of which we had no standard for comparison. In further support of this conclusion is the fact that the spectra for the metabolites are very similar (excepting m/z = 213 in M4 spectra, vide infra) and if the 1-OH 17-click species were for some reason susceptible to facile A-ring dehydration during fragmentation (mass spectrum lacking prominent ions at m/z = 173,175, and 310) it would be anticipated to display a distinct fragment ion spectrum due to disruption of aromaticity. Plausible structures determined with MassFragment software (see Chapter 3.2.6) for signature fragments that contain the steroid A-ring are shown in the spectra of Figure 3.9.

Additional structural insight into the identity of the primary metabolite, M4, was made possible via MS^n analysis using an LTQ ion trap instrument. Based on two unique ion trapping sequences: m/z = 356→338→320→fragments, and m/z = 356→338→213→fragments, it is concluded that m/z = 213 is a kinetic product formed during fragmentation of m/z = 338, the

formation of this species being entirely dependent on the loss of a second equivalent of water from M4 (Scheme 3.1). The overwhelming relative abundance of m/z = 213 in the fragment ion spectrum of M4, coupled with the complete absence of this (or equivalent) species in fragment spectra of 17-click, suggests that the required dehydration step to form m/z = 213 involves the oxygen incorporated into the molecule during CYP3A4-mediated turnover. Thus, the structural identity of this fragment should offer insight as to the location of oxidative turnover of 17-click. To this end, MassFragment software was used to generate a structural proposal (Figure 3.9) for fragment ion $C_{15}H_{17}O$ (calculated m/z = 213.1279, -0.94 ppm), and a structure characterized by fragmentation of the estrogen D-ring of 17-click was determined to be the only plausible solution given the elemental composition of this fragment (see Discussion). In conclusion, addition of a 123-TRZ-heme interaction in the CYP3A4·17EE complex has eliminated the preferred sites of estrogen metabolism entirely (A-ring), and steered the metabolism predominantly towards the D-ring bearing the triazole moiety.

3.4 Discussion

123-TRZ has received great attention in the drug-design arena (*85, 86*) since the discovery in 2001 of novel catalysts for the well-known 1,3-dipolar cyclo-addition reaction between organic azides and alkynes, or the ‘Click’ reaction. The synthetic advantages to the medicinal chemist, via the methods of click chemistry, have prompted widespread use of 123-TRZ as a central scaffold moiety in fragment-based drug design for a wide range of targets (*85, 167*) . Interestingly, despite the prevalence in CYP-targeted drugs of the closely related azole congeners IMZ and 1,2,4-TRZ, the efficacy of 123-TRZ as a CYP pharmacophore has not been established. However, high-affinity interactions of 123-TRZ with transition metals are known; in

fact, 123-TRZ forms complexes with a variety of transition metals including both ferrous and ferric iron species (*133*). Thus, the first goal of the present study was to employ a fragment-based systematic investigation of the relative heme-binding affinity, CYP-binding thermodynamics, and spectral behavior of 123-TRZ in comparison to established azole CYP-pharmacophores IMZ and 1,2,4-TRZ.

Our DFT results suggest that 123-TRZ interacts less favorably than the other azoles but it is competent for type II binding in as much as it can be a stronger ligand than water. The *in silico* energies for the complexes trend with aqueous basicity of the fragments (IMZ (pKa = 6.99) > 1,2,4-TRZ (pKa = 2.45) > 123-TRZ (pKa = 1.15) (*161*)); it was not entirely obvious that this trend should exist because very high basicity (nucleophilicy) for a distal heme ligand might disfavor heme coordination due to charge donation from the proximal thiolate (*168*). 123-TRZ-heme complexes were also calculated to have the longest bond length, as well as lowest bond order compared with the other fragments (IMZ and 1,2,4-TRZ). One interesting conclusion from the computational studies is that 123-TRZ is predicted to ligate heme-iron at both N1and N2, suggesting the possibility that two different routes for heme coordination could be active when binding CYP. Recently, an usually high affinity (0.018 μM, ligand efficiency = 0.88) 123-TRZ fragment species, 4-(3-methylphenyl)-1H-1,2,3-triazole, was discovered to coordinate two Co^{+2} ions simultaneously in human Methionine Amino Peptidase 2 via N1 and N2 during a fragment-based drug screen (*144*). Thus, our DFT results and published work suggest that 123-TRZ could ligate the heme iron of CYPs in two different modes, with the possibility of substituent effects 'steering' ligation to either N1 or N2.

Experimental measures of CYP binding affinity and UV/vis absorbance spectral behavior for 123-TRZ provided further insight for this azole fragment. In buffered aqueous solution, 123-

TRZ bound with modest affinity (up to 367-fold lower compared with 1,2,4-TRZ binding CYP3A4) relative to the other azoles when screened against CYP3A4 and CYP2C9. Spectrally, 123-TRZ displayed smaller redshifts in both the Soret and alpha/beta band regions, as well as decreased effects on the alpha:beta ratio. The relative spectral behavior of 123-TRZ·CYP complexes appears to correlate with lower CYP binding affinity for 123-TRZ and is likely related to the inferior heme binding energetics observed in our calculations. Interestingly, this comparison highlights a perplexing aspect of the binding mechanism for small hydrophilic azole fragments to CYPs. Additional equilibrium binding complexity was observed in the isotherms of 1,2,4-TRZ binding both CYP2C9 and CYP3A4, corroborating a previous type II binding study by Locuson et al. (*40*). In that study the authors speculated that the multiple binding phases observed during equilibrium titration might be explained by considering the multiple nitrogen-ligation states that exist for 1,2,4-TRZ. However, similar binding complexity (and similar binding affinity) observed by the authors for the N(1)-methyl fragment derivative would suggest otherwise; the modification should sterically limit heme ligation to N(4) only. The authors also proposed that 1,2,4-TRZ·CYP complexes may exist as a mixture of directly-ligated and axial H_2O-bridged complexes at equilibrium, which are anticipated to perturb the heme differentially as was shown in this study for a ligand bearing 123-TRZ. However, these hypotheses to explain complex equilibrium binding behavior would require a heterogeneous, slowly-equilibrating protein population and so multiple binding of 1,2,4-TRZ fragment is the more likely explanation. Also described in the study by Locuson et al. was binding isotherm complexity for IMZ binding CYP2C9 (WT) at pH = 7.4 that could be linearized via adjustment of the pH significantly above the fragment pKa (6.99,(*158*)). This behavior is not observed for IMZ binding to the hepta mutant CYP2C9 used here. This discrepancy may reflect modest differences in active site

structure for the wild type vs. the mutant proteins. Also puzzling is the fact that the rank order CYP3A4 affinity measured here for IMZ and 1,2,4-TRZ was reversed relative to the DFT calculations, with the first equivalent (two-site sequential model) of 1,2,4-TRZ binding with greater affinity than IMZ. These results, together with the thermodynamic studies, highlight the important contributions of protein architecture, to fragment-CYP binding energetics.

The chemical similarity between IMZ and 123-TRZ allows for a meaningful comparison of enthalpic (ΔH°) and entropic (ΔS°) components of their binding affinities. Therefore, van 't Hoff analysis was employed to obtain thermodynamic signatures for the CYP3A4 binding interaction. We observed a linear temperature dependence of equilibrium binding constants for these small hydrophilic azole fragments, suggesting that heat capacity changes ($\Delta C°_p$) for fragment-bound complexes are negligible, at least over the temperature range studied here. A negligible heat capacity change (constant ΔH° and ΔS°) upon formation of azole fragment·CYP3A4 complexes is consistent with the hydrophilic nature of IMZ and 123-TRZ, as well as their small size which is not expected to induce conformational changes when ligated to heme iron (*29*). Our thermodynamic results are informative on several levels. First, we found that the large discrepancy in ΔG° between IMZ and 123-TRZ (-5.1 vs. -2.3 kcal/mol at 25°C) binding CYP3A4 in 100 mM KPi is dictated by a much larger entropic penalty for binding in the case of 123-TRZ; surprisingly, the ΔH° term is slightly more favorable for 123-TRZ binding than IMZ, but the entropic difference is a major contribution to their differential affinities. It is tempting to speculate that this phenomenon could be related to the well-documented 123-TRZ tautomeric complexity. 123-TRZ tautomerism is known to be highly dependent on solvent type, polarity, temperature, and 123-TRZ concentration (*128, 130, 132, 169*). In dilute aqueous environments, 123-TRZ exists at ~1:1 ratio of degenerate N1(3)-H tautomers, and the N2-H

tautomer (*128*). 123-TRZ fragment binding to protein may disrupt this equilibrium mixture towards the selection of a single tautomeric form, presumably the symmetric N2-H tautomer that predominates in solvents of low dielectric. Additionally, if ligation to heme iron is favored at the more basic nitrogen positions (N1 and N3), then a tautomeric shift opposite to that induced by fragment binding can be expected. A large unfavorable ΔS° value of -16.5 cal/mol/K has been reported for the tautomerization towards the asymmetric N1(N3)-H tautomer in toluene (*132*). Next, the magnitudes of ΔH° and ΔS° measured for 123-TRZ and IMZ fragments binding CYP3A4 in KPi are comparable to those values reported in a previous solution thermodynamic study of small, IMZ-based ligands for CYP2B4 (*170*). Notably, in that study, the enthalpic signatures (25°C) of phenylimidazole (PI) species 1-PI and 4-PI were either minimally effected (1-CPI, $\Delta\Delta H°_{binding}$ = -0.07 kcal/mol) or dramatically attenuated (4-CPI $\Delta\Delta H°_{binding}$ = + 2.12 kcal/mol) by chloro substitution, suggesting that addition of relatively lipophilic peripheral substituents contributes mostly toward increased, favorable, $\Delta S°_{binding}$, often at the expense of $\Delta H°_{binding}$, a parameter that, in the case of small, rigid, type II ligands such as 123-TRZ and IMZ, may be expected to be dominated by coordinate bond formation. An additional source of the larger entropic penalty for 123-TRZ may be the remaining localized water molecule observed by HYSCORE. These results have particular importance in the context of fragment based drug design strategies that incorporate click chemistry, for CYP inhibitors as well as other targets. The observation that the difference in binding free energy between IMZ and 123-TRZ is largely entropic provides an obvious strategy to incrementally improve the affinity of 123-TRZs; incorporation of hydrophobic groups would likely decrease the entropic cost of binding and increase their affinity very substantially as observed with CYP2B4 and phenylimidazoles.

To test whether 123-TRZ-heme binding interactions are sufficient to dictate overall ligand positioning of drug-like molecules, we sought an ideal molecular framework for 123-TRZ derivatization to use as a model. 17α-ethynylestradiol (17EE) was selected for derivatization because of its well described metabolic profile that allows for some assumptions concerning the molecular details of binding to be inferred: First, 17EE binds in multiple orientations, based on the reported oxidation profile that includes oxygenation on both the estrogen A-ring (2-OH predominant) (*163, 165, 166*) and the acetylenic function of the steroid D-ring (*164*), which imparts its behavior as a mechanism-based inactivator. However, the combination of the substrate's relatively modest partition ratio of ~50, low off-target protein adduction, the lack of reported acetylene-derived carboxylic acid metabolites (*164*), and overwhelming production of 2-OH 17EE (*163-165*), all suggest that the estrogen prefers to bind with its A-ring nearest heme.

The UV/vis binding results for 17-click are striking. Based on historical precedent with nitrogen heterocycles, the type II spectrum induced suggests that the D-ring portion of the molecule now lies nearest the heme to yield an additional coordinate bonding interaction that is not possible in 17EE. In the context of a single heme binding site, this would suggest that the addition of the 123-TRZ causes the estradiol to adopt a different orientation with the TRZ moiety near the heme iron. However, our results are complicated by multiple binding for 17EE; yet binding of the first equivalent of 17EE induces a negligible heme spin shift suggesting our comparison is localized at the catalytically relevant site. Regardless of this complexity it is completely clear that throughout the binding isotherm the high-spin state is favored. Regardless of the correct binding model, it is interesting that, despite the dramatic reversal of the UV/vis binding spectrum to type II for 17-click, no significant increase in ligand affinity was observed. Thus, the TRZ group does not significantly contribute to binding affinity, but rather changes the

binding mode of the steroid nucleus in a nearly isoenergetic complex. An additional observation of some importance is that the 17-click low-spin complex yields a low-spin difference spectrum with lower intensity than the 123-TRZ fragment. We considered the possibility that this could be due to 'incomplete' heme coordination, as suggested by others (*40*). The difference spectra for 17EE is less redshifted and less intense than the spectra obtained from the fragment (Table 3.3).

CW and pulsed EPR techniques proved to be invaluable for understanding the binding and turnover behavior of the [17-click • CYP3A4] complex. The CW EPR spectra show that 123-TRZ and 17-click induce entirely different perturbations in the EPR g-values, suggesting that 123-TRZ-heme interactions are not conserved when present on a drug scaffold. Most profound were the results of HYSCORE analysis which showed conclusively that the 17-click low-spin complex perturbs, yet retains, its axial water ligand. The perturbations of the axial water ligand protons hyperfine splitting values reveal a significant increase in the Fe(III) – H distance by 0.1 Å (2.65 Å → 2.75 Å), consistent with hydrogen bonding between the 123-TRZ fragment of 17-click and axial water. Thus, the [17-click • CYP3A4] complex is speculated to exist at equilibrium as a water-bridged type II ternary complex in which the heme field is perturbed indirectly towards the low-spin state via alteration of the axial water ligand field strength. This implies that the type II optical spectrum observed is the result of the axial water ligand with increased basicity (stronger field ligand) in the presence of 17-click. A similar water-ligated type II complex was observed by Seward et al. between 1,2,4-TRZ antifungal drug fluconazole (*33*) and CYP121 of *Mycobacterium tuberculosis*. In that study, a mixture of water-bridged and directly ligated ligand-bound forms was observed in the crystal structure at 1.90 Å resolution. Notably, our EPR and HYSCORE results reveal a homogeneous low-spin protein fraction, suggesting a preferred ligation state for 17-click. It is intriguing to speculate that this

phenomenon might be more common than previously believed based on the type II spectrum obtained by UV/vis absorbance, which is not distinguishable from many type II spectra in the literature. Additionally, a review of the earlier P450cam literature reveals similar EPR behavior reported for binding of sterically hindered nitrogen heterocycles, at the time classified as 'abnormal' type II ligands (*119*). The CW EPR and HYSCORE results are thus entirely consistent with a lack of affinity increase upon derivatization of 17EE.

The metabolism of 17-click was studied to determine the functional consequences of this unusual heme ligation. In contrast to our expectation that 17-click would dramatically inhibit CYP activity, the estimated turnover number (k_{cat}) of 2.5 min^{-1} for total metabolism demonstrates that 17-click is a good substrate from CYP3A4. In fact, comparison of depletion data obtained for CYP3A4-mediated 17EE oxidation suggests that the rate of 17-click turnover is only moderately slower for the low-spin ligand. This result is similar to recent work by Jones et al., wherein nitrogen-ligated, type II spectral complexes are rapidly metabolized (*38*). Because the spectral results demonstrate that the 123-TRZ moiety of 17-click interacts with heme via H_2O, we found it surprising that the number and relative abundance of the metabolites initially observed were so similar to that observed by others for 17EE.

A combination of high mass accuracy qTOF, and ion trapping (LTQ) mass spectrometries were used to determine structural features of the metabolites. First, comparison of the fragmentation behavior of 17-click and synthesized 2-OH and 4-OH 17-click standards with that of the observed 17-click metabolites allowed us to conclude that steroid A-ring metabolism had been completely abolished for the 123-TRZ derivative. Second, through ion-trapping it was determined that the predominant ion observed in the fragment ion spectrum of M4 originated via loss of the metabolically inserted oxygen atom, and thus probable structures for this fragment ion

that were generated based on elemental composition of this fragment via high mass accuracy qTOF measurements were used to infer the regioselectivity of CYP3A4-mediated oxidation of 17-click. A structure resulting from oxidation in the vicinity of the steroid D-ring was determined to be the only plausible solution for the primary metabolite, M4. Therefore, the mass spectral data support the conclusion that 123-TRZ installation upon the 17EE scaffold alters ligand positioning.

In summary, the 123-TRZ fragment that is isosteric with imidazole and 1,2,4-TRZ fragments found in a wide range of drugs, including those intended to inhibit CYPs, is chemically competent to ligate to the heme of CYPs. However, when incorporated on the scaffold of 17EE, EPR spectra indicate that there is not direct nitrogen ligation. Rather, in the presence of the 123-TRZ-containing 17-click, the sixth axial water is retained and is likely hydrogen bonded to the triazole. This complex, surprisingly, undergoes rapid metabolism, with different regioselectivity than 17EE. Together the results indicate the potential for novel heme coordination by 123-TRZ when installed on a CYP substrate. These results, combined with recent findings published by others (*38, 139*), suggest that low-spin, 'type II' complexes should not be assumed to be inhibitory. Most importantly, we present only the second example, and the first direct EPR-based evidence in the form of HYSCORE, of a triazole ligand that elicits a classic type II UV/vis signature *indirectly* via heme interactions mediated by the axial H_2O ligand. Further studies are required to determine whether the bridged water-heme ligation structure is a general feature of ligands containing the 123-TRZ fragment.

Figures

Table 3.1 Results of gas phase DFT calculations.[#]

Fragment-Heme Complex	ΔE_{rxn} (kcal/mol)	Bond Order	Bond Length Å
IMZ	-5.3	0.311	2.081
1,2,4-TRZ	-3.2	0.285	2.088
123-TRZ (N1)	-1.7	0.258	2.101
123-TRZ (N2)	-2.8	0.248	2.093

[#]s6-31G(d) basis set; U-M06 functional.

Table 3.2 Tabulated UV/vis absorbance data for azole fragment binding CYP3A4 and CYP2C9.

	Soret (nm)	α (nm)	β (nm)	α:β	Difference: Peak (nm)	Difference: Trough (nm)	ΔAbs_{max} (1μM)[#]	ΔAbs_{390} (1μM)[%]	K_D (mM)
CYP3A4[*]	416	565	534	0.94	---	---	---	---	---
123-TRZ	422	565	538	0.77	430	394	0.058	-0.023	14.3 +/- 0.5
1,2,4-TRZ	422	569	537	0.74	432	395	0.0065 0.050	-0.025	K_{D1}=0.0390±0.0071 K_{D2} = 4.80 ± 0.22
IMZ	424	570	538	0.73	432	407	0.065	-0.027	0.381 +/- 0.011
CYP2C9*	418	569	537	1.1	---	---	---	---	---
123-TRZ	420	570	540	0.84	433	411	0.041	---	10.0 +/- 0.4
1,2,4-TRZ	423	572	542	0.78	437	411	0.023 0.044	---	K_{D1}=0.198 ± 0.040 K_{D2} = 2.85 ± 0.82
IMZ	427	574	544	0.77	439	413	0.066	---	0.0989 +/- 0.0018

[*] 20 °C

[#]Maximum peak trough intensity normalized to 1 μM

[%]Used as an estimate of efficiency of type II ligand to decrease inherent high-spin enzyme fraction (type IIa)(*17*).

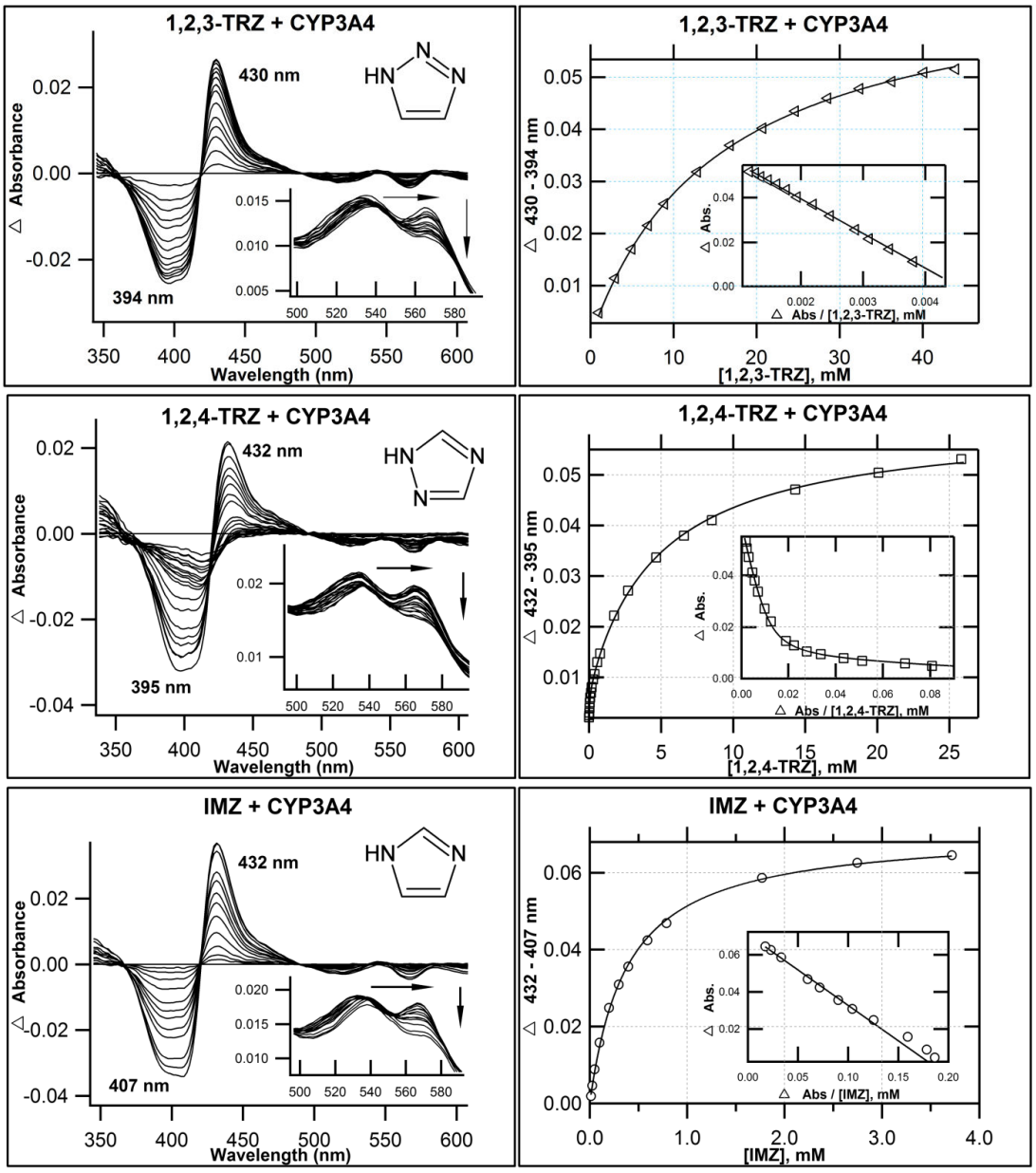

Figure 3.1 Optical titrations and binding isotherms for nitrogen heterocycles binding to CYP3A4. 123-TRZ binding CYP3A4 shows type II behavior. UV/vis equilibrium absorbance titration (20°C) of purified CYP3A4 (1-2 μM; 0.1 M KPi, pH=7.4, + 20% glycerol) with 123-TRZ (top), 1,2,4-TRZ (middle), and IMZ (bottom). Shown are calculated difference spectra (left), with the α and β region of the recorded absolute spectra as inset, and the resultant binding isotherms (right), generated by plotting Δ(peak-trough) intensities as a function of ligand concentration, with best fits used to estimate K_D (Table 2). Interestingly, 1,2,4-TRZ displays complex equilibrium binding behavior (see text) that is most evident as curvature in the Eadie-Hofstee transform (inset), shown here fitted to a two site binding model (Chapter 3.2.9, equation 4).

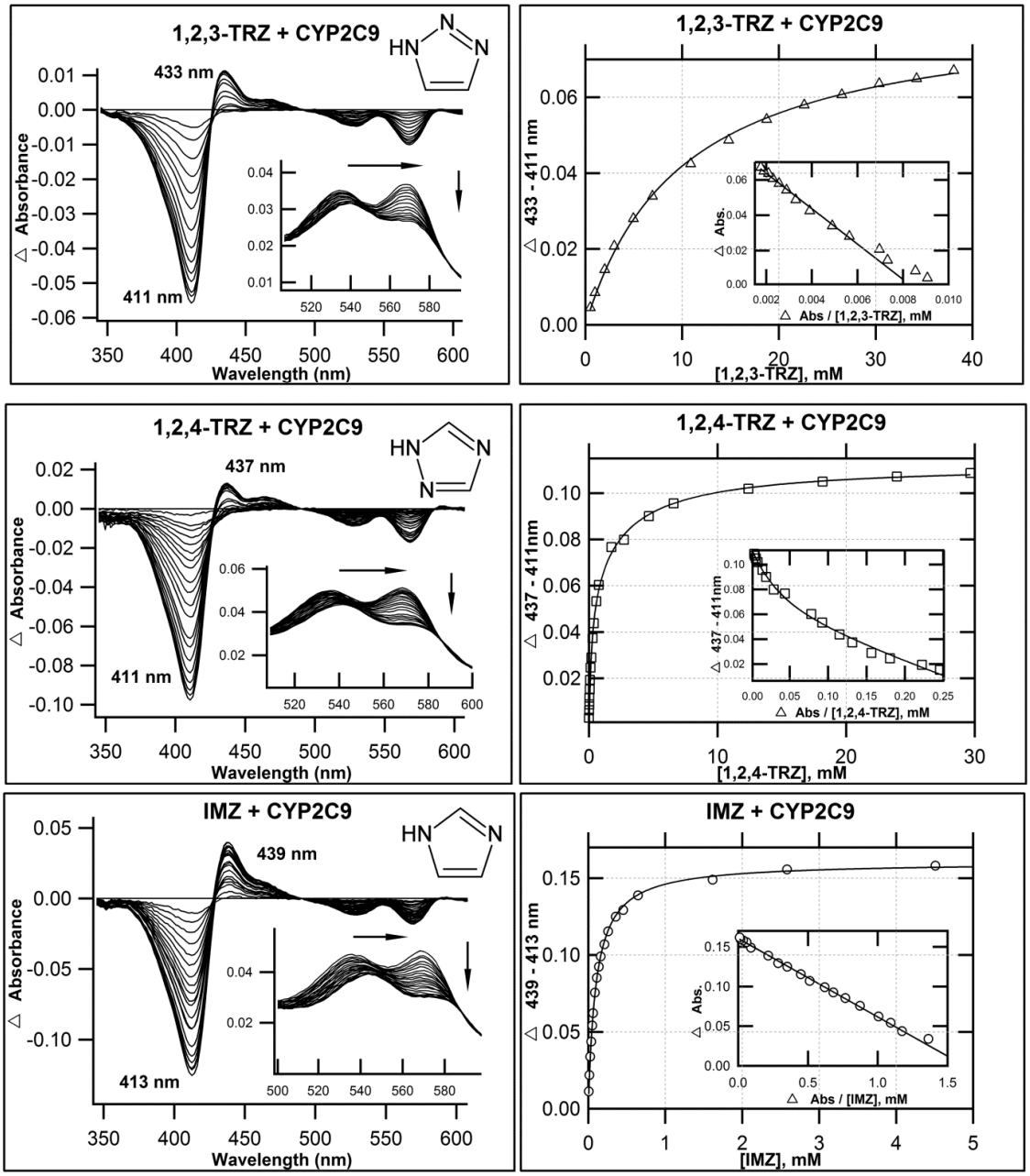

Figure 3.2 Optical titrations and binding isotherms for nitrogen heterocycles binding to CYP2C9. 123-TRZs binding to CYP2C9 yield type II behavior. UV/vis equilibrium absorbance titration (20°C) of purified CYP2C9h (1-2μM; 0.1 M KPi, pH = 7.4, + 20% glycerol) with 123-TRZ (top), 1,2,4-TRZ (middle), and IMZ (bottom). Shown are calculated difference spectra (left), with the α and β region of the recorded absolute spectra as inset, and the resultant binding isotherms (right), generated by plotting Δ(peak-trough) intensities as a function of ligand concentration, with best fits used to estimate K_D (Table 2). As with CYP3A4, 1,2,4-TRZ displays complex equilibrium binding to CYP2C9, which is most evident as curvature in the Eadie-Hofstee transforms (inset). The data fit best to a two site model (Chapter 3.2.9, equation 4) where binding at each site induces similar spin-shifts.

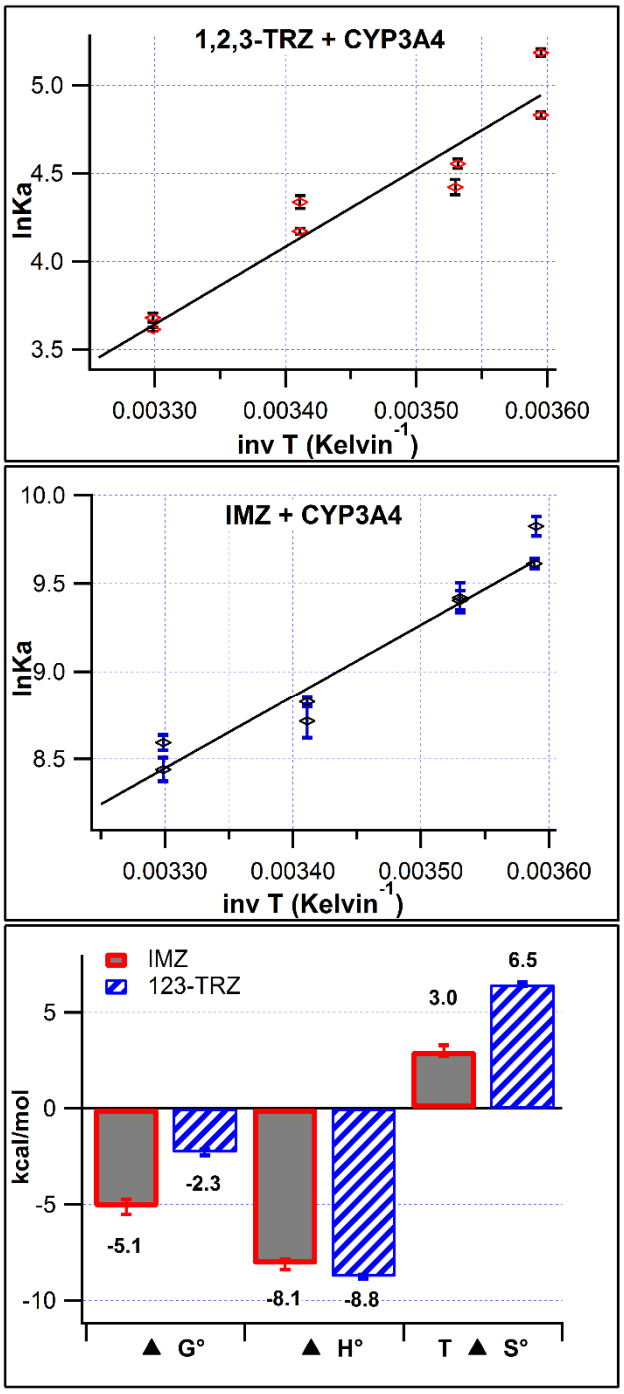

Figure 3.3 van 't Hoff plots demonstrating the temperature dependence (5-30°C) of the equilibrium affinity constant (Ka) for 123-TRZ (top), and IMZ (Middle) binding CYP3A4 (1 µM) in 100 mM KPi (pH = 7.4, +20% glycerol) as measured by UV/vis absorbance titration. Fit results provide estimates for $\Delta H°_{binding}$ and $\Delta S°_{binding}$ and are summarized in the bar graph (bottom) with values of $\Delta G°$ at T = 298 K. Ka values plotted for IMZ represent those obtained after correction of the IMZ titrant concentration to reflect only neutral species (Chapter 3.2.10).

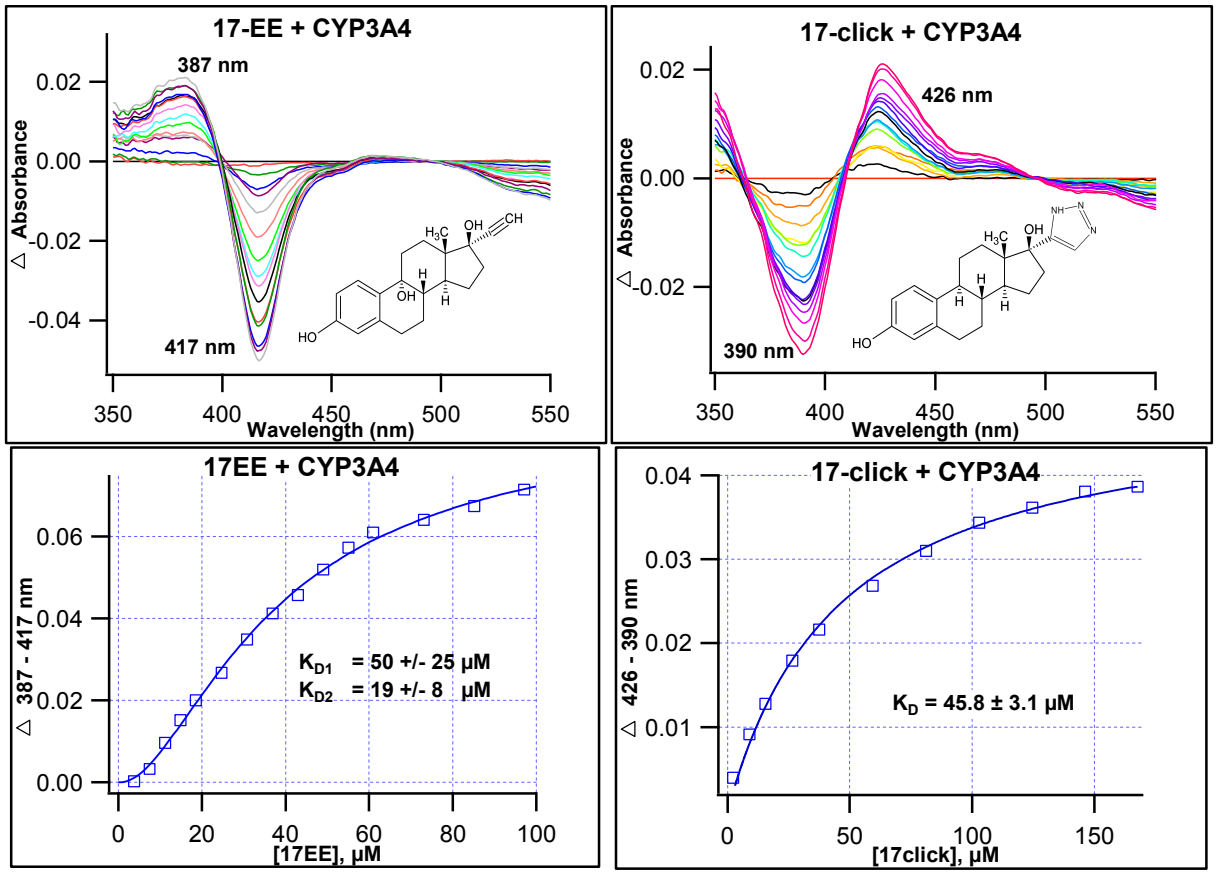

Figure 3.4 Optical titrations and binding isotherms for 17EE and 17-click binding to CYP3A4. Installment of 123-TRZ fragment on the 17EE framework to yield 17-click induces a type I (17EE, top left) to type II (17-click, top right) equilibrium binding conversion. Titrations were conducted in the presence of 2 µM CYP3A4 (100 mM KPi + 20% glycerol, pH=7.4; 20 °C). ,+ 17EE (left), + 17-click (right). Calculated binding isotherm for 17EE (bottom left) fitted best to a sequential two-site binding model where the binding of the first 17EE equivalent is 'spin silent,' while the second 'spin-audible' equivalent binds with positive cooperativity. 17-click binding isotherm (bottom right) displays hyperbolic binding behavior with similar affinity to parent 17EE.

Table 3.3 Comparison of normalized (1μM) UV/vis spectral data for 123-TRZ and 17-click binding CYP3A4.

Ligand	Rel. ΔAbs_{390nm}*(1μM)	Soret Redshift (nm)	ΔAbs_{max} (1μM)#
123-TRZ	1.00	6	0.058
17-click	0.34	2	0.020

*Relative intensity change at 390 nm used to approximate relative efficiency of 123-TRZ ligands to decrease inherent high-spin 3A4 (Type IIa)(*17, 40*)

#Peak minus trough intensity from calculated difference spectrum

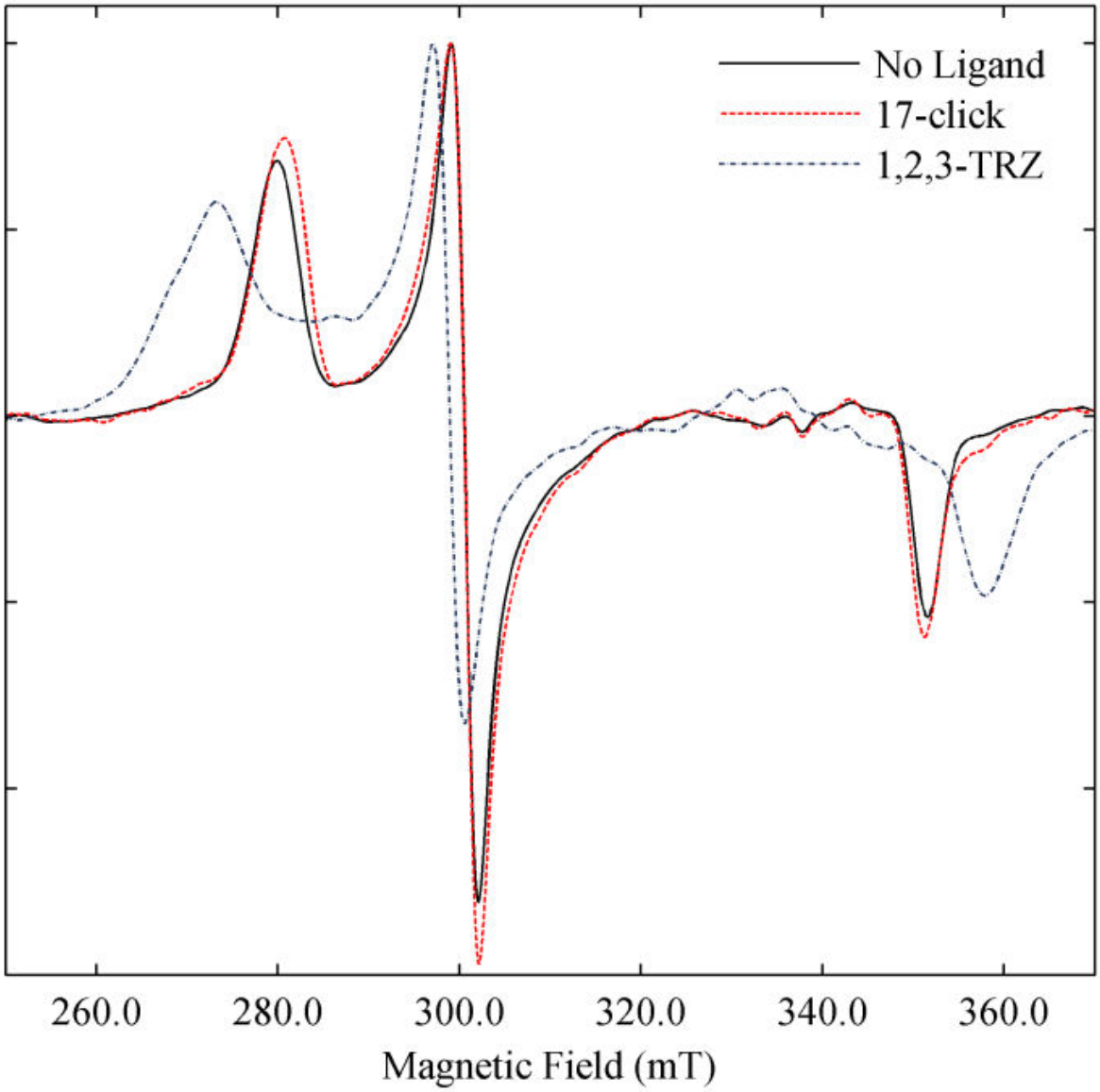

Figure 3.5 X-band CW EPR spectra of ligand-free and ligand-bound low-spin CYP3A4. Spectra of ligand-free (black), 123-TRZ (blue) saturated, and 17-click saturated (red). For all spectra the protein concentration was 45 μM in 0.2 M KPi (pH = 7.4, + 20% glycerol). All experiments were conducted at 15 K and the EPR intensities were normalized.

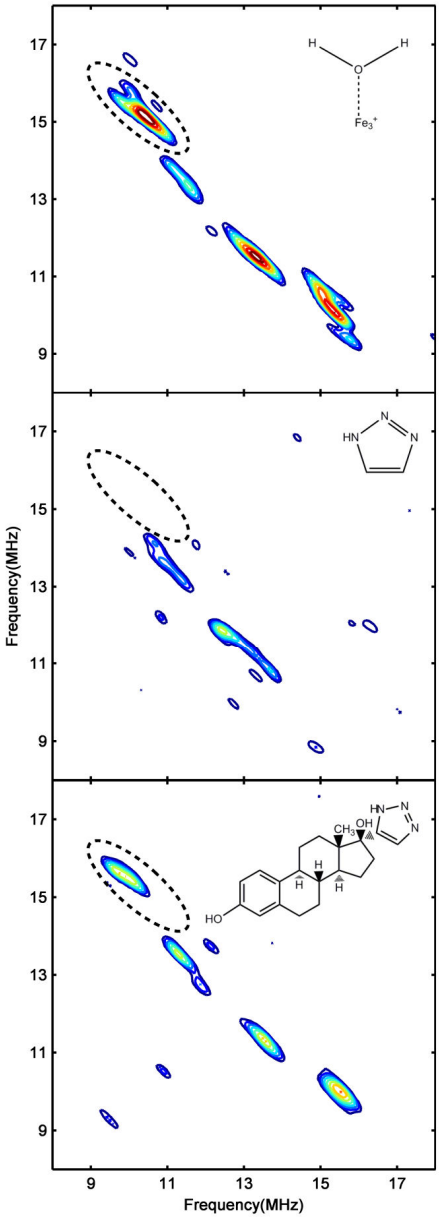

Figure 3.6 HYSCORE spectra of ligand-free and ligand-bound low-spin CYP3A4 corresponding to g_z. Shown is the proton frequency region of the HYSCORE spectra from ligand-free CYP3A4 (Top), CYP3A4 + 50 mM 123-TRZ (Middle), and CYP3A4 + 225 µM 17-click (Bottom). Proton signals corresponding to the axial H_2O protons in ligand-free CYP3A4 (Top) are defined by an ellipse, and are displaced by the type II binding 123-TRZ fragment (Middle). Despite type II binding observed optically, HYSCORE reveals that 17-click binding (Bottom) does not displace H_2O from the heme, but instead alters its ligand field strength. Protein concentration was 45 µM for all samples. Magnetic field strength: ligand-free = 288.0 mT; + 123-TRZ = 283.0 mT; + 17-click = 287.0 mT. All the spectra were normalized to the peaks of highest intensity (i.e. the N2 peak in the (-,+) quadrant).

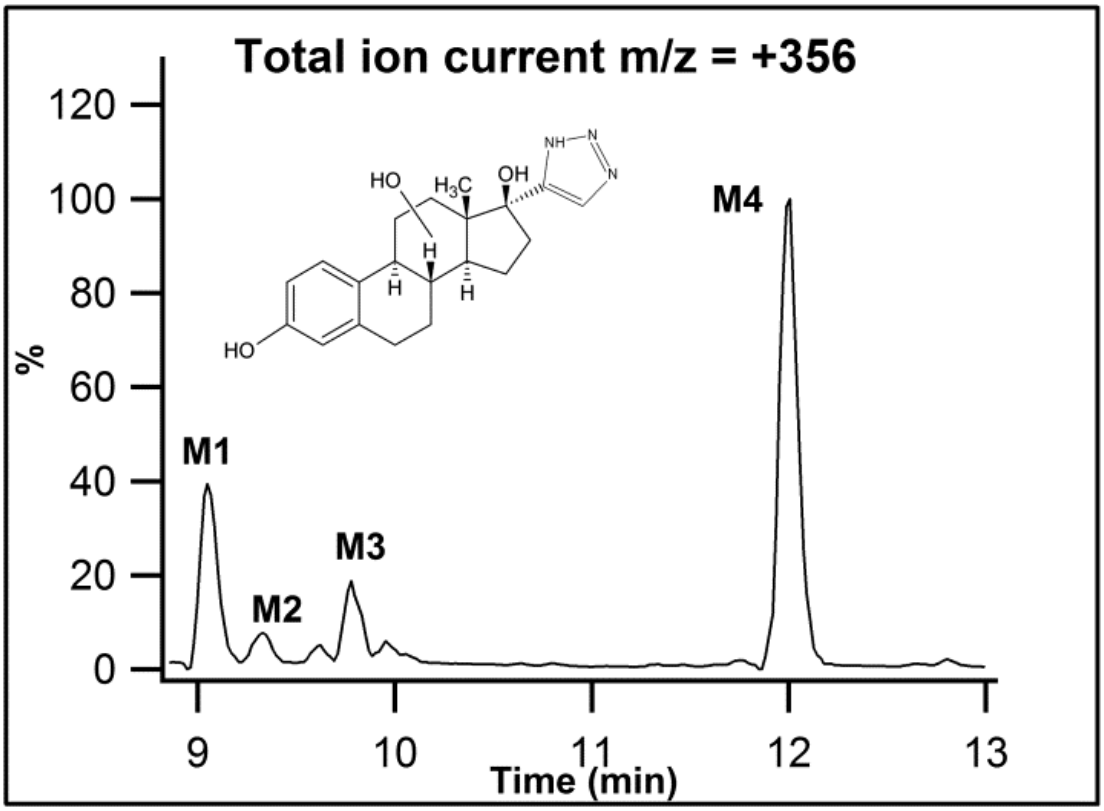

Figure 3.7 17-click Metabolites detected during LC-MS/MS analysis (m/z = 340 +16 (O) = 356) of incubations of 17-click in CYP3A4 Supersomes.

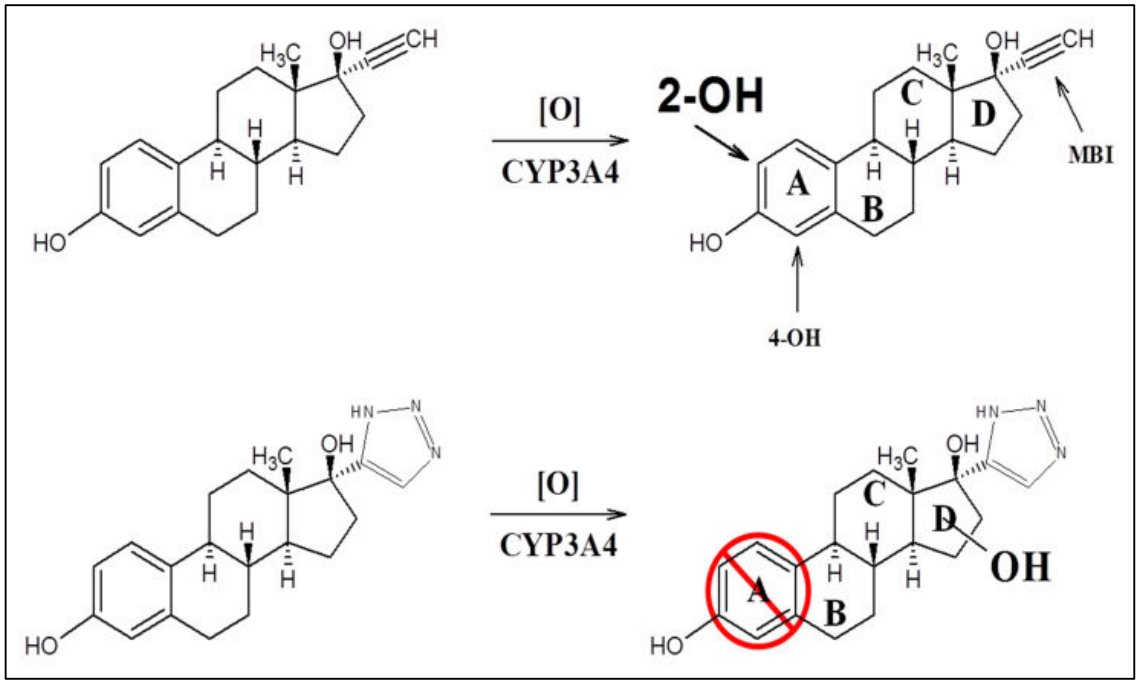

Figure 3.8 Schematic showing primary sites of oxidative metabolism for parent 17EE and the effect of 123-TRZ fragment addition on regioselectivity. When the triazole is added no metabolism occurs on the A-ring but metabolism is directed toward the triazole. Note: the Markush bonded hydroxyl group represents several possible sites of oxidation on or in the vicinity of the steroid D-ring as determined by mass spectrometry (See Results).

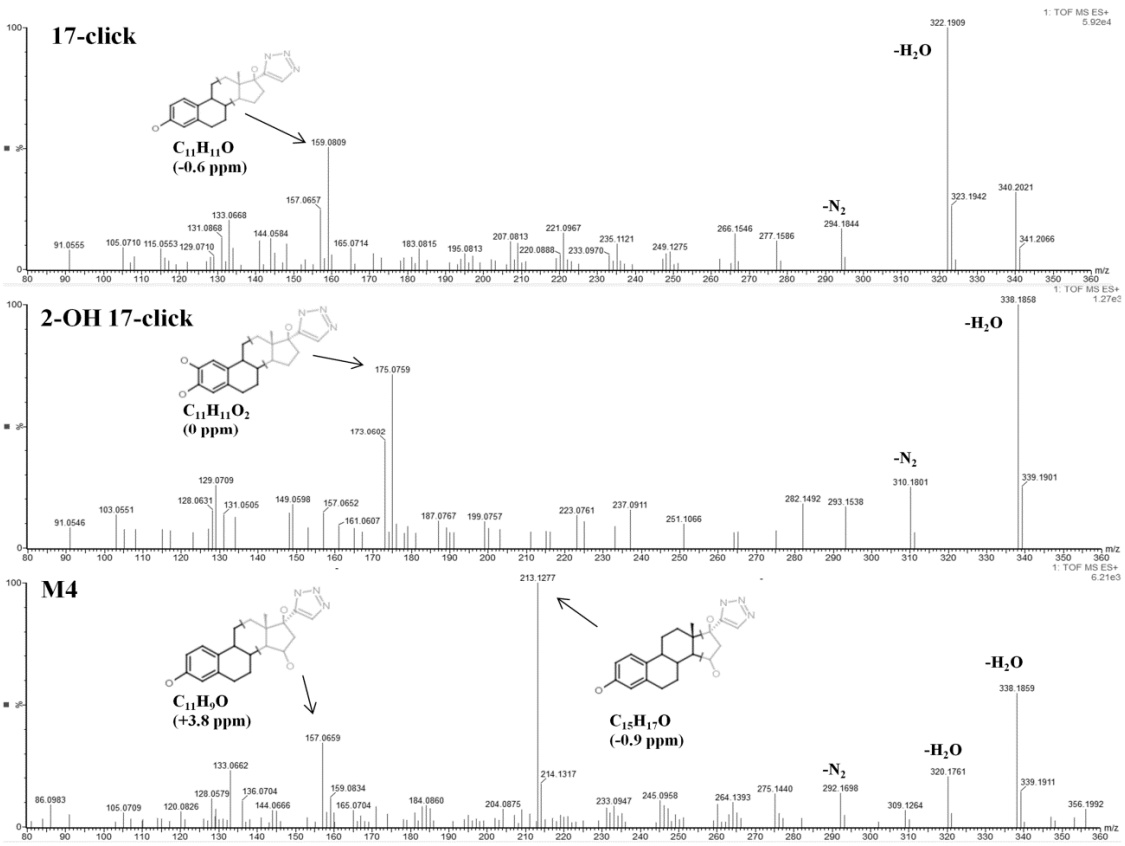

Figure 3.9 MS^E fragment ion spectra. 17-click (m/z = 340.2025 ($C_{20}H_{26}N_3O_2$)) (Top), 2-OH 17-click (Middle), and metabolite M4 (m/z = 356.1974 ($C_{20}H_{26}N_3O_3$)) (Bottom). M4 represents the most abundant metabolite species and closest in retention time to the synthesized 2-OH and 4-OH 17-click. High resolution mass spectra were acquired using a SYNAPT qTOF mass spectrometer in MS^E mode with a collision energy ramp of 15-45V (see Chapter 3.2.6). Structural proposals for highlighted fragments were obtained using MassFragment in MassLynx MS analysis software. Note: the illustrated D-ring location of CYP3A4-mediated oxidation for M4 is indefinite, and merely represents one of few probable turnover positions near/on the steroid D-ring based on results from ion trapping (vide infra).

Table 3.4 Elemental composition of key ion determined by qTOF MSE anlaysis of 17-click, 2-OH 17-click, and predominant metabolite M1.

	Formula	Relative Abundance (%)	Theoretical	Actual	σ (ppm)
17-click	$C_{11}H_9O$	30	157.0653	157.0657	2.5
	$C_{11}H_{11}O$	50	159.0810	159.0809	-0.6
	$C_{20}H_{24}NO$	20	294.1858	294.1844	-4.8
	$C_{20}H_{24}N_3O$	100	322.1919	322.1909	-3.1
	$C_{20}H_{26}N_3O_2$	30	340.2025	340.2021	-1.2
2-OH 17-click	$C_{11}H_9O_2$	30	173.0603	173.0602	-0.6
	$C_{11}H_{11}O_2$	75	175.0759	175.0759	0.0
	$C_{20}H_{24}NO_2$	25	310.1807	310.1801	-1.9
	$C_{20}H_{24}N_3O_2$	100	338.1869	338.1858	-3.3
	$C_{20}H_{26}N_3O_3$	5	356.1974	356.1963	-3.1
M4	$C_{11}H_9O$	40	157.0653	157.0659	3.8
	$C_{15}H_{17}O$	100	213.1279	213.1277	-0.9
	$C_{20}H_{22}NO$	10	292.1701	292.1698	-1.0
	$C_{20}H_{22}N_3O$	15	320.1763	320.1761	-0.6
	$C_{20}H_{24}N_3O_2$	60	338.1869	338.1859	-3.0
	$C_{20}H_{26}N_3O_3$	10	356.1974	356.1971	-0.8

Figure 3.10 MS^4 analysis of primary CYP3A4-mediated metabolite of 17-click (M4) reveals predominant M1daughter ion, m/z = 213, to be a kinetic product of the second dehydration step: m/z = 213 was entirely absent from MS^4 spectra using the sequence 356→338→320→ fragment, while the ion remained in 80% rel. abundance (data not shown) using the sequence 356→338→213→ fragment.

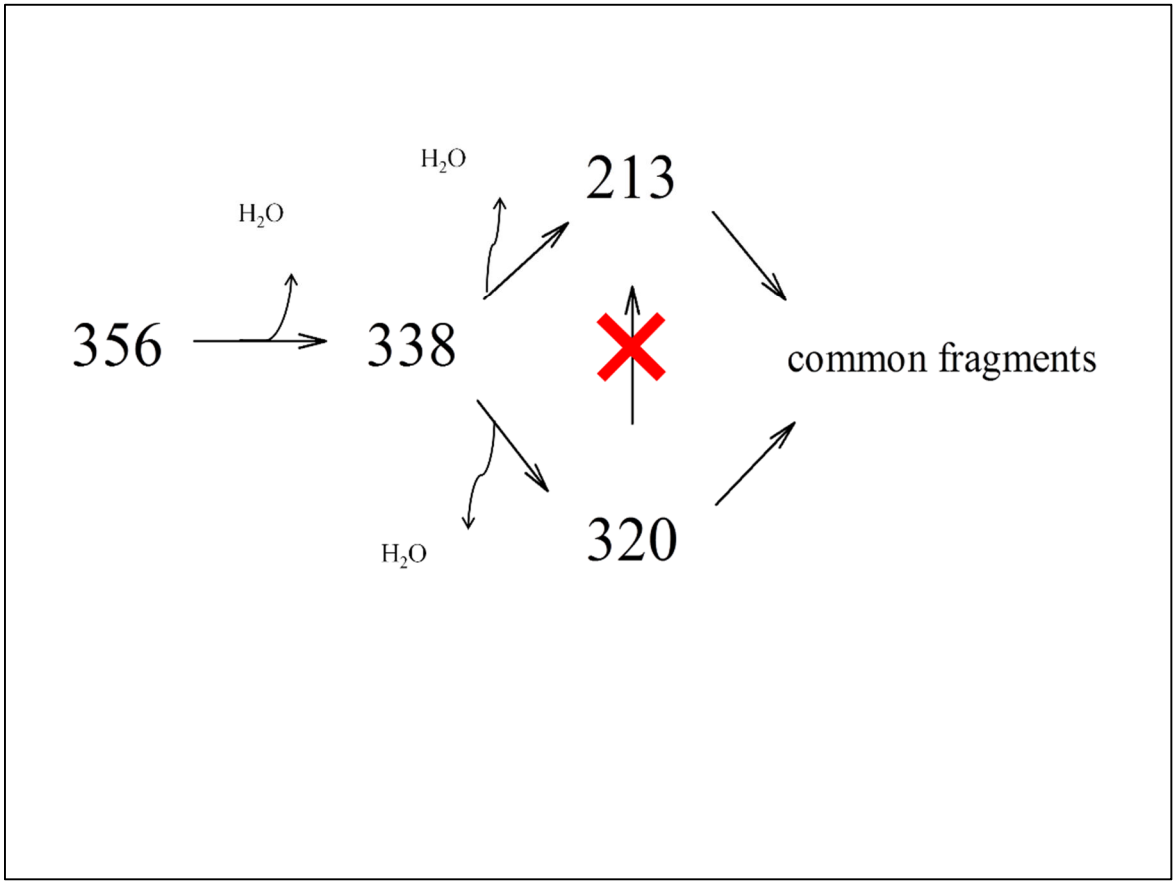

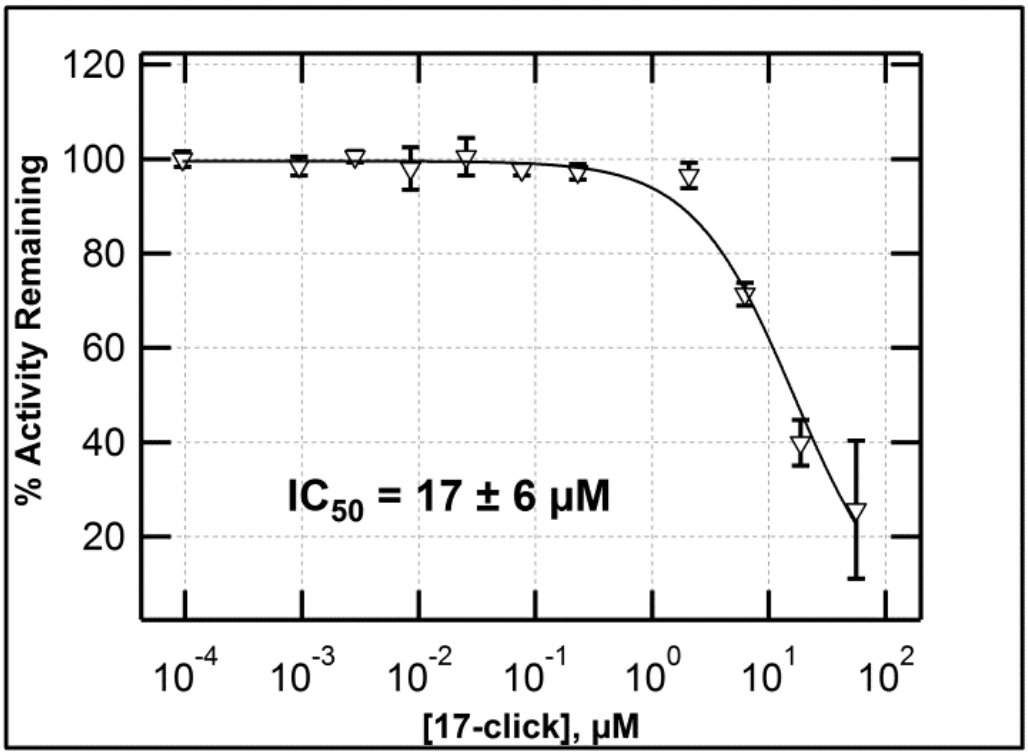

Figure 3.11 IC_{50} measured for 17-click inhibition of CYP3A4-mediated 6β-OH testosterone formation in Supersomes. See Chapter 3.2.5 in main text for assay design and conditions.

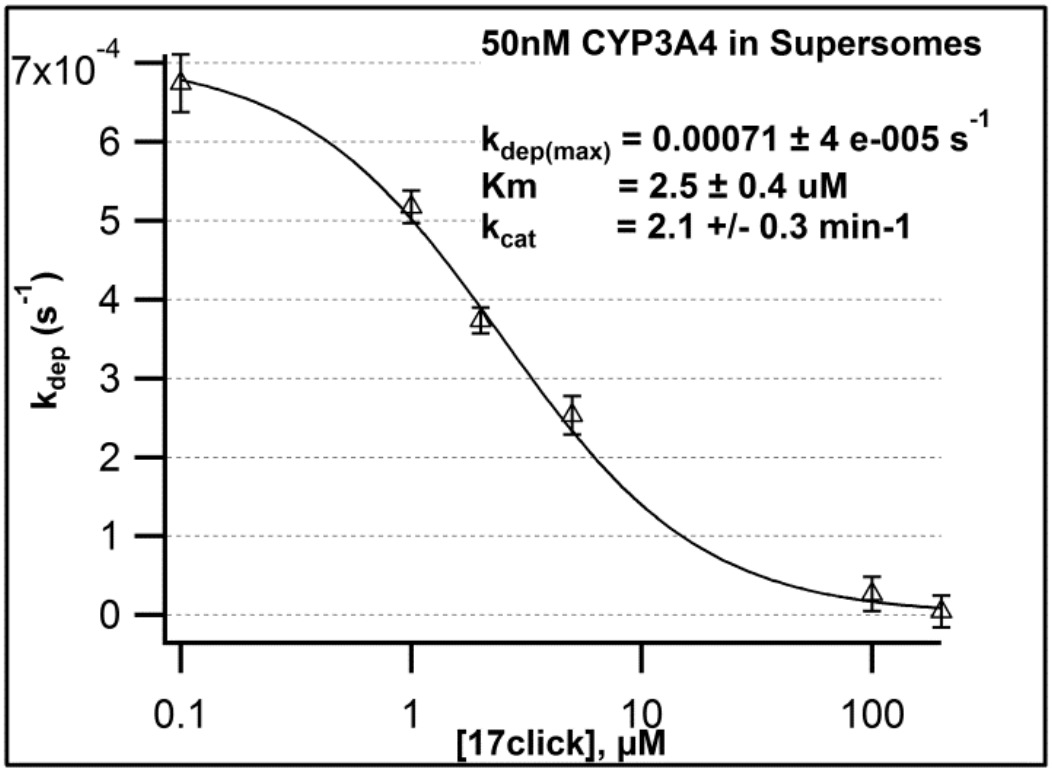

Figure 3.12 kinetic parameters K_M and V_{Max} for CYP3A4-mediated turnover of 17-click in Supersomes determined by LC-MS/MS assay using the methods of substrate depletion. Assay concentration of CYP3A4 was 50 nM based on 0.5 nmol / 0.5 mL CYP concentration provided by the manufacturer.

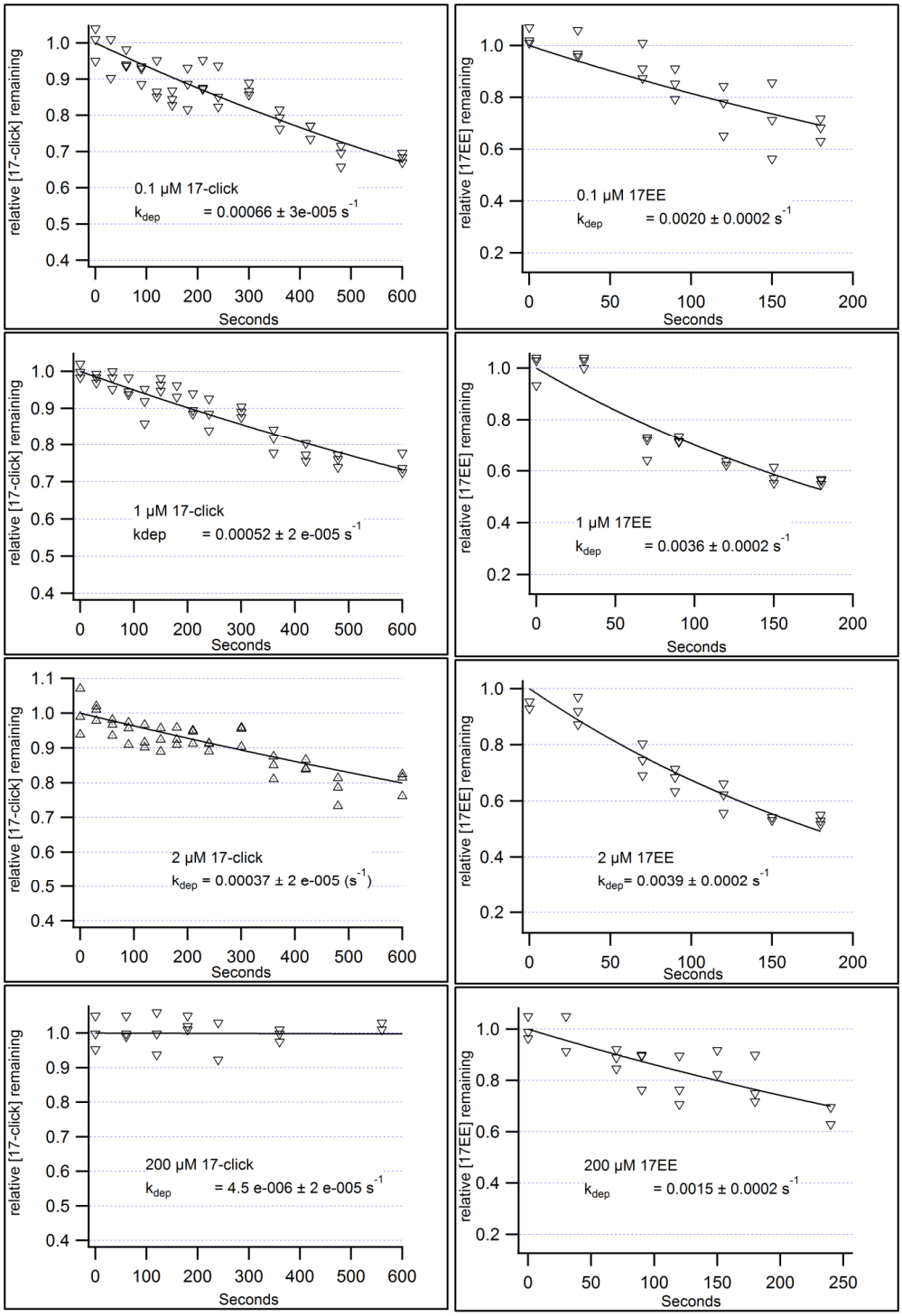

Figure 3.13 Substrate depletion of 17EE and 17-click in the presence of 50 nM CYP3A4 in Supersomes. Depletion of the 17-click (m/z = 340) and 17EE (dansylated derivative, m/z = 530) were monitored by LC-MS/MS assay as described in section Chapter 3.2.4. While accurate determination of kinetic parameters Km and Vmax were only obtained for 17-click (Figure 3.12), comparison of depletion data obtained at low and high concentrations of 17EE suggest metabolism is between 3-10 fold faster for the type I substrate 17EE.

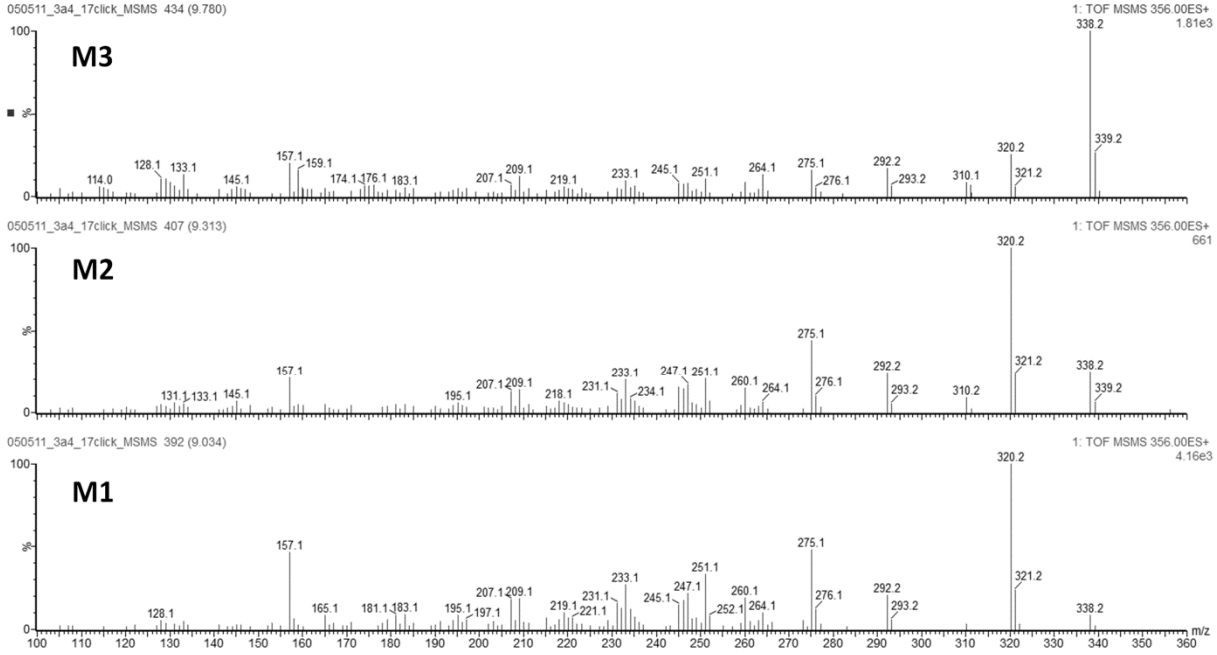

Figure 3.14 qTOF MS/MS analysis of 17click metabolites M3 (Top), M2 (Middle), and M1 (Bottom). Similarity of fragment ion spectra to M4, (predominant fragment ions at m/z = 320, m/z = 292, and m/z = 157) suggests metabolism not occurring on steroid A-ring post 1,2,3-triazole fragment installation (see Results/Discussion).

Chapter 4:

The Impact of Disparate Type II Heme Interactions on CYP Binding and Turnover: A 1,2,3-triazole and Imidazole-Based Analog Library Comparison

4.1 General Introduction to azole inhibitors and motivation for study

As a drug class, azole inhibitors of cytochrome P450 (CYP) are a proven strategy for the management of fungal infection (*12*), with the drugs ketoconazole, fluconazole, and itraconazole being representative examples. Recently, several marketed azole antifungals have shown great promise for combating mycobacterial infection, including tuberculosis (*Mtb*) (*14*). Up to twenty CYPs have been discovered in the *Mtb* genome; of the CYP isoforms that have been isolated, several that have been identified as potential drug targets display high affinity for azoles (*13, 92, 171*). Structurally, it is the presence of a basic nitrogenous heterocycle, most commonly an imidazole (IMZ) or 1,2,4-triazole (124-TRZ) moiety, that distinguishes this drug class and is believed to be a critical determinant of compound affinity and/or inhibitor efficacy for CYP targets (*31, 68*). It is generally believed that the relative propensity of a given azole fragment to coordinate bond with heme iron governs overall inhibitor affinity for CYP (*38, 44*). This type of ligand binding mechanism, known categorically as type II binding, has long been assumed to be a functional dead-end for initiation of the catalytic cycle of the enzyme. This is because hexacoordinate heme geometry in CYP is electronically low-spin with relatively low redox potential (*139, 172*), and thus anticipated to disfavor the necessary one electron reduction by NAD(P)H-dependent redox partners to initiate catalysis. It is precisely this level of

intermolecular specificity between a small molecule azole drug and its CYP target that can be invoked to rationalize the ligand's potential to be a highly effective therapy in certain cases (*68, 173*). Thus, the *local* interactions between azoles and hemes is a source of drug binding for both the target and off-target heme proteins. The author would like to take a moment to define 'local' heme interactions as those involving varying degrees of coordinate covalent bonding *directly* to heme iron; these type II interactions are distinct from the *indirect* low-spin heme interactions involving intermediary molecules such as heme axial H_2O ligand discussed in chapters two and three. Therefore, a more complete understanding of the range of local type II interactions that exist should offer critical insight into both the desirable and undesirable consequences of azole therapy.

CYPs share a common structural similarity in that they all possess heme cofactor—protoporphyrin IX ferric iron chelate—as their catalytic center. Despite this commonality, nature has evolved the ability to fine-tune the electronic and catalytic properties of heme depending on the isoform, and this accounts for the wide range of oxidative chemistries and substrate specificities utilized by this family of proteins that share a common fold (*7, 123*). As corollary, it is not, then, surprising that a range of type II azole-heme interactions are possible depending on the CYP isoform, which can have variable impact on overall ligand affinity, susceptibility to metabolism with influence upon regioselectivity of oxidation, as well as the resultant spectroscopic fingerprint observed for a given CYP-ligand complex. This chapter calls attention to these facts by employing a combination of synthesis, spectroscopy, and functional assay, to thoroughly characterize CYP binding and metabolism of a small library of 'drug-like' 1,2,3-triazoles (123-TRZs) and their IMZ analogs. The goal of this study was to examine relationships between the low-spin spectral fingerprint of type II CYP-azole complexes, azole-ligand affinity,

and ultimately how these structures influence enzyme function. Furthermore, by focusing our spectroscopic characterization on a series of high affinity imidazole-based structural analogs that directly ligate heme iron in CYP3A4, we show that the structural details of low-spin CYP-azole complex play a role, either directly or indirectly, in the functional behavior of the enzyme.

A comparative binding analysis between several diaryl-substituted 123-TRZs and their IMZ analogs was conducted in two diverse isoforms to demonstrate how disparate heme binding energetics can influence overall enzyme affinity differentially depending on the enzyme. For this analysis we chose CYP3A4, a representative 'off-target' CYP often implicated as a source of drug-drug interactions (*174*), and CYP19, the mammalian drug target CYP for which several azole-containing drugs are already in use to treat breast cancer in women (*11*). Next, the azole library was subjected to a thorough CYP3A4-mediated steady-state kinetic turnover analysis to shed light on how disparate type II binding energetics manifest with regard to metabolic velocity and kinetic mechanism for a series of molecules that were designed to conserve peripheral interactions within the protein. Lastly, several CYP3A4-IMZ complexes were chosen for a more rigorous spectroscopic analysis using magnetic circular dichroism (MCD) and continuous wave electron paramagnetic resonance (CW EPR) to further characterize the low-spin enzyme fraction. These results serve as the basis for a discussion of how the details of type II low-spin complexes contribute to CYP catalysis, a concept that has only recently been considered (*139, 175*) in the context of the historical CYP-ligand spectral classification paradigm.

4.2 Experimental Procedures

4.2.1 Materials

All small molecule reagents and/or synthetic precursors, and organic solvents were obtained from Sigma-Aldrich (St. Louis, MO). Protein purification resins and media used for cell culture were obtained from Fisher-Scientific. Competent C41 (DE3) E. coli cells used during CYP gene transformation and protein expression were obtained from Lucigen. Deuterated solvents for NMR analysis were purchased from Cambridge Isotopes (Andover, MA, USA). Supersomes co-expressing cytochrome b_5 and P450 reductase, were purchased from BD Biosciences (San Jose, CA). Water employed during synthesis and in all buffers was of Milli-Q quality from a Barnstead nanopure UV dispenser. Recombinantly expressed and purified human aromatase (CYP19) incorporated in nanodisc was a generous gift from the lab of Dr. Steven G. Sligar. Several of the 1,4 & 1,5-disubstituted 1,2,3-TRZs were synthesized in the lab of Dr. Christopher Seto (Brown University).

^{1}H NMR. Magnetic resonance characterization of synthesized compounds was performed on a Varian (Palo Alto, CA) Inova 500 (500 MHz) spectrometer equipped with a 5mm HCN z-axis PFG triple resonance probe.

4.2.2 Protein expression and purification

CYP3A4 was expressed and purified as previously described (*109*).

4.2.3 Organic synthesis

General click chemistry procedure for synthesis of 1,4-diaryl-substituted-1,2,3-triazoles.

A click chemistry procedure (*86*) for synthesis of 1-(2,4-dichlorobenzyl)-4-phenyl-1,2,3-triazole is described. To a 10 mL round-bottomed flask containing 3.0 mL of DMF:H_2O (4:1) were added 0.20 mmol of phenylacetylene, 5 mol % $CuSO_4$, and 20 mol % sodium L-ascorbate while stirring until solution homogeneity prior to addition of 0.26 mmol 2,4-dichlorobenzyl azide. The solution was allowed to react overnight with gentle heating (60 ℃). For workup of the reaction, the mixture was passed through a pad of florosil to remove excess copper ion then extracted with ethyl acetate. The organic layer was isolated, washed twice with H_2O, and then dried with brine and $MgSO_4$. The evaporated residue was purified on silica gel using CH_2Cl_2 + 1-2% CH_3OH. Yields were essentially quantitative (all 1,4-diaryl 1,2,3-triazole library members were isolated as solids). 1,4-diaryl regioselectivity was verified via 2D NOESY NMR (absence of strong NOE between benzylic protons and inner protons on adjacent aromatic substituent).

1-(2,4-dichlorobenzyl)-4-phenyl-1,2,3-triazole. ^{1}H NMR (δ ppm, J = Hz, $CDCl_3$): 5.70 (2H, s), 7.19 (1H, d, J = 8.4), 7.29 (1H, dd, J = 8.4, 2.0), 7.36 (1H, m), 7.45 (2H, m), 7.50 (1H, d, J = 2.0), 7.79 (1H, d, J = 1.0), 7.84 (2H, d, J = 8.3). ^{13}C NMR: 51.25, 120.13, 126.16, 128.42, 128.73, 129.26, 130.21, 130.72, 131,47, 131.60, 134.49, 136.01, 148.74. MS: [M+Na] = 325.9, [M+H] = 304.0.

1-(2,4-dichlorobenzyl)-4-(4-tertbutylphenyl)-1,2,3-triazole. From 0.20 mmol 4-tertbutyl phenylacetylene. ^{1}H NMR (δ ppm, J = Hz, $CDCl_3$): 1.37 (9H, s), 5.70 (2H, s), 7.15 (1H, d, J = 8.4), 7.27 (1H, dd, J = 8.4, 1.9), 7.47 (2H, d, J = 8.4), 7.49 (1H, d, J = 1.9), 7.77 (1H, s), 7.78 (2H, d, J = 8.4). ^{13}C NMR: 31.31, 34.67, 50.80, 119.78, 125.49, 125.78, 127.55, 127.91, 129.69, 130.91, 131.40, 134.01, 135.39, 148.21, 151.43. MS: [M+Na] = 381.9, [M+H] = 359.9.

1-(2,4-dichlorobenzyl)-4-(5-methoxynaphthyl)-1,2,3-triazole. From 0.20 mmol 2-ethynyl 6-methoxynaphthylene. ^{1}H NMR (δ ppm, J = Hz, $CDCl_3$): 3.94 (3H, s), 5.68 (2H, s), 7.15-7.17 (3H, m), 7.26 (1H, dd, J = 8.1, 1.8), 7.48 (1H, d, J = 2.0), 7.76 (1H, d, J = 8.6), 7.78 (1H, d, J = 8.6), 7.89 (2H, broad), 8.27 (1H, s). ^{13}C NMR: 50.94, 55.35, 105.78, 124.30, 124.38, 125.56, 127.42, 128.02, 128.94, 129.71, 129.79, 131.09, 131.20, 134.10, 134.43, 135.58, 157.99. MS: [M+Na] = 405.9, [M+H] = 383.9.

1-(2,4-dichlorobenzyl)-4-(2,4-difluorophenyl)-1,2,3-triazole. From 0.20 mmol 1-ethynyl-2,4-difluorobenzene. ^{1}H NMR (δ ppm, J = Hz, CD_3OD): 5.79 (2H, s), 7.06 – 7.13 (2H, m), 7.29 (1H, d, J = 8.3), 7.38 (1H, dd, J = 8.3, 2.0), 7.57 (1H, d, J = 2.0), 8.14 (1H, ddd, J = 9.3, 7.56, 6.7), 8.27 (1H, d, J = 3.3). ^{13}C NMR: 50.87, 104.06, 112.13, 114.93, 122.50, 127.94, 128.77, 129.77, 130.94, 131.11, 134.08, 135.55, 159.16, 162.95. MS: [M+Na] = 361.9, [M+H] = 339.9.

General click chemistry procedure for synthesis of 1,5-diaryl-substituted-1,2,3-triazoles.

A representative procedure adapted from Zhang et al. (*176*) for synthesis of 1-(2,4-dichlorobenzyl)-5-phenyl-1,2,3-triazole is described. A benzene solution (1-3 mL) of 3.0 mmol 2,4-dichlorobenzyl azide, 4.5 mmol phenylacetylene and 1 mol % pentamethyl-cyclopentadienyl-bis(triphenylphosphine)ruthenium(II) chloride (Cp*$RuCl(PPh_3)$) was stirred at 80 °C for 2 hr. under nitrogen atmosphere. The reaction progress was monitored by NMR. The crude reaction mixture was evaporated to dryness under vacuum prior to purification by silica gel chromatography using hexane/ether to remove non-polar impurities followed by ether and/or chloroform for elution of the 1,5-disubstituted product. 2D NOESY NMR was employed to verify the 1,5-regioselectivity of the reaction (strong NOE between benzylic protons and inner

protons on adjacent aromatic substituent); all 1,5-disubstituted products were obtained in yields > 80 % as brown oils.

1-(2,4-dichlorobenzyl)-5-phenyl-1,2,3-triazole. ^{1}H NMR (δ ppm, J = Hz, $CDCl_3$): 5.63 (2H, s), 6.78 (1H, d, J = 8.4), 7.17 (1H, dd, J = 8.4, 2.1), 7.24-7.26 (2H, m), 7.38 (1H, d, J = 2.1), 7.43-7.45 (3H, m), 7.81 (1H, s). ^{13}C NMR: 48.75, 126.39, 127.72, 128.51, 129.20, 129.36, 129.47, 129.76, 132.03, 132.93, 134.70, 138.6. MS: [M+Na] = 326.1, [M+H] = 304.1.

1-(2,4-dichlorobenzyl)-5-(4-tertbutylphenyl)-1,2,3-triazole. From 4.5 mmol 4-tertbutyl phenylacetylene. ^{1}H NMR (δ ppm, J = Hz, $CDCl_3$): 1.35 (9H, s), 5.64 (2H, s), 6.76 (1H, d, J = 8.4), 7.17 (1H, dd, J = 8.4, 2.1), 7.21 (2H, d, J = 8.4), 7.41 (1H, d, J = 2.1), 7.46 (2H, d, J =8.4), 7.80 (1H, s). ^{13}C NMR: 31.57, 35.22, 49.18, 123.78, 126.57, 128.08, 128.58, 129.71, 129.84, 132.64, 133.34, 133.52, 135.02, 139.01, 153.47. MS: [M+H] = 360.1.

1-(2,4-dichlorobenzyl)-5-(5-methoxynaphthyl)-1,2,3-triazole. From 4.5 mmol 2-ethynyl 6-methoxynaphthylene. ^{1}H NMR (δ ppm, J = Hz, $CDCl_3$): 3.93 (3H, s), 5.66 (2H, s), 6.84 (1H, d, J = 8.4), 7.15 (2H, dd, J = 8.4, 2.0), 7.20 (1H, dd, J = 9.0, 2.4), 7.28 (1H, dd, J = 8.4, 1.7), 7.36 (1H, d, J = 2.0), 7.63 (1H, s), 7.67 (1H, d, J = 9.0), 7.77 (1H, d, J = 9.0), 7.88 (1H, s). ^{13}C NMR: 49.18, 55.81, 106.08, 120.49, 121.61, 126.26, 128.13, 128.26, 128.35, 128.85, 129.81, 129.89, 130.14, 132.55, 133.34, 133.70, 135.07, 135.17, 159.19. MS: [M+H] = 383.9.

1-(2,4-dichlorobenzyl)-5-(5-bromophenyl)-1,2,3-triazole. From 4.5 mmol 4-bromophenyl acetylene. ^{1}H NMR (δ ppm, J = Hz, $CDCl_3$): 5.59 (2H, s), 6.77 (1H, d, J = 8.4), 7.10 (2H, d, J = 8.7), 7.17 (1H, dd, J = 8.4, 2.1), 7.37 (1H, d, J = 2.1), 7.54 (2H, d, J = 8.7), 7.79 (1H, s). ^{13}C NMR: 49.17, 124.67, 125.72, 128.19, 129.79, 129.94, 130.40, 132.13, 132.86, 133.34, 133.78, 135.29, 137.86. MS: [M+H] =382.2.

Strategy #1 for synthesis of 1,5-diaryl-substituted-imidazoles.

A modified three step procedure adapted from Roumen et al. (*177*) was used for synthesis of 1,5-diaryl-substituted imidazoles 1-(2,4-dichlorobenzyl)-5-(4-tertbutylphenyl)-imidazole and 1-(2,4-dicholorbenzyl)-5-(5-methoxynaphthyl)-imidazole. Step 1 (imidazole protection): A chloroform solution containing 6.8 mmol 4-bromo-1H-imidazole and 19.3 mmol triethylamine were added dropwise to an ice-cold chloroform solution containing 7.4 mmol triphenylmethyl chloride while rapidly stirring. The reaction was allowed to proceed at room temperature for 2 hr. until a pink solid was observed. The reaction crude was washed twice with 15 mL of 0.5 M HCl, and once with 15 mL of $NaHCO_3$, then the organic layer was dried over $MgSO_4$ and evaporated to dryness. The residue was triturated with diethyl ether resulting in pure 1-trityl-4-bromo-imidazole **(1)** product as a white solid (90% yield): ^{1}H NMR (δ ppm, J = Hz, $CDCl_3$) 6.85 (1H, s), 7.11, (6H, m), 7.26 – 7.37 (9H, m), 7.52 (1H, s). MS: [M+H] 243.1 (trityl cation).

Step 2 (S_N2 reaction): To a reaction flask containing 2.56 mmol **(1)** dissolved in warm acetonitrile and chloroform (4:1) were added 2.56 mmol 2,4-dichlorobenzyl chloride and 2.56 mmol NaI. The sealed reaction vial was heated (~ 70 °C) for 30 hrs with rapid stirring. The burgundy solution was removed from heat and 7 mL glacial acetic acid plus 2 mL H_2O were added. The mixture was refluxed for 2 hrs. until a white precipitate coated the reaction flask. 15 mL of 1 M HCl was added and the mixture was transferred to a separatory funnel and extracted twice with two volumes of diethyl ether. The pH of the aqueous layer was adjusted to 8-9 with NaOH forming an off-white opaque solution. The aqueous solution was extracted with CH_2Cl_2 and the organic layer evaporated to dryness. The residue was purified on silica gel using 2% CH_3OH in CH_2Cl_2 yielding 110 mg (~18% yield) of pure 1-(2,4-dichlorobenzyl)-5-bromo-imidazole **(2)**.

Step 3 (Suzuki coupling): Standard protocol described for synthesis of 1-(2,4-dicholorbenzyl)-5-(5-methoxynaphthyl)-imidazole. To a three neck round-bottom flask charged with argon were added 0.18 mmol **(2)**, 5.3 μmol $Pd(PPh_3)_4$, and 0.35 mmol $NaCO_3$. The vessel was sealed under positive pressure of argon prior to the addition of 2.2 mL of degassed dimethoxyethane:H_2O:CH_3CH_2OH solvent mixture (4:2:1) via syringe while stirring to homogeneity. A deoxygenated solution of 0.19 mmol 6-methoxy-naphthaleneboronic acid in the same solvent was added via syringe to initiate the reaction, prior to heating the mixture (75 °C) for 24 hrs. (reaction monitored by TLC). The mixture was concentrated under vacuum before adding ~10 mL chloroform, then washed with sat. $NaHCO_3$, and dried over $MgSO_4$. The 1,5-disubstituted imidazole product was purified from the organic residue via silica gel chromatography using 1% CH_3OH containing 7M NH_3 in CH_2Cl_2. 2D NOESY NMR was employed to verify 1,5-regioselectivity for the reaction sequence (strong NOE between benzylic protons and inner protons on adjacent aromatic substituent).

1-(2,4-dicholorbenzyl)-5-(5-methoxynaphthyl)-imidazole. 38% yield as a clear oil. ^{1}H NMR (δ ppm, J = Hz, $CDCl_3$): 3.93 (3H, s), 5.26 (2H, s), 6.67 (1H, d, J = 8.4), 7.13 (1H, d, J = 1.7), 7.16 (1H, dd, J = 8.4, 2.1), 7.17 (1H, dd, J = 8.4, 1.7), 7.25 (1H, s), 7.33 (1H, dd, J = 8.8, 2.6), 7.39 (1H, d, J = 2.1), 7.61 (1H, s), 7.63 (1H, d, J = 2.6), 7.66 (1H, d, J = 8.4), 7.73 (1H, d, J = 8.8). ^{13}C NMR: 46.20, 53.46, 55.41, 105.62, 119.65, 124.31, 126.82, 127.44, 127.62, 127.76, 128.59, 128.70, 128.97, 129.56, 129.60, 133.03, 133.27, 133.61, 134.12, 134.58, 138.68, 158.27. MS: [M+H] = 383.1.

1-(2,4-dichlorobenzyl)-5-(4-tertbutylphenyl)-imidazole. From 0.19 mmol 4-tertybutylphenyl boronic acid; 20% yield as an off-white solid. ^{1}H NMR (δ ppm, J = Hz, $CDCl_3$): 1.33 (9H, s), 5.21 (2H, s), 6.63 (1H, d, J = 8.4), 7.16 (1H, dd, J = 8.4, 2.1), 7.17 (1H, s), 7.19 (2H, d, J = 8.6),

7.39 (2H, d, J = 8.6), 7.40 (1H, d, J = 2.1), 7.55 (1H, s). ^{13}C NMR: 31.25, 34.69, 46.09, 125.85, 126.26, 127.72, 128.22, 128.29, 128.91, 129.52, 132.99, 133.40, 133.46, 134.51, 138.48, 151.49. MS: [M+H] = 359.1.

1-(2,4-dichlorobenzyl)-5-bromoimidazole **(2)**. 18% yield as a white solid. ^{1}H NMR (δ ppm, J = Hz, $CDCl_3$): 5.52 (2H, s), 7.2-7.45 (3H, m), 7.51 (1H, s), 9.20 (1H, s). MS: [M+H] = 304.9.

Strategy #2 for synthesis of 1,5-diaryl-substituted-imidazoles.

The appropriate 4-substituted imidazole precursor was commercially available for synthesis of 1-(2,4-dichlorobenzyl)-5-phenylimidazole, and 1-(2,4-dichlorobenzyl)-5-(4-bromophenyl)-imidazole; therefore, Suzuki coupling (Step 3 in the previous 1,5-diaryl-substituted imidazole protocol) was unnecessary. To improve yields for the S_N2 reaction step (Step 2), 0.3 mol equivalent of 4-dimethylaminopyridine (DMAP) was used instead of NaI. Purification of the 1,5-diaryl-substitued imidazole products was conducted as described in strategy #1.

1-(2,4-dichlorobenzyl)-5-phenylimidazole. From 6.8 mmol 4-phenylimidazole; 35% yield as a brown oil. ^{1}H NMR (δ ppm, J = Hz, $CDCl_3$): 5.22 (2H, s), 6.65 (1H, d, J = 8.3), 7.17 (1H, dd, J = 8.3, 2.0), 7.20 (1H, s), 7.25-7.28 (2H, m), 7.36-7.39 (3H), 7.40, (1H, d, J = 2.0), 7.63 (1H, s). MS: [M+H] = 303.1.

1-(2,4-dichlorobenzyl)-5-(4-bromophenyl)-imidazole. From 6.8 mmol 4-(4-bromophenyl)-imidazole; 30% yield as an off-white solid. ^{1}H NMR (δ ppm, J = Hz, $CDCl_3$): 5.18 (2H, s), 6.61 (1H, d, J = 8.4), 7.12 (2H, d, J = 8.5), 7.17 (1H, dd, J = 8.4, 2.1), 7.18 (1H, s), 7.41 (1H, d, J =

2.1), 7.50 (2H, d, J = 8.5), 7.58 (1H, s). ^{13}C NMR: 46.15, 122.66, 127.80, 128.23, 128.73, 128.92, 129.68, 130.08, 132.13, 132.92, 133.02, 134.77, 139.11. MS: [M+H] = 381.0.

General click chemistry procedure for synthesis of 4-arylsubstituted-1,2,3-triazoles.

Synthesized as described for 1,4-diaryl-substituted-1,2,3-triazoles except for the following modifications: 5 mol% CuI was used instead of $CuSO_4$, and 0.26 mmol azidotrimethylsilane replaced 2,4-dichlorobenzyl azide.

4-phenyl-1H-1,2,3-triazole. From 0.20 mmol phenylacetylene; 50% yield as a white solid. ^{1}H NMR (δ ppm, J = Hz, $CDCl_3$): 7.36-7.46 (3H, m), 7.82 – 7.84 (2H, m), 8.04 (1H, s). MS: [M+H] = 146.2.

4-(4-tertbutylphenyl)-1H-1,2,3-triazole. From 0.20 mmol 4-(4-tertbutylphenyl)-acetylene; 50% yield of an off-white solid. ^{1}H NMR (δ ppm, J = Hz, $CDCl_3$): 1.34 (9H, s), 7.53 (2H, d, J = 8.6), 7.84 (2H, d, J = 8.6), 8.12 (1H, s). MS: [M+H] = 202.1.

4-(5-methoxynaphthyl)-1H-1,2,3-triazole. From 2-ethynyl-6-methoxynaphthylene; 50% yield as a white solid. ^{1}H NMR (δ ppm, J = Hz, CD_3OD): 3.94 (3H, s), 7.18 (1H, dd, J = 8.9, 2.5), 7.33 (1H, d, J = 2.5), 7.87 (1H, d, J = 8.9), 7.89 (1H, d, J = 8.6), 8.01 (1H, dd, J = 8.6, 1.6), 8.24 (1H, s), 8.36 (1H, d, J = 1.6). MS: [M+H] = 226.1.

4-(4-bromophenyl)-1H-1,2,3-triazole. From 4-bromophenyl acetylene; 50% yield as an off-yellow solid. ^{1}H NMR (δ ppm, J = Hz, $CDCl_3$): 7.58 (2H, d, J = 8.4), 7.70 (2H, d, J = 8.4), 7.95 (1H, s). MS: [M+H] = 224.0.

General procedure for synthesis of 4-arylsubstituted-imidazoles.

4-arylsubstituted-imidazoles were synthesized using reaction step 1 (4-bromoimidazole trityl protection) followed by step 3 (Suzuki coupling) described for synthesis of 1,5-diaryl-substituted imidazoles with the exception that the final workup used is as described for deprotection of the trityl group in step 2 (S_N2 reaction).

4-(4-tertbutylphenyl)-imidazole. From 1.4 mmol 4-tertbutylphenyl boronic acid; 75% yield as off-white solid. ^{1}H NMR (δ ppm, J = Hz, CD_3OD): 1.33 (9H, s), 7.36 (1H, s), 7.41 (2H, d, J = 8.5), 7.61 (2H, d, J = 8.5), 7.70 (1H, s). MS: [M+H] = 201.1.

4-(5-methoxynaphthyl)-imidazole. From 1.4 mmol 6-methoxynaphthalene-2-boronic acid; 75% yield as off-yellow solid. ^{1}H NMR (δ ppm, J = Hz, $CO(CD_3)_2$): 3.92 (3H, s), 7.13 (1H, dd, J = 8.9, 2.3), 7.18 (1H, s), 7.26 (1H, d, J = 2.3), 7.73 (1H, s), 7.77 (1H, d, J = 8.9), 7.79 (1H, d, J = 8.6), 7.97 (1H, dd, J = 8.6, 1.5), 8.29 (1H, d, 1.5). MS: [M+H] = 225.1.

4.2.4 UV/vis absorbance analysis of ligand binding

Ligand binding analysis was conducted using a similar procedure to that described in Chapter 2.2.5 and Chapters 3.2.9. For all tight-binding species (K_s << [E]) the quadratic binding equation (1) was used to account for violation of the free ligand approximation. A good fit of the CYP3A4 binding data to equation (1) was achieved when the [E_t] was allowed to float while holding the offset parameter at zero. In all but one case (IMZ-60) was a significant deviation (± 15 %) from the CYP450 concentration determined using the methods of Omura and Sato (*178*) observed; when fitting CYP3A4-(IMZ-60) binding data the protein concentration was

constrained within ± 15 % of the known CYP3A4 concentration while allowing the offset parameter to float. Good fits to equation (1) for all 123-TRZs and IMZs binding CYP19 were obtained by holding $[E_t]$ at an experimentally determined concentration while allowing for the offset parameter to float.

$$(1)\ \Delta Abs.= [E\cdot L] = [([E_t] + [L_t] + K_s) - (([E_t] + [L_t] + K_s)^2 - 4[E_t][L_t])^{1/2}]/2 + offset$$

Due to solubility limitations of the 1,5-diaryl-substituted 1,2,3-triazoles, when determining the UV/vis spectrum at enzyme saturation, a singular value decomposition (SVD) algorithm written in Python programming language and adapted for use in IGOR Pro 6.1 (Wavemetrics, Lake Oswego, OR.) was employed (*153*). Briefly, the concentration dependent binding spectra were subjected to SVD analysis to separate the individual principal components (PC) scaled by their singular values. It was observed that a single PC adequately accounted for the concentration-dependent spectral response. This PC was then normalized to the spectral amplitude (B_{max}) determined by the fit of the experimental data, and used to construct a 'spectral standard' for enzyme saturation.

For both CYP3A4 and CYP19 binding analysis, the absolute binding spectral intensity was normalized to that measured for the initial binding experiment (123-60 for CYP3A4, and IMZ-60 for CYP19) to account for small differences in enzyme concentration and thus allow for accurate comparison of spectral signatures (B_{max} and Δ388nm (difference spectrum trough intensity)).

4.2.5 Comparison of Gibb's free energy ($\Delta G^{\circ}_{binding}$) for CYP binding

$\Delta\Delta G°_{binding}$ was calculated from the experimental binding data using the K_s parameter recovered in the fits via equation (2):

(2) $\Delta\Delta G°_{binding} = RT\ln(K_{sIMZ}/ K_{s123\text{-}TRZ})$

4.2.6 Calculation of molar volume for variable azole substituent, –R

Molar volume for each variable substitutent (–R) the 123-TRZ/IMZ library was calculated using Spartan '08 (v.1.2.0, Wavefunction, INC., Irvine, CA). Hartree-Fock type calculations were performed using the 3-21G basis set.

4.2.7 Metabolite Identification (MetID)

Initial substrate depletion analysis to assess metabolic stability of the 1,5-diaryl-substituted azoles in the presence of CYP3A4-containing Supersomes was conducted at 1 μM and 5 μM azole concentration using a similar LC-MS/MS assay to that described in Chapter 3.2.4. For metabolite identification, 1 mL incubations contained 100 μL Supersomes (100 pmol CYP3A4, co-expressing P450 reductase and *Cytb5*), 50 μM 1,5-diaryl-substituted azole (1.5% CH_3OH final v/v), 100 mM KPi buffer (pH = 7.4), and 1 mM NADPH. Control incubations without protein and without NADPH were also prepared. The reactions were allowed to proceed open to air for 1hr at 37 ℃ with gentle agitation. The reactions were quenched with 1.5 mL ethylacetate, pelleted by centrifugation, and the organic layer separated and evaporated to dryness. The residue was re-suspended in a minimal amount of acetonitrile : H_2O (3:1) mobile phase prior to injection (Waters Acquity) onto a UPLC coupled to a Waters (Milford, MA)

Synapt High Resolution Quadrupole TOF mass spectrometer via an ESI interface. Chromatographic separation of the mixtures was achieved with a 100 x 2.1 mm Hypersil Gold (Thermo-Sci) C_{18} UPLC column, using a gradient program consisting of 5 – 95% B (B: acetonitrile + 0.1% FA) mobile phase over 15 minutes at 0.3 µL/min. For parent ion detection in full scan mode (50-1500 m/z, positive ESI) the cone voltage was 22 eV, and the collision and transfer energies were held at 5 eV. For acquisition of fragment ion data, a second channel was set up in MS expression mode (MS^E). Fragmentation of each species was achieved using a cone voltage of 35 eV and a collision cell energy ramp from 15-45 eV with the transfer cell maintained at 10 eV. The capillary voltage was maintained at 3.5 keV, the capillary temperature set to 120 ℃, and the de-solvation temperature set to 350 ℃. High mass accuracy was achieved via instrument calibration with sodium formate between 50-1500 m/z before each use, and a lock-spray reference channel sampling leucine encephalin in 10 s intervals with scan rate of 0.5 s. All spectra were combined in Masslynx software and subjected to mass defect filtering with the program Metabolynx based on the input elemental formula of the parent compound. Metabolynx was used to identify probable phase I oxidative transformations based on the filtered parent TIC data, and the MS^E data for the individual species were manually inspected to verify accurate assignments. For the N-dealkylated species determined to be the major metabolite of each compound, authentic 4-arylsubstituted-123-TRZ/IMZ standards were synthesized and analyzed by MS^E to verify the assignments. Metabolite species were quantified via integrated MS ion current peak area relative to the total MS peak area for all metabolites identified in the mixture.

4.2.8 Steady-state turnover kinetic analysis

Steady-state kinetic CYP3A4-mediated turnover analysis was conducted for all eight 1,5-diaryl-substituted azole compounds using an identical assay except that the azole concentration range was adjusted based on the affinity (K_s) measured during binding analysis. Assays were conducted in 96-well plate format using CYP3A4-containing Supersomes coexpressing P450 reductase and *Cytb5*. All reactions were previously determined to be linear in both time and enzyme concentration. Briefly, a protein solution containing 7.5 nM CYP3A4 (based on supplier's determined concentration of 1µM CYP3A4) in 100 mM KPi (pH = 7.4) was divided into 24 separate aliquots (12 analyte concentrations x 2 compounds) prior to addition of the appropriate concentration of 1,5-diaryl-substituted-123-TRZ/IMZ (assays ranged from 150 – 0 µM, 1.5 % CH_3OH v/v). Each 123-TRZ and IMZ analog pair was assayed simultaneously from the same protein solution. The substrate-containing mixes were then dispensed in quadruplicate 90 µL aliquots (3 turnover replicates and 1 minus NADPH control series). 10 µL H_2O were added to the minus NADPH control wells and the plate was subjected to pre-incubation at 37 ºC for 5 min. Reactions were initiated in staggered format by dispensing 10 µL of 10 mM NADPH and allowed to react for 3.5 minutes. The mixtures were quenched with two volumes of acetonitrile:acetic acid (16:1) containing 500 nM 1-benzyl-1,2,3-triazole as internal standard. The quenched plate was spun at 4000g for 5 minutes and the supernatant transferred to a fresh plate for LC-MS/MS analysis. Standard calibration curves were constructed daily from protein solutions containing the appropriate 4-arylsubstituted 123-TRZ/IMZ metabolite standard and were mixed and incubated identically to that of the reaction mixtures except that no NADPH was present.

Metabolite formed during the reactions was detected via injection of the quenched assay solutions onto an API4000 LC-MS/MS QTC (AB Sciex) tandem quadrupole spectrometer

operated in positive ESI mode, and connected to a Waters Acquity UPLC. Separation of the analytes was achieved on a Phenomenex C_{18} UPLC column (50 x 2.1 mm, 1.7 µm particle size). Data was acquired in multiple reaction monitoring mode (MRM) with optimal channel selection and instrument tuning for each species determined automatically in Analyst software. Standard curves were analyzed before and after LC-MS/MS analysis of each assay. Quantification of the metabolite concentration formed during the assay at each initial substrate concentration was achieved by comparison of relative (rel. to IS) MRM ion current to the standard calibration curve generated for each species. Standard calibration curves were constructed via linear regression of the MRM data with most fits weighted 1/x (x = [substrate]).

Plots of velocity/$[E_t]$ vs. [substrate] were fit via non-linear regression analysis in IGOR Pro. For all 1,5-diaryl-substituted-123-TRZs the data were fit to the Michaelis-Menten equation (equation 3) and the K_M and turnover number (k_{cat}) was determined directly from the fit. The kinetic data generated from incubation of 1,5-diaryl-substituted-IMZ substrates fit best to a two-site binding model (equation 4). Akaike information criterion was employed to determine that equation (4) was the better quality model in preference to the simpler kinetic model (equation (3)) to describe the apparent biphasic concentration dependence of the 1,5-diaryl-substituted-IMZ turnover velocity data.

(3) $V = (V_{max}*[S])/(K_M + [S])$

(4) $V = (V_{max1}*K_{M2}*[S]+V_{max2}*[S]^2)/(K_{M1}*K_{M2}+K_{M2}*[S]+[S]^2)$

4.2.9 Electron paramagnetic resonance (EPR)

As described in Chapter 2.2.4

4.2.10 Magnetic circular dichroism (MCD)

As described in Chapter 2.2.5

4.3 Results

4.3.1 Near infrared MCD characterization of the low-spin H_2O-bound resting state and 123-TRZ and IMZ fragment complexes of diverse CYPs

All CYPs are characterized as possessing b-type heme cofactor ligated at the proximal axial iron position by a conserved cysteine residue, normally maintained in the low-spin hexacoordinate ferric resting state via ligation of a water molecule to the axial 6th position (*4, 8, 9*). However, as was mentioned in the introduction, hemoproteins have the ability to tune the electronic properties of this common cofactor, which may play a role in type II binding depending on the interacting moiety. Prior to the initiation of our ligand binding study, we sought to demonstrate the resting state electronic differences amongst diverse CYPs via measurement of near infrared ligand-to-metal charge transfer transitions (nIR LMCT) by MCD (see Chapter 2.1.5). Shown in Figure 4.1 are the nIR MCD spectra obtained for ligand-free CYP3A4, CYP2C9 (d hepta mutant, see Chapter 2.2.2), and CYP51B1(*Mtb*) acquired at 4.7 K between 5-6 Tesla field. All three CT bands are in the range for thiolate-coordinated heme possessing an axial water molecule (~1000-1100 nm) and display relatively low intensity that is characteristic for CYPs (*105, 179, 180*). Interestingly, despite each protein containing an identical heme cofactor, the transition energies are rather widely distributed— + 27.2 kcal/mol (CYP3A4), + 26.4 kcal/mol (CYP2C9), and + 26.1 kcal/mol (CYP51B1). The energy of this

transition is directly related to the axial (Δ) and rhombic (V) crystal field terms (see Chapter 2.1.4) that characterize the energy separation of the low-spin iron(III) t_{2g} d-orbitals (Figure 2.4). These results suggest that distortions of the heme iron crystal field for ligand-free CYPs vary considerably despite identical ligand sets. It is tempting to speculate that this distortion relates to the lability of the Fe(III)-OH_2 bond in the low-spin resting state, such that those CYPs that display a relatively large LMCT energy contain a larger fraction of high-spin enzyme at equilibrium. Interestingly, CYP3A4 maintains as much as 15% high-spin enzyme in purified form (*28*) and has the largest LMCT energy measured for any CYP by MCD. These results demonstrate the inherent variability in the electronic properties of heme cofactor depending on the CYP isoform, and this variability is anticipated to influence type II binding interactions considerably.

As a prelude to the comparative binding analysis of 123-TRZs and IMZs in CYP3A4 we next measured the nIR LMCT transition for the type II CYP3A4 complexes of 123-TRZ and IMZ fragments at 4.7 K and 5-6 Tesla field (Figure 4.2). Both complexes exhibit marked redshifts of this spectral feature relative to the ligand-free state, highlighting the sensitivity of nIR of this electronic transition to axial ligand identity in CYPs. The LMCT feature for IMZ complex lies at 1120 nm corresponding to a transition energy of + 25.5 kcal/mol, while the 123-TRZ complex lies at 1150 nm corresponding to an energy of + 24.9 kcal/mol. The LMCT energy discrepancy (0.6 kcal/mol) between the two low-spin fragment complexes highlights the differential distortion of the heme iron octahedral field induced by these two chemically-disparate azoles. Additionally, the decreased relative nIR LMCT intensity of 123-TRZ complex may suggest a larger degree of rhombic strain exists for the heme octahedral field in the presence of 123-TRZ (*181*). These observations place into context the disparate binding and turnover

behavior observed during the following comparative binding analysis of 123-TRZ and IMZ analogs in CYP3A4 and CYP19.

4.3.2 Steric requirements for heme ligation of di-substituted 1,2,3-triazoles

123-TRZs are unrepresented within the azole inhibitor drug classes, so the steric requirements for heme ligation in CYPs were first defined. Several 1,4-diaryl-substituted 123-TRZs sharing a common 2,4-dichlorobenzyl substituent at the 1-position of the azole moiety (Figure 4.3) were synthesized via Cu(I)-catalyzed azide-alkyne cycloaddition chemistry (click chemistry) and screened for binding to CYP3A4 by UV/vis absorbance titration. All compounds induced a type I spectral response, suggesting that ligand binding displaces axial H_2O to form a high-spin, pentacoordinate heme iron configuration. Low compound solubility precluded accurate measurement of the affinity for all but one compound, 1-(2,4-dichlorobenzyl)-4-phenyl-1,2,3-triazole, for which a $K_s = 16 \pm 3\mu M$ was determined. 123-TRZ fragment (1H-1,2,3-triazole) was previously shown to directly ligate heme iron in CYP3A4 (Chapter 3.3.5) so it was hypothesized that the 1,4-diaryl substitution profile precludes access of 123-TRZ nitrogen to heme iron. Therefore, 1-(2,4-dichlorobenzyl)-5-phenyl-1,2,3-triazole (123-60) was synthesized using ruthenium-based catalyst (see Chapter 4.2.3) to direct exclusive formation of the 1,5-regioisomer. Binding of 123-60 to CYP3A4 elicited a type II spectral response (Figure 4.4), supporting the hypothesis that the 1,4-diaryl substitution pattern causes steric hindrance at the level of the heme iron.

4.3.3 Comparative binding analysis of an isosteric azole analog library: binding energetics and spectral behavior in CYP3A4 and CYP19 (aromatase).

Eight 1,5-diaryl-substituted azole-based compounds shown in Figure 4.5 were synthesized for study of CYP binding and spectral behavior in detail. Four of these compounds contain the weakly basic (pKa = 1.19) 123-TRZ moiety, and the other four compounds are identically substituted but contain relatively basic (pKa = 6.99) IMZ. The focus on analog pairs was aimed to investigate how energetically disparate azole-heme interactions might influence overall compound behavior in the context of a conserved 'drug-like' scaffolding. Two diverse CYP isoforms were selected for use as binding models: CYP3A4, a paradigmatic substrate-promiscuous drug metabolizing CYP, implicated as the source of several adverse drug-drug interactions involving azole drugs (*174*); and CYP19 (human aromatase), a known drug target thought to possess more selective ligand binding requirements based on structural evidence (*182*) and the enzyme's highly specified role of endogenous estrogen production in women (*11*). The binding affinity and spectral behavior observed for 123-TRZ and IMZ fragments (Chapter 3.3.2) were used as comparative benchmarks in order to rationalize the results (vide infra).

Ligand binding to CYP3A4 was monitored by UV/vis heme absorbance difference titrations, and the tabulated affinity (K_s) and B_{max} parameters recovered from non-linear regression analysis of the calculated binding isotherms (see Chapter 4.2.4) for the eight compounds are shown in Table 4.1. Also tabulated are the defining spectral characteristics for each compound at enzyme saturation, including peak & trough wavelength, the associated amplitude of the difference spectrum, and the final location of the Soret band in the absorbance spectrum. The difference in binding free energy for each 123-TRZ/IMZ pair was calculated ($\Delta\Delta G^{\circ}_{binding} = RT\ln(K_{s,IMZ}/K_{s,123\text{-}TRZ})$) to quantify the energetic effect of modulating the heme

binding component of a given CYP-ligand interaction to the overall Gibb's free energy ($\Delta G^{\circ}_{binding}$) of binding the enzyme. The quantity $\Delta\Delta G^{\circ}_{binding}$ obtained previously for the comparison of 123-TRZ and IMZ fragments binding CYP3A4 (see Chapter 3.3.2) was used to interpret the results because this value is assumed to represent a steric-free heme interaction for the respective azole moieties, i.e. it is assumed to be free of significant contributions by secondary contacts with active site residues due to the fragment's small size relative to the total CYP active site volume, and assuming that the solvation of the active site is similar in the presence of IMZ vs.123-TRZ. In addition, $\Delta\Delta E_{DFT}$ values determined previously for 123-TRZ and IMZ fragments on the basis of density functional theoretical (DFT) calculation (see Chapter 3.3.1), were used as a secondary reference.

Key observations from binding analysis in CYP3A4 are as follows: First, in every instance, changing 123-TRZ to IMZ while maintaining an identical substitution profile results in a large affinity gain (16 - 42 fold), despite both compounds yielding type II binding spectra (Figure 4.6) with direct nitrogen ligation (vide infra). This suggests that intrinsic heme binding affinity for the azoles studied here represents a significant fraction of total $\Delta G^{\circ}_{binding}$ in CYP3A4. However, for all but the 123-60/IMZ-60 comparison (Table 4.1), $\Delta\Delta G^{\circ}_{binding}$ values are significantly less than that anticipated based on the two energetic benchmarks, $\Delta\Delta G^{\circ}_{binding}$ and $\Delta\Delta E_{DFT}$ values determined for azole fragment binding. This energetic discrepancy suggests heme interactions are compromised, either by competing favorable interactions between the protein residue architecture and ligand periphery that disrupt a conserved heme ligation structure between analogs, or steric clashes that disrupt optimal positioning of the molecule for coordinate bonding to iron, both of which would decrease the expression of the full $\Delta\Delta G^{\circ}_{binding}$ for the fragments. Interestingly, this proposal is supported by the comparison of the steric parameter

molar volume (V_m) calculated for each variable substituent R-group: only in the case of 123-60/IMZ-60, which are the smallest compounds, sterically, does the $\Delta\Delta G^{\circ}_{binding}$ approach that of 'ideality,' and this could be due to increased access to the heme iron afforded by the less cumbersome substitution profile. Second, there exists a much larger degree of spectral variability between members of the 123-TRZ compound series, particularly in the location of the trough minima in the difference spectra, and in the magnitude of redshift induced in the Soret band of the parent absorbance spectra. This behavior is clearly evident in Figure 4.7, which shows saturated difference spectral overlays for each series. Spectral trough behavior (shape & minimum; type IIa (*19*)) has been used in the past as an indicator of the efficiency with which binding of a given type II compound shifts the resting state heme iron spin equilibrium toward low-spin, and may have implications for enzyme catalysis (vide infra). Lastly, there exists 5-fold greater variance in the peak-trough spectral amplitude at enzyme saturation for 123-TRZs compared to their IMZ analogs.

The binding screen was also conducted with CYP19 (human aromatase) monomerized in monodisperse discoidal lipoprotein particles, or nanodisc, and the affinity results and relevant spectral parameters are tabulated in Table 4.2. Some key observations are as follows: First, all eight compounds bind this drug target CYP with nanomolar affinity, suggesting that the generic azole 1,5-diaryl substitution profile employed here does indeed represent a drug-like azole scaffold for CYP19. Furthermore, the high affinity observed for molecules containing the novel 123-TRZ moiety (novel with respect to marketed azole drugs) suggests it too holds potential as an attractive candidate azole for the development of aromatase inhibitors despite its relatively low intrinsic heme affinity observed for other CYPs such as CYP3A4 and CYP2C9 (see Chapter 3.3.2) compared with more basic isosteres such as IMZ and 124-triazole. Second, as observed for

CYP3A4 binding, type II analogs 123-60/IMZ-60 displayed the largest $\Delta\Delta G^{\circ}_{binding}$ between analogs in the series: -0.80 kcal/mol represents a ~ 4-fold increase in affinity upon switching from 123-TRZ to IMZ. However, for the other three 123-TRZ/IMZ analog pairs, the affinity gains were minimal or non-existent (e.g. 123-67/IMZ-67 $\Delta\Delta G^{\circ}_{binding} = +0.67$ kcal/mol). These results might reflect the more stringent steric requirements (*182*) for access to heme iron in CYP19, consistent with the high substrate specificity of the isoform, and the much smaller active site cavity volume (~400 $Å^3$ vs. 530 $Å^3$ for CYP19 and CYP3A4 respectively). Additional evidence for non-heme contacts being significant for di-substituted azole ligands of CYP19 comes from the observation that 123-65 actually yields a type I response, yet upon change to IMZ-65 a dramatic conversion of the spectrum to type II is observed (Figure 4.8). This does not occur with CYP3A4 where 123-65 elicits a type II spectrum, or reverse type I. The interactions between ligand periphery and enzyme scaffold make a greater contribution for the 123-TRZ compared to the IMZ for CYP19 as a result of the smaller active site. Intriguingly, despite the fact that 123-65 does not appear to participate in coordinate bonding with heme iron, the type II conversion for IMZ-65 binding is met with negligible affinity increase. Lastly, it is noted that type II binding 123-TRZs induce a much lower peak trough spectral amplitude than the IMZ analogs, which appears to be the result of lesser ability to redshift the Soret band than was observed binding CYP3A4, possibly reflecting a strained coordinate bonding arrangement in this isoform.

4.3.4 Metabolic stability and metabolite identification: CYP3A4-mediated catalysis

The susceptibility of 123-TRZ/IMZ analogs to CYP3A4-mediated oxidative turnover was assessed by substrate depletion assay in Supersomes™ expressed with cytochrome P450 reductase and cytochrome b5. Depletion of 1 μM azole in the presence of 50 nM (50 pmol / 1 mL incubation) CYP3A4 was monitored by LC-MS peak area ratios over the course of 20 minutes. Significant depletion was observed for all eight type II binding compounds. Apparent $t_{1/2}$ values were calculated from fits to a simple exponential decay function: from 3.5 – 11.6 min. Depletion behavior observed for all four IMZs (Figure 4.9) fit best to a linear decay model with slopes ranging from -0.035 to (-110) min^{-1} consistent with enzyme saturation for the duration of the assay due to the compounds' nanomolar affinity for CYP3A4.

A metabolomics approach based on high mass accuracy mass spectrometry was employed to compare the number and diversity of metabolites formed during turnover of the apparent type II binding 123-TRZ and IMZ analogs. Reactions were scaled up to produce the necessary quantity of metabolites for accurate detection. Control incubations were included that contained no NADPH or no CYP. The reaction mixtures were analyzed by high resolution UPLC qTOF mass spectrometry with data acquired in MS expression mode (MS^E, Synapt™) so that high mass accuracy data were obtained for both parent and associated fragments for all NADPH-dependent species. The raw total ion current (TIC) data were filtered based on mass defect using MetaboLynx software (MassLynx software suite), to facilitate identification of likely phase I metabolite species (Chapter 4.2.7), and the results are shown in Table 4.3. The MS data suggest differences with regards to the number and type of hydroxylated species formed for each 123-TRZ/IMZ analog pair, but that these pathways are minor based on MS peak area ratios relative to the total NADPH-dependent metabolite pool detected for each compound. In every incubation, a single NADPH-dependent metabolite dominated the TIC chromatogram based on MS peak area,

although the relative predominance of this species appeared to vary much more for the 123-TRZs (67 - 94 %) than the IMZs (84 - 90%). The m/z of the primary metabolites, as well as the MS^E fragment spectra of each, are consistent with an N-dealklyation reaction at the benzylic carbon of the 2,4-dichlorobenzyl substituent common to all azole library members. In order to verify this structural proposal, authentic 4-phenyl-imidazole and 4-phenyl-1H-1,2,3-triazole metabolite standards (Scheme 4.1) were obtained for the 123-60/IMZ-60 pair, and both retention times and MS^E spectra matched that of the primary metabolites. The remaining 4-aryl-substituted 123-TRZ and IMZ N-dealkylated standards were synthesized and verified as primary metabolites by MS in turn.

4.3.5 Azole-dependent atypical kinetics displayed by type II binding 1,5-diaryl-substituted azoles

CYP3A4-mediated turnover of all eight 123-TRZ and IMZ library members is dominated by a common N-dealkylation pathway. This fact afforded the unique opportunity to contrast how disparate heme binding energetics between type II binding 123-TRZ and IMZ analog pairs can manifest kinetically during steady-state turnover measures in CYP3A4. Moreover, the apparent facile metabolism for tight-binding IMZs was surprising, so a measure of catalytic velocity was of interest to rationalize this phenomenon mechanistically. A Supersomes™-based kinetic assay was developed that emphasized minimization of both time (3.5 min) and protein concentration (7.5 nM) to avoid substrate depletion and non-specific binding of the hydrophobic compounds, respectively. Formation of the N-dealkylated products was monitored by LC-MSMS, and reaction velocities quantified via calibration curves constructed from the synthesized metabolite standards. Simple hyperbolic kinetics were observed for all 123-TRZ library members. The

parameters K_M (Michaelis-Menten constant) and k_{cat} (turnover number) were recovered from non-linear regression analysis using the Michaelis-Menten equation, and are tabulated in Table 4.4. Some key observations for turnover of the 123-TRZs are as follows: Despite the fact that all four compounds yield an apparent type II binding response, each is an excellent CYP3A4 substrate, with turnover number (k_{cat}) ranging from 10.9 – 29.1 min^{-1}. These velocities are comparable to those observed for typical 'good' CYP3A4 substrates in vitro, most of which are known to yield a type I spectral response (*183*). This would imply that type II interactions between heme and 123-TRZ may be of minimal consequence with regard to enzyme inhibition. However, a good positive correlation ($R^2 = 0.991$, Figure 4.11) is observed between apparent type II binding affinity (K_s) determined spectrally, and the kinetic turnover number (k_{cat}), suggesting some degree of inverse relationship between 123-TRZ heme interaction efficiency and metabolic stability.

In dramatic contrast to the simple kinetic behavior displayed by the 123-TRZs, all four IMZ analogs displayed atypical kinetics characterized as biphasic. A two-site sequential binding model derived using the methods of King & Altman (*91*) described the data well based on Akaike information criterion (Chapter 4.2.4). Figure 4.10 compares the kinetic plots obtained for each analog pair including the best fit. The recovered parameters (K_{M1}, K_{M2}, k_{cat1}, k_{cat2}) are given in Table 4.5. The results suggest the IMZs bind with both a high affinity, low reaction velocity component, and a low affinity, high reaction velocity component. Interestingly, there was no evidence of multiple binding during UV/vis spectral difference analysis, and this suggests that the second IMZ equivalent binds without perturbing the heme spin state. This phenomenon has been observed for several CYP3A4 substrates (*26, 28, 118*) and highlights the tenuous nature of reliance upon spin state change to accurately report ligand binding. A good correlation was

observed only between K_s and k_{cat1} ($R^2 = 0.893$, Figure 4.11), supporting the notion that the second equivalent indeed binds silently with respect to the spin state equilibrium but not with respect to the catalytic properties. Additionally, a moderate correlation (Figure 4.11) was observed ($R^2 = 0.71$) between spectral parameter B_{max}, which is dependent upon the magnitude of both Soret redshift and relative decrease in high-spin enzyme fraction during binding, and k_{cat1}. This relationship suggests variability in type II heme-binding efficiency exists between these tight-binding IMZs, and has an effect upon the ability of the ligand to abolish CYP catalytic function.

4.3.6 Detection of type II binding magnetic heterogeneity for high CYP3A4 affinity IMZs by EPR and correlation of crystal field parameters with enzyme function

All eight analog library members were susceptible to facile turnover by CYP3A4, so the library was subjected to EPR analysis to characterize the structural nature of the low-spin complexes, initially to verify whether all were directly ligating to the heme iron. The behavior of the g-value shifts for all eight compounds were consistent with type II binding (g_z increase/g_x decrease with broadening; g_y increase) (*119*). Thus, in stark contrast with the mono-substituted 123-TRZs discussed in Chapters 2 & 3 that prefer indirect heme binding modes, the di-substituted molecular scaffold used here appears to favor direct ligation of the 123-TRZ moiety to the heme iron.

Because IMZs are commonly found in CYP-targeted inhibitor drugs, we analyzed the nature of the spectra acquired for the IMZ structural analogs in greater detail. Figure 4.12 shows the EPR spectra acquired at 77 K for the IMZ analogs in complex with CYP3A4, including best

fits obtained in Easyspin (Chapter 2.2.4). Interestingly, all four complexes exists as heterogeneous mixtures of at least two distinct magnetically non-equivalent low-spin species present at enzyme saturation, evidenced by irregularly broadened spectral features consistent with multiple, unresolved species. With the aid of least squares regression analysis, unique g-values were recovered for the various species, which also allowed for calculation of the axial, Δ/λ, and rhombic, V/λ, crystal field parameters (see Chapters 2.1.4 & 2.2.4), and these results are tabulated in Table 4.7. Some key observations are as follows: First, despite very similar optical signatures for each IMZ analog as measured by UV/vis absorbance, the marked structural heterogeneity observed in the EPR spectra is not conserved across IMZs, as is reflected in the wide range of g-values. Thus, the EPR spectra suggests structural variability exists at the level of the heme even for tight-binding IMZs that are anticipated to interact efficiently with the iron. Only a single nitrogen atom of IMZ is available for coordination to iron in this particular substitution profile, so it is possible that the heterogeneity detected represents a distribution of coordinate bonding lengths, and/or angles relative to the heme iron and/or proximal thiolate ligand (*184*). Alternatively, the spectral heterogeneity could represent differential perturbations of heme field resulting from non-equivalent heme-protein conformations existing throughout the sample while saturated with IMZ ligand. The potential existence of multiple conformers of CYP3A4 that are present in slow equilibrium, has been suggested by others to rationalize atypical kinetic behavior (*185*). Next, a moderate correlation ($R^2 = 0.66$) was observed (Figure 4.13) between the axial crystal field parameter (Δ/λ) for the individual species detected by EPR and the turnover number (k_{cat1}) measured for the first component during steady-state turnover kinetic measurements. A correlation between these two parameters suggests that a larger axial distortion of the heme iron crystal field—reflecting an increase in charge density about the heme

Fe(III) in CYP3A4—by a directly N-ligated type II binding IMZ species renders it less susceptible to metabolism. Finally, a correlation was observed between the axial crystal field parameter and the spectral B_{max}, highlighting a similar dependence of both parameters upon axial ligand field strength.

4.3.7 CYP3A4-(IMZ) binding heterogeneity detected by MCD

Further insight into the differential type II binding behavior exhibited by structurally analogous IMZs came from detailed optical analysis by magnetic circular dichroism (MCD). MCD spectroscopy provides additional information about the heme field compared with conventional absorbance spectroscopy. This is because MCD is a signed quantity (both positive and negative optical transitions) based on differential absorption of left and right circularly polarized light by a chromophore placed within a longitudinally aligned magnetic field (see Chapter 2.1.5). The technique was applied here to scrutinize the absorbance spectra more rigorously to detect signs of the structural heterogeneity that was observed by EPR but was not obvious in the conventional absorbance spectra of the CYP3A4-IMZ complexes. In addition, MCD allowed near infrared ligand-to-metal charge transfer transitions (nIR LMCT) associated exclusively with low-spin enzyme (*137*) to be readily detected. The MCD approach was complemented by comparison of the diaryl-substituted IMZ MCD spectra with the spectroscopic signature of the IMZ fragment reference CYP3A4 complex to facilitate detection of deviations from ‘ideal’ type II binding structure. As was highlighted in chapter two, this is the first known MCD study of a mammalian drug-metabolizing CYP, and so the data serve as an important reference for the interaction of CYP3A4 with type II binding azole species.

Figures 4.14-.15 presents the UV/vis MCD spectrum collected at 5 Tesla magnetic field for ligand-free CYP3A4 at 298K and 4.7K, respectively, as well as the corresponding absorbance spectrum at 298K for comparison. The MCD data presented in Figures 4.16-.17 for the CYP3A4-azole complexes were acquired at liquid helium temperature (4.7K) between 5-6 Tesla in order to provide a substantial sensitivity enhancement to the transitions unique to the low-spin enzyme fraction in the visible spectrum between 495-750 nm, and was necessary to detect the weak intensity nIR CT transitions. Visible MCD spectra (Figue 4.16) of CYP3A4 in complex with 123-TRZ fragment are given for comparison to the corresponding IMZ fragment complex to highlight the unique spectral features displayed by energetically disparate type II-binding moieties. Also given in Figure 4.16 are MCD data acquired for the highest affinity, least metabolically labile IMZ in the series, IMZ-64, as well as the lowest affinity, most metabolically labile structural analog, IMZ-65. Key spectral observations in the visible MCD spectra are as follows: First, it is immediately evident by comparison with the absorbance spectrum in this region that the MCD spectra are relatively complex; the spectral region between 495-750nm is known to contain several overlapping electronic transitions, many that are unique to either the low-spin or high-spin heme states (*123*), although at liquid helium temperatures a significant sensitivity enhancement is provided the low-spin species (*106*) that can obscure detection of high-spin transitions. The spectral complexity in this region has been ascribed to the presence of several overlapping ligand-to-metal charge transfer (LMCT) bands with various degrees of xy and/or z molecular orbital polarization as defined by the coordinate axis imposed upon the heme cofactor with the axial ligands defining z. It is not surprising then that both the energy and the intensity of these bands appear to be dramatically affected by type II ligand binding. The heterogeneity of the spectra in the region 640 - 690 nm is magnified as an inset to Figure 4.16,

and is comprised of several thiolate(π)-to-iron(III) CT transitions that have varying degrees of z-polarization, (*123, 124*). Second, pronounced differences in the MCD spectral behavior of IMZ and 123-TRZ fragment complexes are evident in the visible region, the most dramatic being that IMZ binding induces an apparent coalescence of the two peaks of positive intensity observed at 528 nm and 548 nm for ligand-free CYP3A4. Next, with regards to the substituted CYP-IMZ complexes, the visible MCD spectrum of CYP3A4-(IMZ-64) appears to mirror the spectrum of CYP3A4-(IMZ) complex more closely than CYP3A4-(IMZ-65) with regard to peak location and intensity. However, IMZ-64 displays a unique spectral feature at 580nm not clearly present in the spectra of IMZ-65 and IMZ complexes. In stark contrast, CYP3A4 complex of IMZ-65 exhibits a relatively low MCD spectral amplitude for several features common to IMZ-64 and IMZ complexes. Thus, MCD can detect structural differences between these two complexes optically (consistent with their markedly dissimilar EPR spectra) despite each type II ligand possessing an identical imidazole moiety. It is tempting to suggest that the more facile CYP3A4-mediated turnover of IMZ-65 (k_{cat1} = 1.39 min^{-1}) relative to IMZ-64 (k_{cat1} = 0.36 min^{-1}) is related to the apparent type II 'strain' observed both optically and by EPR (compare range of V/Δ, Table 4.7) for the former ligand. This assessment is consistent with the calculated values of the axial distortion parameters (Δ/λ) determined for each species by EPR that demonstrated a larger axial crystal field effect for IMZ-64 binding (Table 4.7) that could be related to the efficiency of type II ligation for these structural analogs. Table 4.8 compiles the peak and trough wavelengths and their associated intensities, as well as crossover points in the spectrum.

Additional structural information that highlights differences between IMZ-64 and IMZ-65 comes from examination of their respective nIR MCD spectra (Figure 4.17). The nIR LMCT band of IMZ-65 is redshifted by 10 nm to 1130nm, and has an altered lineshape with low

intensity relative to IMZ and IMZ-64. This observation also corroborates the EPR measurements by demonstrating the two type II ligands differentially affect the heme iron crystal field in complex with CYP3A4, a fact demonstrated via calculated axial (Δ/λ) and rhombic (V/λ) crystal field parameters. In contrast, IMZ-64 exhibits high fidelity to the IMZ spectrum with respect to peak maxima, lineshape, and intensity. Finally, it is notable how well the reference fragment nIR spectrum and the nIR spectrum from a 'good' type II compound (IMZ-64) in this series agree—this lends credence to the approach and suggests that minimal electronic changes occur upon substitution of IMZ with the aryl substituents used here, so the heterogeneity observed by EPR for the IMZ analogs (and type II 'strain' by MCD) is due to geometric and/or steric induced strain rather than electronic differences of the IMZ moiety induced by substituent effects.

4.4 Discussion

A comprehensive understanding of azole-heme interactions in CYP is of significant import to the fields of drug discovery, pharmacokinetics and drug metabolism, and to human health, in general. Historically, biophysical studies of CYP-ligand interactions have categorized compounds on the basis of heme optical spectral perturbations observed during equilibrium binding analysis. Specifically, a CYP ligand will generally be classified as either a potential substrate or an inhibitor based on rather generic optical criteria, i.e. whether binding induces a 'type I' or 'type II' spectral response, respectively. These core assumptions are largely based on the early CYP research done with the bacterial isoform CYP101 (P450cam), an enzyme displaying regulated catalytic activity that is highly coupled to binding-induced modulation of spin state and redox potential (*16*). However, it has been recently suggested that our

understanding of type II binding interactions is inadequate, and the recent literature is rife with examples of facile turnover of high affinity apparent type II compounds, including some that appear to impart a thermodynamic barrier to enzyme reduction by lowering heme redox potential (*7, 139*). This suggestion is clearly supported by the example of tight-binding type II thiazole inhibitor ritonavir. Ritonavir is known to bind with low nanomolar affinity to its target CYP3A4 and favor a low redox potential of the heme (*172*), yet ritonavir is readily metabolized by the same isoform (*186*). Furthermore, this drug is oxidized at the very same azole moiety that coordinate bonds so efficiently to the enzyme's catalytic center, a phenomenon difficult to explain mechanistically (*186, 187*). A goal of this study was to shed light on how energetically disparate azole-heme interactions in CYP might lead to differences in ligand binding and turnover behavior amongst structurally similar compounds. Importantly, an additional aim was to explore how a compilation of spectroscopic information could be utilized to detect and characterize type II structural complexity amongst high affinity, 'drug-like' ligands, such as the IMZs studied here, to show that the details of the low-spin enzyme fraction may be an important contributor to the catalytic properties of the enzyme. In essence, the results are meant to instill an appreciation of the *range* of type II interactions that must be considered for this important compound class, so that we can begin to understand the mechanisms of type II ligand turnover.

For our binding study, we chose to focus on structurally analogous 123-TRZ and IMZ-based compounds that harbor type II moieties that lie on energetically disparate ends of the CYP-azole binding spectrum. This decision was made so as to demonstrate how extremes in heme binding affinity translate to spectral behavior for structurally analogous molecules all classified as type II. Additionally, we were interested to learn whether affinity increases observed when replacing an energetically weak (123-TRZ) type II interaction with a strong (IMZ) one are

commensurate with attenuation of CYP catalytic activity, as would be expected based on traditional ligand classification criteria. A small molecule library was designed with the aim of conserving peripheral ligand contacts while selectively modulating the heme interaction component of binding, all within the context of a drug-like scaffold. 123-TRZs are unrepresented in the CYP-targeted azole drug classes, and it is assumed that the relatively low compound basicity (pK_a = 1.15) and/or nucleophilicity has hindered their elaboration for CYP-targeted therapeutics. However, 123-TRZ has become a common structural moiety in drugs for a variety of targets (*85, 86*), but their interactions with CYPs are largely unexplored. This is in stark contrast to the regioisomeric 1,2,4-triazole, a moiety ubiquitous in the azole drug class. Identically-substituted IMZ analogs were chosen for synthesis to show that even in cases where molecules hold the potential to interact strongly with the heme (IMZ pK_a = 6.99), the ligand-bound structure and turnover potential is not always predictable on the basis of classic optical criteria. Furthermore, the decision to contrast ligand binding in CYP3A4 and CYP19 (human aromatase) provided a platform to study representative off-target (CYP3A4) and on-target (CYP19) azole interactions. This enzymatic diversity expanded our azole interaction spectrum significantly.

Differential binding free energy ($\Delta\Delta G^{\circ}_{binding}$) between 123-TRZ/IMZ analog pairs was our initial metric of detection to identify potentially strained type II binding interactions in CYP3A4 and CYP19. We chose as a comparative benchmark $\Delta\Delta G^{\circ}_{binding}$ = -2.8 kcal/mol, measured for sterically-unhindered, directly-ligating (type II) fragments 123-TRZ and IMZ in CYP3A4. Significant deviations of $\Delta\Delta G^{\circ}_{binding}$ from our benchmark 'ideal' type II binding value were measured for each 123-TRZ/IMZ analog pair when binding either CYP3A4 or CYP19. Structure-dependent deviations from the ideal $\Delta\Delta G^{\circ}_{binding}$ for each 123-TRZ/IMZ pair likely

result from protein-ligand interactions remote from the azole ring, that make the local heme interactions relatively less important. Sterics also appear to play a role based on the observation of type I binding for 123-65 in CYP19, as well as the fact that the molar volume calculated for each variable substituent appeared to partially explain the closer agreement of $\Delta\Delta G^{\circ}_{binding}$ for the 123-60/IMZ-60 pair relative to the fragments in CYP3A4. Based on this assessment, analogs 123-60/IMZ-60 are expected, then, to have the greatest amount of structural similarity in complex with CYP3A4 (*19, 40*). Alternatively, this variability may simply represent differential coupling free energy between the two azole moieties and conserved peripheral contacts within the protein active site. It must be noted that our benchmark $\Delta\Delta G^{\circ}_{binding}$ value was measured for CYP3A4 binding, and there is the possibility that intrinsic heme affinity of the two azoles are significantly different in CYP19, a phenomenon that would not be accounted for by our alternate metric of heme interaction efficiency, $\Delta\Delta E_{DFT}$, that was calculated in the gas phase in the absence of protein influence. Importantly, in Chapter 2 we documented a much lower intrinsic affinity for 123-TRZ fragment binding CYP51B1 (*Mtb*) than for CYP2C9 binding, demonstrating that heme interactions in the absence of sterics in one CYP isoform can deviate significantly in another. Thus, the generally lower absolute $\Delta\Delta G^{\circ}_{binding}$ values measured for the di-substituted library analogs binding CYP19 may reflect a non-conserved energetic discrepancy between two azole species, but that seems unlikely. It is clear, based on the fact that affinity differences between analog pairs are much lower than what was observed in CYP3A4, that azole-heme interactions contribute less to overall binding free energy for this diaryl substitution profile in CYP19. Furthermore, the measured high affinity for type I compound 123-65 that changed only slightly upon introduction of a type II interaction in IMZ-65 suggests a combination of greater steric requirements and lower intrinsic heme affinity may be operating for

binding of these azoles to CYP19. Regardless, the high binding affinity for CYP19 of all eight compounds studied here supports our choice of diaryl substitution as representative of a drug-like azole scaffold. Lastly, it must be stated that while comparisons of CYP binding affinity across similar molecular entities can be informative based on the lines of reasoning presented, optical measures are entirely dependent on binding-induced spin shift as an accurate reporter of ligand occupancy.

The CYP3A4 binding spectra themselves appear to be quite informative with regard to the relatively low type II binding energetics displayed by 123-TRZs relative to the tight-binding IMZs. In general, the 123-TRZs studied here displayed larger variability in their respective absorbance fingerprints. Specifically, the 123-TRZs appeared highly variable in their ability to induce a spin shift (based on decrease in absorbance at ~388 nm, Table 4.1), and to redshift the heme Soret. Additionally, the Soret band of each complex at saturation exhibited variable molar extinction (data not shown), in contrast to the IMZs at saturation, which appeared more consistent. This variability is perhaps best represented in the overlaid difference spectra obtained for the saturated CYP3A4 complexes and shown in Figure 4.7. Thus, using conventional absorbance measures as a guide, the larger variability observed in the absorbance spectral fingerprint for the 123-TRZs suggests a relatively larger degree of bound state structural heterogeneity exists, and is probably related to the more tentative nature of the coordinate bond formed with the heme iron compared to that with high affinity IMZs. Interestingly, MCD was able to resolve a degree of spectral variability between IMZ-64 and IMZ-65 not readily detected by optical absorbance analysis of the CYP3A4 complexes. Although IMZ-65 did display a moderately lower absorbance spectral amplitude compared with the other IMZ structural analogs, this discrepancy was magnified by MCD, where variability in several spectral features

in the visible MCD spectrum compared with IMZ indicate type II 'strain,' possibly indicative of a bound state structure where the Fe(III)-N bond is not optimized. Near infrared MCD spectra of this complex appeared to confirm this speculation, as the LMCT feature suffered from low spectral amplitude and a modest redshift, which indicates an altered heme iron crystal field compared with IMZ-64 and the IMZ reference complex (*137*). Lastly, there did appear to be more variability in the optical difference spectra obtained for CYP19-IMZ complexes (Table 4.3), which could be related to the low values of $\Delta\Delta G^{\circ}_{binding}$ measured across the library for this isoform as compared with their 123-TRZ analogs.

EPR analysis of the IMZs proved to be a much more sensitive measure of structural heterogeneity at the level of the heme iron than conventional absorbance. All four diaryl-substituted IMZs in complex with CYP3A4 exhibit marked structural heterogeneity in their respective EPR spectra. The individual species were distinguishable on the basis of curve fitting, and the spread of g-values exhibited by the compounds was surprising, given that all contain an identical IMZ and showed no obvious sign of 'incomplete' heme coordination (*40*) based on their absorbance spectral behavior and high affinity (K_s) binding. Heterogeneity observed by EPR for azole-bound CYP complexes could be the result of protein conformational heterogeneity, either due to multiple conformers in solution that are in slow-equilibrium, or result from rapid freezing of the EPR sample. Alternatively, the heterogeneity may indicate a distribution of multiple IMZ ligation states, having variable coordinate bond lengths and/or angles relative to the heme and proximal cysteinate ligand. We favor the latter hypothesis due to the negative correlation that we observe between calculated axial crystal field parameter (Δ/λ) and turnover number (k_{cat1}), where it is assumed that the axial distortion parameter relates to the efficiency with which the heme is held by the ligand in a metabolically stable low-spin state.

Thus, all imidazole ligands are not identical in the way they interact with the heme. Two assumptions that are inherent in our interpretation must be stated: one is that k_{cat1} is an accurate functional reporter on the 'spectrally-audible' heme binding site that is solely responsible for the absorbance changes measured during binding; and second, that the EPR spectra at saturation report exclusively on the binding site nearest heme iron, which we equate with this same spectrally-audible binding site. Intriguingly, whereas historically the ratio of [High-Spin CYP]/[Low-Spin CYP] has been used as a gauge of expected catalytic rates, the details of the low-spin species have not been examined in the context of functional behavior, because the low-spin form has been considered to be inactive. These data further refine the contribution of the low-spin complexes to catalytic behavior by demonstrating heterogeneity across a series of *substrates* with an identical heme-ligating moiety.

The results of turnover analysis were quite revealing and highlight the interesting ways in which type II binding heterogeneity can manifest in the catalytic properties of CYPs. While facile CYP3A4-mediated oxidative turnover of all eight compounds was observed, the 123-TRZ series are more labile. This might be explained by their relatively larger degree of type II structural heterogeneity that can be inferred from the large differences of optical signatures across the CYP3A4-(123-TRZ) complexes. Specifically, the large variability in apparent spin shift for these complexes (Table 4.1) could indicate a significant amount of penta-coordinate heme complex exists at saturation, but to variable extents amongst the complexes. Additionally, the variability observed for the energy of the heme Soret could indicate compromised coordinate bonding interactions with the iron that lead to several non-equivalent intermediate ligated states. Thus, it is not clear whether the faster metabolism of the 123-TRZs is due to a direct reduction mechanism involving a strained hexacoordinate complex, or whether a rapid bound-state

equilibrium mechanism involving turnover of an active pentacoordinate high-spin fraction in the presence of a predominant hexacoordinate dead-end complex occurs—both of these mechanisms have been examined in detail by Jones et al. (*139*). Furthermore, although the IMZs were also demonstrated to exist as heterogeneous mixtures at the level of the heme, the fact that magnetic resonance was required to resolve these subtleties of structure suggest a more disparate range of bound-state structures exists for the 123-TRZs analogs.

Perhaps the most surprising differences between the analog series comes from the steady-state turnover analysis. CYP3A4-mediated turnover of all of the 123-TRZs obey typical Michaelis-Menten type kinetics, yet remarkably with a change of only a single atom to yield IMZ analogs, the reactions become unequivocally biphasic, which suggests multiple binding. This was unexpected, as there is no evidence for multiple binding when monitored spectroscopically, and suggests that a second, low affinity, equivalent of diaryl-substituted IMZ binds without perturbing the heme spin state. It is proposed that multiple binding observed only for the IMZ library members can be rationalized on the basis of the structural heterogeneity observed optically for the 123-TRZs and discussed above. It is possible that 123-TRZs are more 'active' in the bound state, exhibiting a larger degree of translation and rotation in the bound state relative to the IMZ analogs, and thus harbor a larger effective molar volume; alternatively, it is possible that the 123-TRZ moiety encourages retention of additional active site water molecules (as was demonstrated in Chapters 2 & 3) that exclude the additional binding equivalent observed in the IMZ complexes. In these respects, the more favorable heme binding energetics of IMZ-containing analogs appear to restrict the first bound molecule of azole in a relatively 'fixed', albeit heterogeneous, state during the CYP active site residence time of any single CYP-ligand binding event, which, in turn, allows for a second, non-heme binding

molecule to be accommodated. Interestingly, oxidative regiochemistry appears to be preferred at the same benzylic carbon across the whole library, suggesting some level of thermodynamic control during turnover that is not influenced significantly by differential binding stoichiometry or heme ligation energetics.

Although only two IMZ library members were studied by MCD, the spectral data essentially confirmed the EPR results in that marked heterogeneity appears to exist for tight-binding IMZs as well. The fidelity of both the visible and nIR spectral features for IMZ-64 compared with IMZ is impressive. This may suggest that IMZ-64 binding is relatively free of steric clash, or 'type II strain.' The agreement between IMZ-64 and IMZ reference fragment does not imply a lack of structural binding heterogeneity for the latter, but simply that the two species behave similarly at the level of the heme. In Chapter 2 we present EPR data for IMZ fragment bound to CYP2C9 that show at least two species present. Thus, even for the simplest azole fragments, heterogeneous heme interactions exist. The assessment of conserved CYP3A4 heme binding interactions between IMZ-64 and IMZ is supported by the high CYP3A4 affinity of IMZ-64, as well as its decreased susceptibility to CYP3A4-mediated turnover as compared with the other IMZ library members, and may suggest that the IMZ moiety is optimally placed for coordinate bonding. In contrast, the MCD spectra for IMZ-65 appear to deviate in several respects from the IMZ spectrum, which may represent suboptimal type II binding, and might explain the decreased affinity of this compound in the series, as well as its faster turnover velocity. The nIR MCD spectrum of IMZ-65 is quite revealing; the CT band is characterized by a ~ 10 nm redshift and dampened intensity relative to IMZ and IMZ-64. A redshifted nIR CT band relative to IMZ and IMZ-64 indicates a lower $3d_{yz}$ orbital hole energy (+ 0.22 kcal/mol) due to alteration of one or both axial (Δ) and rhombic (V) crystal field distortion parameters

experienced by the iron (III), while the nIR intensity is a function of V, as has been treated theoretically by others (*106, 137, 181*).

In this chapter, the importance of heme binding energetics to overall compound affinity, metabolic stability, and possibly, spectroscopic signature, have been demonstrated. Additionally, our data demonstrate facile metabolism of several type II binding compounds, including several high affinity drug-like IMZ-containing species, further highlighting the inadequacy of the traditionally rigid spectral classification paradigm for CYP-ligands. Importantly, it has been demonstrated using a variety of biophysical techniques that the spectroscopic details of the low-spin type II CYP-azole complex can provide a wealth of structural insight that may be potentially useful when rationalizing ligand affinity, as well as effects upon the catalytic function of the enzyme.

Figures

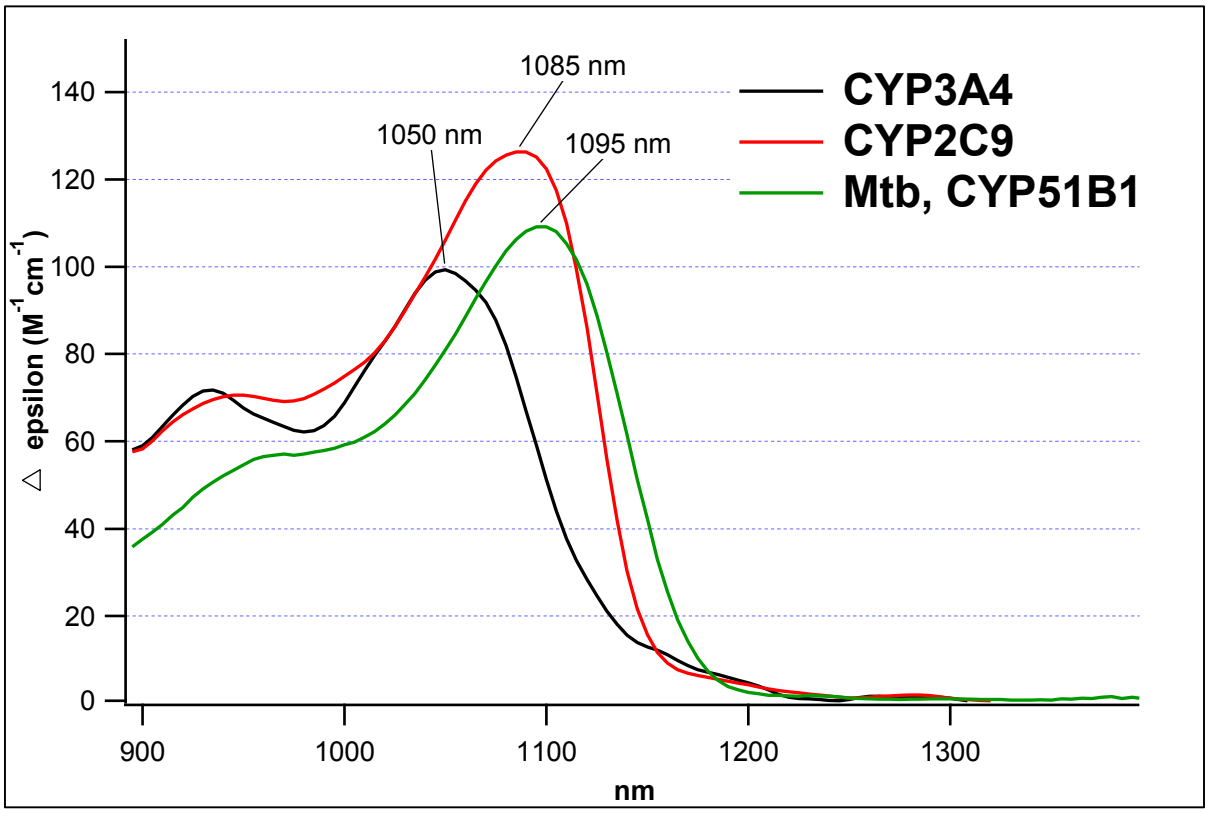

Figure 4.1 nIR MCD spectra of LMCT feature for ligand-free, low-spin CYPs acquired at 4.7 K between 5 - 6 Tesla field. Protein concentrations ranged from 400 – 770 μM and all samples contained 50 - 200 mM KPi (pH = 7.4 - 7.5) + 55 % d8 glycerol. The inherent electronic diversity of the common CYP heme cofactor amongst diverse isoforms is highlighted by the spread of (a_{1u} → d_{yz}, a_{2u} → d_{yz}) LMCT transition energies (range = 1.1 kcal/mol). These electronic differences are anticipated to influence the resting spin equilibrium, and effect the range of type II binding interactions that occur during binding of nitrogenous heterocycles.

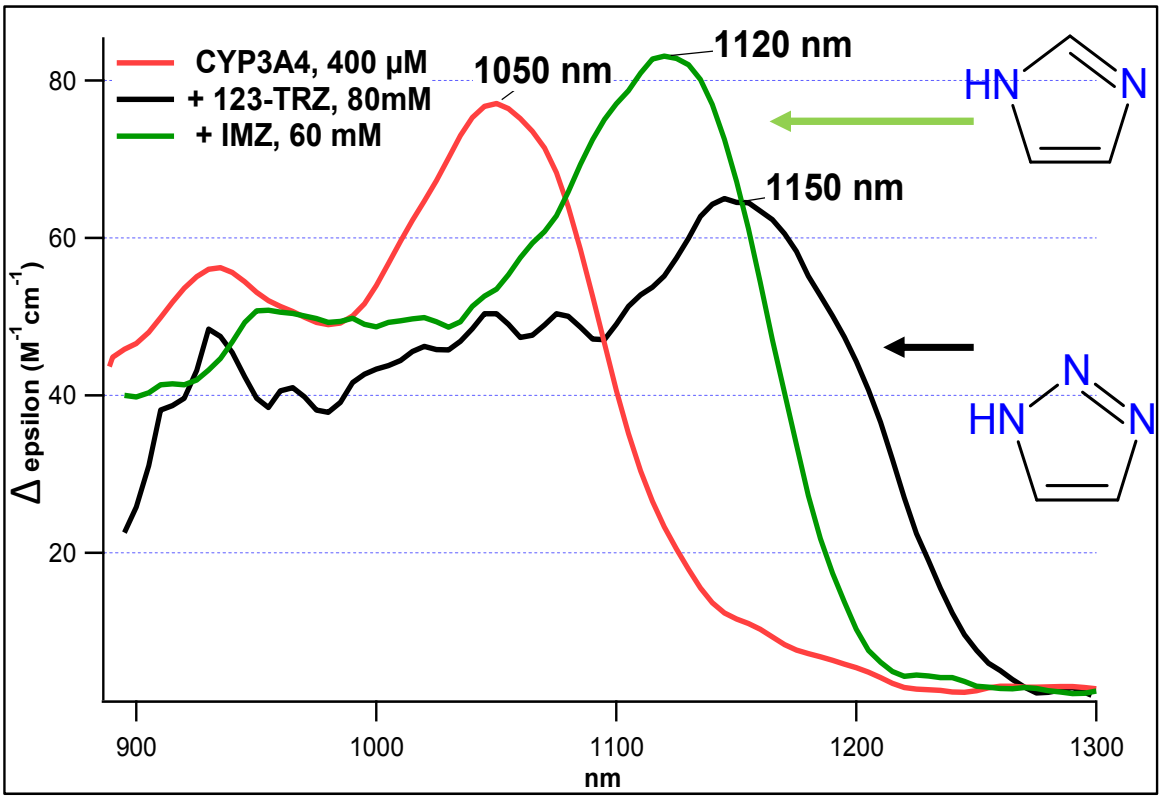

Figure 4.2 nIR MCD spectra obtained at 4.7 K for ligand-free CYP3A4 (red, 400 µM), and saturated with azole fragments 123-TRZ (black, 80 mM), and IMZ (green, 60 mM). Ligand-free and 123-TRZ-saturated spectra obtained at 5 Tesla field; the IMZ-saturated spectrum was obtained at 6 Tesla. The bands display typical broad positive intensities with variable fine structure evident in the shoulder to higher energy. This spectral transition represents two specific ligand-to-metal-charge transfer (LMCT) transitions ($a_{1u} \rightarrow d_{yz}$, $a_{2u} \rightarrow d_{yz}$) from the heme macrocycle HOMOs to the non-degenerate t_{2g} orbitals of low-spin, ferric iron. Note the large band separation for the peak of each species highlighting the utility of nIR MCD for identifying the heme axial ligand sets. The energy separation of this transition for the different azole complexes corresponds to 0.64 kcal/mol, and depends on both on axial (Δ/λ) and rhombic (V/λ) crystal field distortions induced in heme Fe(III) by binding azole ligand. The results suggest significant differences in how each azole fragment distorts the heme field, a phenomenon possibly rationalized by the more diffuse electronics of 123-TRZ (*129*) relative to IMZ, among other physicochemical factors, and suggests the relative strength of azole-heme interactions is more complex than simple basicity/nucleophilicity arguments.

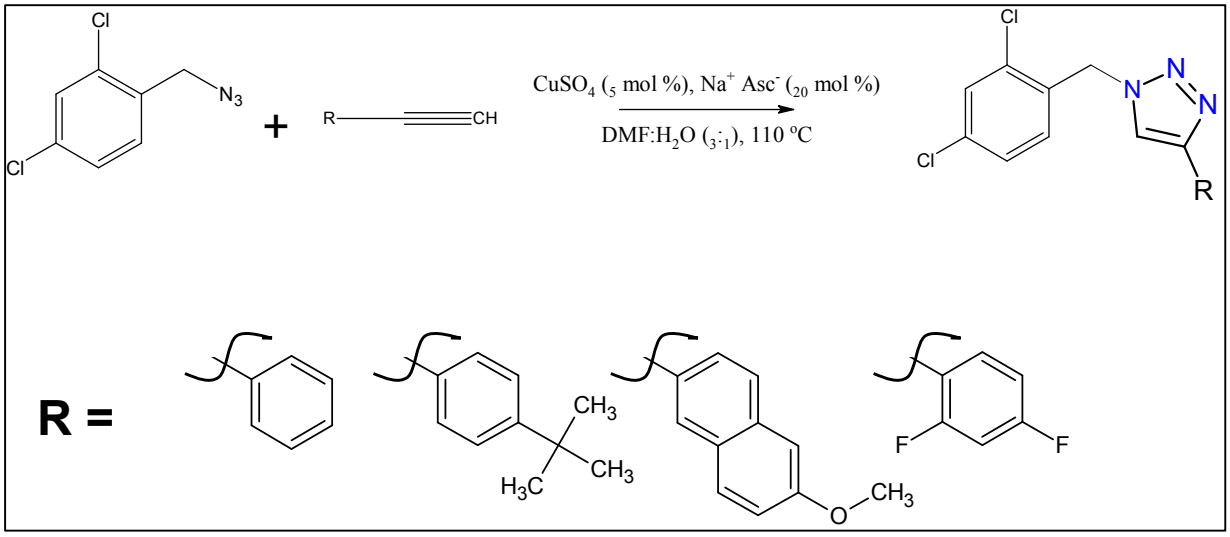

Figure 4.3 1,4-diaryl-substituted 1,2,3-triazoles synthesized and screened for CYP3A4 binding analysis.

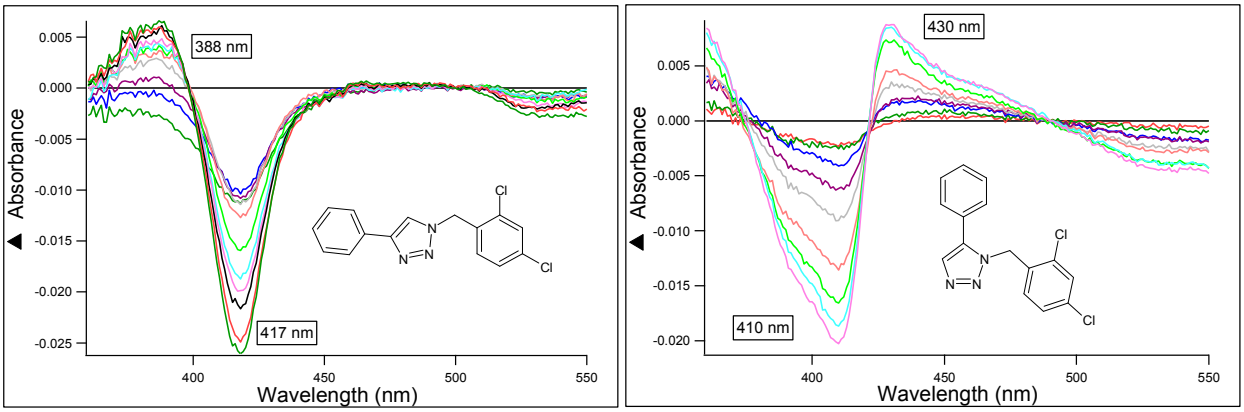

Figure 4.4 Steric requirements for type II binding of diaryl-substituted 1,2,3-triazoles to CYP3A4. Representative CYP3A4 UV/vis absorbance difference spectra for 1,4 and 1,5-diaryl regioisomers that demonstrate type I to type II spectral conversion upon changing the diaryl substitution pattern of 1,2,3-triazole. The results suggest that only 1,5-disubstituted isomers are able to interact with heme iron by way of coordinate bonding due to steric constraints at the level of the heme.

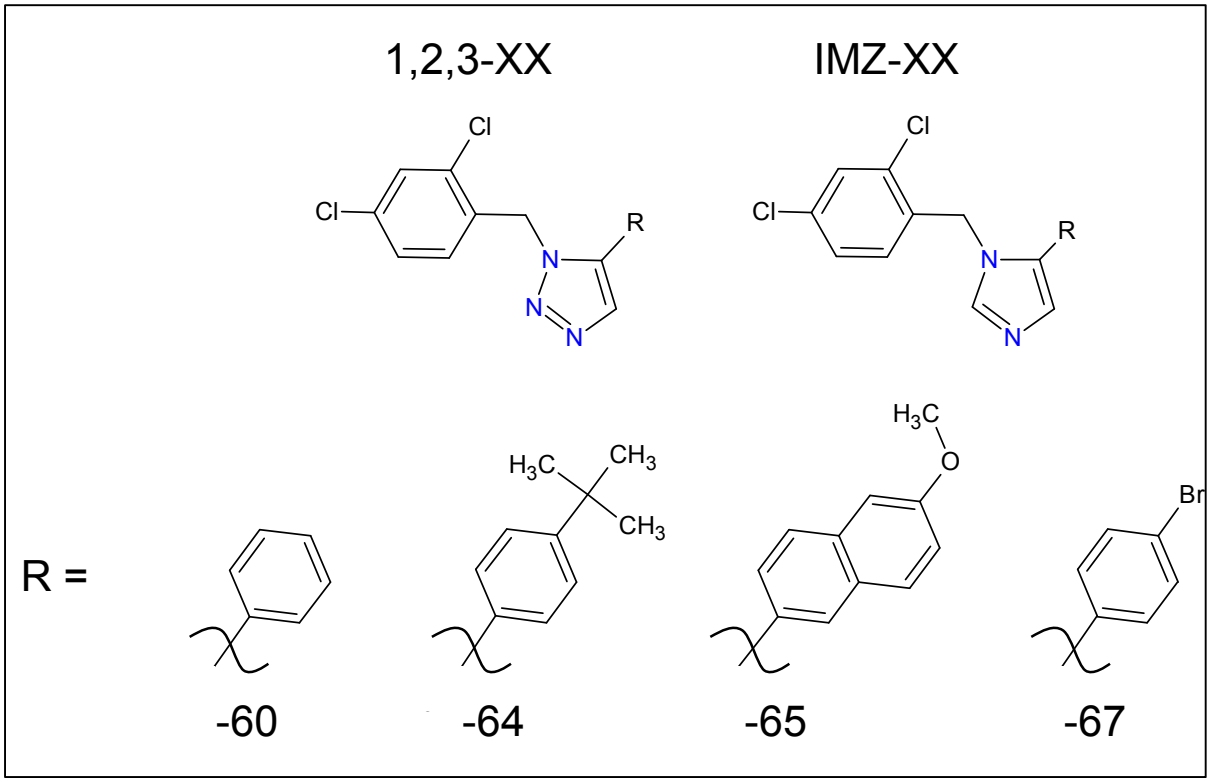

Figure 4.5 1-(2,4-dichlorobenzyl)-5-aryl-substituted azole library used for this study. The nomenclature used in the text is based on variable prefixes 123- or IMZ- to denote 1,2,3-triazole and imidazole respectively, followed by a common numbering system designating the variable substituent identity at the C5 position of the azole.

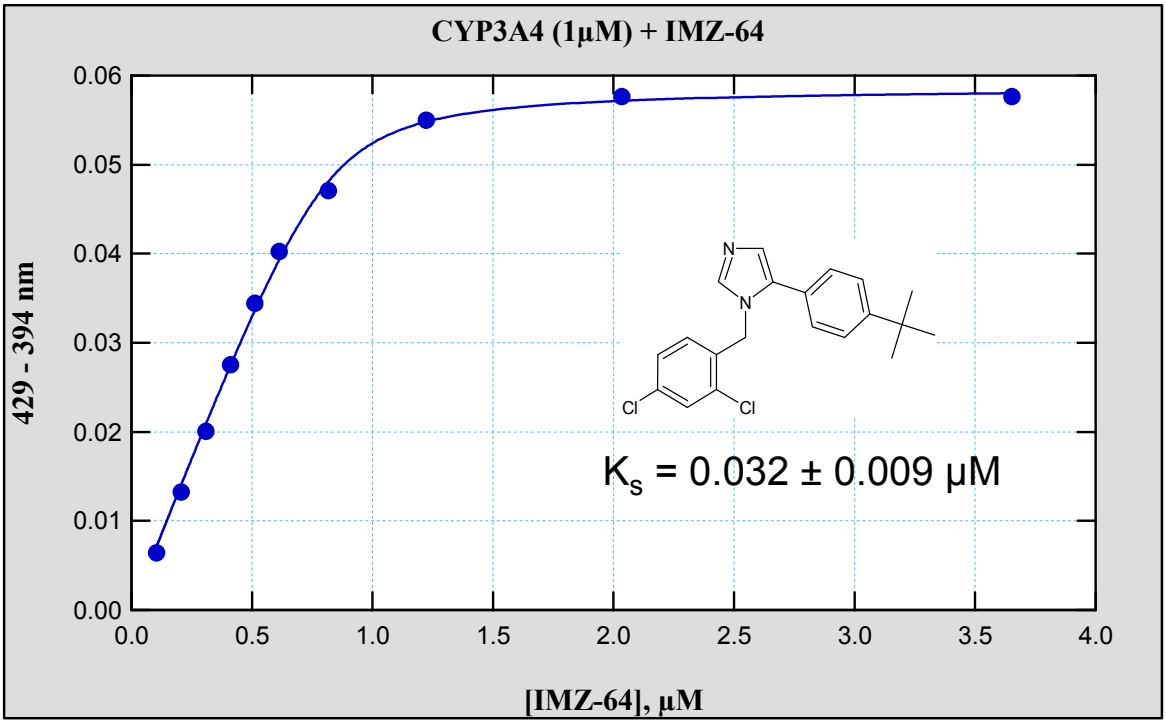

Figure 4.6 Representative CYP3A4 binding isotherm calculated for tight-binding IMZ-64 during UV/vis absorbance titration. Substantial affinity increases (18-100 fold) were observed when comparing IMZ analogs to 1,5-diaryl-substituted 123-TRZs. Note the deviation from hyperbolic binding by the clear presence of an inflection developing in the limit of the known CYP3A4 concentration (1µM). Affinity (K_s) was determined via non-linear regression to the quadratic binding equation (see Chapter 4.2.4).

Table 4.1 Tabulated CYP3A4 binding spectral results for 1,5-di-substituted 123-TRZs and corresponding IMZ analogs acquired at 25°C in 100 mM KPi, pH = 7.4, + 20% glycerol. Note, to facilitate accurate comparison of peak-trough amplitude (B_{max}), all spectra were normalized in CYP3A4 concentration relative to that present during titration of 123-60. Also included are the energetic benchmarks $\Delta\Delta G^{\circ}_{binding}$ (experimentally determined for CYP3A4) and $\Delta\Delta E_{DFT}$ (calculated by DFT) describing the energetic discrepancy between 123-TRZ and IMZ fragments, a benchmark value of which the efficiency of type II binding between all analog library comparisons were assessed (see Chapter 4.3.3).

	K_s, μM	+/-	$\Delta\Delta G^{\circ}$ (kcal/mol)	Bmax (norm to 123-60)	+/-	Molar Volume (-R), (Å^3)	Peak (nm)	Trough (nm)	Soret (nm)	Δ388 nm
123-60	19.9	3.7		0.039	0.003		430	410	423	-0.010
IMZ-60	0.479	0.056	**-2.20**	0.057	0.001	98.9	430	399	424	-0.028
123-64	0.82	0.23		0.044	0.001		426	393	422	-0.018
IMZ-64	0.054	0.016	**-1.61**	0.059	0.001	169.9	429	394	424	-0.026
123-65	4.04	0.43		0.026	0.001		429	411	423	-0.005
IMZ-65	0.361	0.064	**-1.43**	0.051	0.001	156.4	430	409	424	-0.023
123-67	4.60	0.31		0.037	0.001		425	394	420	-0.014
IMZ-67	0.286	0.033	**-1.64**	0.057	0.001	116.9	429	393	423	-0.025
1H-1,2,3-triazole				0.056	-		430	394	422	
Imidazole			**-2.80**	0.064	-		432	407	424	
	Calc.	**ΔΔE (kcal/mol)**	**-2.5**							

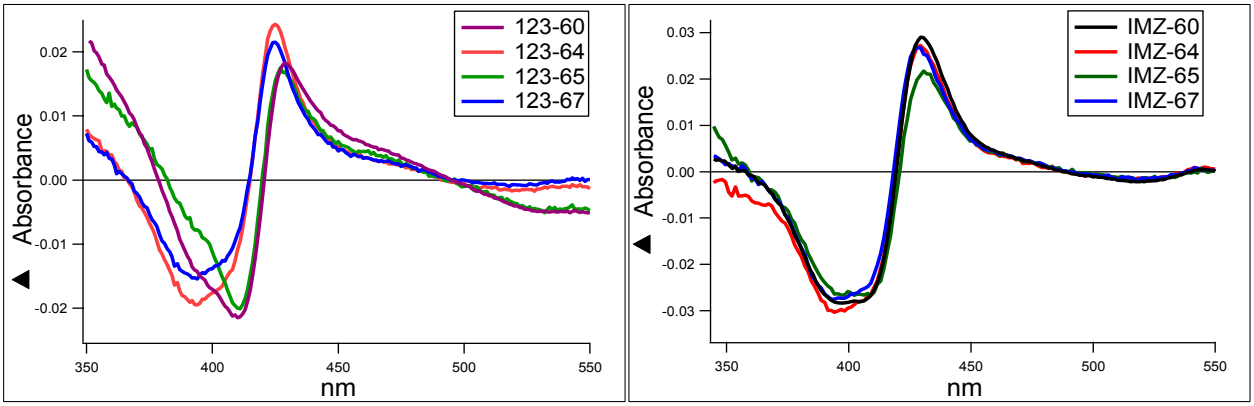

Figure 4.7 Fluctuating spectral behavior observed by UV/vis absorbance difference for CYP3A4-(123-TRZ) complexes (left); in contrast, the optical behavior appears more stable for the tighter-binding IMZ series. All binding data were normalized in protein concentration to facilitate accurate comparison of spectral amplitudes (see Chapter 4.2.4).

Table 4.2 Tabulated CYP19 (aromatase) in nanodisc binding and spectral results for 1,5-di-substituted-1,2,3-triazoles and corresponding imidazole analogs at 25°C in 100 mM KPi, pH = 7.4, + 10% glycerol. Note, to facilitate accurate comparison of peak-trough amplitude (B_{max}), all spectra were normalized in CYP19 concentration relative to that present during titration of IMZ-60. Interestingly, all 123-TRZ based compounds were tight-binders (nM affinity, Ks) suggesting this unrepresented triazole isomer may be useful for the development of aromatase inhibitor drugs. Surprisingly, the type I to type II conversion (Figure 4.8) observed for binding analog pair XX-65 did not result in increased affinity, suggesting heme interactions may be strained, or of relatively little importance to overall ligand binding affinity for this substituent profile.

	K_s, µM	+/-	ΔΔG° (kcal/mol)	Bmax (norm to IMZ-60)	+/-	Peak	Trough	Soret
1,2,3-60	0.514	0.099		0.0074	0.0002	424	391	417
IMZ-60	0.133	0.023	**-0.80**	0.023	0.001	428	394	420
1,2,3-64	0.434	0.054		0.0090	0.0002	427	409	418
IMZ-64	0.433	0.085	**0.00**	0.022	0.001	428	400	420
1,2,3-65	0.709	0.076	**TYPE I**	N/A	N/A	382	416	N/A
IMZ-65	0.785	0.105	**0.06**	0.025	0.001	430	408	421
1,2,3-67	0.212	0.088		0.0081	0.0006	425	396	418
IMZ-67	0.656	0.26	**0.67**	0.034	0.003	427	395	421

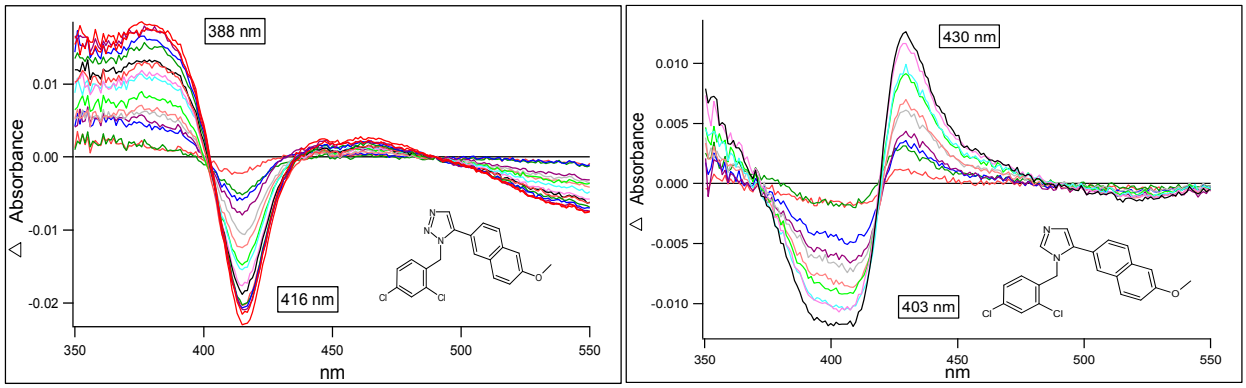

Figure 4.8 Type I to type II conversion observed for 123-65/IMZ-65 binding to aromatase (CYP19) incorporated nanodiscs in 100 mM KPi (pH = 7.4), + 10% glycerol. The type I spectrum induced by 123-65 binding suggests that azole substituent interactions with the protein (and/or sterics) are significant compared to (123-TRZ)-heme interactions in this complex. Surprisingly, the additional coordinate bonding interaction with heme iron in the CYP19-(IMZ-65) complex imparts only moderate affinity gain (K_s ~ 2-fold decrease) suggesting the influence of the heme interaction for this particular structure is minimal.

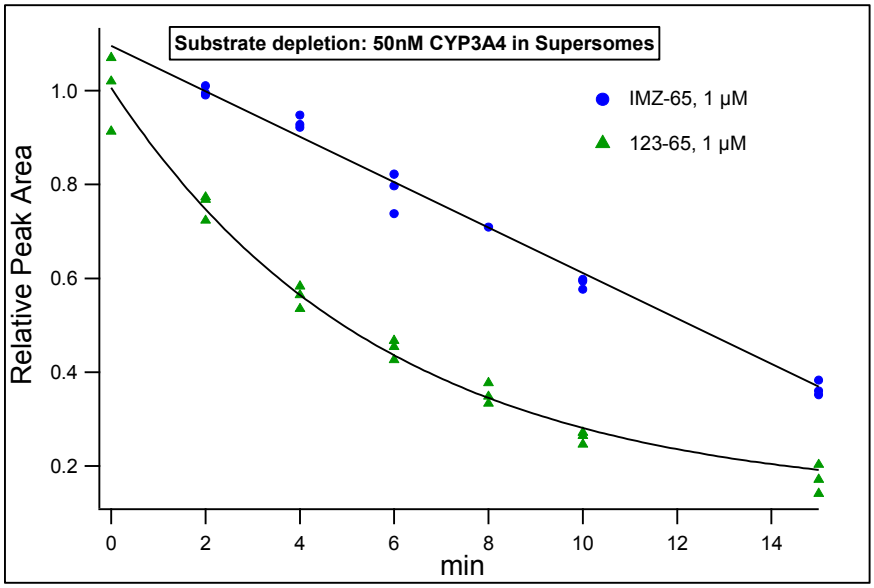

Figure 4.9 Representative CYP3A4-mediated depletion plot of analogs 123-65/IMZ-65. Depletion of 1 µM 1,5-disubstituted parent azole in the presence of 50 nM CYP3A4 (Supersomes) was monitored by LC/MS peak area ratios. The decay of parent IMZs appeared linear over the course of the incubation, consistent with the high affinity of the IMZ-based compounds studied for CYP3A4.

Table 4.3 Results of high mass accuracy metabolite ID study. Putative metabolites were identified on the basis of mass defect filtering of the total ion current (TIC). The percentages reported represent peak area ratio of a given metabolite species relative to the total integrated peak area for all detected metabolites.

123-TRZs	123-60	123-64	123-65	123-67	**IMZs**	IMZ-60	IMZ-64	IMZ-65	IMZ-67
% of total peak area									
Parent	30.2	20.5	56	11		49.7	70.5	61	35
N-dealkylation	60.8	50	32	84		45	23	32	57
Hydroxylation	6.7	6.3	11	5		2	3	2	1
#	2	3	2	2		3	3	2-3	~3
other	2.4	15	1					4	
Di-hydroxylated						0.27			
Hydroxylation + N-dealkylation		3.8				2.6	1.5		6
N-dealkylation %	87.0	66.6	72.7	94.4		90.2	83.6	84.2	89.1

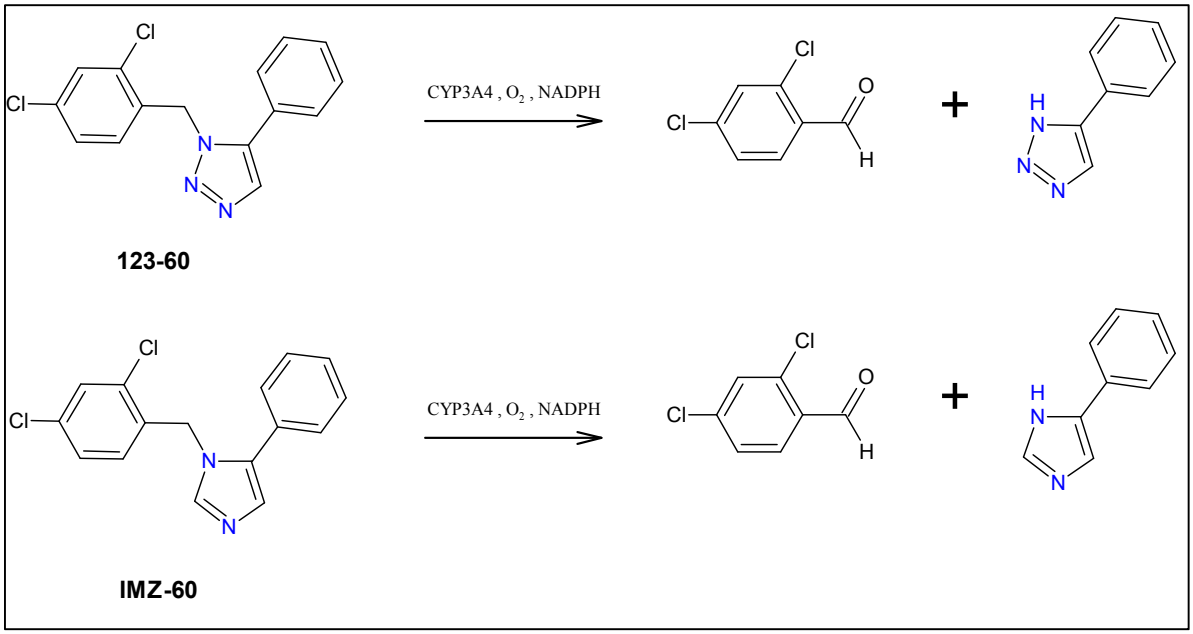

Figure 4.10 Common CYP3A4-mediated N-dealkylation pathway that dominates oxidative turnover of all type II binding 123-TRZ and IMZ analog library members studied here. The necessary 4-substitued 123-TRZ and IMZ metabolites were synthesized for use as standards during steady-state kinetic trials.

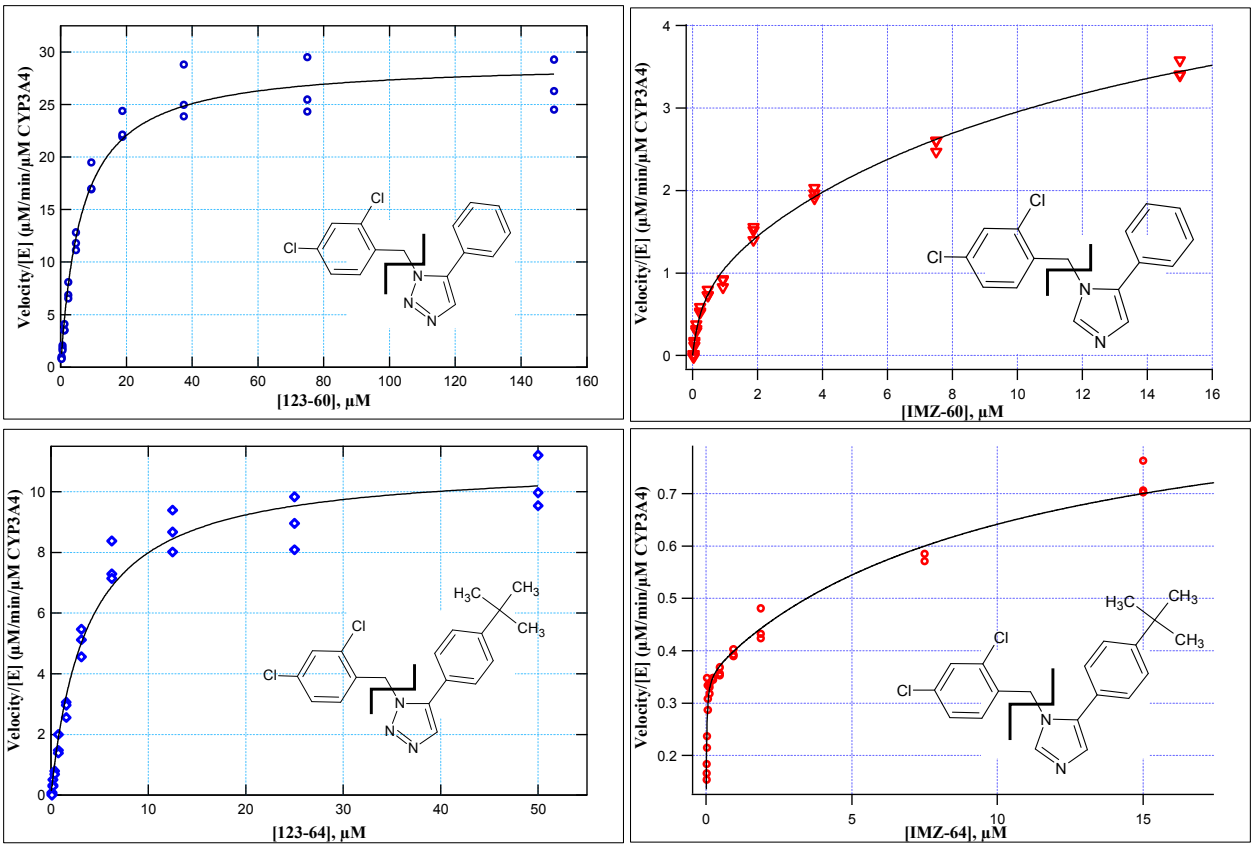

Figure 4.11a CYP3A4-mediated N-dealkylation steady-state kinetic v/[E_t] vs. [S] plots compared for 123-TRZ and IMZ based analogs. All apparent type II binding 123-TRZs studied were rapidly metabolized and displayed simple Michaelis-Menten kinetics. In contrast, although IMZ analogs were also readily turned over, they exhibited distinctly biphasic kinetics consistent with multiple binding. Interestingly, no evidence of multiple binding was observed during optical absorbance titration of the IMZs. This suggests the second binding equivalent is spectrally-silent.

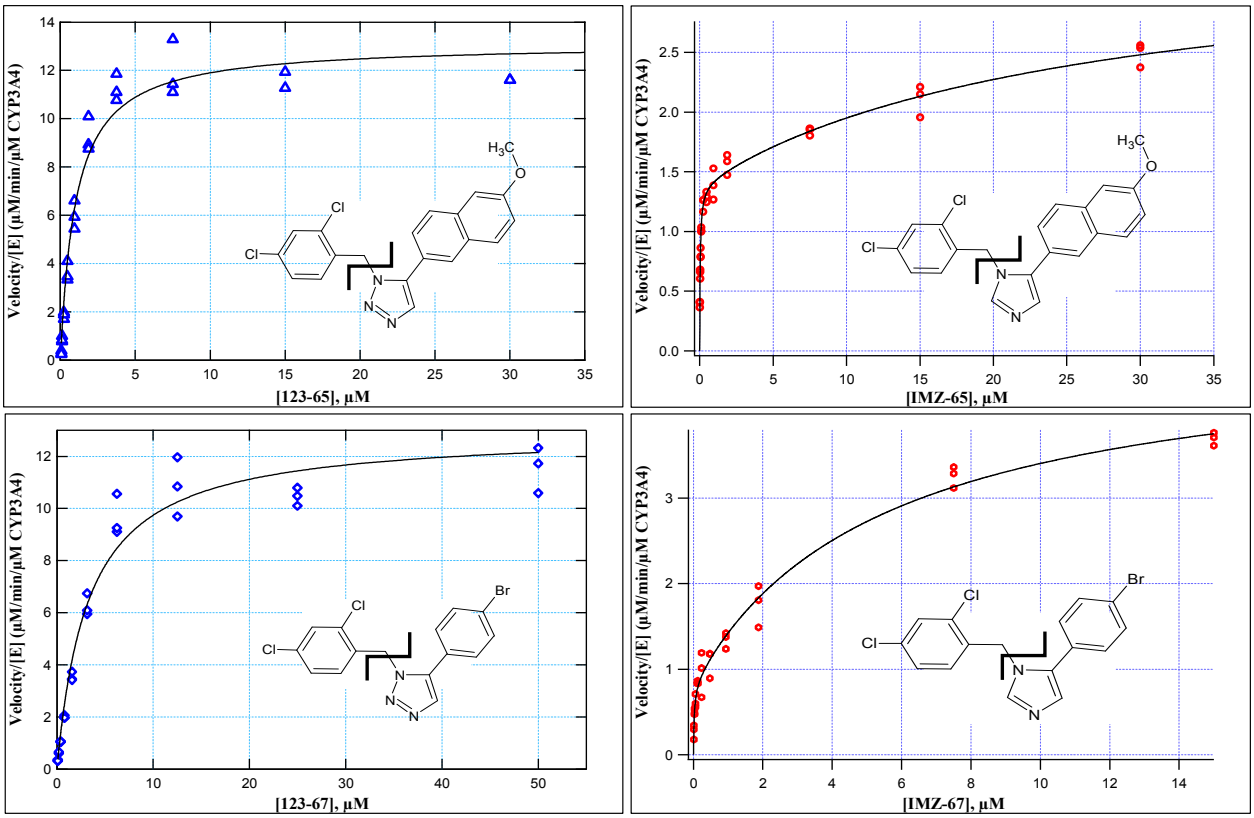

Figure 4.11b CYP3A4-mediated N-dealkylation steady-state kinetic v/[E_t] vs. [S] plots compared for 123-TRZ and IMZ based analogs. All apparent type II binding 123-TRZs studied were rapidly metabolized and displayed simple Michaelis-Menten kinetics. In contrast, although IMZ analogs were also readily turned over, they exhibited distinctly biphasic kinetics consistent with multiple binding. Interestingly, no evidence of multiple binding was observed during optical absorbance titration of the IMZs. This suggests the second binding equivalent is spectrally-silent.

Table 4.4 - 4.5 Steady-state kinetic parameters recovered from non-linear regression analysis of the v/[E_t] vs. [S] plots measured for CYP3A4-mediated N-dealkylation of 123-TRZ and IMZ analogs in Supersomes. All 123-TRZs displayed simple hyperbolic kinetics and were fit to the Michaelis-Menten equation; in contrast, all IMZ analogs displayed biphasic kinetics, indicative of multiple binding, and were fit to a two site-sequential binding model. Interestingly, no evidence of multiple binding was observed during optical absorbance titration of the IMZs suggesting that the second binding equivalent is spectrally silent.

	K_M (μM)	+/-	k_{cat} (min^{-1})	+/-
123-60	6.38	0.59	29.1	0.7
123-64	3.69	0.37	10.9	0.3
123-65	1.02	0.11	13.1	0.4
123-67	3.11	0.35	12.6	0.4

	K_{M1} (μM)	+/-	k_{cat1} (min^{-1})	+/-	K_{M2} (μM)	+/-	k_{cat2} (min^{-1})	+/-
IMZ-60	0.315	0.11	1.06	0.21	13.9	4.5	5.71	0.64
IMZ-64	0.014	0.003	0.36	0.01	10.3	2.8	0.98	0.06
IMZ-65	0.039	0.004	1.39	0.0036	26.3	8.8	3.4	0.4
IMZ-67	0.024	0.009	0.85	0.09	5.6	0.9	4.8	0.2

Table 4.6 Fold-increase in affinity (K_s) and fold-decrease turnover number (k_{cat}) observed for IMZ/123-TRZ analogs during comparative binding and turnover analysis. Note: k_{cat1} obtained from the fit of IMZ turnover velocity data to a two-site sequential model was used for the comparison.

Ligand	Ks (fold-change)	kcat (fold-change)
-60	42	27
-64	18	30
-65	11	9
-67	16	15

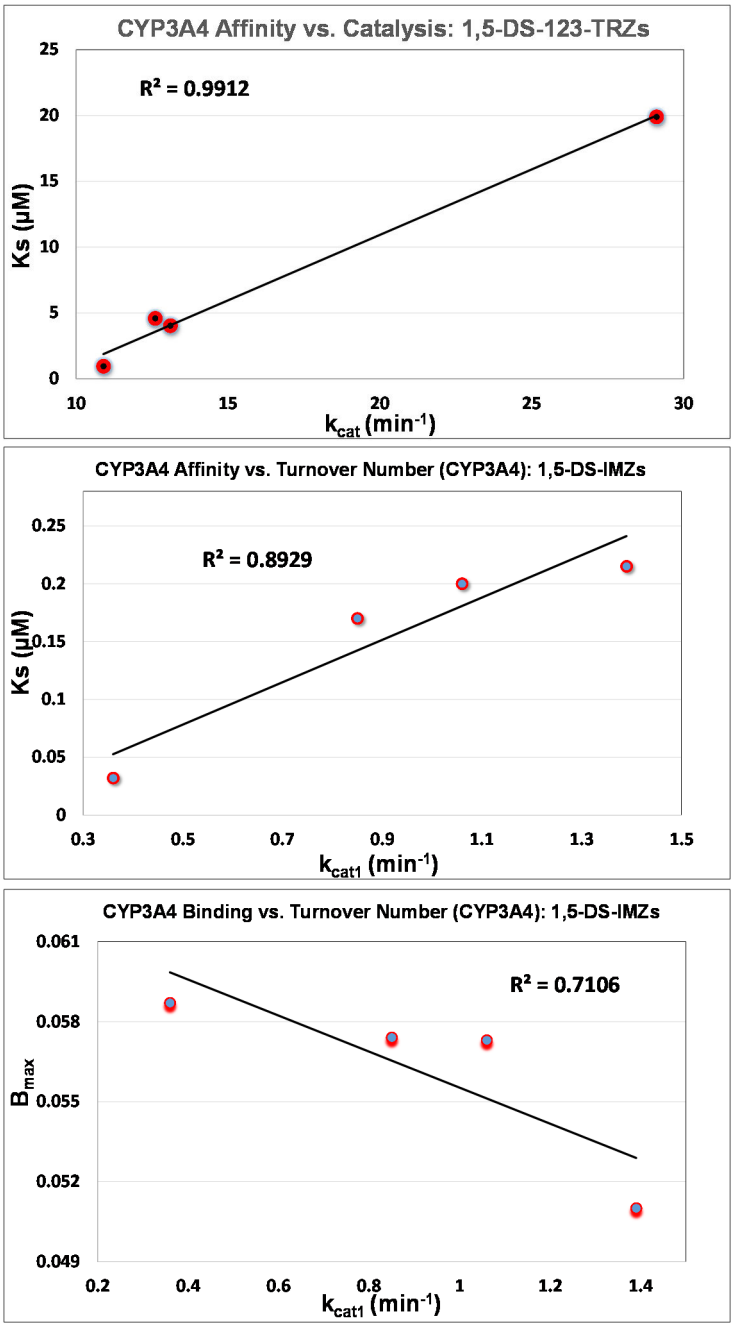

Figure 4.12 Correlations between recovered CYP3A4-mediated turnover number (k_{cat}) for N-dealkylation reaction and UV/vis absorbance spectral parameters for diaryl-substituted 123-TRZ and IMZ library members. (top) A good correlation exists between measured affinity (K_s) and turnover number (k_{cat}) for the 123-TRZs suggesting a relationship between type II heme binding efficiency and turnover velocity. (middle) A similar correlation exists only between K_s and k_{cat1} for the IMZ series, which exhibit biphasic kinetics indicative of multiple binding. (bottom) Moderate correlation between measured spectral amplitude and turnover number (k_{cat1}) for the IMZs suggesting a degree of variability in heme ligation efficiency exists even for tight-binding imidazoles.

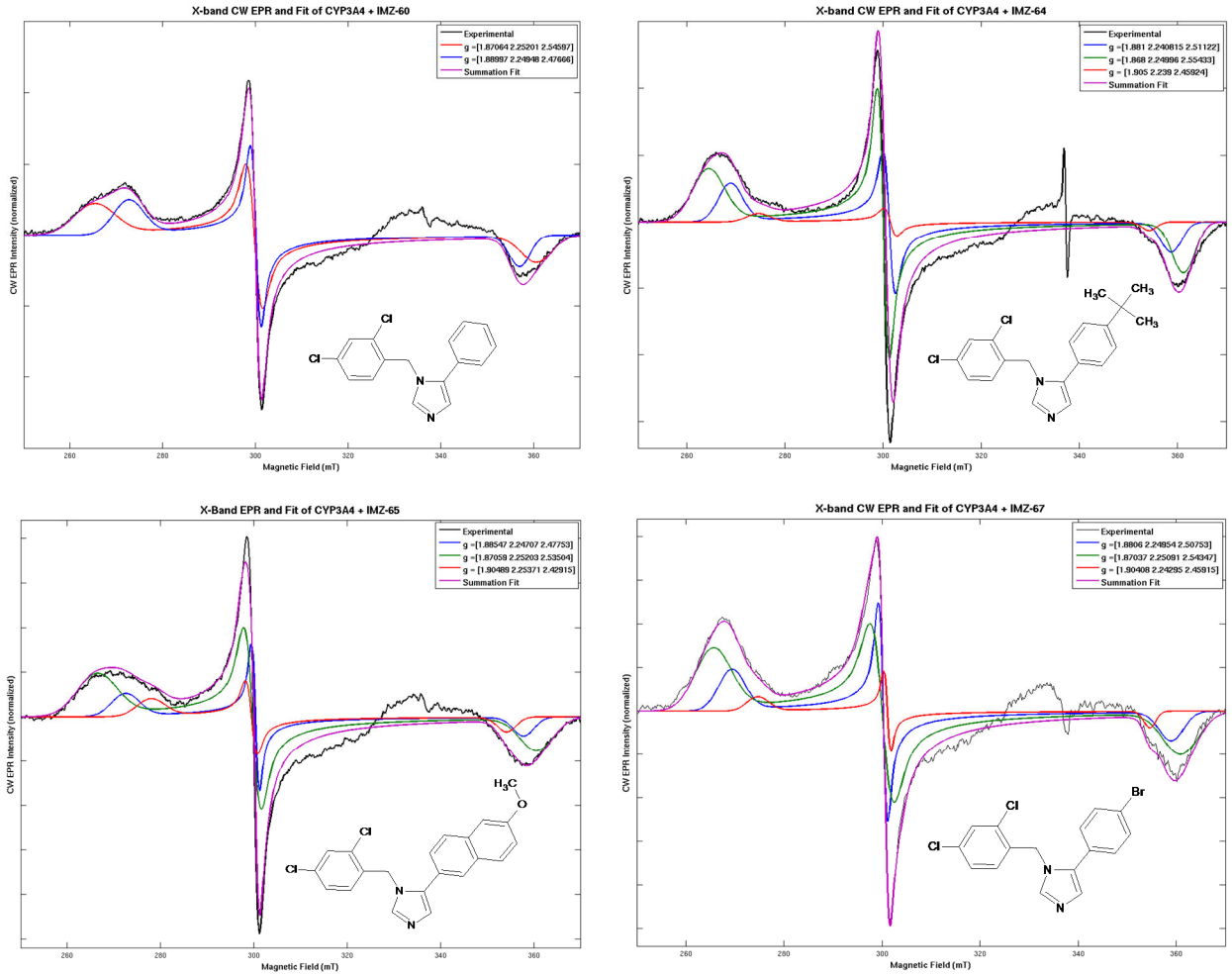

Figure 4.13 Tight-binding IMZs display type II structural heterogeneity in CYP3A4. CW EPR spectra for CYP3A4 complexes of 1,5-disubstituted-imidazoles acquired at 77K. The spectra display the best fits obtained in EasySpin for each spectral species to highlight the magnetic heterogeneity that exists. This heterogeneity may represent a distribution of coordinate bond lengths, rotation angles, etc. Protein concentration was 200 µM (200 mM KPi, pH = 7.4, + 20% glycerol).

Table 4.7 Tabulated EPR g-values for each species detected in spectra of CYP3A4-IMZ complexes with calculated crystal field parameters. Accurate g-values were obtained for the multiple species present in each spectrum via least-squares regression analysis in Easyspin (Chapter 2.2.4). The axial (Δ) and rhombic (V) crystal field parameters are calculated as a unitless quantity in terms of the spin orbit coupling constant (λ) for ferric ion (see Chapter 2.1.4).

Species	Ligand	gz	gy	gx	Δ/λ	V/λ	V/Δ
CYP3A4	N/A	**2.418**	**2.249**	**1.922**	**5.333**	**4.946**	**0.927**
a	IMZ-60	2.477	2.249	1.89	5.184	4.231	0.816
b		2.546	2.252	1.871	5.209	3.726	0.715
a	IMZ-64	2.554	2.25	1.868	5.240	3.669	0.700
b		2.511	2.241	1.881	5.394	3.953	0.733
a	IMZ-65	2.535	2.252	1.871	5.153	3.782	0.734
b		2.478	2.247	1.885	5.150	4.188	0.813
c		2.429	2.254	1.905	5.013	4.708	0.939
a	IMZ-67	2.543	2.251	1.87	5.197	3.735	0.719
b		2.508	2.25	1.881	5.200	3.984	0.766
c		2.459	2.243	1.904	5.435	4.446	0.818

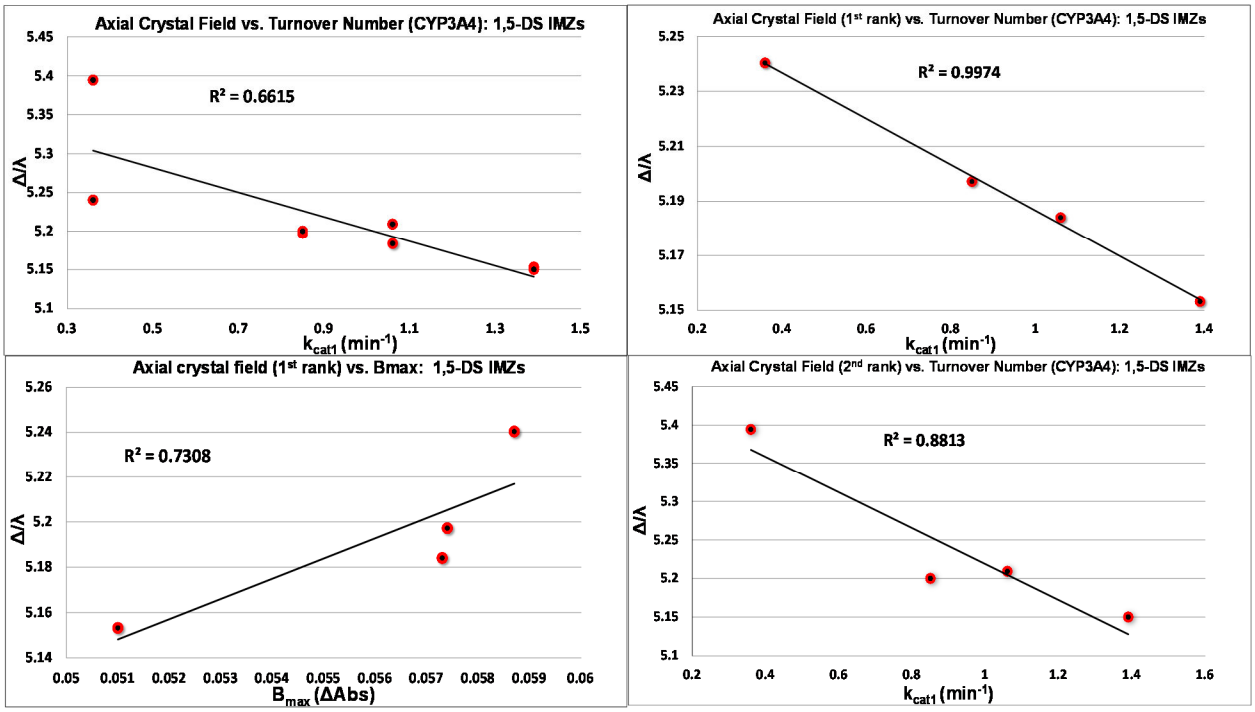

Figure 4.14 Functional and spectral correlations observed with axial crystal field parameter (Δ/λ) for N-Fe(III) ligated type II IMZ species detected by EPR. A correlation exists between Δ/λ and both spectral B_{max} and steady-state kinetic turnover number (k_{cat1}) determined for 1,5-disubstituted-imidazole library members in complex with CYP3A4. The axial crystal field parameter was calculated by the methods of Taylor (Chapter 2.2.4) from the g-values determined for each unique species detected in heterogeneous EPR spectra of the CYP3A4-IMZ complexes. The correlations suggests that type II IMZ ligands that maintain a larger axial distortion of the low-spin heme iron crystal field display relatively attenuated metabolism, and exhibit larger perturbations of the heme spin state equilibrium and Soret transition energy. (top left) Δ/λ for both 1st and 2nd rank components (integrated EPR spectral area) of each EPR spectrum correlated with steady state kinetic turnover number (k_{cat1}); (top right) Δ/λ correlation between 1st rank components and turnover number; (bottom right) Δ/λ correlation between 2nd rank components and turnover number; (bottom left) correlation between B_{max} optical parameter and 1st rank Δ/λ.

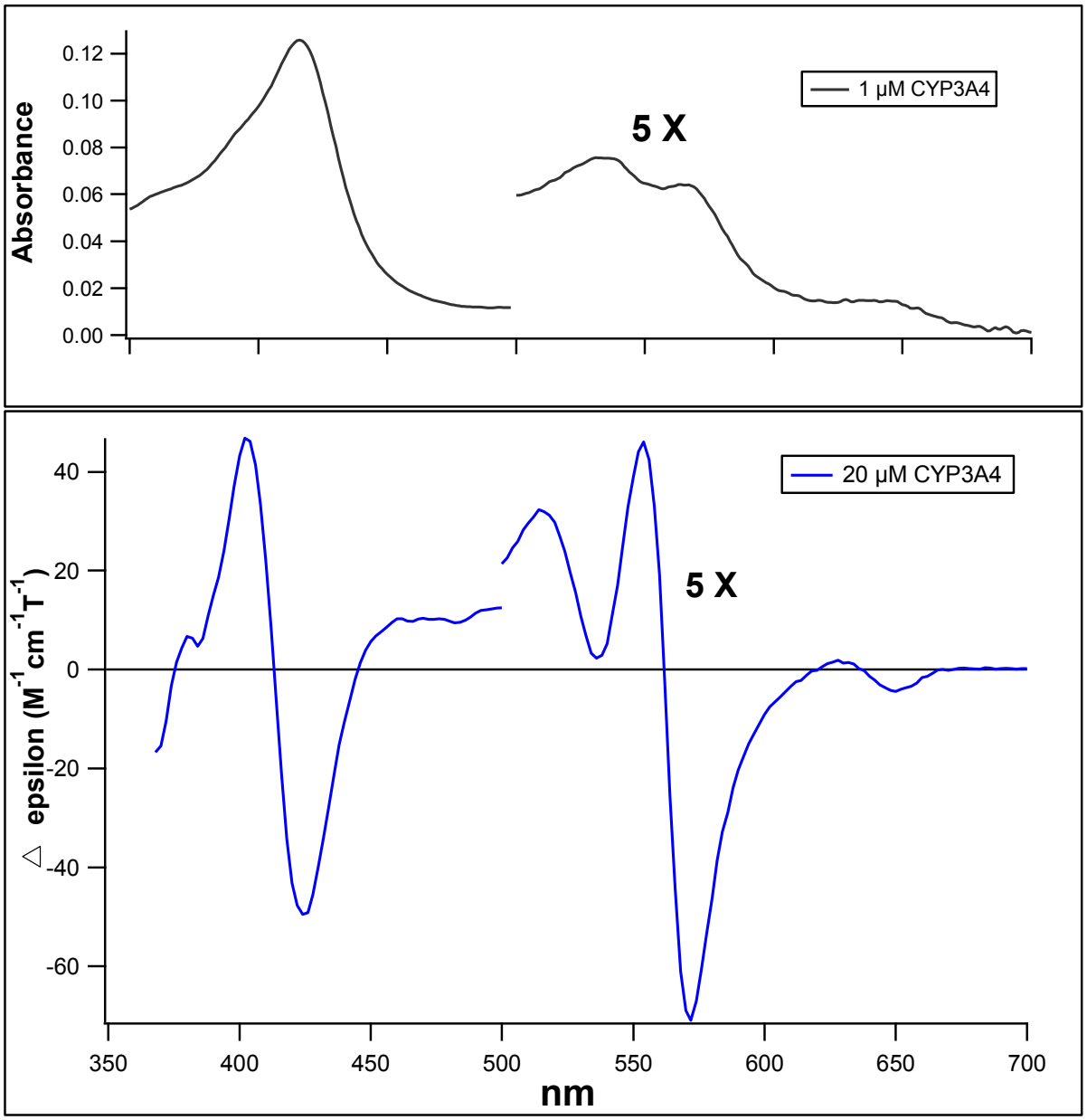

Figure 4.15 Comparison of UV/vis MCD spectrum (bottom) of ligand-free 3A4 at 298 K and 5 Tesla (100mM KPi + 20% glycerol), and the UV/vis absorbance spectrum (top) taken at 298 K. The pathlength used in MCD is 0.1 cm and thus requires higher protein concentration that that normally used for absorbance. The α:β region of the spectra (Q-region) is magnified as indicated to enhance the spectral features relative to the Soret. Note the added spectral details present within the Q-region of the MCD spectrum induced by the magnetic field; this region was the focus for the azole binding study here.

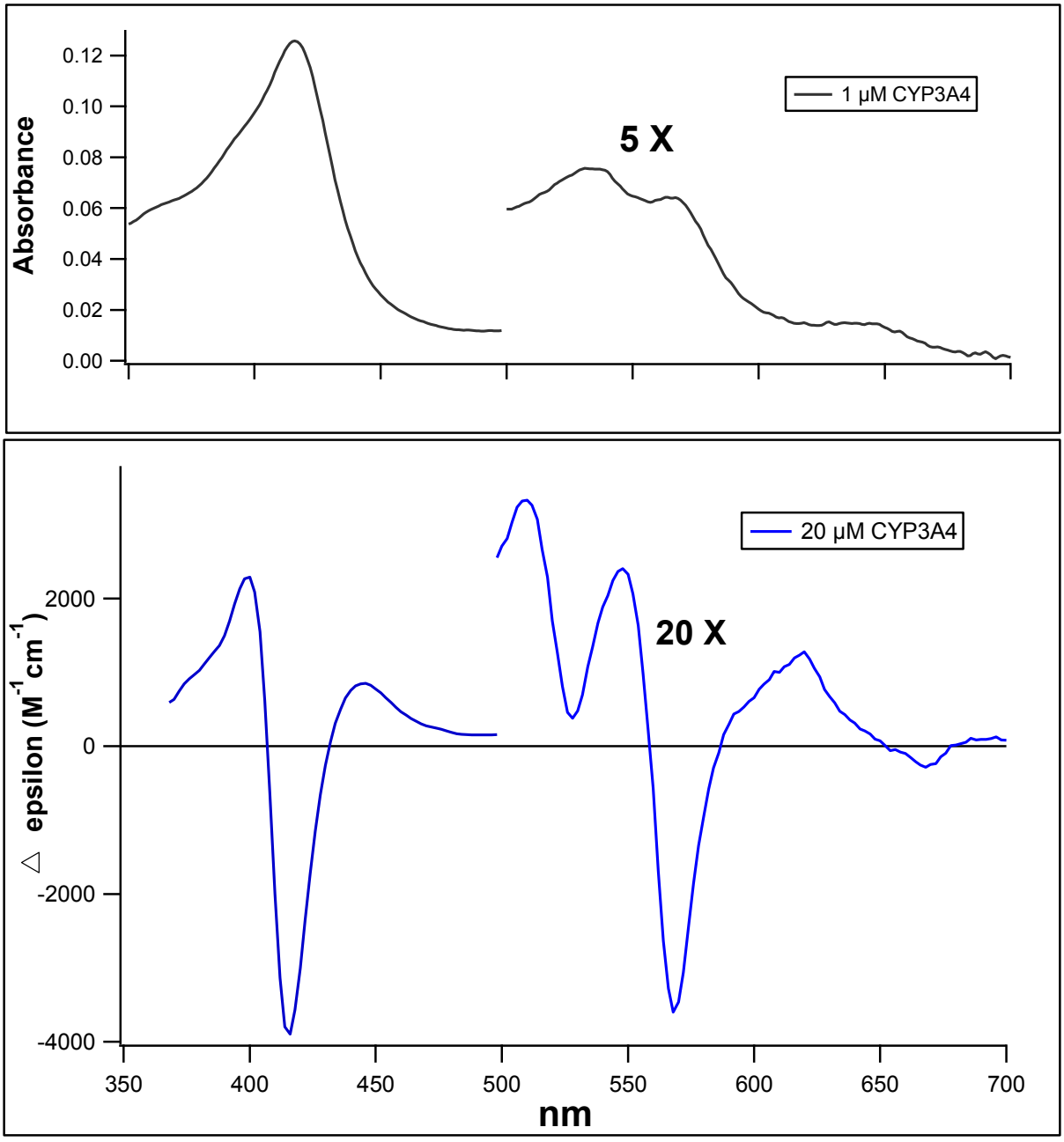

Figure 4.16 Comparison of UV/vis MCD spectrum (bottom) of ligand-free 3A4 at 4.7 K and 5 Tesla (100mM KPi + 55% glycerol, d8), and the UV/vis absorbance spectrum (top) taken at 298 K. The α:β region of the spectra (Q-region) is magnified as indicated to enhance the spectral features relative to the Soret. Note the ~ 4 fold increase in ratio of intensity of the Soret band to the region between 500-700 nm at low temp, consistent with dominance of the spectrum by C-term intensity, which is characteristic of paramagnetic hemoproteins.

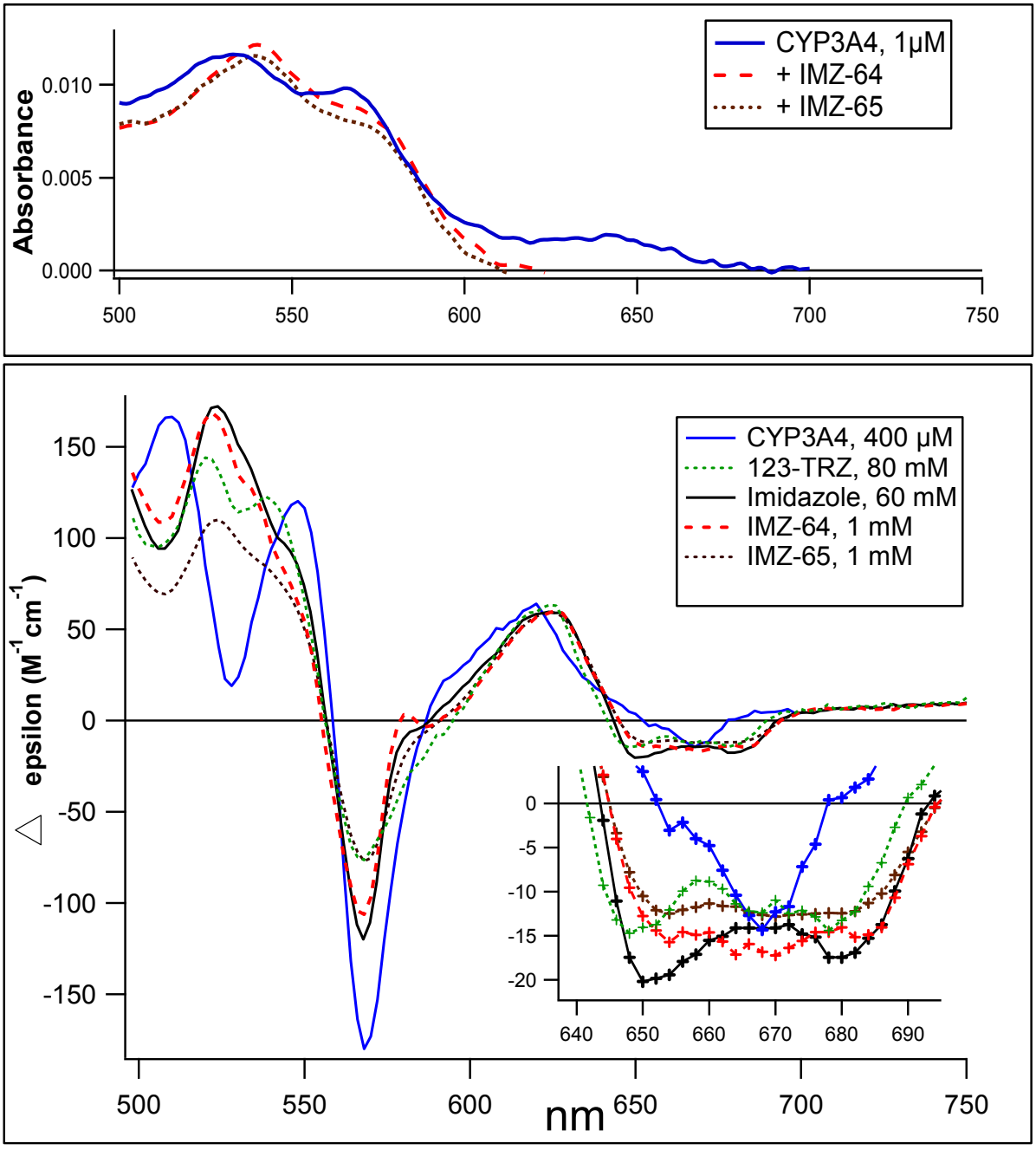

Figure 4.17 Visible MCD spectra obtained at 4.7 K for ligand-free CYP3A4 and select diaryl-substituted-IMZ complexes, and associated IMZ and 123-TRZ fragment references. The visible absorbance spectrum (298 K) for ligand-free CYP3A4 and in complex with IMZ-64/65 is shown at the top for comparison. The inset of the plot highlights the behavior of the spectrum centered near 670 nm that is rich in XY polarized CT features. A notable difference between the IMZ spectra and 123-TRZ complexes is the near complete coalescence of the peaks between 500-550 nm into one. Additionally, IMZ-64 displays a unique feature near the crossover at ~ 580 nm not observed for IMZ reference fragment complex or 123-TRZ. The spectrum of IMZ-65 complex

(the lowest affinity and most metabolically-labile IMZ library member) deviates considerably from the IMZ fragment reference. In contrast, the MCD spectral fingerprint of IMZ-64 (the highest affinity and least metabolically-labile library member) maintains relatively high fidelity to that of IMZ complex. These results suggest a degree of structural heterogeneity exists between IMZ-64 and IMZ-65 with IMZ-64 structure more closely related to the IMZ fragment structure at the level of the heme iron. Thus, IMZ-65 is anticipated to suffer from 'incomplete' heme coordination, which is possibly related to the increased turnover measured during steady-state turnover analysis. All samples contained 200 mM KPi (pH = 7.4) + 55% d8 glycerol buffer.

Table 4.8 CYP3A4, 298K, 5 Tesla

Ligand	Soret Peak (nm)	Δε ($M^{-1}cm^{-1}T^{-1}$)	Soret Crossover (nm)	Soret Trough (nm)	Δε ($M^{-1}cm^{-1}T^{-1}$)	Peak (nm)	Δε ($M^{-1}cm^{-1}T^{-1}$)	Trough (nm)	Δε ($M^{-1}cm^{-1}T^{-1}$)	Peak (nm)	Δε ($M^{-1}cm^{-1}T^{-1}$)	Crossover (nm)	Trough (nm)	Trough (nm)	Crossover (nm)	Minima (nm)	Δε ($M^{-1}cm^{-1}T^{-1}$)
none	402	46.8	413	424	-49.5	514	6.47	536	0.46	554	9.2	562	572	-14.2	620	650	-0.88

CYP3A4, visible 5-6 Tesla MCD spectra (4.7K) for select azole complexes

Ligand	Trough	Δε ($M^{-1}cm^{-1}$)	Peak (nm)	Δε ($M^{-1}cm^{-1}$)	Trough (nm)	Δε ($M^{-1}cm^{-1}$)	Peak (nm)	Δε ($M^{-1}cm^{-1}$)	Crossover (nm)	Trough (nm)	Δε ($M^{-1}cm^{-1}$)	Crossover (nm)	Peak (nm)	Δε ($M^{-1}cm^{-1}$)	Crossover (nm)	Minima* (nm)	Δε ($M^{-1}cm^{-1}$)
none	--	--	507	165.9	528	18.9	548	120.2	559	568	-179.8	587	620	64.0	650	668	-14.4
123-TRZ	506	92.9	521	141.7	530	112.2	538	120.6	556	568	-78.8	596	626	60.6	640	648	-17.0
IMZ	508	94.8	523	172.6	n/a	n/a	n/a	n/a	556	568	-119.4	589	626	59.6	643	650	-19.8
IMZ-64	508	108.7	522	168.3	n/a	n/a	n/a	n/a	555	568	-106.6	592	626	60.2	644	664	-16.8
IMZ-65	508	69.3	524	110.2	n/a	n/a	n/a	n/a	556	569	-76.8	592	624	59.3	644	654	-11.8

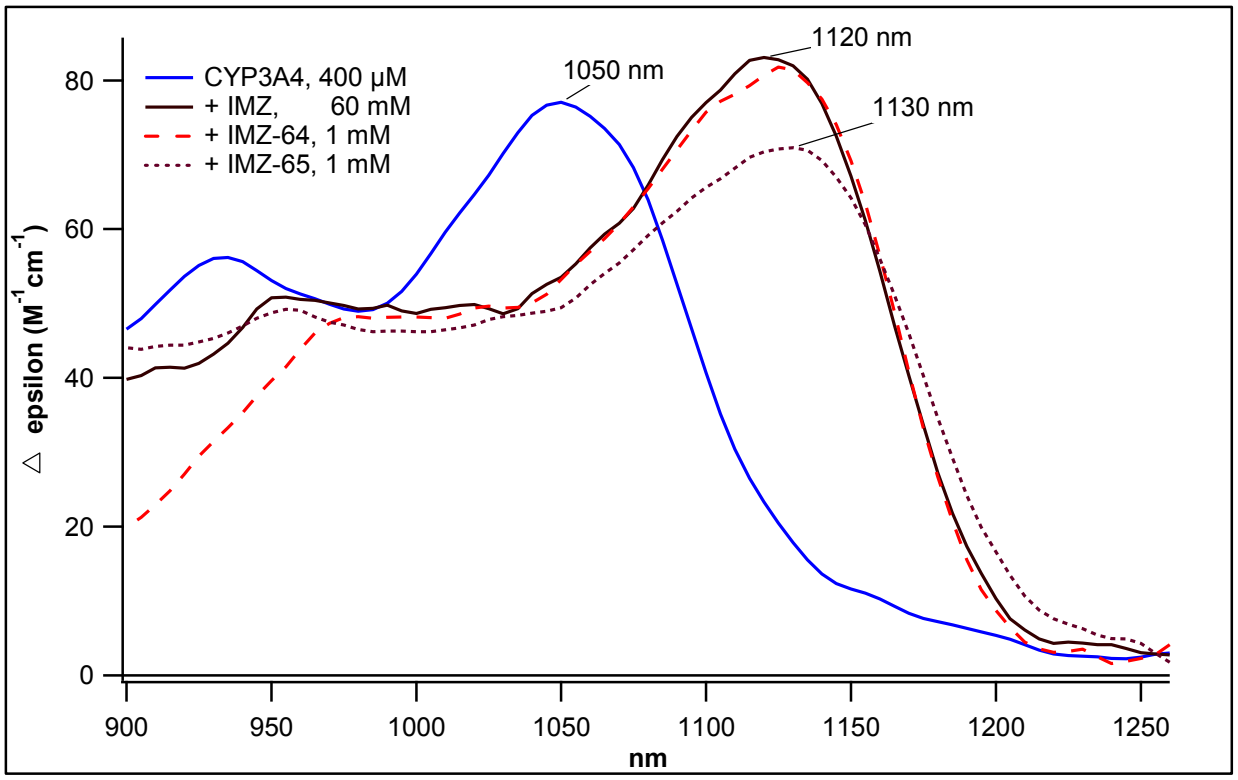

Figure 4.18 nIR MCD spectra for CYP3A4 and associated IMZ complexes taken at 4.7 K. Spectra of the IMZ complexes were obtained at 6 Tesla, while the ligand-free spectrum was acquired at 5 Tesla. Note the CYP3A4-(IMZ-64) complex appears to mirror the steric-free IMZ reference spectrum well, displaying similar lineshape, peak wavelength, and spectral amplitude, although some differences exist in the fine structure present to lower wavelengths. This is consistent with the visible MCD spectrum. In contrast, the nIR spectrum of CYP3A4-(IMZ-65) has altered peak shape, wavelength, and amplitude relative to IMZ reference, which suggests that IMZ-65 perturbs the heme field differentially (See Chapter 4.4); this observation is also consistent with deviations from the IMZ reference exhibited in the visible spectrum. These results highlight both the utility of using steric free azole reference fragments as spectroscopic measures to gauge 'type II strain,' as well as the strength of nIR MCD as a sensitive measure of subtle differences in heme ligation state. All samples contained 200 mM KPi (pH = 7.4) + 55% d8 glycerol buffer.

References

1. F. P. Guengerich, *Chem. Res. Toxicol.* **14**, 611 (2001).
2. M. B. Murataliev, R. Feyereisen, F. A. Walker, *Biochim. Biophys. Acta (BBA) - Proteins & Proteomics* **1698**, 1 (2004).
3. J. H. Dawson, L. A. Andersson, M. Sono, *J. Biol. Chem.* **258**, 13637 (1983).
4. M. Sono, M. P. Roach, E. D. Coulter, J. H. Dawson, *Chem. Rev.* **96**, 2841 (1996).
5. T. L. Poulos, B. C. Finzel, I. C. Gunsalus, G. C. Wagner, J. Kraut, *J. Biol. Chem.* **260**, 6122 (1985).
6. K. Auclair, P. Moënne-Loccoz, P. R. Ortiz de Montellano, *J. Am. Chem. Soc.* **123**, 4877 (2001).
7. P. Hlavica, *Curr. Drug Metab.* **8**, 594 (2007).
8. D. Goldfarb, M. Bernardo, H. Thomann, P. M. H. Kroneck, V. Ullrich, *J. Am. Chem. Soc.* **118**, 2686 (1996).
9. H. Thomann, M. Bernardo, D. Goldfarb, P. M. H. Kroneck, V. Ullrich, *J. Am. Chem. Soc.* **117**, 8243 (1995).
10. S. Shaik, D. Kumar, S. P. De Visser, A. Altun, W. Thiel, *Chem. Rev.* **105**, 2279 (2005).
11. P. A. Cole, C. H. Robinson, *J. Med. Chem.* **33**, 2933 (1990).
12. Y. Koltin, C. A. Hitchcock, *Curr. Opin. Chem. Biol.* **1**, 176 (1997).
13. K. J. McLean, D. Clift, D. G. Lewis, M. Sabri, P. R. Balding, M. J. Sutcliffe, D. Leys, A. Munro. *Trends Microbiol.* **14**, 220 (2006).
14. K. J. McLean, K. R. Marshall, A. Richmond, I. S. Hunter, K. Fowler, T. Kieser, S. S. Gurcha, G. S. Besra, A. W. Munro, *Microbiology* **148**, 2937 (2002).
15. K. J. McLean, P. Carroll, D. G. Lewis, A. J. Dunford, H. E. Seward, R. Neeli, M. R. Cheesman, L. Marsollier, P. Douglas, W. E. Smith, I. Rosenkrands, S. T. Cole, D. Leys, T. Parish, A. W. Munro, *J. Biol. Chem.* **283**, 33406 (2008).
16. S. G. Sligar, *Biochemistry* **15**, 5399 (1976).
17. J. B. Schenkman, *Biochemistry* **9**, 2081 (1970).
18. J. B. Schenkman, S. G. Sligar, D. L. Cinti, *Pharmacol. Ther.* **12**, 43 (1981).
19. J. B. Schenkman, D. L. Cinti, S. Orrenius, P. Moldeus, R. Kraschnitz, *Biochemistry* **11**, 4243 (1972).
20. T. L. Poulos, B. C. Finzel, A. J. Howard, *J. Mol. Biol.* **195**, 687 (1987).
21. S. G. Sligar, I. C. Gunsalus, *Proc. Natl. Acad. Sci.* **73**, 1078 (1976).
22. K. Kumaki, M. Sato, H. Kon, D. W. Nebert, *J. Biol. Chem.* **253**, 1048 (1978).
23. T. L. Poulos, A. J. Howard, *Biochemistry* **26**, 8165 (1987).
24. M. J. Honeychurch, H. A. O. Hill, L.-L. Wong, *FEBS Lett.* **451**, 351 (1999).
25. E. M. Isin, F. P. Guengerich, *J. Biol. Chem.* **281**, 9127 (2006).
26. E. M. Isin, F. P. Guengerich, *J. Biol. Chem.* **282**, 6863 (2007).
27. D. R. Davydov, H. Fernando, B. J. Baas, S. G. Sligar, J. R. Halpert, *Biochemistry* **44**, 13902 (2005).
28. A. G. Roberts, A. P. Campbell, W. M. Atkins, *Biochemistry* **44**, 1353 (2005).
29. P. A. Williams, J. Cosme, D. M. Vinkovic, A. Ward, H. C. Angove, P. J. Day, C. Vonrhein, I. J. Tickle, H. Jhoti, *Science* **305**, 683 (2004).
30. H. Park, S. Lee, J. Suh, *J. Am. Chem. Soc.* **127**, 13634 (2005).
31. L. H. Danni, P. Jin-Young, G. Larry, W. Lucy, *Proteins: Struct. Funct. Bioinf.* **55**, 895 (2004).

32. R. Raag, T. L. Poulos, *Biochemistry* **30**, 2674 (1991).
33. H. E. Seward, A. Roujeinikova, K. J. McLean, A. W. Munro, D. Leys, *J. Biol. Chem.* **281**, 39437 (2006).
34. I. G. Denisov, Y. V. Grinkova, M. A. McLean, S. G. Sligar, *J. Biol. Chem.* **282**, 26865 (2007).
35. E. M. Isin, C. D. Sohl, R. L. Eoff, F. P. Guengerich, *Arch. Biochem. Biophys.* **473**, 69 (2008).
36. G. P. Miller, F. P. Guengerich, *Biochemistry* **40**, 7262 (2001).
37. D.-S. Lee, Y.-S. Park, K. Yamane, E. Obayashi, H. Hori, Y. Shiro, *Biochemistry* **40**, 2669 (2001).
38. CC. Peng, J. T. Pearson, D. A. Rock, C. A. Joswig-Jones, J. P. Jones, *Arch. Biochem. Biophys.* **497**, 68 (2010).
39. J. T. Pearson, J. J. Hill, J. Swank, N. Isoherranen, K. L. Kunze, W. M. Atkins. *Biochemistry* **45**, 6341 (2006).
40. C. W. Locuson, J. M. Hutzler, T. S. Tracy, *Drug. Metab. Dispos.* **35**, 614 (2007).
41. J. M. Hutzler, R. J. Melton, J. M. Rumsey, M. E. Schnute, C. W. Locuson, L. C. Wienkers. *Chem. Res. Toxicol.* **19**, 1650 (2006).
42. A. Verras, I. D. Kuntz, P. R. Ortiz de Montellano, *J. Med. Chem.* **47**, 3572 (2004).
43. D. Harris, G. Loew, *J. Am. Chem. Soc.* **115**, 8775 (1993).
44. CC. Peng, J. L. Cape, T. Rushmore, G. J. Crouch, J. P. Jones, *J. Med. Chem.* **51**, 8000 (2008).
45. M. M. Ahlstrom, I. Zamora, *J. Med. Chem.* **51**, 1755 (2008).
46. B. K. Stewart, W. M. Christopher, L. V. Marcel, D. T. Richard, *Proteins: Struct. Funct. Bioinf.* **58**, 836 (2005).
47. P. Hlavica, *Biochim. Biophys. Acta, Proteins Proteomics* **1764**, 645 (2006).
48. G. Morra, A. Genoni, M. A. C. Neves, K. M. Merz, G. Colombo, *Curr. Med. Chem.* **17**, 25 (2010).
49. I. Golly, P. Hlavica, *Arch. Biochem. Biophys.* **292**, 287 (1992).
50. A. J. Dunford, K. J. McLean, M. Sabri, H. E. Seward, D. J. Heyes, N. S. Scrutton, A. W. Munro, *J. Biol. Chem.* **282**, 24816 (2007).
51. H. Ouellet, L. M. Podust, P. R. O. de Montellano, *J. Biol. Chem.* **283**, 5069 (2008).
52. L. M. Podust, H. Ouellet, J. P. von Kries, P. R. Ortiz de Montellano, *J. Biol. Chem.* **284**, 25211 (2009).
53. J. N. Lampe, R. Brandman, S. Sivaramakrishnan, P. R. Ortiz de Montellano, *J. Biol. Chem.* **285**, 9594 (March 26, 2010, 2010).
54. C. C. Liu, P. G. Schultz, *Nat. Biotech.* **24**, 1436 (2006).
55. P. Rydberg, T. H. Rod, L. Olsen, U. Ryde, *J. Phys. Chem. B* **111**, 5445 (2007).
56. T. I. Oprea, G. Hummer, A. E. Garcia, *Proc. Natl. Acad. Sci.* **94**, 2133 (1997).
57. D. R. Davydov, G. Hui Bon Hoa, J. A. Peterson, *Biochemistry* **38**, 751 (1998).
58. S. B. Philson, P. G. Debrunner, P. G. Schmidt, I. C. Gunsalus, *J. Biol. Chem.* **254**, 173 (1979).
59. T.-j. Deng, L. M. Proniewicz, J. R. Kincaid, J. Yeom, I. D. G. Macdonald, S. G. Sligar, *Biochemistry* **38**, 13699 (1999).
60. D. C. Haines, D. R. Tomchick, M. Machius, J. A. Peterson, *Biochemistry* **40**, 13456 (2001).
61. G. Truan, J. A. Peterson, *Arch. Biochem. Biophys.* **349**, 53 (1998).
62. H. Yeom, S. G. Sligar, H. Y. Li, T. L. Poulos, A. J. Fulco, *Biochemistry* **34**, 14733 (1995).

63. J. P. Clark, C. S. Miles, C. G. Mowat, M. D. Walkinshaw, G. A. Reid, N. D. A. Simon, S. K. Chapman, *J. Inorg. Biochem.* **100**, 1075 (2006).
64. J. R. Cupp-Vickery, T. L. Poulos, *Nat. Struct. Biol.* **2**, 144 (1995).
65. J. R. Cupp-Vickery, O. Han, C. R. Hutchinson, T. L. Poulos, *Nat. Struct. Mol. Biol.* **3**, 632 (1996).
66. D. L. Harris, Y.-T. Chang, G. H. Loew, *Mol. Eng* **5**, 143 (1995).
67. R. Raag, T. L. Poulos, *Biochemistry* **28**, 917 (1989).
68. P. R. Balding, C. S. Porro, K. J. McLean, M. J. Sutcliffe, J-D, Maréchal, A. W. Munro, S. P. deVisser, *J. Phys. Chem. A* **112**, 12911 (2008).
69. V. Cojocaru, P. J. Winn, R. C. Wade, *Biochim. Biophys. Acta, Gen. Subj.* **1770**, 390 (2007).
70. V. Helms, R. C. Wade, *Biophys. J.* **69**, 810 (1995).
71. R. C. Wade, *J. Comput.-Aided Mol. Des.* **4**, 199 (Jun, 1990).
72. R. C. Wade, K. J. Clark, P. J. Goodford, *J. Med. Chem.* **36**, 140 (1993).
73. R. C. Wade, P. J. Goodford, *J. Med. Chem.* **36**, 148 (1993).
74. V. Helms, E. Deprez, E. Gill, C. Barret, G. Hui Bon Hoa, R. C. Wade. *Biochemistry* **35**, 1485 (1996).
75. H. Volkhard, C. W. Rebecca, *Proteins Struct. Funct. Genet.* **32**, 381 (1998).
76. C. di Primo, H. Gaston Hui Bon, P. Douzou, S. Sligar, *Eur. J. Biochem.* **193**, 383 (1990).
77. R. Santos, J. Hritz, C. Oostenbrink, *J. Chem. Inf. Model.* **50**, 146 (2009).
78. K. Schleinkofer, Sudarko, P. J. Winn, S. K. Ludemann, R. C. Wade, *EMBO Rep.* **6**, 584 (2005).
79. G. J. Kleywegt, M. R. Harris, J-yu, Zou, T. C. Taylor, A. Wahlby, T. A. Jones, *Acta Crystallogr., Sect. D: Biol. Crystallogr.* **60**, 2240 (2004).
80. M. Petrek, M. Otyepka, P. Banas, P. Kosinova, J. Koca, J. Damborsky. *BMC Bioinf.* **7**, 316 (2006).
81. K. Kumaki, M. Sato, H. Kon, D. W. Nebert, *J. Biol. Chem.* **253**, 1048 (1978).
82. L. M. Podust, T. L. Poulos, M. R. Waterman, *Proc. Natl. Acad. Sci.* **98**, 3068 (2001).
83. L. C. Montemiglio, S. Gianni, B. Vallone, C. Savino, *Biochemistry* **49**, 9199 (2010).
84. CC. Peng, W. Shi, J. D. Lutz, K. L. Kunze, J. O. Liu, W. L. Nelson, N. Isoherranen, *Drug Metab. Dispos.* **40**, 426 (2012).
85. M. Meldal, C. W. Tornoe, *Chem. Rev.* **108**, 2952 (2008).
86. H. C. Kolb, K. B. Sharpless, *Drug Discovery Today* **8**, 1128 (2003).
87. H. Ouellet, P. M. Kells, P. R. Ortiz de Montellano, L. M. Podust, *Bioorg. Med. Chem. Lett.* **21**, 332 (2011).
88. A. E. Rettie, J. P. Jones, *Annu. Rev. Pharmacol. Toxicol.* **45**, 477 (2005).
89. A. E. Rettie, K. R. Korzekwa, K. L. Kunze, R. F. Lawrence, A. C. Eddy, T. Aoyama, H. V. Gelboin, F. J. Gonzalez, W. F. Trager, *Chem. Res. Tox.* **5**, 54 (2002).
90. M. A. Hummel, L. J. Dickmann, A. E. Rettie, R. L. Haining, T. S. Tracy, *Biochem. Pharmacol.* **67**, 1831 (2004).
91. K. R. Korzekwa, N. Krishnamachary, M. Shou, A. Ogai, R. A. Parise, A. E. Rettie, F. J. Gonzalez, T. S. Tracy, *Biochemistry* **37**, 4137 (1998).
92. H. Ouellet, J. B. Johnston, P. R. Ortiz de Montellano, *Arch. Biochem. Biophys.* **493**, 82 (2010).
93. C. M. Sassetti, D. H. Boyd, E. J. Rubin, *Mol. Microbiol.* **48**, 77 (2003).

94. L. M. Podust, J. P. von Kries, A. N. Eddine, Y. Kim, L. V. Yermalitskaya, R. Kuehne, J. Ouellet, T. Warrier, M. Altekoster, J.-S. Lee, J. Rademann, H. Oschkinat, S. H. E. Kaufmann, M. R. Waterman. *Antimicrob. Agents Chemother.* **51**, 3915 (2007).
95. A. Bellamine, A. T. Mangla, W. D. Nes, M. R. Waterman, *Proc. Natl. Acad. Sci.* **96**, 8937 (1999).
96. K. J. McLean, A. J. Warman, H. E. Seward, K. R. Marshall, H. M. Girvan, M. R. Cheesman, M. R. Waterman, A. W. Munro, *Biochemistry* **45**, 8427 (2006).
97. K. J. McLean, P. Lafite, C. Levy, M. R. Cheesman, N. Mast, I. A. Pikuleva, D. Leys, A. W. Munro, *J. Biol. Chem.* **284**, 35524 (2009).
98. C. P. S. Taylor, *Biochim. Biophys. Acta, Protein Struct.* **491**, 137 (1977).
99. F. A. Walker, *Coord. Chem. Rev.* **185-186**, 471 (1999).
100. D. L. Brautigan, B. A. Feinberg, B. M. Hoffman, E. Margoliash, J. Peisach, W. E. Blumberg, *J. Biol. Chem.* **252**, 574 (1977).
101. G. Zoppellaro, K. L. Bren, A. A. Ensign, E. Harbitz, R. Kaur, H. -P Hersleth, U. Ryde, L. Hederstedt, K. K. Andersson, *Biopolymers* **91**, 1064 (2009).
102. J. Peisach, J. O. Stern, W. E. Blumberg, *Drug Metab. Disp.* **1**, 45 (1973).
103. J. Peisach, W. E. Blumberg, A. Adler, *Ann. N.Y. Acad. Sci.* **206**, 310 (1973).
104. R. Tsai, C. A. Yu, I. C. Gunsalus, J. Peisach, W. Blumberg, W. H. Orme-Johnson, H. Beinert, *Proc. Natl. Acad. Sci.* **66**, 1157 (1970).
105. J. McMaster, V. S. Oganesyan, *Curr. Opin. Struct. Biol.* **20**, 615 (2010).
106. M. R. Cheesman, C. Greenwood, A. J. Thomson, A. G. Sykes, in *Advances in Inorganic Chemistry*. (Academic Press, 1991), vol. 36, pp. 201-255.
107. F. Paulat, N. Lehnert, *Inorg. Chem.* **47**, 4963 (2008).
108. P. A. Williams, J. Cosme, A. Ward, H. C. Angove, D. Matak Vinkovic, H. Jhoti, *Nature* **424**, 464 (2003).
109. C. M. Woods, C. Fernandez, K. L. Kunze, W. M. Atkins, *Biochemistry* **50**, 10041 (2012).
110. J. Tienan, K. Shin, Y. Yoshinori, *Eur. J. Org. Chem.* **2004**, 3789 (2004).
111. M. K. Bowman, in *Electron Paramagnetic Resonance - A Practitioner's Toolkit,* M. Brustalon, E. Giamello, Eds. (John Wiley & Sons, Hoboken, 2009), pp. 159-194.
112. S. A. Dikanov, M. K. Bowman, *J. Magn. Reson. A* **116**, 125 (1995).
113. S. A. Dikanov, A. M. Tyryshkin, M. K. Bowman, *J. Magn. Reson.* **144**, 228 (2000).
114. A. G. Roberts, M. J. Cheesman, A. Primak, M. K. Bowman, W. M. Atkins, A. E. Rettie. *Biochemistry* **49**, 8700 (2010).
115. S. Stoll, A. Schweiger, *J. Magn. Reson.* **178**, 42 (2006).
116. S. B. Piepho, P. N. Schatz, *Group Theory in Spectroscopy with Applications to Magnetic Circular Dichroism* (Wiley, New York, 1983).
117. P. M. Shaw, N. A. Hosea, D. V. Thompson, J. M. Lenius, F. P. Guengerich, *Arch. Biochem. Biophys.* **348**, 107 (1997).
118. I. G. Denisov, B. J. Baas, Y. V. Grinkova, S. G. Sligar, *J. Biol. Chem.* **282**, 7066 (2007).
119. J. H. Dawson, L. A. Andersson, M. Sono, *J. Biol. Chem.* **257**, 3606 (1982).
120. S. Van Doorslaer, E. Vinck, *Phys. Chem. Chem. Phys.* **9**, 4620 (2007).
121. S. A. Dikanov, M. K. Bowman, *J. Magn. Reson. Ser. A* **116**, 125 (1995).
122. S. A. Dikanov, A. M. Tyryshkin, M. K. Bowman, *J. Magn. Reson.* **144**, 228 (2000).
123. N. Lehnert, *J. Inorg. Biochem.* **110**, 83 (2012).
124. N. Lehnert, S. D. George, E. I. Solomon, *Curr. Opin. Chem. Biol.* **5**, 176 (2001).

125. G. Smulevich, A. Feis, C. Indiani, M. Becucci, M. P. Marzocchi, *J. Biol. Inorg. Chem.* **4**, 39 (1999).
126. F. Neri, D. Kok, M. A. Miller, G. Smulevich, *Biochemistry* **36**, 8947 (1997).
127. A. Feis, M. P. Marzocchi, M. Paoli, G. Smulevich, *Biochemistry* **33**, 4577 (1994).
128. E. J. Minkin V., Katritzky A., Garnovskii A, Denisko O., *Adv. Heterocycl. Chem.* **76**, 159 (2000).
129. M. Mandado, N. Otero, R. A. Mosquera, *Tetrahedron* **62**, 12204 (2006).
130. F. Tomas, J. L. M. Abboud, J. Laynez, R. Notario, L. Santos, S. O. Nilsson, J. Catalan, R. M. Claramunt, J. Elguero, *J. Am. Chem. Soc.* **111**, 7348 (1989).
131. I. Novak, T. Abu-Izneid, B. Kovač, L. Klasinc, *J. Phys. Chem. A* **113**, 9751 (2009).
132. L. Lunazzi, F. Parisi, D. Macciantelli, *J. Chem. Soc., Perkin Trans. 2*, 1025 (1984).
133. R. S. D. Moore D.S., *Adv. Inorg. Chem.* **32**, 171 (1988).
134. D. Russo, *Chem. Phys.* **345**, 200 (2008).
135. M. E. Johnson, C. Malardier-Jugroot, T. Head-Gordon, *Phys. Chem. Chem. Phys.* **12**, 393 (2010).
136. K. M. Halverson, B. A. Barry, *Biophys. J.* **85**, 1317 (2003).
137. P. M. A. Gadsby, A. J. Thomson, *J. Am. Chem. Soc.* **112**, 5003 (1990).
138. P. Belin, M. H. Le Du, A. Fielding, O. Lequin, M. Jacquet, J-B. Charbonnier, A. Lecoq, R. Thal, M. Courçon, C. Masson, C. Dugave, R. Genet, J-L. Pernodet, M. Gondry, *Proc. Natl. Acad. Sci.* **106**, 7426 (2009).
139. J. Pearson, U. P. Dahal, D. Rock, CC. Peng, J. O. Schenk, C. Joswig-Jones, J. P. Jones, *Arch. Biochem. Biophys.* **511**, 69 (2011).
140. R. Raag, S. A. Martinis, S. G. Sligar, T. L. Poulos, *Biochemistry* **30**, 11420 (1991).
141. S. A. Martinis, W. M. Atkins, P. S. Stayton, S. G. Sligar, *J. Am. Chem. Soc.* **111**, 9252 (1989).
142. E. M. J. Gillam, T. Baba, B. R. Kim, S. Ohmori, F. P. Guengerich, *Arch. Biochem. Biophys.* **305**, 123 (1993).
143. K. T. Olkkola, J. Ahonen, P. J. Neuvonen, *Anesthesia & Analgesia* **82**, 511 (1996).
144. M. Congreve, G. Chessari, D. Tisi, A. J. Woodhead, *J. Med. Chem.* **51**, 3661 (2008).
145. X. Rugang, C. Qiuyun, X. Jin, Z. Huaming, *Steroids* **55**, 488 (1990).
146. R. W. Noble, Q. H. Gibson, *J. Biol. Chem.* **245**, 2409 (1970).
147. R. S. Obach, A. E. Reed-Hagen, *Drug Metab. Dispos.* **30**, 831 (2002).
148. A. Nath, W. M. Atkins, *Drug Metab. Dispos.* **34**, 1433 (2006).
149. Y. Zhao, D. G. Truhlar, *Acc. Chem. Res.* **41**, 157 (2008).
150. M. Swart, M. Guell, J. M. Luis, M. Sola, *J. Phys. Chem. A* **114**, 7191 (2010).
151. B. M. Bode, M. S. Gordon, *J. Mol. Graphics Modell.* **16**, 133 (1998).
152. A. Das, J. Zhao, G. C. Schatz, S. G. Sligar, R. P. Van Duyne, *Anal. Chem.* **81**, 3754 (2009).
153. A. G. Roberts, S. E. A. Sjogren, N. Fomina, K. T. Vu, A. Almutairi, J. R. Halpert, *Biochemistry* **50**, 2123 (2011).
154. A. G. Roberts, J. Yang, J. Halpert, S. Nelson, K. T. Thummel, W. M. Atkins, *Biochemistry* **50**, 10804 (2011).
155. D. R. Davydov, E. Deprez, G. H. B. Hoa, T. V. Knyushko, G. P. Kuznetsova, Y. M. Koen, A. I. Archakov, *Arch. Biochem. Biophys.* **320**, 330 (1995).
156. H. Fukada, K. Takahashi, *Proteins Struct. Funct. Bioinf.* **33**, 159 (1998).
157. H. C. Helgeson, D. H. Kirkham, *Am. J. Sci.* **274**, 1199 (1974).
158. N. G. Robert, K. Nand, M. L. Rebecca, *J. Phys. Chem. Ref. Data* **31**, 231 (2002).

159. E. C. W. Clarke, D. N. Glew, *Trans. Faraday Soc.* **62**, (1966).
160. P. C. Hariharan, J. A. Pople, *Theor. Chim. Acta.* **28**, 213 (1973).
161. J. A. J. Catalan, J. Elguero, *Adv. Heterocycl. Chem.* **41**, 187 (1987).
162. D. Goldfarb, M. Bernardo, H. Thomann, P. M. H. Kroneck, V. Ullrich, *J. Am. Chem. Soc.* **118**, 2686 (1996).
163. B. Wang, R. I. Sanchez, R. B. Franklin, D. C. Evans, S.-E. W. Huskey, *Drug Metab. Dispos.* **32**, 1209 (2004).
164. H.-l. Lin, U. M. Kent, P. F. Hollenberg, *J. Pharm. Exp. Therapeutics* **301**, 160 (2002).
165. F. P. Guengerich, *Mol. Pharmacol.* **33**, 500 (1988).
166. F. Peter Guengerich, *Life Sci.* **47**, 1981 (1990).
167. A. Krasinski, Z. Radic, R. Manetsch, J. Raushel, P. Taylor, K. B. Sharpless, H. C. Kolb, *J. Am. Chem. Soc.* **127**, 6686 (2005).
168. M. Sono, J. H. Dawson, *J. Biol. Chem.* **257**, 5496 (1982).
169. D. S. Wofford, D. M. Forkey, J. G. Russell, *J. Org. Chem.* **47**, 5132 (1982).
170. B. K. Muralidhara, S. Negi, C. C. Chin, W. Braun, J. R. Halpert, *J. Biol. Chem.* **281**, 8051 (2006).
171. J. B. Johnston, P. M. Kells, L. M. Podust, P. R. Ortiz de Montellano, *Proc. Natl. Acad. Sci.* **106**, 20687 (2009).
172. I. F. Sevrioukova, T. L. Poulos, *Proc. Natl. Acad. Sci.* **107**, 18422 (2010).
173. C. Sheng, W. Zhang, J. Ji, M. Zhang, Y. Song, H. Xu, J. Zhu, Z. Miao, Q. Jiang, J. Yao, Y. Zhou, J. Zhu, J. Lu, *J. Med. Chem.* **49**, 2512 (2006).
174. K. E. Thummel, G. R. Wilkinson, *Annu. Rev. Pharmacol. Toxicol.* **38**, 389 (1998).
175. C-C. Peng, J. T. Pearson, D. A. Rock, C. A. Joswig-Jones, J. P. Jones, *Arch. Biochem. Biophys.* **497**, 68-81 (2010).
176. L. Zhang, X. Chen, P. Xue, H. H. Y. Sun, I. D. Williams, K. B. Sharpless, V. V. Fokin, G. Jia, *J. Am. Chem. Soc.* **127**, 15998 (2005).
177. L. Roumen, J. W. Peeters, J. M. A. Emmen, I. P. E. Beugels, E. M. G. Custers, M. de Gooyer, R. Plate, K. Pieterse, P. A. J. Hilbers, J. F. M. Smits, J. A. J. Vekemans, D. Leysen, H. C. J. Ottenheijm, H. M. Janssen, J. J. Rob, Hermans, *J. Med Chem.* **53**, 1712 (2010).
178. T. Omura, R. Sato, *J. Biol. Chem.* **239**, 2370 (1964).
179. H. M. Girvan, H. S. Toogood, R. E. Littleford, H. E. Seward, W. E. Smith, I. S. Ekanem, D. Leys, M. R. Cheesman, A. W. Munro, *Biochem J.* **417**, 65 (2009).
180. J. McKnight, M. R. Cheesman, A. J. Thomson, J. S. Miles, A. W. Munro, *Eur. J. Biochem.* **213**, 683 (1993).
181. A. J. Thomson, P. M. A. Gadsby, *J. Chem. Soc., Dalton Trans.* **0**, 1921 (1990).
182. D. Ghosh, J. Griswold, M. Erman, W. Pangborn, *Nature* **457**, 219 (2009).
183. S. Rendic, *Drug Metab. Rev.* **34**, 83 (2002).
184. S. H. Bui, K. J. McLean, M. R. Cheesman, J. M. Bradley, S. E. J. Rigby, C. W. Levy, D. Leys, A. W. Munro, *J. Biol. Chem.* **287**, 19699 (2012).
185. W. M. Atkins, H. Qian, *Biochemistry* **50**, 3866 (2011).
186. T. Koudriakova, E. Iatsimirskaia, I. Utkin, E. Gangl, P. Vouros, E. Storozhuk, D. Orza, J. Marinina, N. Gerber, *Drug Metab. Dispos.* **26**, 552 (1998).
187. G. N. Kumar, A. D. Rodrigues, A. M. Buko, J. F. Denissen, *J. Pharmacol. Exp. Ther.* **277**, 423 (1996).